Technische Universität München

TUM School of Natural Sciences

TUM

Regulating Synthetic Dissipative Matter through Chemically Fueled Reaction Cycles: Exploring Kinetics-Properties Relationships

Xiaoyao Chen

Vollständiger Abdruck der von der TUM School of Natural Sciences der Technischen Universität München zur Erlangung des akademischen Grades einer

Doktorin der Naturwissenschaften (Dr. rer. nat.)

genehmigten Dissertation.

Vorsitz:

apl. Prof. Dr. Wolfgang Eisenreich

Prüfende der Dissertation:

1. Prof. Dr. Job Boekhoven

2. Prof. Dr. Guillermo Monreal Santiago

Die Dissertation wurde am 17.06.2024 bei der Technischen Universität München eingereicht und durch TUM School of Natural Sciences am 10.07.2024 angenommen.

Abstract

Dissipative matter is any matter that can only be sustained by a continuous supply of energy; thereby, it exists out of equilibrium and is ubiquitous in nature, from inanimate matter to living matter. Different from in-equilibrium matter, which is thermodynamically controlled, dissipative matter is under kinetic control and thermodynamically labile. Life is indeed a prime example of dissipative matter. In cells, energy harvested from light or chemicals is converted and transferred to small molecules with high chemical potential. Those energy-rich molecules are chemical fuels to regulate all kinds of biological dissipative matter via chemical reaction cycles. As a result, the kinetics of chemical reaction networks regulates the properties of the dissipative matter. Also, multiple theories on dissipative matter have predicted how chemically fueled matter's properties respond to the reaction kinetics. While there is a clear understanding of matter and its behavior in or close to equilibrium, the current state of our knowledge regarding the kinetics-properties relationship of dissipative matter is limited due to the absence of suitable synthetic examples or models. Therefore, this thesis aims to use chemically fueled self-assembly and phase separation as a model for dissipative matter. Specifically, the aim has been to develop reaction cycles that regulate dissipative matter and test the relation between energy dissipation rates and the underlying material properties.

In chemically fueled self-assembly, the chemical reaction cycle that transduces energy consists of at least two concurrent reactions, i.e., an activation reaction that activates building blocks to assemble and a deactivation reaction that deactivates the building blocks to disassemble. Despite the wealth of chemical reactions, it is challenging to establish suitable reaction cycles due to the crucial requirement that the activation and deactivation of molecules must occur continuously in a single system, mediated by separate reagents. Besides, the repeated cycles of activation and deactivation require a high turnover of molecules (precursors), indicating any side reactions would be detrimental to the chemically fueled assembly.

I first show how we manage to suppress the side product *N*-acylurea in a carbodiimide-fueled reaction cycle by testing the effects of fuels' structures, precursors' concentration and structures, additives, temperature, and pH. The optimal condition for a highly effective carbodiimide-driven cycle is a combination of low temperature, low pH, and 10% pyridine as a fuel fraction (Chapter 6). Then, I discuss a new carbodiimide-fueled reaction cycle that forms transient 5(*4H*)-oxazolones. This reaction cycle is robust enough to operate under a wide range of conditions, effective in utilizing the fuel, versatile in the scope of the precursor, and able to

drive different chemically fueled assemblies. Most importantly, the activated state, 5(*4H*)-oxazolone, has a long half-life, making it possible to catalyze the deactivation through hydrolysis of the oxazolone without changing the pH or temperature (Chapter 7). Finally, I show how chemically fueled coacervates driven by the oxazolone-forming cycle respond to the reaction cycle kinetics, especially to the deactivation. By increasing the pyridine amount to accelerate the deactivation and decrease the half-life of the oxazolones, droplets take a longer time to emerge and reach a stable size in a steady state. Most importantly, droplets' stable size is decreased (Chapter 8).

In conclusion, this thesis shows how to obtain synthetic dissipative matter driven by a chemically fueled cycle and how the chemically fueled matter responds to accelerated deactivation. This thesis could provide a deeper understanding of dissipative matter and propose a new strategy in the field of system chemistry to create synthetic dissipative matter. It could also serve as an inspiring experimental model to demonstrate how the kinetics of a chemical reaction cycle can exert control over the properties of chemically fueled matter and inspire further research in this area.

Zusammenfassung

Dissipative Materie sind Strukturen, die nur durch eine kontinuierliche Energiezufuhr aufrechterhalten werden können; sie existieren daher außerhalb des Gleichgewichts sind in der Natur allgegenwärtig, von unbelebter Materie bis hin zu lebende Materie. Im Gegensatz zu nicht im Gleichgewicht befindlicher Materie, die thermodynamisch kontrolliert wird, steht dissipative Materie unter kinetischer Kontrolle und ist thermodynamisch labil. Leben ist in der Tat ein Paradebeispiel für dissipative Materie. In Zellen wird die aus Licht oder Chemikalien gewonnene Energie umgewandelt und in kleine Moleküle mit hohem chemischem Potenzial übertragen. Diese energiereichen Moleküle sind chemische Brennstoffe, die über chemische Reaktionszyklen alle Arten biologischer dissipativer Materie regulieren. Infolgedessen reguliert die Kinetik chemischer Reaktionsnetzwerke die Eigenschaften der dissipativen Materie. Außerdem haben mehrere Theorien zu dissipativer Materie vorhergesagt, wie die Eigenschaften chemisch angetriebener Materie auf die Reaktionskinetik reagieren. Obwohl ein klares Verständnis von Materie und ihrem Verhalten im oder nahe dem Gleichgewicht existiert, ist der aktuelle Wissensstand über die Kinetik-Eigenschafts-Beziehung dissipativer Materie aufgrund mangelnder synthetischer Beispiele oder Modelle begrenzt. Daher zielt diese Arbeit darauf ab, chemisch angetriebene Selbstassemblierung und Phasentrennung als Modell für dissipative Materie zu etablieren. Konkret bestand das Ziel darin, Reaktionszyklen zu entwickeln, die dissipative Materie regulieren und die Beziehung zwischen Energiedissipationsraten und den zugrunde liegenden Materialeigenschaften zu testen.

Bei der chemisch angetriebenen Selbstassemblierung besteht der chemische Reaktionszyklus, der Energie umwandelt, aus mindestens zwei gleichzeitigen Reaktionen, genauer aus einer Aktivierungsreaktion, die die Bausteine aktiviert, damit diese assemblieren können, und einer Deaktivierungsreaktion, die die Bausteine deaktiviert, woraufhin sie sich wieder zerlegen. Trotz der Fülle an chemischen Reaktionen ist es eine Herausforderung, geeignete Reaktionszyklen zu finden, da die Aktivierung und Deaktivierung von Molekülen in einem einzigen System kontinuierlich und durch unterschiedliche Reagenzien vermittelt erfolgen muss. Außerdem erfordern die wiederholten Aktivierungs- und Deaktivierungszyklen einen hohen Umsatz an Molekülen (Vorläufermolekülen), was bedeutet, dass Nebenreaktionen sich nachteilig auf die chemisch angetriebene Assemblierung auswirken würden.

Ich zeige zunächst, wie wir es schaffen, die Bildung des Nebenprodukts N-Acylharnstoff in einem Carbodiimid-betriebenen Reaktionszyklus zu unterdrücken, indem wir die Auswirkungen der Strukturen der Brennstoffe, der Konzentration und Struktur der Vorläufer,

der Additive, der Temperatur und des pH-Werts testen. Die optimale Bedingung für einen effizienten Carbodiimid-betriebenen Zyklus ist eine Kombination aus niedriger Temperatur, niedrigem pH-Wert und 10 % Pyridin als Brennstoffanteil (Kapitel 6). Dann bespreche ich einen neuen Carbodiimid-betriebenen Reaktionszyklus, der vorübergehende 5(*4H*)-Oxazolone bildet. Dieser Reaktionszyklus ist robust genug, um unter einer Vielzahl von Bedingungen zu funktionieren, er ist effektiv bei der Nutzung des Brennstoffs, vielseitig im Hinblick auf den Umfang des Vorläufers und in der Lage, verschiedene chemisch betriebene Baugruppen anzutreiben. Am wichtigsten ist, dass der aktivierte Zustand, das 5(*4H*)-Oxazolon, eine lange Halbwertszeit hat, wodurch es möglich ist, die Deaktivierung durch Hydrolyse des Oxazolons zu katalysieren, ohne den pH-Wert oder die Temperatur zu ändern (Kapitel 7). Abschließend zeige ich, wie chemisch angetriebene Koazervate, die durch den Zyklus der Oxazolonbildung angetrieben werden, auf die Kinetik des Reaktionszyklus, insbesondere auf die Deaktivierung, reagieren. Durch Erhöhen der Menge an Pyridin zur Beschleunigung der Deaktivierung und damit zur Verkürzung der Halbwertszeit der Oxazolone dauert es länger, bis Tröpfchen entstehen und im Gleichgewichtszustand eine stabile Größe erreichen. Am wichtigsten ist, dass die stabile Größe der Tröpfchen mit der Halbwertszeit der Oxazolone variiert (Kapitel 8).

Zusammenfassend zeigt diese Arbeit, wie man synthetische dissipative Materie erhält, die durch einen chemisch angetriebenen Zyklus reguliert werden, und wie die chemisch angetriebene Materie auf eine beschleunigte Deaktivierung reagiert. Diese Arbeit könnte ein tieferes Verständnis von dissipativer Materie liefern und eine neue Strategie im Bereich der Systemchemie vorschlagen, um synthetische dissipative Materie zu erzeugen. Sie könnte auch als inspirierendes experimentelles Modell dienen, um zu demonstrieren, wie die Kinetik eines chemischen Reaktionszyklus die Eigenschaften chemisch angetriebener Materie steuern kann, und weitere Forschungen auf diesem Gebiet anregen.

Abbreviations

ADP	adenosine diphosphate
ATP	adenosine triphosphate
CCC	critical coacervation concentration
CKII	casein kinase II
DCC	N, N′-dicyclohexylcarbodiimide
DIC	N,N′-diisopropylcarbodiimide
DNA	deoxyribonucleic acid
EDC	1-ethyl-3-(3-dimethylaminopropyl)carbodiimide
ERN	enzymatic reaction network
e.g.	exempli gratia, for example
et al.	et alii/aliae, and others
FMRP	Fragile X mental retardation protein
GDP	guanosine diphosphate
GTP	guanosine triphosphate
HPLC	high-performance liquid chromatography
i.e.	id est, that is
LLPS	liquid-liquid phase separation
LMP	low melting point
MLOs	membraneless organelles
mRNA	messenger ribonucleic acid
NHS	N-Hydroxysuccinimide
NTP	nucleoside triphosphate
^{1}H NMR	Proton nuclear magnetic resonance
P_i	inorganic phosphate
PP2A	protein phosphatase 2A
PSS	polystyrene sulfonate
PTFE	polytetrafluoroethylene
PVA	polyvinyl alcohol
RNA	ribonucleic acid
S6K1	S6 kinase 1
TEM	transmission electron microscopy
TRIS	Tris(hydroxymethyl)aminomethane
UV	ultraviolet

Table of Contents

1. Dissipative Matter

In nature, dissipative matter is ubiquitous, ranging from inanimate matter such as hurricanes, Rayleigh–Bénard convection, and Belousov–Zhabotinsky reaction to all living organisms.[1-7] This type of matter consists of particles, agents, or constituents that consume energy from the environment, and therefore such matter exists out of equilibrium.[8-10] In sharp contrast to its counterpart, in-equilibrium matter, which does not require a supply of energy to sustain and is stable under thermodynamic control, dissipative matter is dynamic and thermodynamically labile. Dissipative matter can sustain itself as long as the energy is available, but once the energy is depleted or removed, it will fall into equilibrium as ruled by thermodynamics. However, with a continuous supply of energy, a high degree of complexity of dissipative matter can be obtained. This complexity can result in emergent properties, that is, properties of a whole system that cannot be predictable solely from the properties of its constituent parts.[9] Life is a prime example of dissipative matter due to its dependency on continuous energy from light or chemical fuels. In the following, I will first illustrate the feature of dissipative matter by its free-energy landscape. Then, I will explicate what life is and how life is sustained by energy.

1.1 Free-energy Landscape

For in-equilibrium matter, the final state of its units is determined by thermodynamics and normally settles in a global minimum in the free-energy landscape. Therefore, the process through which this final state is achieved is unimportant (Figure 1.1 A).[9] Additionally, the distribution of its units between the initial and final states depends on the difference in their energy levels and the amount of free energy available, and the exchange of units between the two states is possible but occurs at equal rates.[8]
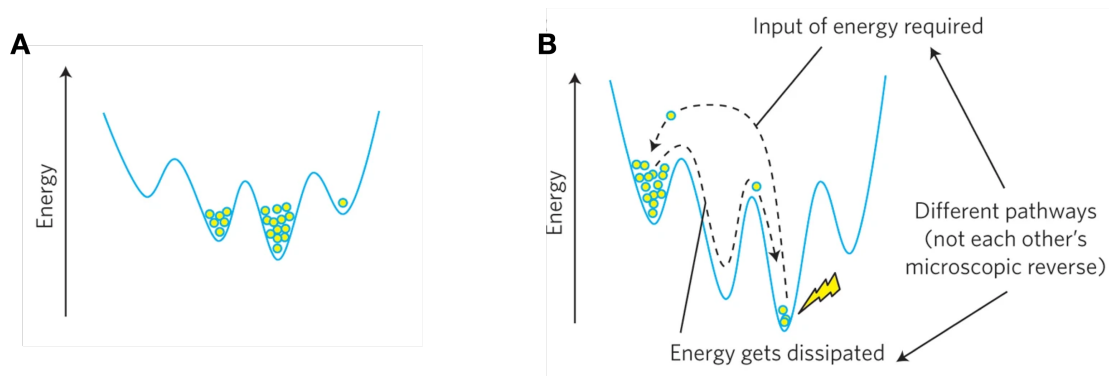

Figure 1.1 Representation of the Gibbs free energy landscape for **(A)** in-equilibrium matter and **(B)** dissipative matter. Reproduced with permission from Springer Nature, Copyright © 2015.[9]

In contrast, for dissipative matter, its units initially reside at the global minimum of the energy landscape. They then get "pushed" by a supply of energy into a higher energy state where their structures or properties are changed, which can be referred to as an activation process. Afterward, these units fall back to their initial state as energy dissipates, which can be referred to as a deactivation process (Figure 1.1 B).[8-9] As long as energy is available, this transition between the two states will repeat continuously, i.e., the continuous supply of energy allows a continuous transition between states. Besides, the distribution of the units between the two states reflects the balance between continuous activation and deactivation pathways, indicating that dissipative matter is under kinetic control and thermodynamically labile. As a result, dissipative matter is more complex than in-equilibrium matter due to the continuous interconversion among multiple states of its units. This inherent complexity increases the possibility of interesting, entirely new unpredictable functions.[8-9]

1.2 Life is Dissipative Matter

Researchers struggle to reach a consensus on the definition of life due to its complexity and diversity, but some specific biological traits describe what it is.[11-12] Since all living matter we know consists of cells—the basic unit, we can use cells to identify the biological traits of life.[13-14] Briefly, living systems require (1) compartmentalization to organize complex biochemical reactions both spatially and temporally by regulating and localizing reagents, (2) information processing including replication, transcription, and translation to store, maintain and express the genetic information, (3) growth and division to reproduce new individual organisms, (4) adaptation to changes in the environment, thus allowing evolution, (5) energy transduction to maintain a far-from-equilibrium steady-state (homeostasis). All those features are crucial to life, but energy transduction is always included when a minimalistic definition of life needs to be given. For example, physicists view life as a thermodynamically open system that uses environmental gradients to create imperfect self-replicas.[15] In line with the definition adopted by NASA: life is "a self-sustained chemical system capable of undergoing Darwinian evolution".[16] One would wonder why it is important for living systems to sustain out of equilibrium by energy transduction.

Not everything far from equilibrium can be considered alive, but everything in equilibrium is not alive.[17] Relying on the continuous consumption of energy from the environment, living organisms can avoid the rapid decay into the inert state of equilibrium, i.e., death, and possess the capability to reconfigure, adapt, amplify signals, self-replicate, and self-heal in a highly dynamic fashion.[18] Moreover, with a constant energy supply, living systems can show

emergent behavior at different hierarchical levels.[19-20] At the molecular level, molecules self-assemble into complex structures like cytoskeletal filaments, such as microtubules and actin filaments. Those cytoskeletal filaments and molecular motor proteins then form molecular machinery. At the mesoscopic level, together with various associated proteins, molecular machinery self-organizes into higher-order subcellular structures, such as the nucleus, the Golgi apparatus, and the mitotic spindle. Those active subcellular structures build up biological cells that further self-organize into complex, energy-consuming tissues and entire organisms. Each level of hierarchical organization is associated with the emergence of entirely new properties, which can only arise out of equilibrium.

Therefore, life is dissipative matter sustained by continuous energy from the surroundings. The technical term is metabolism, but how is energy transduced? Still, we explain this from a cellular perspective. The energy harvested from light or chemicals is converted and transferred to small molecules in cells. These small molecules store the energy and release it when needed. So far, several key molecules, such as ATP, NADH, acetyl-CoA, S-adenosylmethionine, carbamoyl phosphate, UDP-glucose, and isopentenyl-PP, have been proven to be able to power cell metabolism.[21] They have a distinct structural motif and use group transfer chemistry to drive otherwise unfavorable reactions and allow the accumulation of useful quantities of materials far away from equilibrium. Importantly, they are kinetically stable but thermodynamically activated molecules that can be unlocked by metabolic enzymes. Combined with proteins, the energy stored in those molecules can be transferred to create more complex structures, maintain concentration gradients, and enable the active transport of molecules. To cells, those energy-rich molecules are chemical fuels to power cellular work.

1.3 Conclusion

Dissipative matter is sustained by a constant supply of energy and is under kinetic control and thus thermodynamically labile. It is dynamic, reconfigurable, complex, and can display emergent behavior. Living systems are indeed a prime example of dissipative matter that relies on a constant flux of energy transduced from light or chemicals to sustain. Even though inanimate dissipative matter exists in nature, living matter is the most compelling illustration of the functional richness of dissipative systems.[9] Therefore, in the following chapter, I will exemplify multiple examples of biological dissipative matter to explain how the dissipation of energy from chemical fuels such as ATP and GTP leads to diverse cellular functions. The investigation of biological dissipative matter provides a better understanding of life and insights into designing synthetic analogs.

2. Biological Chemically Fueled Matter

As discussed above, biological dissipative matter is sustained by a constant dissipation of energy. As the energy is transferred to small molecules which are seen as chemical fuels, I refer to biological dissipative matter as biological chemically fueled matter. Constant energy dissipation is essential to maintain life, such as regulating temperature or chemical gradients and adapting after damage.[20] However, a fundamental question in biology is how life achieves these functions while continuously dissipating energy. Therefore, in this section, I will use biological examples from microtubules, molecular machinery to membranelles organelles (MLOs) to demonstrate how chemical fuels are transduced to endow cells with diverse functions, such as the emergence of ordered structures, maintenance of concentration gradients, force exertion, and the regulation of reagents in a compartment.

2.1 Microtubules

In cells, chemical fuels are used to create structures via self-assembly.[19] For instance, microtubules and actin filaments are dynamic structures of cytoskeletal components because they undergo NTP-fueled cycles of assembly (polymerization) and disassembly (depolymerization). Here, I take the formation of microtubules as an example to demonstrate how self-assembly is regulated by chemical fuels in cells. Microtubules are an assemblage of the protein tubulin, a heterodimer consisting of two polypeptides, α-tubulin and β-tubulin (Figure 2.1 A).[22-23] In addition, a third tubulin isoform, γ-tubulin, binds specific proteins to form an γ-tubulin ring complex that initiates microtubule assembly by binding the α-tubulin of an αβ-heterodimer. Microtubules usually consist of 13 linear protofilaments assembled around a hollow core with a diameter of around 24 nm. The protofilaments, composed of head-to-tail (-α-β-α-β-) arrays of αβ-heterodimers, are arranged in parallel. Due to this specific organization, microtubules (like actin filaments) are polar structures with two distinct ends: a fast-growing plus end and a slow-growing minus end. The difference in the two ends results from the different nature of α- and β-tubulin.
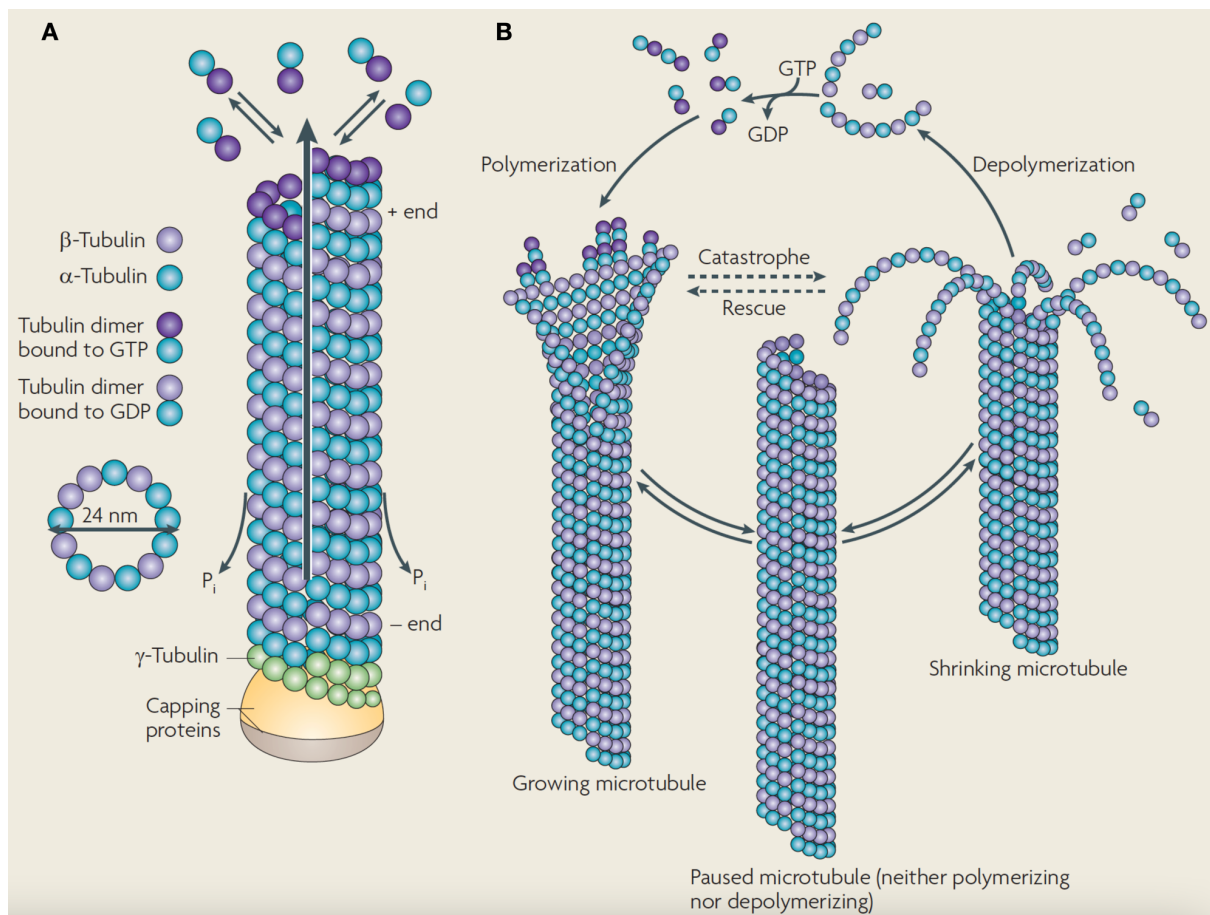
Figure 2.1 Overview of microtubule structure and dynamic instability regulated by GTP hydrolysis. **(A)** Microtubule structure. **(B)** Illustration of dynamic instability: GTP hydrolysis, growing, paused, and shrinking microtubule. Reproduced with permission from Springer Nature.[22]

Both α- and β-tubulin bind GTP, while only the GTP bound to β-tubulin is hydrolyzed to GDP during or shortly after assembly. GDP bound to β-tubulin weakens the binding affinity of tubulin for adjacent molecules, resulting in the disassembly and the dynamic behavior of microtubules. Therefore, microtubules can undergo treadmilling where shrinkage of microtubules occurs at the minus end with GDP-bound tubulin while growth of microtubules happens at the plus end by the addition of GTP-bound tubulin spontaneously. Treadmilling can be seen as a flow of subunits from the minus end to the plus end and does not change the average length of the microtubules.

Microtubules also exhibit an intriguing behavior—dynamic instability where individual microtubules alternate between cycles of growth and shrinkage (Figure 2.1 B).[22-25] Whether microtubules grow or shrink depends on the GTP-bound tubulin addition rate relative to the GTP hydrolysis rate. When the rate of tubulin addition and the rate of GTP hydrolysis are balanced, microtubules reach a steady state where neither polymerization nor depolymerization is favored. If GTP hydrolysis is slower than new GTP-bound tubulins are added, a GTP cap

remains at the plus end, and the growth of microtubules will continue. Conversely, if the GTP hydrolysis is more rapid than adding new GTP-bound tubulins, GTP-bound tubulin at the plus end will hydrolyze to GDP-bound tubulins. Consequently, GDP-bound tubulins dissociate from the microtubules, leading to rapid shrinkage and disassembly of microtubules. Due to this dynamic instability, most microtubules can be continually and rapidly turned over in cells, which is particularly critical for the formation of mitotic spindles during mitosis.

2.2 Molecular Machinery

Chemical fuels also play a crucial role in powering molecular machinery that undergoes conformational changes to perform diverse functions, such as force generation, motility, and chemical gradient regulation.[26] Typical examples are cytoskeletal motor proteins such as myosin, kinesin, and dynein that move along cytoskeletal filaments. Those cytoskeletal motors are responsible for muscle contraction, transportation of cell organelles, chromosomes, and other cargoes within cells, and even cellular migration.[26-27] For example, in muscle cells, myosin catalyzes ATP hydrolysis and undergoes conformational change, converting the energy stored in ATP to a force to contract the muscle (Figure 2.2). Studies of muscle contraction reveal that myosin heads slide or walk along actin filaments. The affinity of myosin to the actin filament is different before and after ATP hydrolysis. However, unlike microtubules, ADP-bound myosin binds strongly to actin filaments, while ATP-bound myosin binds weakly. Once ADP is released and ATP is bound, the affinity of myosin to the actin filament is weakened, which causes myosin dissociation from actin filaments (Step 1). Subsequently, myosin hydrolyzes ATP to ADP and phosphate (P_i), inducing a first conformational change in the head, i.e., myosin head rotates into a "cocked" state where the energy released by ATP hydrolysis is stored as elastic energy (Step 2). Myosin then binds actin filaments (Step 3) and becomes unstable. P_i is then released together with the release of elastic energy, causing a second conformational change in the head, i.e., the myosin head was straightened to move the actin filament. This movement is known as the "power stroke". Last, ADP is released, and fresh ATP is bound to myosin, which dissociates myosin from actin filaments and starts a new cycle. The combination of multiple power strokes results in muscle contraction.[26-28]
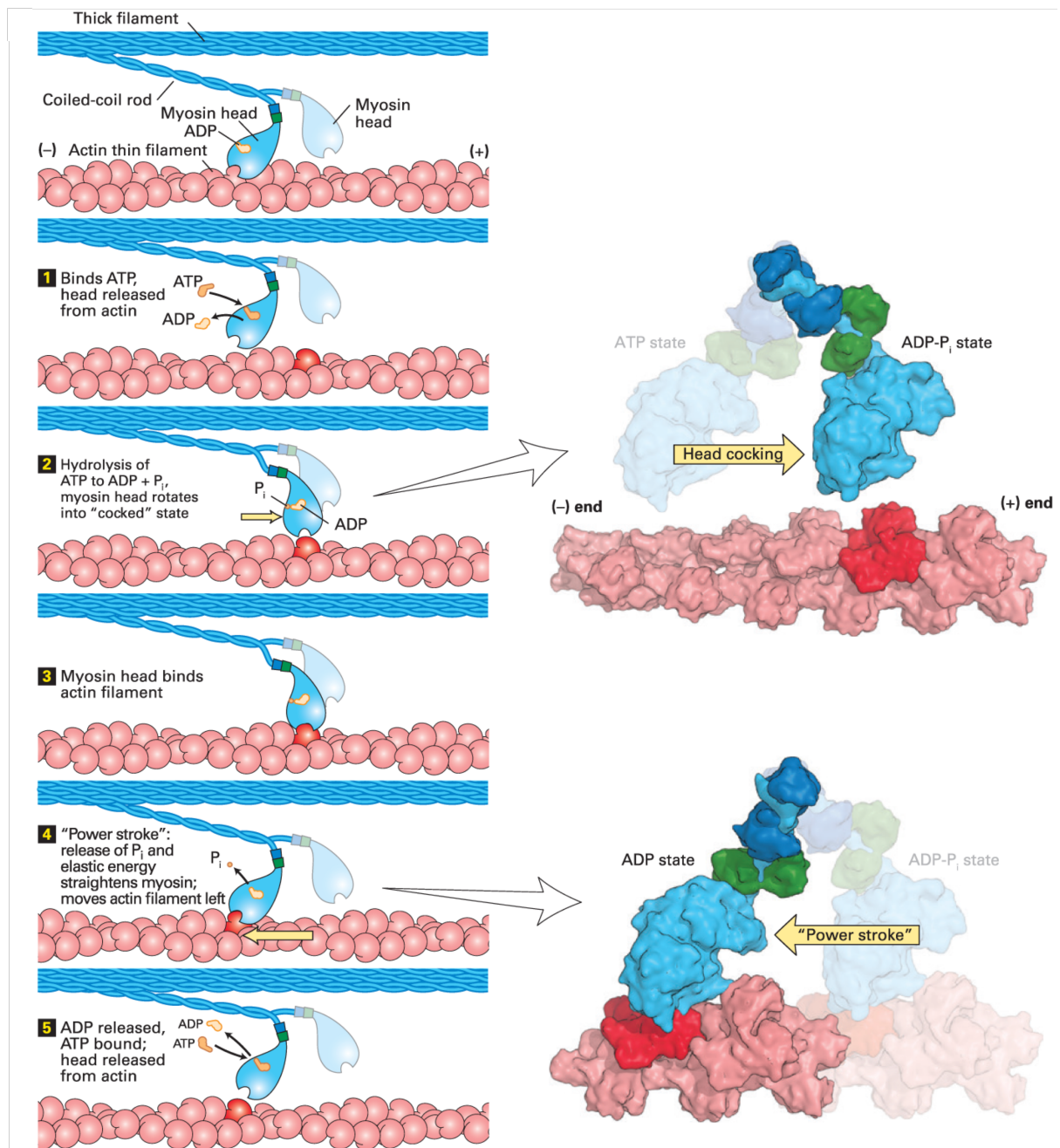
Figure 2.2 Movement of myosin along an actin filament powered by ATP. Left: an ordered sequence of steps (1 – 5) involved in the movement of myosin along actin filaments. Right: molecular models of the myosin head with a conformational change in the "cocked" state and after the "power stroke". Adapted with permission from Molecular Cell Biology 9e by Harvey Lodish, et al. Copyright 2021, 2016, 2013, 2008 by W.H. Freeman. All rights reserved. Used by permission of the publisher Macmillan Learning.[26]

Another example of molecular machinery in cells is transmembrane ATPase pumps. Those ATPase pumps transfer the energy from ATP to induce a conformational change that allows the transportation of ions, such as Na^+, K^+, Ca^{2+}, and H^+, against their concentration gradients across a membrane.[26] Take the Ca^{2+} ATPase pump in the sarcoplasmic reticulum (SR) membrane of skeletal muscle cells as an example (Figure 2.3), in the first step, two Ca^{2+} ions and an ATP bind to their responding binding sites of ATPase enzyme, followed by the

phosphorylation of aspartate, converting ATP to ADP. This phosphorylation changes the conformation of the ATPase enzyme and pushes two Ca^{2+} ions across the membrane. Afterward, the phosphorylated aspartate is hydrolyzed, liberating inorganic phosphate and inducing conformational change to return the enzyme to its initial state for the next cycle. In this cycle, ATP hydrolyzes to ADP, and the enzyme is temporarily phosphorylated and changes its conformation so that calcium can be transported from one side to the other side of a membrane, thereby creating a transmembrane calcium gradient.
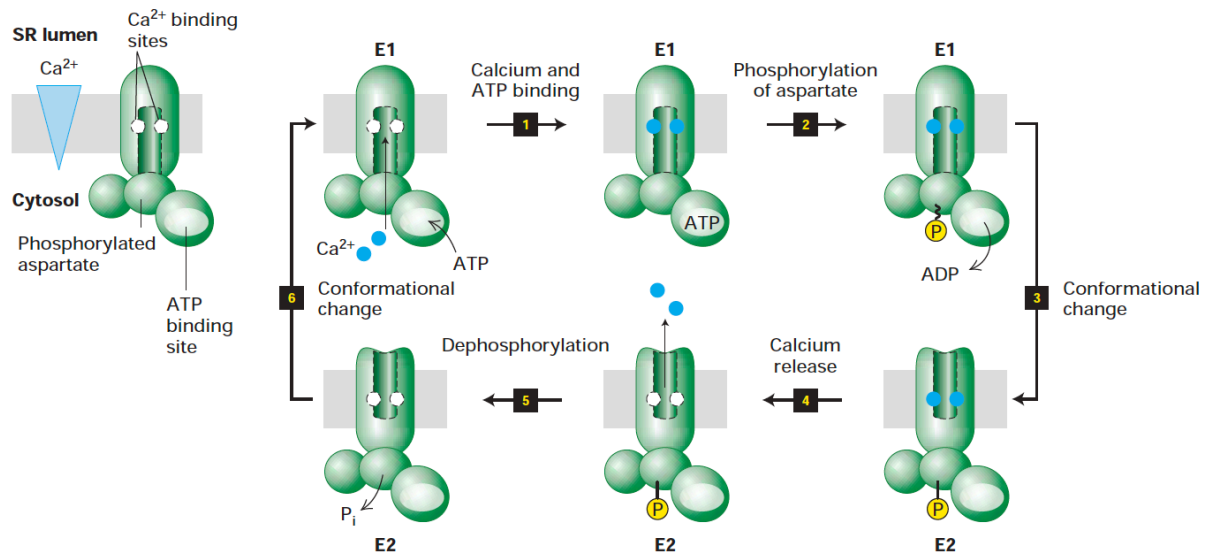
Figure 2.3 ATP-powered Ca^{2+} ATPase pump in the SR membrane of skeletal muscle cells. Left: representative illustration of Ca^{2+} ATPase pump. Right: a complete cycle consists of an ordered sequence of steps $(1-6)$ for coupling ATP hydrolysis and the unidirectional transport of Ca^{2+} ions across the membrane. Reproduced with permission from Molecular Cell Biology 9e by Harvey Lodish, et al. Copyright 2021, 2016, 2013, 2008 by W.H. Freeman. All rights reserved. Used by permission of the publisher Macmillan Learning.[26]

2.3 Membranelles Organelles

Membraneless organelles (MLOs), also referred to as biomolecular condensates, are formed through liquid-liquid phase separation of macromolecules like proteins and RNA via multiple weak attractive interactions.[29-33] They can be described as liquid-like droplets within cells. Examples in the cytosol of eukaryotes are centrosomes, neuronal granules, P granules, or stress granules.[33] These organelles lack a surrounding membrane and allow rapid diffusion of macromolecules within the droplet and into the surrounding cytosol. Hence, evidence shows that these MLOs can concentrate specific biomolecules within them and exert control over biochemical pathways. However, if the liquid droplets undergo maturation, where solid aggregates are formed, the matured MLOs may lose their functions and can be the cause of diseases.[34-36] Therefore, cells must control the assembly and disassembly of MLOs.
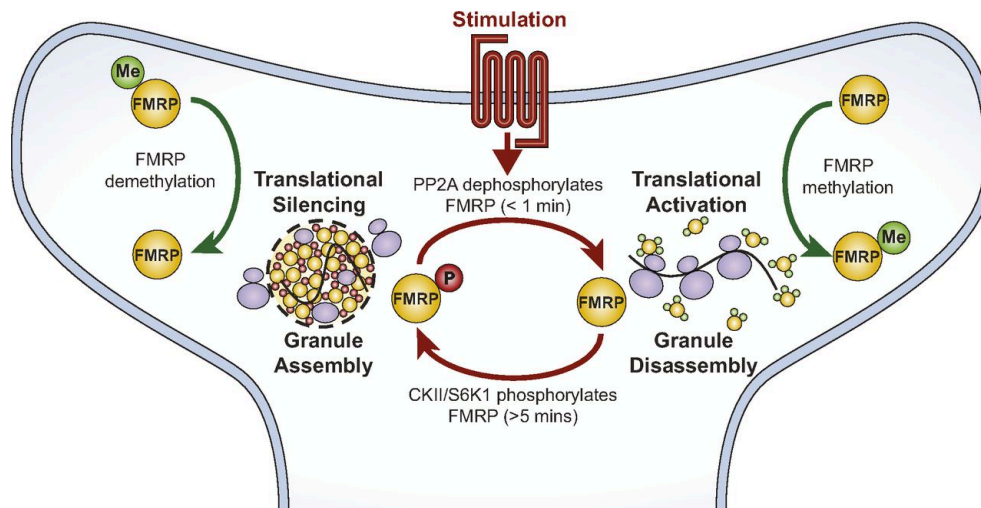
Figure 2.4 Kinase-phosphatase modulation of reversible neuronal granule assembly that regulates mRNA translation. Upon stimulation, dephosphorylation induces neuronal granule disassembly and translational activation of mRNA, while Poststimulation (>5 min), phosphorylation promotes neuronal granule assembly and translational silencing. Methylation and demethylation also complement the reversible neuronal granule assembly.[37] Reproduced with permission from Copyright © 2019, the Authors.[37]

One way through which cells regulate MLOs is by chemical reactions, such as phosphorylation, methylation, and acetylation.[29, 38-39] For example, phosphorylation and dephosphorylation modulate the assembly and disassembly of neuronal granules that regulate mRNA translation (Figure 2.4).[37, 40-42] Those neuronal granules consist of Fragile X mental retardation protein (FMRP) and RNA. Normally, phosphorylation of FMRP is catalyzed by kinases, such as ribosomal protein S6 kinase 1 (S6K1) and casein kinase II (CKII), while dephosphorylation of FMRP is catalyzed by protein phosphatase 2A (PP2A). During neuronal stimulation, PP2A dephosphorylates FMRP, promoting neuronal granule disassembly and activating mRNA translation. Poststimulation (>5 min), PP2A activity is inhibited. Instead, CKII/S6K1 phosphorylates FMRP, promoting neuronal granule assembly and restoring mRNA translation to the inhibited status (translational silencing). Moreover, FMRP methylation and demethylation also complement the reversible neuronal granule assembly and play a role in the regulation of mRNA translation. FMRP methylation complements granule disassembly and translation activation by weakening the binding capacity of FMRP to mRNA and polyribosomes, while FMRP demethylation complements granule formation by triggering higher-order interactions of FMRP with mRNA, polyribosomes, and other proteins. Moreover, P granules are another example of such MLOs regulated by phosphorylation and dephosphorylation. However, unlike neuronal granules, phosphorylation of the highly enriched MEG protein disassembles P granules, whereas dephosphorylation of MEG assembles P granules. [43]

2.4 Conclusion

In cells, chemical fuels like ATP and GTP are used to power diverse cellular processes, such as the formation of cytoskeleton filaments, the performance of molecular machinery, and the reversible assembly of membraneless organelles (MLOs). Those examples showed the features of biological chemically fueled matter to be out-of-equilibrium, dynamic, and reconfigurable. Although biological examples are useful tools for understanding dissipative matter, the biological materials used in the experiments are expensive, time-consuming, and unstable.[44] Hence, synthetic chemically fueled matter with cheap, robust, off-the-shelf sources is desired and of great interest.

3. Synthetic Chemically Fueled Matter

Sparked by the unique properties of biological dissipative matter, the quest for synthetic analogs has attracted significant interest and had a distinct impact on systems chemistry. This section demonstrates the great progress made in synthetical chemically fueled matter. The major challenge to create such synthetic matter is the current scarcity of suitable chemical reaction cycles, even though numerous chemical reactions are available.[9] In this section, I discuss the design considerations of chemical reaction cycles and present several recently developed cycles, including a versatile cycle driven by carbodiimides. After that, I exemplify various synthetic chemically fueled matter, such as fibers, oil droplets, and coacervate-based droplets. Those synthetical examples also demonstrate how the kinetics of a reaction cycle regulate the resulting properties. Meanwhile, I showed how theoretic models had been used to predict and understand the kinetically regulated properties of chemically fueled droplets.

3.1 Chemically Fueled Reaction Cycles

3.1.1 Design Considerations

Several design considerations for designing a chemical reaction cycle pertain to the fuel, the catalyst (precursor), and the concurrent reactions. Again, biology provides the most compelling illustration of these considerations. As discussed above, cells use the energy released by chemical fuels like NTPs (ATP and GTP) to power otherwise unfavorable processes and reactions. NTPs have a high chemical potential but are kinetically stabilized under physiological conditions because their phosphate groups carry negative charges that repel electron-rich nucleophilic molecules like hydroxide ions.[45] These ions could attack the electrophilic center of the phosphate anhydride bonds, leading to uncontrolled bond cleavage and the loss of stored energy. Therefore, a catalyst is required to release the stored energy for its intended purpose. Those catalysts are enzymes containing an amino acid that can undergo phosphorylation and dephosphorylation.[46] Here, the phosphorylation and dephosphorylation consist of the chemical reaction cycle that transduces the energy stored in NTPs. Overall, in these reaction cycles, the net reaction is the hydrolysis of NTPs, and the enzymes (catalysts) are not altered and can thus undergo thousands of cycles.

Typically, a chemically fueled reaction cycle comprises a minimum of two reactions, i.e., an activation reaction and a deactivation reaction (Figure 3.1 A). The activation reaction is the exergonic reaction between a catalyst (precursor) and a fuel, yielding an activated catalyst and

releasing a waste with a lower chemical potential. The deactivation reaction returns the activated catalyst to its original state through another pathway than the activation. Normally, deactivation is a reaction between the activated catalyst and a highly abundant species like the solvent such that the reaction occurs spontaneously. This reaction should be strongly favored toward the original catalyst, making it, practically speaking, irreversible. Therefore, a delicate balance between an activation and a deactivation should be established to allow a nonlinear evolution of the transient product without any further external signal. This balance also allows internal control over the temporal fate of the chemically fueled matter, empowered by mastering kinetic control over the activation and deactivation.[47] Overall, those biological examples taught us three important design considerations: (1) we require fuels with a high chemical potential that is not easily liberated spontaneously, (2) a catalyst that liberates the chemical energy of the fuel,[48] and (3) the activation and deactivation are independent and occur simultaneously and continuously in a single system. In the process of activation and deactivation, the catalyst performs its function.

3.1.2 Synthetic Chemically Fueled Reaction Cycles

Besides the reaction cycles driven by NTPs,[49] several other chemically fueled reaction cycles have been recently developed. In 2010, van Esch's group reported the first chemically fueled reaction cycle used to control the assembly and disassembly of molecules.[50] This reaction cycle is driven by the hydrolysis of methylating agents (Figure 3.1 B). The catalyst (in their work referred to as a precursor) is a small molecule with two carboxylates that reacts with the methyl iodide (fuel) to form a methyl ester that could assemble, while the hydroxide-triggered hydrolysis of the ester restored the catalyst leading to disassembly. Later, the same group reported a similar reaction cycle driven by the hydrolysis of dimethyl sulfate.[51-52] Reaction cycles driven by redox chemistry have also been explored.[53-55] For example, Hermans group developed a reaction cycle driven by the oxidation of dithionite ions into hydrogen sulfite (Figure 3.1 C).[53] In the activation reaction, a catalyst, perylene diimide derivative (PDI^{2-}), was oxidized by oxygen and converted to the uncharged PDI, which self-assembled. In the deactivation reaction, the PDI product reacted with dithionite to restore its original state while releasing hydrogen sulfite as waste, leading to disassembly. Besides, Hermans reported a reaction cycle involving the formation of hydroxy sulfonate (Figure 3.1 D).[56-57] In an assembled state, a catalyst, an aldehyde containing a saccharide derivative (SachCHO), can react with dithionite (DT) to form a water-soluble hydroxy sulfonate, leading to disassembly. After reacting with formaldehyde, which is formed in situ, the hydroxy sulfonate converts back

to the aldehyde, restoring the assembly. Moreover, some other reaction cycles based on the thiol-ester exchange,[58] thiol-disulfide exchange,[59] reversible formation of positive charges on a tertiary amine,[60] pH variation[47, 61-62] have also been explored.
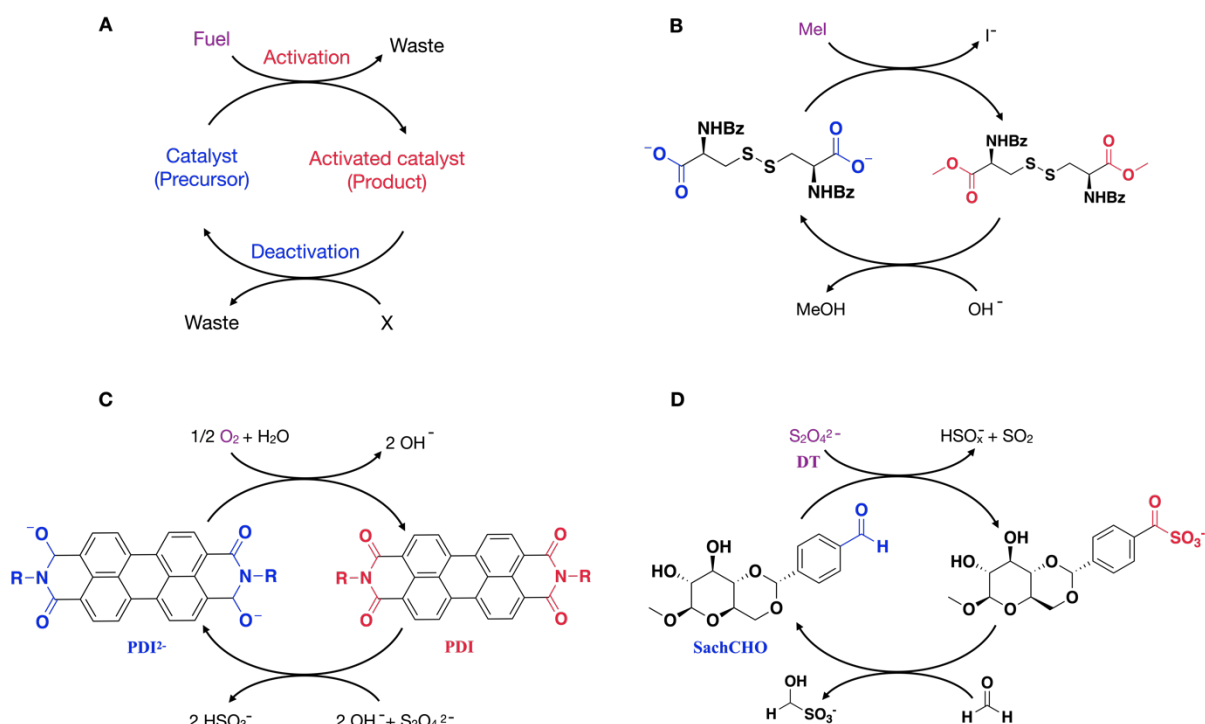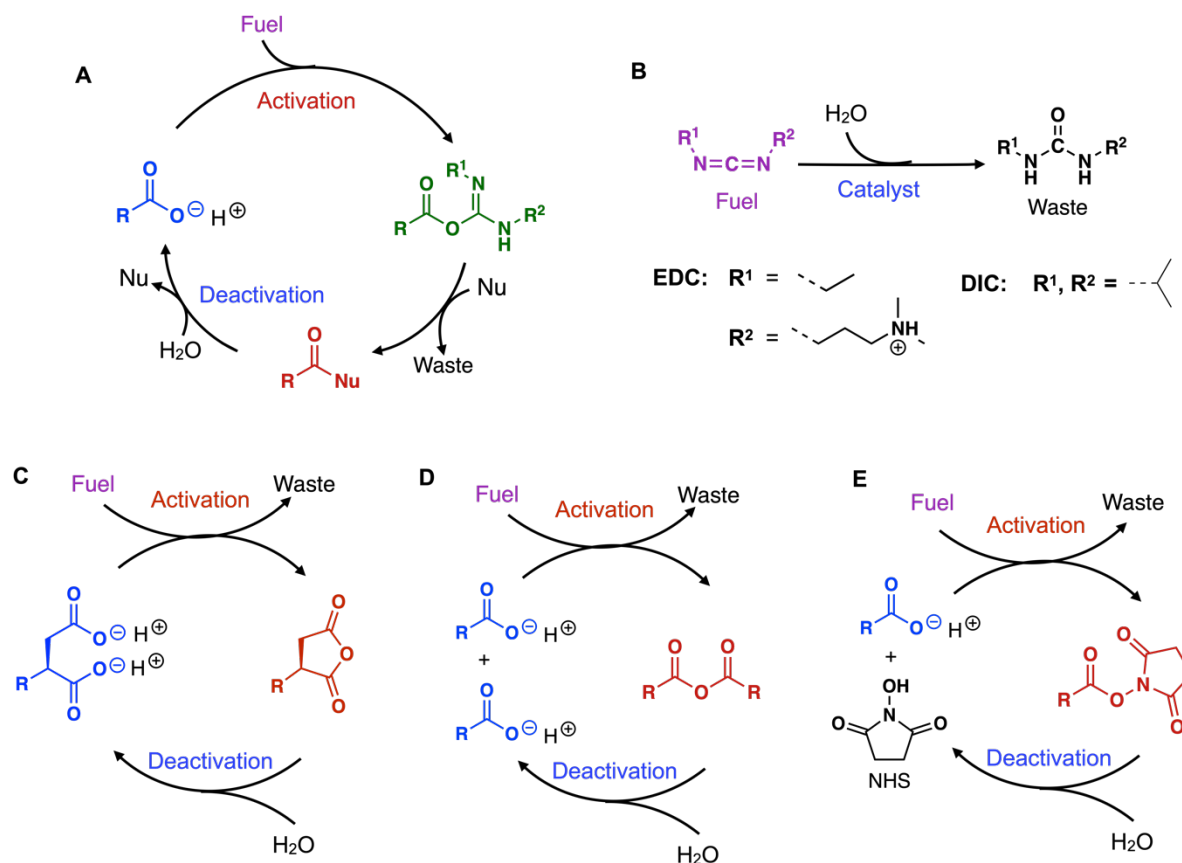

Scheme 3.1 Schematic representation of chemically fueled reaction cycles. **(A)** The components and reactions of a chemically fueled reaction cycle. The chemically fueled reaction cycle is based on (B) the hydrolysis of methylating agents, **(C)** redox chemistry, and **(D)** the formation of hydroxy sulfonate.

In 2017, the Boekhoven and Hartley groups published a carbodiimide-driven reaction cycle simultaneously. [63-64] Like NTPs, carbodiimides are incredible fuels because a high amount of energy is also released in their hydrolysis. Besides, they are relatively stable since they are relatively unreactive toward nucleophilic attack by water, which is the solvent. Specifically, EDC (1-ethyl-3-(3-dimethylaminopropyl)carbodiimide) has a half-life of 37 h in water at pH 7.[65] Similar to the hydrolysis of NTPs, a catalyst that liberates the chemical energy of carbodiimides is required. This catalyst is a carboxylic acid in our reaction cycle. In the activation reaction, the precursor with a carboxylic acid reacts with the carbodiimide to form *O*-acylurea, an intermediate (depicted in green in Scheme 3.2 A), followed by an attack of a second nucleophile which yields the product and urea as waste. In the deactivation reaction, this product reacts with water and hydrolyzes back to its carboxylic acid (Scheme 3.2 A). Thus, the hydration of a carbodiimide is the net reaction, and the carboxylate acts as the catalyst for the hydration of the carbodiimide (Scheme 3.2 B). With carboxylates as a catalyst, the hydration occurs in several steps, which lower the highest energy barrier of the direct hydration, and thus, the overall hydration occurs orders of magnitude faster compared to without

carboxylic acid. Moreover, the carboxylic acid does not convert itself in the overall process but transiently changes its chemical nature, which can be used for a function. Notably, there is a difference between the carbodiimides and NTPs as fuels. In the NTP-fueled cycles, part of the fuel is transiently transferred. In contrast, carbodiimides function as an energy supply but are not part of the activated catalyst.[63-64, 66]

Scheme 3.2 Carbodiimide-Driven Reaction Cycles.[48] **(A)** Schematic representation of a carbodiimide-driven reaction cycle. **(B)** The net reaction in the cycle: the hydration of the carbodiimide. **(C)** Intramolecular anhydrides are formed when building blocks (precursors or catalysts) bear two carboxylic groups and experience an intramolecular attack. **(D)** Intermolecular anhydrides are formed when catalysts only bear one carboxylic group and undergo an intermolecular attack from a second carboxylic acid. **(E)** NHS-esters are formed when catalysts only bear one carboxylic group and undergo an intermolecular attack from an NHS.

Because carbodiimides are popular peptide coupling reagents, the diversity of our fuels is high. It ranges from polar, water-soluble carbodiimides like EDC to more apolar carbodiimides like DIC (N,N′-diisopropylcarbodiimide) and DCC (N,N′-dicyclohexylcarbodiimide). The latter can be applied as fuels in organic solvents or mixtures of organic solvents. We found optimal conditions for the chemically fueled reaction cycle to be 200 mM MES buffer with EDC as a fuel at a pH range between 3.5 and 7.4.[67] A lower pH decreases the reactivity of the carboxylic acids, and no activated building block is found. A pH higher decreases the electrophilicity of the carbodiimides. Hardly any product is found beyond pH 7.4. Notably, anhydride hydrolysis,

i.e., the deactivation reaction, is practically insensitive to pH at this range. MES is a perfectly suitable buffer within this range as it has sufficient capacity at these pH values. Moreover, it is non-nucleophilic, unlike more common buffers like phosphate, carbonate, or TRIS. Nucleophilic buffers react with the fuel, leading to poor cycle performance.

Various activated catalysts are obtained through this cycle depending on the second nucleophile, including intramolecular anhydrides, intermolecular anhydrides, and NHS-esters. Intramolecular anhydrides (Scheme 3.2 C) are obtained if the catalyst contains two carboxylic groups, such as succinic acid derivatives.[63] In contrast, an intermolecular anhydride (Scheme 3.2 D) or an NHS-ester (Scheme 3.2 E) is formed if the catalyst only bears one carboxylic group in the absence or presence of NHS, respectively.[66, 68-69] Generally, there are advantages and disadvantages for each specific cycle. In the intramolecular anhydride-forming cycle, the transient products have short half-lives of less than 2 min[63, 70-71] and our record holder is the tripeptide Fmoc-AVD at 18 s.[63] A short half-life can be advantageous in achieving dynamic supramolecular materials but also poses challenges in tuning the properties of the supramolecular materials via adjusting the half-life. For example, the half-life of intramolecular anhydrides cannot be decreased because anhydrides already hydrolyze rapidly by reaction with water. The intramolecular anhydride-forming cycle also uses its fuel effectively; i.e., because of the neighboring carboxylate, almost all O-acylurea is converted into anhydride instead of hydrolyzing. A significant disadvantage is that the scope of the precursor is limited to succinic or glutaric acid derivatives.

In contrast, the NHS-ester-forming cycle and intermolecular anhydride-forming cycle both have a broad scope of precursors and yield products with longer half-lives. For example, NHS-esters have half-lives in a 200−300 min range,[72] while intermolecular anhydrides have intermediate half-lives among these three reaction cycles.[64, 66] However, the main downside of the intermolecular anhydride-forming cycle is the hydrolysis of the O-acylurea or its rearrangement into the N-acylurea, which decreases the efficiency of the fuels.

Side products like N-acylurea are a severe issue of reaction cycles. The catalyst must undergo hundreds of thousands of turnovers. If a side reaction yields a stable product, the building block can no longer act as a catalyst for the reaction cycle. For example, a 1% side reaction would remove 63% of the building block after as little as 100 turnovers. In the carbodiimide-driven reaction cycle, a well-known side reaction is the N-acylurea formation when the O-acylurea intermediate undergoes irreversible $N−O$ arrangement. This first-order side reaction can be suppressed by ensuring O-acylurea is as short-lived as possible, i.e., having a high

concentration of a second nucleophile or using a catalyst with a nucleophile in the proximity, like aspartic acid or adding catalytic amounts of additional reagents, e.g., pyridine or DMAP.[73] The kinetics of the reaction cycle are analyzed using techniques that give quantitative concentrations with reasonable time intervals, like HPLC and ^{1}H NMR. We recently found that short-lived anhydrides hydrolyze on the acidic HPLC column, and we thus developed a method to quench all chemical reactions in the cycle immediately using benzylamine.[74] The activation is inhibited because EDC loses its reactivity at a high pH caused by benzylamine. In contrast, the deactivation is stopped by converting the *O*-acylurea and anhydride to its corresponding, stable benzylamide.

Since the carbodiimide-fueled reaction cycle was established, it has gained widespread attention and has been used to regulate molecules' self-assembly or phase separation. By careful molecular design of catalysts, various chemically fueled matter can be formed, such as chemically fueled fibers,[63, 70-72, 75-79] coacervate- and oil-based droplets,[66, 80-88] colloids,[89] vesicles,[90-91] micelles,[92] clusters of NPs,[68-69] molecular motors or pumps,[93-94] and transient DNA folding.[95]

3.2 Chemically Fueled Fibers

The cytoskeleton filaments, such as microtubules and actin filaments, are fibers driven by NTPs. Similarly, artificial chemically fueled fibers can also be formed. In 2010, the first example of chemically fueled fiber was reported by the van Esch Group driven by the hydrolysis of methyl iodide.[50] The kinetics of the alkylation of carboxylates were slow, leading to long-lived fibers for up to 15 days. To accelerate the kinetics to allow faster switching between assembly and disassembly, they used a more reactive alkylating agent (dimethyl sulfate) and adjusted the pH of the buffer, thus enabling the formation and decay of chemically fueled fibers on time scales of hours (Figure 3.1 A-C).[51] Since then, increasing examples of chemically fueled fibers have been reported. Hermans reported a gel-sol-gel transition based on the reaction cycle involving the formation of hydroxy sulfonate.[56-57] They also reported a method to keep chemically fueled fibers in a steady state by a continuous influx of ATP.[49]

The Walther group reported pH-responsive chemically fueled fibers whose lifetimes can be programmed over orders of magnitude—from minutes to days in a closed system.[47, 62] They created transient pH jumps by combining a fast activator and a slow dormant deactivator. For example, the simultaneous injection of a directly available base (fast activator) that creates a fast pH rise and an ester-containing molecule (dominant deactivator) that slowly hydrolyzes and furnishes an acid to decrease pH leads to a transient alkaline pH state.[47] On the other way

around, a transient acidic pH state can also be achieved by the simultaneous injection of an acidic buffer (fast activator) that creates a fast pH decrease and urea (dominant deactivator) that generates NH_3 in the urease-catalyzed manner to increase pH (Figure 3.1 D). When a pH-responsive dipeptide was coupled to the transient pH jumps, self-regulating, dynamic hydrogels with programmed lifetimes were obtained and were useful for fluidic guidance or burst release (Figure 3.1 E, F).[62] Besides using two-component pH jumps, they recently reported autonomous soft robots based on active hydrogels using a one-component transient pH flip created by tribromoacetic acid.[61]
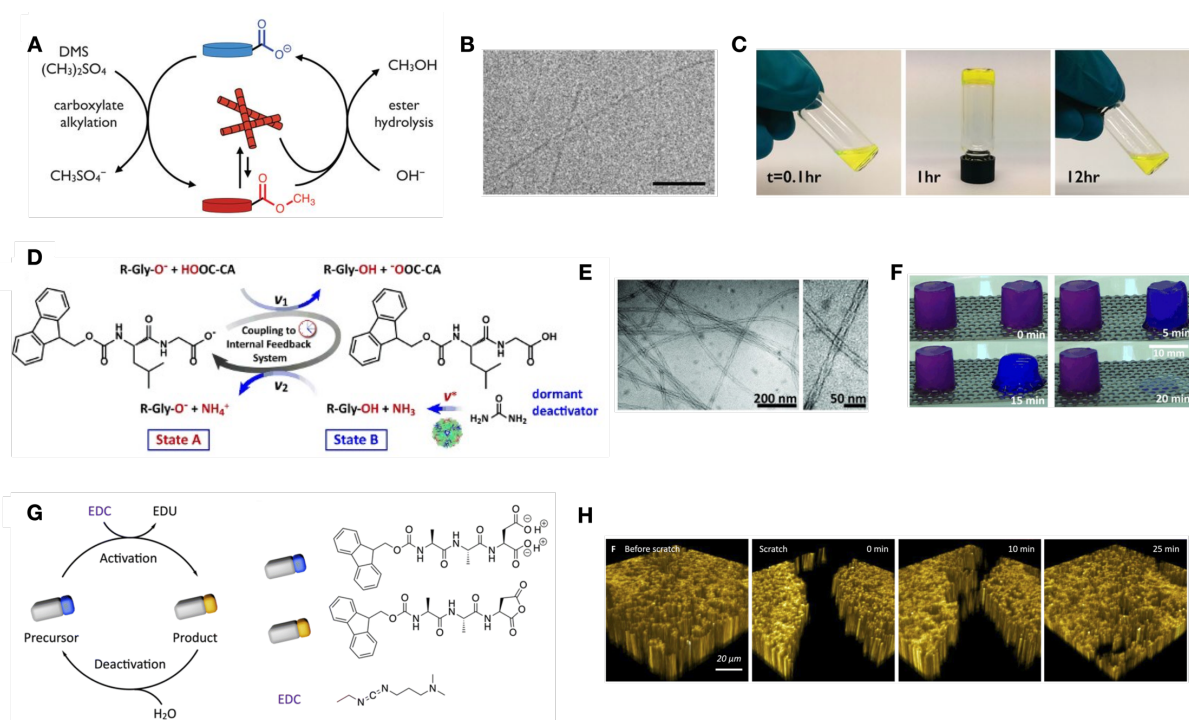
Figure 3.1 Selected examples of chemically fueled fibers. **(A-C)** Fibers driven by a reaction cycle based on the hydrolysis of methylating agents. Reprinted with permission from **AAAS.**[51] **(A)** The reaction cycle uses dimethyl sulfate as fuel. **(B)** Cryogenic transmission electron microscopy (cryo-TEM) micrographs of a gel, scale bar = 100 nm. **(C)** Time-lapse photography of a transient gel. **(D-E)** Fibers driven by a reaction cycle based on a pH-flip. Adapted with permission from © 2015 Wiley-VCH Verlag GmbH & Co. KGaA, Weinheim.[62] **(D)** The reaction cycle of a fast pH decrease and a slow pH rise. **(E)** Cryo-TEM images of the twisted nanofibrils. **(F)** Time-lapse photography of self-erasing hydrogels for burst release. **(G, H)** Self-healing fibers driven by a carbodiimide-fueled reaction cycle. Adapted with permission from the Royal Society of Chemistry.[96] **(G)** Representative reaction cycle producing intramolecular anhydride of tripeptide Fmoc-AAD-OH. **(H)** Confocal fluorescence microscopy in x/y/z dimension of fibers before performing a scratch and after the scratch.

The Boekhoven group reported chemically fueled fibers driven by a carbodiimide-fueled reaction cycle (Scheme 3.2 C). A tripeptide Fmoc-AVD converts to its anhydride after being activated by EDC, turning a liquid into a self-standing hydrogel.[63] Interestingly, reciprocal coupling between the self-assembly and the reaction cycle was observed.[71, 79] The reaction cycle regulated the self-assembly process, and in turn, the self-assembly accelerated the EDC

consumption and the hydrolysis of the anhydride, resulting in faster activation and deactivation. The accelerated activation resulted from the change in the microenvironment of peptides. During the assembly, the microenvironment of peptides became more hydrophobic, changing the activation pathway from the slow step-wise to the faster-concerted proton transfer. The acceleration of deactivation may be attributed to the β-sheet hydrogen-bonding interactions. Careful molecular design can adjust the degree of reciprocal coupling, and a decelerated deactivation was observed.[79] Moreover, the self-assembly behavior can be controlled by tuning the attractive and repulsive interactions between precursors and products by molecular design and salt addition.[70] However, deactivated peptides did not immediately disassemble from the fiber. Instead, they could get activated again and make the fiber a co-assembly of products and precursors. Due to the co-assembly, a self-healing hydrogel can be obtained (Figure 3.1 G, H).[96]

Active hydrogels can also be obtained using the intermolecular anhydride-forming reaction cycle that links two non-assembling components (Scheme 3.2 D).[78] The Adams group reported a gel-to-gel transition of an amphiphilic precursor using this strategy.[76] Moreover, covalently crosslinked gel can be obtained by crosslinking multiple carboxylic acids. Konkolewicz group was the first to report a transient hydrogel formation upon cross-linking carboxylic acids of polymers with EDC.[97] Apart from polymers, small molecules with multiple carboxylic acids can also be crosslinked upon adding EDC to form a transient hydrogel that could be applied as a writable and self-erasing material.[98] Besides, an ester-forming reaction cycle driven by a carbodiimide was also used to connect two non-assembling components to get fibers. Das group used histidine derivates with a hydrophobic tail (C18-H) and 4-nitrophenol (NP) to form esters upon adding EDC. The esters and the acid C18-H could co-assemble to form a fiber network.[77]

Even though fibers can be successfully obtained in chemically fueled reaction cycles, a significant drawback of fibers cannot be neglected: kinetic trapping is inevitable.[99] We observed that the catalyst or precursor remains assembled after deactivation, and the fiber was not transient. That means kinetic trapping prevents disassembly after deactivation and decreases the dynamicity of the assembly, leading to huge difficulties in obtaining dynamic life-like materials, such as microtubules that are very dynamic with growth and shrinkage in a way like treadmills. Hence, other dissipative matter without kinetic trapping is under investigation.

3.3 Chemically Fueled Droplets

Cells contain numerous droplets, including lipid organelles and membraneless organelles (MLOs), that play a crucial role in various cellular processes. These droplets store and organize molecules, buffer noise, and influence signaling pathways.[33, 100-101] They are kept away from equilibrium by chemical reaction cycles, which results in properties that differ from the behavior in equilibrium. Although these droplets are widespread, a clear understanding of their formation dynamics, aging, and impact on cellular processes is missing. Synthetic and theoretical models are of great interest in understanding the physicochemical principles underlying the functioning of these droplets. In this section, I first discuss the use of theoretical models to predict and understand the kinetically controlled properties of chemically fueled droplets. Additionally, I focus on synthetic droplets that have been recently reported and are based on oil and coacervate components.

3.3.1 Theoretical Models

Chemically fueled droplets in cells are kept from equilibrium by chemical fuels, and their unique properties are under kinetic control. However, the mechanism by which kinetic control can result in behavior different from that dictated by thermodynamics is elusive. Increasing theoretical models have been developed to predict and understand those droplets' formation, growth, and division. For example, numerical calculations have predicted that chemically fueled droplets can resist Ostwald ripening and evolve to a stable droplet size.[102] Under other conditions, their spontaneous self-division is even possible.[103]

3.3.1.1 Suppression of Ostwald Ripening

A system of multiple droplets is thermodynamically unstable because droplets strive to minimize their free energy by reaching a minimal interface area.[104-105] This means that larger droplets (smaller surface-to-volume ratio) are energetically favored over multiple smaller droplets with the same total droplet volume. Consequently, droplets coarsen over time, i.e., grow and fuse by coalescence and Ostwald ripening until one big and stable droplet is formed. To stabilize emulsions, both these processes must be suppressed.

Ostwald ripening is a phenomenon where larger droplets grow at the expense of smaller ones.[106-107] This occurs due to the Laplace pressure differences between droplets.[108] In simple terms, tiny droplets have higher Laplace pressure than larger droplets, leading to a concentration gradient of droplet molecules from smaller to larger droplets. Jülicher group showed that Ostwald ripening can be suppressed when chemical reactions regulate droplets.[102]

Still, at least two chemical reactions that take place simultaneously regulate those droplets, i.e., an activation reaction that converts soluble precursor A into a self-assembling product B at the expense of a chemical fuel and a deactivation reaction that reverts product B to precursor A. They developed two models where activation and deactivation are delocalized into separate phases to suppress Ostwald ripening.

In the first model, the activation (A → B) with a rate constant of k_f occurs outside the droplets, while deactivation (B → A) with a rate constant of k_b happens inside the droplets (Figure 3.2 A). Therefore, the activated building blocks must diffuse into a droplet before deactivating, while the deactivated building blocks leave the droplet before they are reactivated.[102, 109] This causes a droplet material influx and efflux that is regulated by the kinetics of the chemical reaction cycle. Since the activated building blocks diffuse until they enter a droplet, the influx of activated building blocks scales with the surface area of the droplets. Moreover, since the deactivation scales linearly with the number of activated building blocks, which scales with the volume of the droplets, the efflux of deactivated building blocks scales with the volume of the droplet. When the influx and efflux are balanced, a stationary droplet size that depends on the chemical reaction rates can be reached. Consequently, all droplets eventually evolve to this stationary size, i.e., droplets larger than this stationary size will shrink due to a low surface-to-volume ratio. In comparison, droplets smaller than this stationary size will grow due to a high surface-to-volume ratio. Therefore, this model suppresses Ostwald ripening by allowing multiple droplets to coexist and grow toward a stationary size at a steady state. Interestingly, in this case, the stationary size of multiple droplets is proportional to $k_b^{-1/3}$, indicating that a faster deactivation or a shorter half-life of activated building blocks leads to smaller droplets.[102]
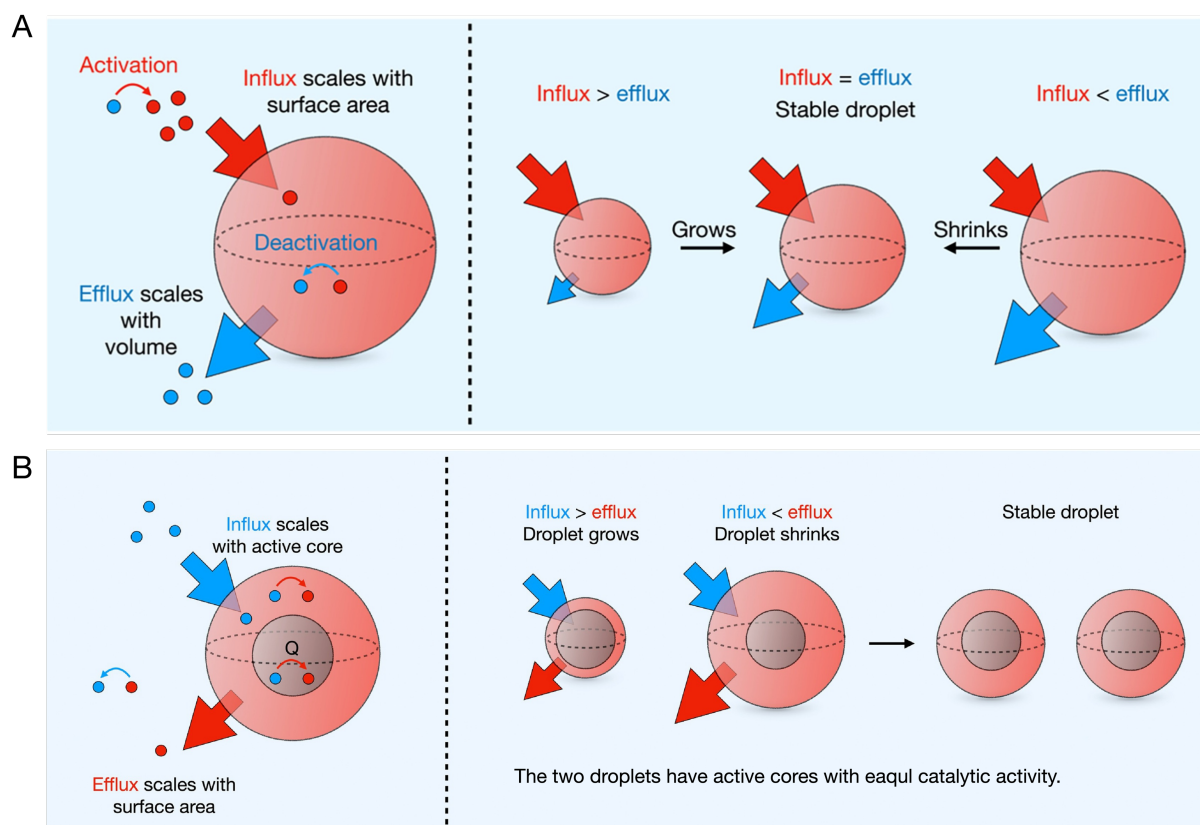
Figure 3.2 Schematic representation of chemically fueled droplets where activation and deactivation are delocalized into separate phases to suppress Ostwald ripening. **(A)** Deactivation of building blocks occurs inside, and activation occurs outside the droplet. The balance between surface-dependent influx and volume-dependent efflux regulates whether a droplet grows or shrinks. At a stationary size, influx and efflux are balanced. Due to a high surface-to-volume ratio, small droplets grow while large droplets shrink due to a low surface-to-volume ratio. All droplets evolve to this stationary size eventually. **(B)** Autocatalytic droplets with an active core: activation of building blocks occurs inside, and deactivation occurs outside the droplet. The balance between active core-dependent influx and surface area-dependent efflux regulates whether a droplet grows or shrinks. For multiple droplets with equal catalytic activity that is sufficiently large, smaller droplets grow at the expense of larger droplets until they reach the same size. Adapted with permission from © 2022 The Author(s), Published by Elsevier Inc.[109]

In the second model, the deactivation (B → A) happens outside the droplets, while the activation occurs inside the droplets (figure 3.2 B). That means the droplet catalyzes to produce its building blocks: A + B → 2B. This design is hence seen as an autocatalytic system.[102, 109] However, because the activated building blocks can only be produced from preexisting droplets, it is difficult for droplets to nucleate. Therefore, they introduce active cores that not only catalyze the production of activated building blocks but facilitate the nucleation of the droplets. In this case, the influx scales with the active core's catalytic activity (Q), while the efflux scales with the surface area of the droplets. The catalytic activity value can determine the droplets' stability, number, and size. For instance, the catalytic activity must be larger than the critical catalytic activity Q_c to allow nucleation and larger than a threshold value Q_{stab} to ensure

multiple droplets are stable. Hence, the number of stable droplets can be set by the number of active cores with catalytic activity higher than Q_{stab}.

For multiple droplets with equal catalytic activity that is sufficiently large, the influx is more important for small droplets than for large droplets; smaller droplets, therefore, grow at the expense of larger droplets until they reach the same size. Furthermore, for multiple droplets with unequal catalytic activity but larger than Q_{stab}, droplets around the core with a higher catalytic activity grow faster, and the ratio of their catalytic activities determines the ratio of the droplet volumes. Therefore, the active cores can determine how the active building blocks are distributed among the droplets. Autocatalytic systems with active cores thus suppress Ostwald ripening by allowing multiple droplets to coexist and grow, while the size of droplets can be the same or different depending on the catalytic activity of active cores. Autocatalytic systems with active cores can explain the growth behaviors of centrosomes during cell division.[110] Centrioles serve as active cores that initiate and stabilize centrosome growth, suppressing Ostwald ripening and resulting in two equal-sized centrosome droplets during cell division.

3.3.1.2 Self-Division

As discussed above, multiple droplets are thermodynamically unstable because they grow and fuse by coalescence and Ostwald ripening, resulting in increasing size and decreasing numbers with time. This behavior contrasts with that of cells, which have a stable size and increase in number through division. This raises the question of how droplets can divide and propagate. Jülicher group showed that spherical droplets regulated by chemical reactions can grow and spontaneously divide into two smaller daughter droplets of equal size, reminiscent of cellular behavior, serving as a model for prebiotic protocells.[103] They used a simple model, the same as we discussed above, for the case where activation happens outside the droplet and deactivation happens inside. The building block B phase separates from the dilute solvent phase to form the droplet and spontaneously reverts to the soluble precursor A inside the droplet and leaves. In the dilute phase, due to B having a higher chemical potential than A, the precursor A cannot be spontaneously converted to building block B unless a fuel C with a high chemical potential is used and converts to a waste C' with a low chemical potential (Figure 3.3 A).
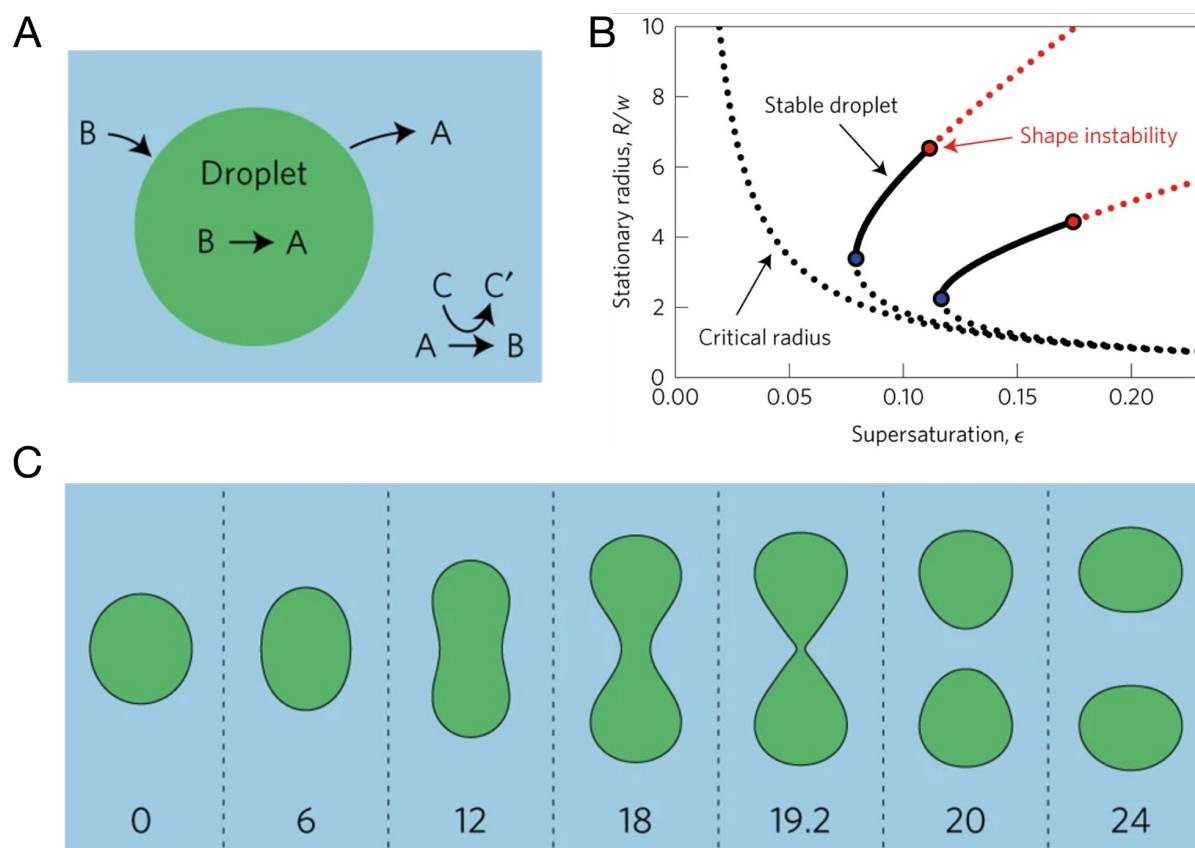
Figure 3.3 Self-division of active droplets. **(A)** Simple model of active droplets with building block B and soluble component A. The system is driven by a chemical fuel C that converts the soluble A into building block B and is transformed into the waste product C'. Building block B phase separates from the dilute phase to form droplets and spontaneously reverts to the soluble A inside the droplet and leaves. **(B)** The stationary radius R of spherical droplets is shown as a function of supersaturation ε for different values of normalized turnover $v / v_0 = 0$, 1, and 3 (from left to right). Solid black lines represent the radii of stable droplets. Dotted lines indicate states where droplets are unstable with respect to shape (red) and size (black). **(C)** A sequence of shapes of a dividing droplet at different times from numerical calculations. A droplet undergoes sequential processes: growth toward its stationary size, elongation, dumbbell shape formation, and split into two daughter droplets. Adapted with permission from Copyright © 2016, Springer Nature Limited.[103]

As discussed before, Ostwald ripening can be suppressed, and multiple droplets can stably coexist with a stationary size. However, by tuning the supersaturation ε (excess concentration of B in solvent phase) and the turnover v of B inside droplets, the droplets can undergo a shape instability and split into two smaller droplets despite their surface tension. For a given turnover, droplets with a stationary size only exist for sufficiently large supersaturation (Figure 3.3 B). Droplets smaller than the critical radius (black dotted lines) shrink, while droplets larger than the critical radius grow toward the stationary radius (black solid line). The turnover balances the influx of B due to supersaturation at the stationary radius. Thus, larger turnover leads to smaller droplets. However, by increasing supersaturation, a spherical droplet undergoes shape instability when its radius reaches a critical value R_{div}. This spherical droplet starts to elongate, forms a dumbbell shape, and then splits into two smaller droplets of equal size. The two

daughter droplets then grow until a new division occurs, mimicking the division of living cells (Figure 3.3 C).

3.3.1 Oil Droplets

In water, oil droplets are formed via the liquid-liquid phase separation of oil molecules. For example, in a vinaigrette, oil droplets separate from vinegar. Those oil droplets have hydrophobic microenvironments and lack a surrounding membrane. Boekhoven group reported chemically fueled oil droplets based on the activation of precursors with a hydrophobic tail of a carbon chain.[66, 86-87] The precursors can be diacids such as succinate derivates or monoacids. Upon activation by EDC, the soluble precursors convert to their anhydrides that phase-separate into oil droplets (activation outside of droplets). Upon the formation of oil droplets, water and precursors are excluded from the oil phase, resulting in deactivation only occurring in the dilute phase (Figure 3.4 A). That means only the anhydride in solution can hydrolyze; thus, the droplets exert a self-protection mechanism, i.e., protecting its anhydride from hydrolysis. In this case, the concentration of anhydrides in solution equals their solubility, and the deactivation rate equals the deactivation rate constant multiplied by the solubility. Since both factors are constant, the deactivation rate is also constant, resulting in anhydride hydrolysis in a zero-order manner, such as the liner hydrolysis of C_8- and C_{10}-succinic anhydride (Figure 3.4 B).[88] Besides, the deactivation rate decreases with decreasing solubility of anhydrides. That is why the poorly soluble C_{10}-succinic anhydride deactivates drastically slower than C_8-succinic anhydride. However, when the anhydrides cannot phase-separate, there is no self-protection mechanism, and anhydrides decay with pseudo-first-order kinetics, which is the case for C_4- and C_6- succinic anhydrides (Figure 3.4 B). Excitingly, this self-protection mechanism can be used to release hydrophobic drugs linearly and exhibit parasitic behavior.[86, 88]
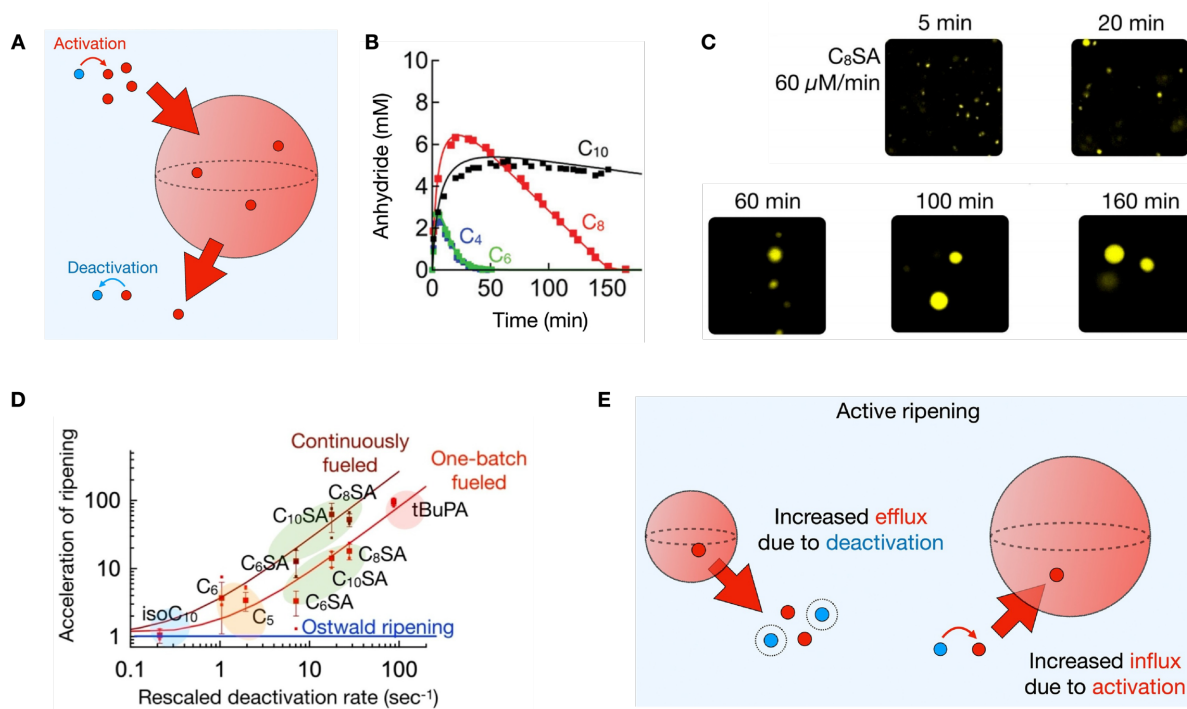
Figure 3.4 Chemically fueled oil droplets formed in a carbodiimide-fueled reaction cycle. **(A)** A schematic representation of a droplet where activation and deactivation occur outside the droplet because fuel and water are excluded from the droplet. **(B)** Kinetic profile of anhydride with a different hydrophobic tail as a function of time after adding fuel. Markers represent HPLC data, while lines stand for fits from the kinetic model. **(C)** Time-lapsed micrographs of C_8 succinic acid with continuous fueling of 60 μM/min fuel. **(D)** Ripening accelerated as a function of the deactivation rate for various activated building blocks. **(E)** Schematic representation of the mechanism of active ripening. **(A, E)**Adapted with permission from © 2022 The Author(s), Published by Elsevier Inc.[109] **(B)** Adapted with permission from the Royal Society of Chemistry.[88] **(C, D)**Adapted with permission from © 2020 The Authors. Published by Wiley-VCH GmbH.[111]

Moreover, when these oil droplets were maintained in a steady state by continuously adding fuel, a behavior of accelerating Ostwald ripening was observed. For example, with a constant flux of 60 μM/min fuel, C_8-succinic anhydride droplets coarsened into a few large droplets within 2 h without any evidence of droplet fusion (Figure 3.4 C), which is considerably faster than the Ostwald ripening of passive droplets with similar interfacial surface tension and solubility.[111] Moreover, the Boekhoven group found that a higher deactivation rate led to a faster ripening of droplets (Figure 3.4 D).[111] They explained the acceleration of Ostwald ripening by an increased flux between small and large droplets (Figure 3.4 E). Since the deactivation reaction occurs in the solution, small droplets with higher Laplace pressure are preferentially dissolved, resulting in increased efflux of anhydrides from small droplets. Once the anhydrides hydrolyze back to their acids, the activation occurs, creating new anhydrides that diffuse into larger droplets with low Laplace pressure, increasing the influx. As a result, both reactions contributed to an accelerated ripening.

Due to the hydrophobic nature of oil droplets, they can only up-concentrate hydrophobic guest molecules and exert self-protection of their components, reducing their ability to allow rapid exchange of molecules with the dilute phase. Thus, alternative membraneless models containing water are desirable for understanding MLO functioning.

3.3.2 Coacervate Droplets

Coacervate droplets are hydrated droplets formed spontaneously via liquid-liquid phase separation of macromolecules in solution, driven by the same types of underlying interactions as MLOs, such as charge-charge, dipole-dipole, p-p stacking, cation-p interactions, hydrogen bonding, hydrophobic effects, and biomolecular recognition.[112-113] Thus, coacervate droplets are considered a great membaraneless model and have a clear potential to mimic the material properties of MLOs. Coacervates can be subdivided into simple and complex coacervates. Complex coacervates are formed via the complexation of two oppositely charged polymers,[114-115] while simple coacervates only involve a single self-associating molecule.[116-119] Recently, coacervates have been explored by synthetic polymers,[120-122] proteins in vitro,[116-117, 123-124] polysaccharides,[123, 125-126] peptides,[112, 118, 127-129] and polynucleotides.[130-133]

The formation and properties of coacervate droplets can be controlled by adjusting the binding strength between the droplet molecules. Both intrinsic and extrinsic factors can influence this binding strength. Intrinsic factors are related to the structure of the molecules, such as their charge multivalency, charge density, the type of counterions, the nature of the charge, and non-covalent interactions.[120, 134-136] For example, peptides with arginine residues are more prone to forming coacervates than lysine residues because guanidium cations have stronger cation-π interactions.[134, 137-138] Extrinsic factors include salt, pH, temperature, and the concentration of droplet molecules.[115, 122, 126, 139] Normally, coacervation is favored when the charge ratio of polyanions and polycations is balanced.[140] Increasing the salt concentration in the solution can weaken the coacervation and even cause the coacervation's disappearance because the polymers' charges are screened.[122] Moreover, chemical reactions are a powerful tool for regulating the formation and properties of coacervates. Reactions involving redox chemistry,[118-119] enzymes,[131, 133, 141] and light[142-143] were reported.

3.3.2.1 Drive by an Enzymatic Reaction Network

As mentioned in Chapter 2.3, MLOs are chemically fueled droplets whose assembly and disassembly are regulated by the continuous dissipation of chemical energy. To better mimic and understand MLOs, coacervate droplets driven by chemically fueled reaction cycles are

proposed and have been explored. In 2018, Spruijt group reported reversible ATP-peptide coacervate droplets coupled to an enzymatic reaction network (ERN) that transiently generates ATP.[141] The two enzyme-catalyzed reactions take place simultaneously. Thus, droplet nucleation, coarsening, and dissolution occur under the same reaction conditions and can be repeated multiple times. By using phosphate donor phosphoenolpyruvate (PEP) as a first fuel, pyruvate kinase catalyzes the conversion of ADP to ATP that condenses in droplets with a polycation (poly-L-lysine). However, by using D-glucose (penultimate phosphate acceptor) as a second fuel, hexokinase catalyzes the reversion of ATP to ADP, resulting in droplet dissolution due to the weak charge interaction of ADP with poly-L-lysine. The kinetics of these two enzyme-catalyzed reactions determine the rate of droplet formation and dissolution; thus, the droplets can act as a chemical timer by balancing the kinetics of both enzyme-catalyzed reactions, i.e., droplets forming or dissolving at specific times.

Similarly, by coupling to an ERN of concurrent ATP-powered ligation (using T4 DNA ligase) and endonuclease-controlled restriction (using BsaI), Walther group reported transient DNA coacervates via multivalency-driven LLPS of programmable sequence-defined functionalized nucleic acid polymers (SfNAPs).[144] Once ATP is added to a solution of small DNA-based building blocks with complementary sticky ends and enzymes, SfNAPs are formed via ligation and further hybridize, resulting in multivalency-driven LLPS to coacervate droplets. Due to the cleavage of phosphodiester bonds in SfNAPs catalyzed by BsaI, the SfNAPs are decomposed to building blocks, and the droplets dissolve. The programmable nature of the DNA system allows orthogonal polymerization of SfNAPs, enabling sorted LLPS of two different SfNAPs in parallel for multicomponent coacervates. Moreover, those DNA coacervates can entrap bioactive species to improve the efficiency of enzymatic cascades.

3.3.2.2 Driven by a Carbodiimide-fueled Reaction Cycle

Besides chemically fueled coacervates driven by ERNs, Boekhoven group pioneered chemically fueled complex coacervates driven by a carbodiimide-fueled reaction cycle without enzymes.[80] They used a zwitterionic peptide with the sequence of Ac-F(RG)$_n$D-OH as a precursor, where the cationic arginines (R) are separated by noncharged glycines (G). Upon activation by EDC, the two anionic carboxylates are converted into their anhydride, which abolishes two negative charges, i.e., the product is overall positive (Figure 3.5 A). Therefore, the cationic anhydrides induce complex coacervation with anionic polymers such as RNA (poly-U), while the zwitterionic precursors do not. Hydrolysis of the anhydrides leads to the dissolution of the coacervate droplets (Figure 3.5 B). That is, droplets are regulated by the

kinetics of the reaction cycle, i.e., emerging only when fuel is present but decaying when fuel is depleted. Due to this design, where the precursors have a poor affinity for RNA and stay outside the droplets while anhydrides reside inside, the activation occurs outside while deactivation occurs inside the droplets.
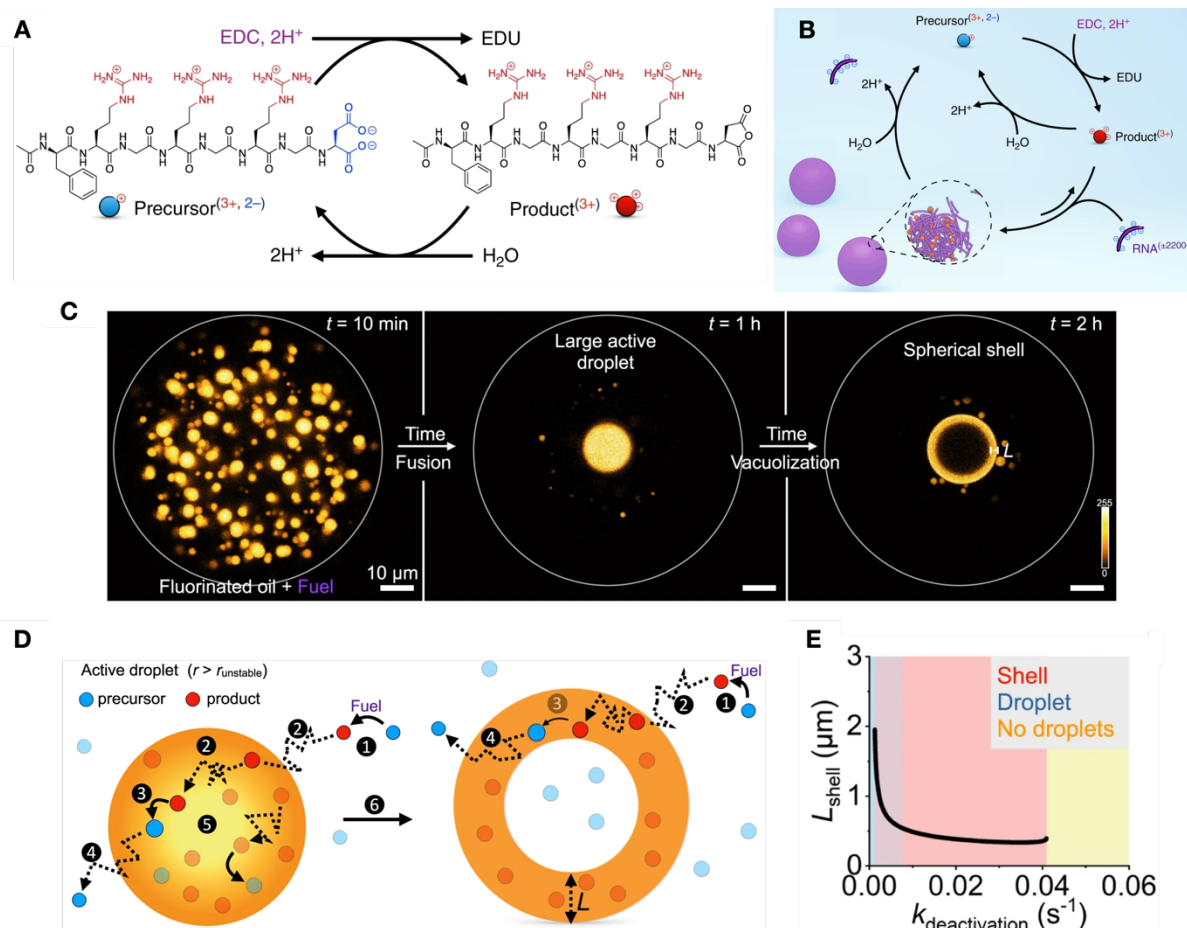
Figure 3.5 Chemically fueled complex coacervate-based droplets formed in a carbodiimide-fueled cycle. **(A)** The reaction cycle turns a zwitterionic peptide (precursor) into a cationic transient anhydride (product). **(B)** Schematic representation of the chemical reaction cycle combined with complex coacervation with RNA (poly-U). The chemical reaction cycle regulates the influx and efflux of droplet materials. Adapted with permission from Copyright © 2020, The Author(s).[80] **(C)** Time-lapsed micrographs of large microreactors in Z-projections in a steady state. Surfactant-stabilized microfluidic droplets (microreactors, grey outline) containing precursor, PSS, sulforhodamine B, and MES buffer were embedded in a fluorinated oil that contained fuel. The grey circle represents the size of the microreactor. **(D)** The mechanism of spherical shell formation involves 6 sequential steps: activation outside the droplet, product diffusion into the droplet, deactivation inside the droplet, precursor diffusion out of the droplet, product depletion in the core, and droplet transition to the spherical shell. **(E)** The shell thickness L_{shell} predicted by the model for a microreactor with a radius of 25 μm as a function of varying deactivation rate constants. Adapted with permission from Copyright © 2023, The Author(s).[83]

Since those droplets are formed via complex coacervation of cationic peptides and polyanions and regulated by the chemical reaction cycle, factors such as fuel input, the structure of peptides, and the structure and length of polyanions affect the dynamics of emerging coacervates. At near-stoichiometric fuel concentrations compared to precursor, the coacervates were dynamic

and dissolved completely through vacuolization and occasional fragmentation, while at higher concentrations of fuel (3x excess), metastable droplets that persisted beyond the lifetime of the anhydrides were formed. Compared to dynamic droplets, more peptides per unit of RNA or a higher ratio of cations to anions are present in metastable droplets, resulting in an increased barrier to disassembly. Moreover, a careful molecular design of peptides is needed for dynamic droplets. When the ratio of cations to anions is too low, no coacervates are formed, while coacervates are formed even before fuel if the ratio is too high.[81] Besides, too long polyanions do not induce coacervates but precipitate upon fuel, and polyanions that bind strongly to the peptide tend to form metastable droplets.[81, 84]

Regulated by the kinetics of the reaction cycle, these droplets display exciting properties that endow them with the potential as a model for membraneless organelles. For example, within their limited lifetime, these droplets can transiently up-concentrate a range of functional RNA sequences, which can remain in a folded active state.[80] Moreover, multiphase droplets are formed, and the transitions from multilayers with an RNA shell to multilayers with an RNA core occur if the droplets have two types of polyanions. Those transitions result from the kinetic control over the liquidity of the droplets, offering insights into how cells tune the complex architectures of membraneless organelles with liquid to solid-like cores and shells.[82]

Applying this droplet model in a steady state where fuel diffuses continuously into an aqueous microreactor from a reservoir in a fluorinated oil phase, the spherical droplets can undergo a morphological transition into a liquid, spherical shell that can be sustained.[83] The mechanism is related to gradients of short-lived droplet material. Since activation predominantly occurs outside, whereas deactivation occurs inside the droplets, a diffusion gradient of product from outside the droplet toward its core leads to the core's instability and the transition into a shell (Figure 3.5 C, D). Moreover, the droplet volume scales linearly with the microreactor volume, but shells were only formed when the microreactor was sufficiently large to form droplets larger than 150 μm^3. This corresponds to a threshold radius of 3.3 μm, below which the droplet's core remains stable due to its higher product concentration (calculated by a model) than the spinodal decomposition concentration. Above this threshold radius, the product concentration in the core falls below the spinodal decomposition concentration. Thus, the core cannot remain stable, resulting in a spherical shell. However, the thickness of the spherical shells L_{shell} was relatively constant over an extensive range of droplet volumes. Since the shell formation is caused by the gradient of the short-lived product, the product's diffusion and the deactivation rate constant affect the L_{shell}. From the model, a faster product's diffusion constant leads to a thicker shell due to a weaker gradient, but a too-fast diffusion results in no droplets.

Besides, with increasing deactivation rate constant, L_{shell} initially decreases rapidly but then becomes quite stable over a broad range of rate constants. Still, no droplets are found if the product deactivates too fast, i.e., the product is too short-lived (Figure 3.5 E).

3.4 Conclusion and Outlook

Synthetic chemically fueled matter is of great interest in mimicking biology and building life-like materials from the bottom up. To create this matter, a chemical reaction cycle that consists of two concurrent reactions, i.e., an activation reaction and a deactivation reaction, is essential for energy transduction. So far, several chemical reaction cycles have been developed based on the hydrolysis of methylating agents, oxidation of reducing agents, hydrolysis of ATP, hydration of carbodiimides, and others. Using these chemical reaction cycles, different chemically fueled assemblies have also been created inspired by biology, such as fibers for cytoskeleton filaments and droplets for membraneless organelles. Moreover, theoretical models were developed to predict and understand the properties of chemically fueled droplets, such as suppressing Ostwald ripening and self-division. These works demonstrate how the reaction cycle's kinetics regulate the chemically fueled matter's temporary formation and properties. Notably, the half-lives of unstable products are critical to the properties of the chemically fueled matter because they assemble before decaying. If the half-life is too short, no assemblies will be formed, while a half-life that is too long can result in metastable assemblies that lack dynamics. Therefore, it is of great interest to test how chemically fueled matter responds to the half-life of active molecules, which requires changing the deactivation rate constant. Although modifying the working temperature or pH can alter the deactivation rate constant and consequently the product's half-life, it also spontaneously modifies the phase diagram of the product, resulting in more difficulties in comparing the properties of chemically fueled matter. This means a reaction cycle that can adjust the product's deactivation or half-life under the same temperature and pH is currently unavailable and is of great interest in obtaining tunable properties of the resulting assemblies.

4. Aim of the Thesis

Examples from biology, theory, and systems chemistry demonstrate that dissipative matter has properties regulated by the chemically fueled reaction and thus differs drastically from its in-equilibrium counterparts. While we start to understand how kinetics affect certain aspects of dissipative matter, we have only scratched the surface. Therefore, this thesis aimed to test how dissipative matter's properties respond to the active molecules' half-life in a chemically fueled reaction cycle. Like in biological systems, the maintenance of dissipative matter would require the molecules to undergo thousands of activation and deactivation events. That means in a chemically fueled reaction cycle, any side reactions would be detrimental to the dissipative matter. Hence, the first aim of this thesis was to seek a solution for suppressing any side reactions in the carbodiimide-fueled reaction cycle. Another challenge to tuning the properties of chemically fueled matter is that the half-life of intramolecular anhydrides cannot be decreased with catalysts—they hydrolyze rapidly by reaction with water. Therefore, the second aim of this thesis was to develop a carbodiimide-fueled reaction cycle that produced longer-lived activated molecules such that I could catalyze the hydrolysis and, thus, tune their half-life. The last aim of this thesis was to achieve chemically fueled coacervate droplets driven by a carbodiimide-fueled reaction cycle in which the half-life of activated molecules can be tuned. With such chemically fueled droplets, I could test how half-life affects the properties of the droplets.

5. Outline of the Thesis

In this thesis, we obtained chemically fueled coacervate droplets with tunable properties regulated by the half-life of activated molecules in a carbodiimide-fueled reaction cycle. In the introductory chapter, I described the features of dissipative matter and used biological examples to demonstrate how dissipative matter is sustained by chemical fuels. Furthermore, I demonstrated the chemically fueled reaction cycles recently reported and the dissipative matter obtained in these cycles. I also showed how theoretical models have been developed to predict and understand the relationship between chemically fueled droplets' properties and the reaction cycle's kinetics.

In Chapter 4, I describe the aims of this thesis—the challenges that need to be overcome to tune the properties of chemically fueled matter. I focus on the carbodiimide-fueled reaction cycle, which suffers from the formation of side products, limited precursor scope, and difficulty tuning active molecules' half-life. In the following three chapters, I discuss how we approached this goal step by step.

In Chapter 6, we managed to suppress catalyst poisoning by testing the effects of carbodiimide structure, catalyst concentration and structure, additives, temperature, and pH. It turned out EDC was the desired fuel in the aqueous solution. Higher catalyst concentration, a catalyst with two adjacent carboxylic groups, additives like pyridine, low temperature, and low pH helped produce less N-acylurea. Finally, a combination of low temperature, low pH, and 10% pyridine as a fuel fraction was optimal for a highly effective carbodiimide-driven cycle.

In Chapter 7, we introduced a carbodiimide-fueled reaction cycle that forms longer-lived transient 5(4H)-oxazolones via an intramolecular cyclization, which occurs when precursors bear one carboxylic group and an amide group at the alpha position. This reaction cycle is robust enough to operate under a wide range of conditions, effective in utilizing the fuel, versatile to the scope of the precursor, and able to drive different chemically fueled assemblies. Most importantly, the product 5(4H)-oxazolone has a longer half-life than the intramolecular anhydride, making it possible to catalyze the hydrolysis of the oxazolone by using catalysts and thus decreasing its half-life without changing the pH or temperature.

In Chapter 8, we obtained active coacervate droplets with tunable properties by running the oxazolone-forming reaction cycle under the optimized working condition we established in Chapter 6. We first confirmed that the active molecule's half-life could be adjusted by pyridine. The half-life of oxazolone can be decreased from 15 minutes with 3 mM pyridine to 5 minutes with 10 mM pyridine. Then, we observed complex coacervation when a polyanion PSS was

added to the system. By changing the amount of pyridine, we could control the properties of the active coacervate droplets in a steady state, such as their time to emerge and to reach a stationary state. Most importantly, we could decrease their stationary size by decreasing the half-life of the active molecules.

Finally, I conclude my thesis in Chapter 9 and give a brief outlook on the future of the field.

6. Suppressing Catalyst Poisoning in the Carbodiimide-Fueled Reaction Cycle

In catalytic reaction cycles, catalysts (precursors) need to undergo thousands of activation and deactivation steps; thus, side reactions are disastrous in terms of the fuel's efficiency, the turnover of the catalysts (precursors), and the properties of the chemically fueled matter. In this chapter, I aimed to optimize the working condition of a carbodiimide-fueled reaction cycle to suppress side reactions, especially the formation of *N*-acylurea. I tested various parameters from the effects of carbodiimide structure, catalyst concentration, catalyst structure, additives, temperature, to pH. It turned out that EDC was the desired fuel in the aqueous solution. Increasing catalyst concentration resulted in less *N*-acylurea formation, but the influence wore off. Catalysts with two carboxylic groups tended to form intramolecular anhydrides with less *N*-acylurea. However, *N*-acylurea formation became more favored if the two carboxylic groups were far apart. Moreover, additives serving as a trapping agent could suppress *N*-acylurea, and pyridine performed best, but its ability also wore off with increasing concentration. Low temperature and low pH gave a higher effective reaction cycle. Notably, a combination of low temperature, low pH, and 10% pyridine as a fuel fraction was optimal for a highly effective carbodiimide-driven cycle. Finally, I applied this combination to a case study. I showed that the difference between optimal conditions and sub-optimal conditions could be the difference between chemically fueled assemblies or not. This work will provide guidelines for using carbodiimide-fueled reaction cycles to regulate chemically fueled matter by choosing the optimal conditions.

This section states the individual work of each author in the publication above. J. Boekhoven, X. Chen, and O. Zozulia conceived the research. J. Boekhoven and X. Chen designed the experiments, analyzed the data, and wrote the manuscript. H. Soria-Carrera wrote the kinetic model, fitted all the data, and corrected the manuscript. O. Zozulia synthesized non-commercial compounds.

Chemical Science

ROYAL SOCIETY OF CHEMISTRY

EDGE ARTICLE

Check for updates

All publication charges for this article have been paid for by the Royal Society of Chemistry

Suppressing catalyst poisoning in the carbodiimide-fueled reaction cycle†

Xiaoyao Chen, [ID] Héctor Soria-Carrera, [ID] Oleksii Zozulia [ID] and Job Boekhoven [ID] *

In biology, cells regulate the function of molecules using catalytic reaction cycles that convert reagents with high chemical potential (fuel) to waste molecules. Inspired by biology, synthetic analogs of such chemical reaction cycles have been devised, and a widely used catalytic reaction cycle uses carboxylates as catalysts to accelerate the hydration of carbodiimides. The cycle is versatile and easy to use, so it is widely applied to regulate motors, pumps, self-assembly, and phase separation. However, the cycle suffers from side reactions, especially the formation of *N*-acylurea. In catalytic reaction cycles, side reactions are disastrous as they decrease the fuel's efficiency and, more importantly, destroy the molecular machinery or assembling molecules. Therefore, this work tested how to suppress *N*-acylurea by screening precursor concentration, its structure, carbodiimide structure, additives, temperature, and pH. It turned out that the combination of low temperature, low pH, and 10% pyridine as a fraction of the fuel could significantly suppress the *N*-acylurea side product and keep the reaction cycle highly effective to regulate successful assembly. We anticipate that our work will provide guidelines for using carbodiimide-fueled reaction cycles to regulate molecular function and how to choose optimal conditions.

Introduction

Chemical reaction networks that catalyze the conversion of a reagent with high chemical potential (fuels) into lower-chemical-potential "waste" molecules are used to power the cells' molecular machinery or molecular assembly. The ATP-driven ATPase pump and GTP-driven dynamic assembly of tubulin into microtubules are prototypical examples.[1–3] Inspired by such biomolecular machinery, reaction cycles that catalytically convert fuels into waste have been devised to power synthetic molecular machineries like the dynamic assembly of fibers driven by the hydrolysis of methylating agents[4] or the rotation of a molecular motor catalyzed by the hydration of carbodiimides.[5] In these reaction cycles, two chemical reactions operate simultaneously: (1) an activation reaction is the reaction between the high chemical potential (which we call fuel) and a catalyst, which activates the catalyst, and (2) a deactivation reaction that reverts the activated catalyst to its original state (Scheme 1A). The free energy released by the two reactions can be used to operate molecular machinery or to regulate self-assembly. For example, suppose the activated catalyst can self-

assemble in its short lifetime. In that case, the corresponding assemblies are dynamic because their building blocks are constantly exchanged with freshly activated building blocks. These exchange dynamics result in kinetically controlled assemblies vastly different from their in-equilibrium counterparts. Similarly, if the activated catalyst can undergo a supramolecular interaction, the chemical fuel can power supramolecular machinery like pumps or motors.

Our group and the Hartley group introduced a particularly powerful reaction cycle driven by the hydration of carbodiimide-based fuels (Scheme 1B).[6–8] In the activation, the carbodiimide fuel activates a carboxylate-containing catalyst, for example, by converting it into its corresponding anhydride. The anhydride spontaneously hydrolyzes in the deactivation. Thus, the carboxylate catalyzes the hydration of the carbodiimide fuel to its corresponding urea waste by transiently becoming an activated catalyst in the form of an anhydride. The carbodiimide-fueled reaction cycle has gained widespread attention. It is frequently used to regulate the phase separation of complex coacervate- and oil-based droplets,[9–12] the formation of macrocycles,[7,13,14] the aggregation of nanoparticles,[15] the formation of vesicles and tubes,[16–18] the self-assembly of peptides into fibers,[6,19–26] the crystallization of amino acids,[27] and the cross-linking of polymer networks.[28–32] More recently, the cycle was used to drive molecular motors and regulate molecular pumps,[5,33] and control DNA folding.[34]

Despite its success, the carbodiimide-driven reaction cycle has drawbacks. Most prominently are side reactions that arise from the intermediate *O*-acylurea state—after the reaction

Department of Chemistry, School of Natural Science, Technical University of Munich, Lichtenbergstrasse 4, 85748 Garching bei München, Germany. E-mail: job. boekhoven@tum.de

Chemical Science
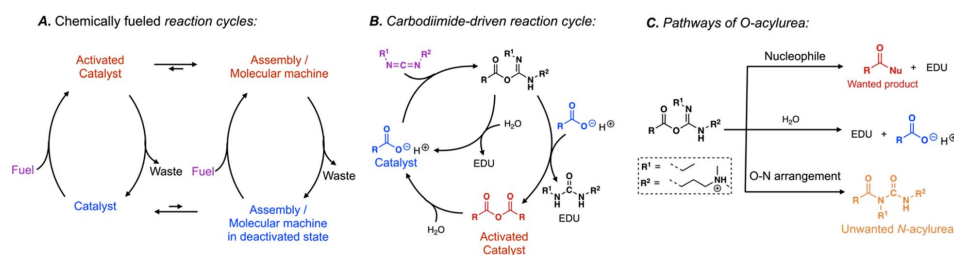
Scheme 1 Simplified representation of (A) chemically fueled reaction cycles used to regulate self-assembly or molecular machinery, (B) our carbodiimide-fueled reaction cycle to form anhydrides, and (C) pathways of the intermediate *O*-acylurea.

between the carbodiimide and the catalyst, this short-lived species is formed[35] and reacts in three pathways (Scheme 1C). Firstly, it reacts with a nucleophile like a carboxylate to form the desired activated catalyst. Secondly, the *O*-acylurea can hydrolyze by reacting with water which means the catalyst is recovered without performing its function, *i.e.*, inefficient fuel use. Lastly, the *O*-acylurea undergoes an intramolecular O–N arrangement, yielding its corresponding *N*-acylurea.[35–38] This reaction is irreversible; thus, forming *N*-acylurea decreases the fuel's efficiency and irreversibly destroys the catalyst, *i.e.*, the side reaction poisons the catalyst. The latter reaction is disastrous for chemically fueled reaction cycles. In context, even if only 5% of converted fuel yielded the *N*-acylurea, 99% of the catalyst would be poisoned after it undergoes 100 activation–deactivation cycles ($0.95^{100} = 0.59\%$). The elegance of chemically fueled biomolecular machinery is that it can run thousands of cycles. For synthetic molecular machinery to live up to these levels, catalyst poisoning through side reactions must be understood and suppressed.

Our previous research mainly utilized aspartates and succinates as catalysts, which possess a second carboxylate in proximity, leading to the formation of a 5-membered anhydride.[6,39] In these reaction cycles, the intramolecular cyclization reaction was rapid, resulting in the absence of *N*-acylurea formation. Additionally, we also investigated reaction cycles involving catalysts with only one carboxylate to form NHS esters, intermolecular anhydrides and oxazolones.[40–43] In all those reaction cycles, *N*-acylurea is formed. We tried either by using a high fuel-to-catalyst ratio or adding a significant amount of pyridine as an additive to suppress this side product. However, a quantitative understanding or a general rule of the extent to which parameters such as pH, temperature, additives, carbodiimide structures, and catalyst structures can suppress *N*-acylurea has not been established. Therefore, in this work, we tested how simple parameters could be varied to suppress any side reaction in the popular carbodiimide-fueled reaction cycle. The concentration and the structure of the catalyst, the structure of the carbodiimides, the presence of additives, and environmental conditions like temperature and pH were all screened using a kinetic analysis to suppress unwanted *N*-acylurea and increase the yield of the main product. Our work provides guidelines for using carbodiimide-fueled reaction cycles to

regulate molecular function by choosing the optimal conditions. We apply these guidelines to a case study and show that the difference between optimal conditions and sub-optimal conditions can be the difference between chemically fueled assemblies or not.

Results and discussion

In our reaction cycle, we used propionic acid (C_3) as a catalyst because it forms a symmetric anhydride that does not self-assemble. We used the C_3 in 200 mM MES buffer at pH 6 at 21 °C in all experiments unless stated differently. First, we studied the effect of the fuel on the formation of the *N*-acylurea side product. We initiated the reaction cycle by adding 15 mM EDC, CMC, or DIC to 75 mM C_3 (EDC = 1-ethyl-3-(3-dimethylaminopropyl)carbodiimide, CMC = *N*-cyclohexyl-*N*-(2-morpholinoethyl)carbodiimide methyl-*p*-toluenesulfonate, DIC = *N*,*N*-diisopropylcarbodiimide). After 24 hours, we measured the amount of catalyst that had disappeared by analytical HPLC. We assume here that the formation of the *N*-acylurea is the only pathway by which the precursor is irreversibly converted. Put differently, the concentration *N*-acylurea is equal to the concentration precursor lost. CMC formed the largest amount of unwanted *N*-acylurea (53%, as expressed in the amount of fuel used to make *N*-acylurea), and EDC ranked second with a value of 33% (Fig. 1A). DIC showed the least formation of *N*-acylurea (17%). Because of DIC's poor water solubility, we focused the rest of this study on EDC.

One pathway to suppressing *N*-acylurea formation is to ensure the *O*-acylurea is as short-lived as possible. The *O*-acylurea lifetime can be decreased by increasing the precursor concentration or adding additives like pyridine.[44] Increasing the catalyst (C_3) concentration increased the nucleophile concentration, making *O*-acylurea more vulnerable towards being attacked by a second catalyst and resulting in less *N*-acylurea and higher desired product anhydride. Hence, we first studied the effect of precursor concentration on forming *N*-acylurea by fueling the reaction cycle with 50 mM EDC with varying concentrations of C_3 (50, 100, 200, and 300 mM). To follow the kinetics of the reaction cycle, we used a benzylamine quenching method developed by our group[45] to measure the concentration of the product and EDC by converting the anhydride to a stable
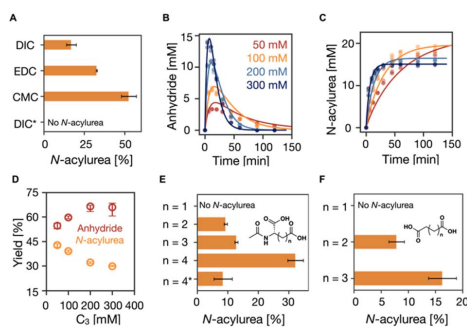
Edge Article

Fig. 1 The influence of fuels and catalysts on the suppression of N-acylurea. (A) The influence of the structure of fuels on the suppression of N-acylurea. The conditions are 75 mM C_3 in 200 mM MES buffer at pH 6 at 21 °C fueled with 15 mM EDC, CMC, and DIC. * was the reaction cycle conducted at pH 5 at 5 °C with 1.5 mM (10% of the fuel) pyridine. (B–D) The influence of the catalyst concentration. The kinetics profiles of (B) anhydride concentration and (C) N-acylurea concentration in the reaction cycles of 50, 100, 150, and 200 mM C_3 fueled with 50 mM EDC in MES buffer (200 mM, pH 6 at 21 °C). HPLC data (markers) and the kinetic model (lines), $n = 3$. (D) The yields of anhydride and N-acylurea as a fraction of fuel against C_3 concentration. Error bars for yield of anhydride are the 95% confidence interval. (E and F) The influence of the structure of the catalyst on the suppression of N-acylurea. Derivates of (E) N-acetyl-L-aspartic acid and (F) succinic acid. * was the reaction cycle conducted at pH 5 at 5 °C with 5 mM (10% of the fuel) pyridine.

benzylamide and EDC to a guanidine, respectively. We also used a kinetic model to fit the experimental data of species involved in the reaction cycle every minute by solving a set of ordinary differential equations (see ESI†).[7,46] The rate constants were determined by the model, and we could calculate the efficiency of the cycle, i.e., the percentage of fuel used to form the transient intermolecular anhydride. We found that, with increasing C_3 concentration, the EDC was consumed faster (Table S2, Fig. S2 and S11†), yielding a higher maximum anhydride concentration (3 mM to 14 mM) which was present for a shorter period (Fig. 1B). Most importantly, the N-acylurea showed only a moderate decrease from 20 mM to 15 mM, respectively (Fig. 1B and C). Since the anhydride is a transient product whose activation (formation) and deactivation (hydrolysis) occur simultaneously, the fraction of fuel successfully used to make the anhydride cannot be directly calculated by measuring the anhydride concentration. However, we used the kinetic model to calculate this fraction—by integrating the anhydride hydrolysis.[7] Increasing C_3 concentration from 50 mM to 300 mM increased the effective yield from 55% to 66%, while the N-acylurea yield decreased from 43% to 30% (Fig. 1D).

From these effective yields, we can define a term we call the selectivity (S), i.e., how much fuel is used for anhydride production relative to N-acylurea production (eqn (1)). S scales from +100% to −100%, where −100% implies only N-acylurea is formed and +100% implies only anhydride is formed. We are aiming for an S of 100%. S is slightly different from simply

comparing the yields, as S is independent of the O-acylurea hydrolyzed. Thus, it is not a measure of the cycle's efficiency but rather a description of the selectivity of anhydride over N-acylurea.

$$S = \frac{\text{yield}_{\text{anhydride}} - \text{yield}_{N\text{-acylurea}}}{\text{yield}_{\text{anhydride}} + \text{yield}_{N\text{-acylurea}}} \times 100 \qquad (1)$$

Increasing the C_3 concentration from 50 mM to 300 mM increased the selectivity from 12% to 38% (Fig. S2Q†). Notably, the effect tended to wear off as the concentration C_3 increased. Taken together, increasing the C_3 concentration increases the likelihood of forming the wanted anhydride, but the effect wears off. Besides, decreasing the yield of the N-acylurea product to 30% is insufficient for supramolecular machinery—it would imply that less than 1% of the catalyst is present after as little as four cycles.

Given that the N-acylurea side product formation decreased with increasing C_3 concentration, we tested the effect of local concentration effects on the reaction cycle—we used dicarboxylate catalysts that can form intramolecular anhydride in a ring-closing reaction. We evaluated the ring-size effect in aspartate-like (Fig. 1E) and succinate-like derivatives (Fig. 1F) and varied the side chain length from 1 carbon to 4 carbons. We fueled 100 mM dicarboxylate catalysts with 50 mM EDC and determined the lost catalyst concentration to measure the N-acylurea concentration formed after 24 hours. No catalyst was lost for N-acetyl-L-aspartate ($n = 1$, 5- membered anhydride, Fig. 1E), and HPLC showed no new N-acylurea peak. As the neighboring carboxylates were spaced farther from one another by increasing the number of carbons, an increasing concentration of N-acylurea was formed. For example, when the side chain has two carbons ($n = 2$, N-acetyl-L-glutamate, corresponding to a 6-membered ring anhydride), 9% of the catalyst is lost. This value rises to 32% when the side chain has four carbons ($n = 4$). Similar effects were observed for the succinic acid series ($n = 1$, 2, and 3, Fig. 1F). Taken together, as the distance between the O-acylurea and the second carboxylate as a nucleophile increases, the local concentration effect is suppressed, leading to more unwanted side product.

Next, we tested the role of additives in suppressing the unwanted N-acylurea. We focused on trapping agents, i.e., reagents like pyridine, that react rapidly with the O-acylurea to form intermediates that cannot rearrange to the N-acylurea (Fig. 2A).[47,48] Besides pyridine, we tested the performance of 1,2,4-triazole, and DMAP (4-dimethylaminopyridine), by fueling 100 mM C_3 with 50 mM EDC with 10 mM of the additives. Compared to the reaction cycle without additives, 1,2,4-triazole and DMAP showed a very limited ability to increase the efficiency and selectivity of the reaction cycle with similar yields of N-acylurea (40%) and anhydride (60%) (Fig. 2B, S3 and S12†). In contrast, pyridine significantly suppressed N-acylurea formation to 5% of the EDC added, while 92% of EDC was used to form anhydride (Fig. 2B and S3†).

In terms of the mechanism of action, we studied how additives modify the kinetic constants of the reaction cycle.
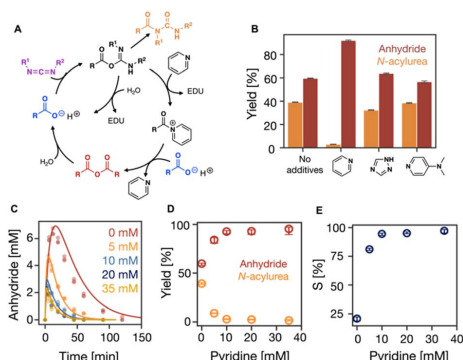
Fig. 2 The influence of additives on the suppression of *N*-acylurea. (A) Simplified representation of the reaction cycle with additives, pyridine as an example. (B) The efficiency of the reaction when additives like pyridine, 1,2,4-triazole, and DMAP were used. (C) The kinetic profiles of anhydride concentration in the reaction cycles of 100 mM C$_3$ fueled with 50 mM EDC with 0, 5, 10, 20, 35 mM pyridine in MES buffer (200 mM, pH 6 at 21 °C). HPLC data (markers) and the kinetic model (lines), $n = 3$. (D) The yields of anhydride and *N*-acylurea as a fraction of fuel against the pyridine concentration. Error bars for yield of anhydride are the 95% confidence interval. (E) Selectivity as defined in eqn (1) against the pyridine concentrations.

According to our hypothesis, reactions involving *O*-acylurea as a reagent will be significantly modified. In the case of pyridine, anhydride formation (k_2) and *O*-acylurea hydrolysis (k_3) were one order of magnitude faster compared to the without or other additives (Table S3, Fig. S3†). All additives favor anhydride hydrolysis (k_4), while pyridine accelerated hydrolysis most, 12-fold faster than without pyridine, thereby shortening the anhydride half-life from 9 minutes to 46 seconds. Moreover, the decreased half-life also decreased the maximum anhydride formed to 2.5 mM (Table S3, Fig. S3†). Although all additives reduced the half-life of the anhydride, 1,2,4-triazole showed the least catalytic activity and did not significantly decrease the maximum anhydride concentration (Table S3, Fig. S3†). These differences in catalytic activity can be explained by their nucleophilicities in water at pH 6. Even though DMAP has a greater nucleophilicity than pyridine,[49] its nucleophilicity is decreased because it is protonated at pH 6. DMAP has a higher pK_a (9.7)[50] in water than 1,2,4-triazole (pK_a = 2.4)[51] and pyridine (pK_a = 5.23).[52] Therefore, at pH 6, 1,2,4-triazole and pyridine are not pronated, but 1,2,4-triazole showed the least catalytic ability, because azoles are less nucleophilic than pyridines.[53]

As we established that pyridine is the most successful additive, we tested the effect of its concentration by fueling 100 mM C$_3$ with 50 mM EDC with various amounts of pyridine on the selectivity. With increasing pyridine concentration from 0 to 35 mM, the reaction cycle became faster with accelerated rate constants of all reactions. Especially, EDC consumption was faster (Table S4, Fig. S4 and S13†), and anhydride was present for as short as 50 minutes (Fig. 2C). Between a pyridine concentration of 0 and 35 mM, the maximum anhydride

decreased from 6.5 mM to 1.6 mM (Fig. 2C) due to the accelerated hydrolysis. However, it remained roughly constant above 10 mM pyridine. Similarly, the amount of EDC used to form the unwanted *N*-acylurea significantly decreased from 39% to 1% but only marginally decreased beyond 10 mM pyridine (Fig. 2D and S4†). Therefore, pyridine concentrations greater than 10 mM result in similar values in the consumption of EDC to produce both anhydride and *N*-acylurea (Fig. 2D, Table S4†). These optimized conditions greatly improve over the original conditions.

In our kinetic model, we do not consider the formation of the acylpyridinium ion formed due to the reaction between *O*-acylurea and pyridine. Hence, all constants related to *O*-acylurea also consider the acylpyridinium ion, which is why they monotonically change with pyridine concentration (Table S4, Fig. S4†). *S* was 20% without pyridine and increased to 97% with 35 mM pyridine, indicating the *N*-acylurea gets much less favored with increasing pyridine. Still, no significant increase was observed between 10 mM pyridine and 35 mM pyridine (Fig. 2E), suggesting the effect of pyridine concentration wears off.

Next, we tested the effect of temperature on the suppression of *N*-acylurea by fueling 100 mM C$_3$ with 50 mM EDC at 5, 21, and 35 °C. An increase in temperature tends to increase reaction rates while decreasing selectivity. Indeed, with increasing temperature, the overall reaction cycle became faster (Fig. 3A, S5 and S14, Table S5†). The anhydride concentration peaked at around 5 mM at all the temperatures, but the half-lives of the anhydride decreased from 16 min (5 °C) to 4 min (35 °C), respectively. Moreover, the concentration of *N*-acylurea doubled from 10 mM (5 °C) to 20 mM (35 °C) when increasing the temperature (Fig. S5†). From the kinetic model, it became clear that the amount of EDC used to make anhydride decreased slightly while the fraction of EDC used for *N*-acylurea increased significantly (Fig. 3B). We calculated the selectivity factor, which increased from 20% (21 °C) to 50% (5 °C) and a marginal decrease to 18% (35 °C) (Fig. 3C). We conclude that the formation of the unwanted *N*-acylurea can be suppressed at lower temperatures.

Similarly, we tested the effect of pH on the suppression of *N*-acylurea by fueling 100 mM C$_3$ with 50 mM EDC in 200 mM MES buffer at 21 °C at pH 5, 6, and 7. With increasing pH, the overall reaction cycle became much slower because the rate of EDC consumption dropped by orders of magnitude (Table S5, Fig. S6 and S15†). Moreover, with increasing pH from 5 to 7, the anhydride hydrolysis decreased, resulting in an increased anhydride half-life from 7.5 to 19.2 min (Table S5,† Fig. 3D). Due to the decreased reactivity of EDC, the maximum anhydride concentration dropped drastically (Fig. 3D). Nevertheless, the amount of EDC used to produce anhydride varied minimally, with similar values for pH 5 and 7, around 46%, and a slight increase to 60% at pH 6 (Fig. 3E). However, the formed *N*-acylurea concentration increased drastically from pH 5 to 7 (Fig. S6† and 3E). In line with these data, the selectivity decreased from 58% to −3% with increasing pH (Fig. 3F), which implies that at higher pH, more EDC is used to make the unwanted *N*-acylurea than the wanted anhydride. Overall, pH 5
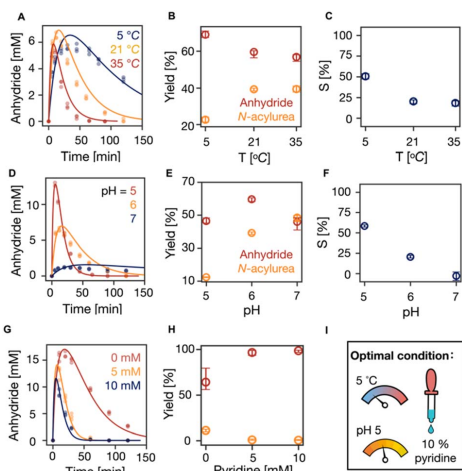
Edge Article

Fig. 3 The influence of temperature and pH on the suppression of *N*-acylurea. (A, D and G) The kinetics profiles of anhydride concentration in the reaction cycles of 100 mM C_3 that were fueled with 50 mM EDC in MES buffer (200 mM) (A) at pH 6 under 5, 21 and 35 °C without pyridine, (D) at pH 5, 6 and 7 at 21 °C without pyridine, (G) at pH 5 at 5 °C with 0, 5, 10 mM pyridine. HPLC data (markers) and the kinetic model (lines), $n = 3$. (B, E and H) The yields of anhydride and *N*-acylure as a fuel fraction under different conditions above. Error bars for yield of anhydride are the 95% confidence interval. (C and F) Selectivity as defined in eqn (1) against temperature and pH, respectively. (I) The optimal condition of our reaction cycle: low temperature at 5 °C, low pH at 5, and the addition of 10% pyridine as a fraction of fuel.

showed the best ability to suppress *N*-acylurea and keep the reaction cycle efficient.

We realized from all these data that lower temperature and pH lead to an efficient reaction cycle. We further sought optimized conditions by running the cycle under these conditions at pH 5, 5 °C with 0, 5, and 10 mM pyridine, decreasing the maximum anhydride concentration (Fig. 3G, S7 and S16, Table S6†). At the same time, it suppressed *N*-acylurea (Fig. S7†). The effectiveness of suppressing *N*-acylurea leveled off when the pyridine was more than 5 mM which is 10% of the fuel (Fig. 3H). Indeed, the selectivity significantly increased from 71% (0 mM pyridine) to 98% (10 mM pyridine) (Fig. S7Q†).

Therefore, we conclude that the optimal condition for our reaction cycle is to use dicarboxylic acids as catalysts that lead to 5-membered anhydrides like aspartic acid or succinic acid derivatives. When other catalysts are used, we suggest using 10% pyridine as a fraction of the fuel at pH 5 at 5 °C. Under those optimal conditions, *N*-acylurea was completely suppressed in the cycle of C_3 with DIC (Fig. 1A and S7, Table S6 and S17†). Moreover, the reaction cycle of the *N*-acetyl-ʟ-aspartate derivate with a 4-carbon side chain ($n = 4$) under our optimal condition resulted in a 4-times decrease in the yield of *N*-acylurea side product (Fig. 1E). Furthermore, we conducted refueling experiments of 100 mM C_3 with 50 mM EDC under the

optimal condition of pH 5 at 5 °C with 5 mM pyridine (10% of the fuel) for 10 times (Fig. S10A†). The yield of the unwanted *N*-acylurea in each refueling experiment stays constant and only 4.2 mM *N*-acylurea accumulated after 10 times of refueling. With our kinetic model, we simulated that the catalyst can now undergo over 142 times of refueling before its concentration falls below 1% (Fig. S10B†). In stark contrast, the catalyst was depleted after 5 times of refueling under the standard condition (pH 6, 21 °C without pyridine) (Fig. S10C†).

We tested our newly optimized condition in a case using a catalyst that could phase-separate, *i.e.*, butyric acid (C_4). Due to the extra methylene group compared to C_3, the activated catalyst of C_4 phase separates to form oil droplets. We ran reaction cycles by fueling 100 mM C_4 with 100 mM EDC under the sub-optimal condition (pH 6 without pyridine) and optimal condition (pH 5 with 10% pyridine as a fraction of EDC). Both reaction cycles were run at 21 °C to compare the phase separation better because phase separation is strongly temperature-dependent.[54] The reaction cycle under the sub-optimal condition did not turn turbid, suggesting no assembly was observed. However, under the optimal condition, the reaction solution became turbid within 30 seconds after EDC was applied, and this turbidity persisted for 5 minutes, as observed on UV/vis spectroscopy (Fig. 4A). Confocal fluorescence microscopy confirmed that the transient assembly consisted of oil droplets (Fig. 4B). The total volume of the droplets calculated from the confocal fluorescence microscopy peaked at 579 ± 70 μm around 2 min after EDC was added and decreased to 0 after 5 minutes (Fig. 4C). Moreover, the hydrodynamic diameter of the
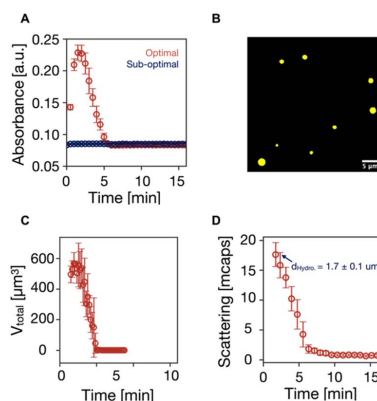
Fig. 4 Assembly obtained under the optimal condition. (A) Absorbance at 600 nm by UV/vis spectroscopy as a measure of turbidity of the reaction cycles of 100 mM C_4 fueled with 100 mM EDC in 200 mM MES buffer at 21 °C under sub-optimal (pH 6 without pyridine) and optimal (pH 5 with 10% pyridine) conditions. (B) Confocal fluorescence microscopy image of the oil droplets obtained in the reaction cycle under the optimal condition described in (A). (C) The total volume of oil droplets as a function of time was obtained from confocal fluorescence microscopy. (D) Scattering rate of the droplets as a function of time.

droplets was 1.7 ± 0.1 μm on dynamic light scattering (DLS) (Fig. 4D). The scattering intensity profile further confirmed that droplets emerged upon the application of EDC and decayed after EDC was depleted. The droplets' lifetime was also consistent with the values obtained on UV/vis spectroscopy and confocal fluorescence microscopy. Taken together, using the optimal *versus* sub-optimal conditions can make the difference between obtaining chemically fueled functions or not.

Conclusions

The carbodiimide-driven reaction cycle has proven a powerful catalytic reaction in powering supramolecular machinery, self-assembly, and phase separation. Nevertheless, side reactions poison the catalyst, which is disastrous for these reaction cycles. We tested the effects of various parameters on suppressing side product *N*-acylurea in a carbodiimide-driven reaction cycle, including fuel structure, catalyst concentration, catalyst structure, additives, temperature, and pH. Increasing catalyst concentration results in less *N*-acylurea formation, but the influence wore off. Catalysts with two carboxylic groups tend to form intramolecular anhydrides with less *N*-acylurea. However, *N*-acylurea formation becomes more favored if the two carboxylic groups are far apart. Moreover, pyridine performed best, but its ability also wore off with increasing concentration. Low temperature and low pH gave a higher effective reaction cycle. Hence, a combination of low temperature, low pH, and 10% pyridine as a fuel fraction is the optimal condition for a highly effective carbodiimide-driven cycle. We believe our work would provide helpful suggestions for using carbodiimide-fueled reaction cycles to regulate molecular function about how to choose an optimal condition.

Data availability

The data that support the findings of this study are available from the corresponding author upon reasonable request.

Author contributions

J. B., X. C. O. Z. conceived the research. J. B. and X. C. designed the experiments, analyzed the data, and wrote the manuscript. H. S. C. wrote the kinetic model, fitted all the data, and corrected the manuscript. O. Z. did synthesis.

Conflicts of Interest

The authors declare no competing financial interest.

Acknowledgements

References

1 J. V. Moller, P. Nissen, T. L. Sorensen and M. l. Maire, Transport mechanism of the sarcoplasmic reticulum Ca2+-ATPase pump, *Curr. Opin. Struct. Biol.*, 2005, **15**, 387–393.

2 C. Toyoshima, Structural aspects of ion pumping by Ca2+-ATPase of sarcoplasmic reticulum, *Arch. Biochem. Biophys.*, 2008, **476**, 3–11.

3 G. J. Brouhard and L. M. Rice, Microtubule dynamics: an interplay of biochemistry and mechanics, *Nat. Rev. Mol. Cell Biol.*, 2018, **19**, 451–463.

4 J. Boekhoven, W. E. Hendriksen, G. J. M. Koper, R. Eelkema and J. H. van Esch, Transient assembly of active materials fueled by a chemical reaction, *Science*, 2015, **349**, 1075–1079.

5 S. Borsley, E. Kreidt, D. A. Leigh and B. M. W. Roberts, Autonomous fuelled directional rotation about a covalent single bond, *Nature*, 2022, **604**, 80–85.

6 M. Tena-Solsona, B. Riess, R. K. Grotsch, F. C. Lohrer, C. Wanzke, B. Kasdorf, A. R. Bausch, P. Muller-Buschbaum, O. Lieleg and J. Boekhoven, Non-equilibrium dissipative supramolecular materials with a tunable lifetime, *Nat. Commun.*, 2017, **8**, 15895.

7 L. S. Kariyawasam and C. S. Hartley, Dissipative Assembly of Aqueous Carboxylic Acid Anhydrides Fueled by Carbodiimides, *J. Am. Chem. Soc.*, 2017, **139**, 11949–11955.

8 X. Chen, M. A. Wurbser and J. Boekhoven, Chemically Fueled Supramolecular Materials, *Acc. Mater. Res.*, 2023, **4**, 416–426.

9 C. Donau, F. Spath, M. Sosson, B. A. K. Kriebisch, F. Schnitter, M. Tena-Solsona, H. S. Kang, E. Salibi, M. Sattler, H. Mutschler and J. Boekhoven, Active coacervate droplets as a model for membraneless organelles and protocells, *Nat. Commun.*, 2020, **11**, 5167.

10 F. Spath, C. Donau, A. M. Bergmann, M. Kranzlein, C. V. Synatschke, B. Rieger and J. Boekhoven, Molecular Design of Chemically Fueled Peptide-Polyelectrolyte Coacervate-Based Assemblies, *J. Am. Chem. Soc.*, 2021, **143**, 4782–4789.

11 C. Donau, F. Spath, M. Stasi, A. M. Bergmann and J. Boekhoven, Phase Transitions in Chemically Fueled, Multiphase Complex Coacervate Droplets, *Angew. Chem., Int. Ed.*, 2022, **61**, e202211905.

12 B. J. Niebuur, H. Hegels, M. Tena-Solsona, P. S. Schwarz, J. Boekhoven and C. M. Papadakis, Droplet Formation by Chemically Fueled Self-Assembly: The Role of Precursor Hydrophobicity, *J. Phys. Chem. B*, 2021, **125**, 13542–13551.

Edge Article

13 M. M. Hossain, J. L. Atkinson and C. S. Hartley, Dissipative Assembly of Macrocycles Comprising Multiple Transient Bonds, *Angew. Chem., Int. Ed.*, 2020, **59**, 13807–13813.

14 M. M. Hossain, I. M. Jayalath, R. Baral and C. S. Hartley, Carbodiimide-Induced Formation of Transient Polyether Cages**, *ChemSystemsChem*, 2022, **4**, e202200016.

15 R. K. Grotsch, C. Wanzke, M. Speckbacher, A. Angi, B. Rieger and J. Boekhoven, Pathway Dependence in the Fuel-Driven Dissipative Self-Assembly of Nanoparticles, *J. Am. Chem. Soc.*, 2019, **141**, 9872–9878.

16 C. Wanzke, A. Jussupow, F. Kohler, H. Dietz, V. R. I. Kaila and J. Boekhoven, Dynamic Vesicles Formed By Dissipative Self-Assembly, *ChemSystemsChem*, 2019, **2**, e1900044.

17 A. Englert, J. F. Vogel, T. Bergner, J. Loske and M. von Delius, A Ribonucleotide <?> Phosphoramidate Reaction Network Optimized by Computer-Aided Design, *J. Am. Chem. Soc.*, 2022, **144**, 15266–15274.

18 J. Sun, J. Vogel, L. Chen, A. L. Schleper, T. Bergner, A. J. C. Kuehne and M. von Delius, Carbodiimide-Driven Dimerization and Self-Assembly of Artificial, Ribose-Based Amphiles, *Chem. –Eur. J.*, 2022, **28**, e202104116.

19 K. Dai, J. R. Fores, C. Wanzke, B. Winkeljann, A. M. Bergmann, O. Lieleg and J. Boekhoven, Regulating Chemically Fueled Peptide Assemblies by Molecular Design, *J. Am. Chem. Soc.*, 2020, **142**, 14142–14149.

20 B. A. K. Kriebisch, A. Jussupow, A. M. Bergmann, F. Kohler, H. Dietz, V. R. I. Kaila and J. Boekhoven, Reciprocal Coupling in Chemically Fueled Assembly: A Reaction Cycle Regulates Self-Assembly and Vice Versa, *J. Am. Chem. Soc.*, 2020, **142**, 20837–20844.

21 S. Panja and D. J. Adams, Chemical crosslinking in 'reactive' multicomponent gels, *Chem. Commun.*, 2022, **58**, 5622–5625.

22 S. Panja, B. Dietrich and D. J. Adams, Chemically Fuelled Self-Regulating Gel-to-Gel Transition, *ChemSystemsChem*, 2019, **2**, e1900038.

23 Z. F. Yao, Y. Kuang, P. Kohl, Y. Li and H. A. M. Ardoña, Carbodiimide-Fueled Assembly of π-Conjugated Peptides Regulated by Electrostatic Interactions, *ChemSystemsChem*, 2023, **5**, e20230000.

24 S. Bal, K. Das, S. Ahmed and D. Das, Chemically Fueled Dissipative Self-Assembly that Exploits Cooperative Catalysis, *Angew. Chem., Int. Ed.*, 2019, **58**, 244–247.

25 S. Mondal and D. Haldar, A transient non-covalent hydrogel by a supramolecular gelator with dynamic covalent bonds, *New J. Chem.*, 2021, **45**, 4773–4779.

26 X. Chen, B. A. K. Kriebisch, A. M. Bergmann and J. Boekhoven, Design rules for reciprocal coupling in chemically fueled assembly, *Chem. Sci.*, 2023, **14**, 10176–10183.

27 F. Schnitter, B. Riess, C. Jandl and J. Boekhoven, Memory, switches, and an OR-port through bistability in chemically fueled crystals, *Nat. Commun.*, 2022, **13**, 2816.

28 M. A. Würbser, P. Schwarz, J. Heckel, A. M. Bergmann, A. Walther and J. Boekhoven, Chemically Fueled Block Copolymer Self-Assembly into Transient Nanoreactors, *ChemSystemsChem*, 2021, **3**, e2100015.

29 C. W. H. Rajawasam, C. Tran, M. Weeks, K. S. McCoy, R. Ross-Shannon, O. J. Dodo, J. L. Sparks, C. S. Hartley and D. Konkolewicz, Chemically Fueled Reinforcement of Polymer Hydrogels, *J. Am. Chem. Soc.*, 2023, **145**, 5553–5560.

30 B. Zhang, I. M. Jayalath, J. Ke, J. L. Sparks, C. S. Hartley and D. Konkolewicz, Chemically fueled covalent crosslinking of polymer materials, *Chem. Commun.*, 2019, **55**, 2086–2089.

31 J. Heckel, S. Loescher, R. T. Mathers and A. Walther, Chemically Fueled Volume Phase Transition of Polyacid Microgels, *Angew. Chem., Int. Ed.*, 2021, **60**, 7117–7125.

32 X. Lang, U. Thumu, L. Yuan, C. Zheng, H. Zhang, L. He, H. Zhao and C. Zhao, Chemical fuel-driven transient polymeric micelle nanoreactors toward reversible trapping and reaction acceleration, *Chem. Commun.*, 2021, **57**, 5786–5789.

33 S. Borsley, D. A. Leigh, B. M. W. Roberts and I. J. Vitorica-Yrezabal, Tuning the Force, Speed, and Efficiency of an Autonomous Chemically Fueled Information Ratchet, *J. Am. Chem. Soc.*, 2022, **144**, 17241–17248.

34 M. Stasi, A. Monferrer, L. Babl, S. Wunnava, C. F. Dirscherl, D. Braun, P. Schwille, H. Dietz and J. Boekhoven, Regulating DNA-Hybridization Using a Chemically Fueled Reaction Cycle, *J. Am. Chem. Soc.*, 2022, **144**, 21939–21947.

35 F. Kurzer and K. Douraghi-Zadeh, Advances in the chemistry of carbodiimides, *Chem. Rev.*, 1967, **67**, 107–152.

36 D. F. DeTar and R. Silverstein, Reactions of Carbodiimides. I. The Mechanisms of the Reactions of Acetic Acid with Dicyclohexylcarbodiimide1,2, *J. Am. Chem. Soc.*, 1966, **88**, 1013–1019.

37 D. F. DeTar and R. Silverstein, Reactions of Carbodiimides. II. The Reactions of Dicyclohexylcarbodiimide with Carboxylic Acids in the Presence of Amines and Phenols1,2, *J. Am. Chem. Soc.*, 1966, **88**, 1020–1023.

38 D. F. DeTar, R. Silverstein and F. F. Rogers Jr, Reactions of Carbodiimides. III. The Reactions of Carbodiimides with Peptide Acids1,2, *J. Am. Chem. Soc.*, 1966, **88**, 1024–1030.

39 P. S. Schwarz, S. Laha, J. Janssen, T. Huss, J. Boekhoven and C. A. Weber, Parasitic behavior in competing chemically fueled reaction cycles, *Chem. Sci.*, 2021, **12**, 7554–7560.

40 R. K. Grotsch, A. Angi, Y. G. Mideksa, C. Wanzke, M. Tena-Solsona, M. J. Feige, B. Rieger and J. Boekhoven, Dissipative Self-Assembly of Photoluminescent Silicon Nanocrystals, *Angew. Chem., Int. Ed.*, 2018, **57**, 14608–14612.

41 M. Tena-Solsona, C. Wanzke, B. Riess, A. R. Bausch and J. Boekhoven, Self-selection of dissipative assemblies driven by primitive chemical reaction networks, *Nat. Commun.*, 2018, **9**, 2044.

42 C. M. E. Kriebisch, A. M. Bergmann and J. Boekhoven, Fuel-Driven Dynamic Combinatorial Libraries, *J. Am. Chem. Soc.*, 2021, **143**, 7719–7725.

43 X. Chen, M. Stasi, J. Rodon-Fores, P. F. Grossmann, A. M. Bergmann, K. Dai, M. Tena-Solsona, B. Rieger and J. Boekhoven, A Carbodiimide-Fueled Reaction Cycle That Forms Transient 5(4H)-Oxazolones, *J. Am. Chem. Soc.*, 2023, **145**, 6880–6887.

42

44 S. E. Denmark and G. L. Beutner, Lewis base catalysis in organic synthesis, *Angew. Chem., Int. Ed.*, 2008, **47**, 1560–1638.

45 F. Schnitter and J. Boekhoven, A Method to Quench Carbodiimide-Fueled Self-Assembly, *ChemSystemsChem*, 2020, **3**, e2000037.

46 L. S. Kariyawasam, J. C. Kron, R. Jiang, A. J. Sommer and C. S. Hartley, Structure-Property Effects in the Generation of Transient Aqueous Benzoic Acid Anhydrides by Carbodiimide Fuels, *J. Org. Chem.*, 2020, **85**, 682–690.

47 N. De Rycke, F. Couty and O. R. David, Increasing the reactivity of nitrogen catalysts, *Chem. –Eur. J.*, 2011, **17**, 12852–12871.

48 V. Lutz, J. Glatthaar, C. Wurtele, M. Serafin, H. Hausmann and P. R. Schreiner, Structural analyses of N-acetylated 4-(dimethylamino)pyridine (DMAP) salts, *Chem. –Eur. J.*, 2009, **15**, 8548–8557.

49 F. Brotzel, B. Kempf, T. Singer, H. Zipse and H. Mayr, Nucleophilicities and carbon basicities of pyridines, *Chem. –Eur. J.*, 2007, **13**, 336–345.

50 T. Fulga, M. Onciu and C. I. Chiriac, Syntheses of esters from carboxylic acids and diphenyl carbonate-4-dimethylaminopyridine at room temperature, *Rev. Roum. Chim.*, 2003, **48**, 869–872.

51 L. Siwen, Z. Zhen, Z. Yuelan and L. Meilin, 1H-1,2,4-Triazole: An Effective Solvent for Proton-Conducting Electrolytes, *Chem. Mater.*, 2005, **17**, 5884–5886.

52 A. Gero and J. J. Markhamm, Studies on pyridines: I. The basicity of pyridine bases, *J. Org. Chem.*, 1951, **16**, 1835–1838.

53 M. Baidya, F. Brotzel and H. Mayr, Nucleophilicities and Lewis basicities of imidazoles, benzimidazoles, and benzotriazoles, *Org. Biomol. Chem.*, 2010, **8**, 1929–1935.

54 H. Eisenberg and G. Felsenfeld, Studies of the temperature-dependent conformation and phase separation of polyriboadenylic acid solutions at neutral pH, *J. Mol. Biol.*, 1967, **30**, 17–37.

Electronic Supplementary Information for:

Suppressing catalyst poisoning in the carbodiimide-fueled reaction cycle

Xiaoyao Chen,[1] Héctor Soria-Carrera,[1] Oleksii Zozulia,[1] Job Boekhoven[1*]

[1] Department of Chemistry, School of Natural Sciences, Technical University of Munich, Lichtenbergstrasse 4, 85748 Garching, Germany.

MATERIALS

Materials. (S)-2-Aminoadipic Acid, and (S)-2-Aminoheptanedioic acid were purchased from BLDpharm. adipic acid, glutaric acid, succinic acid, N-Acetyl-L-aspartic acid (Ac-D-OH), N-Acetyl-L-glutamic acid (Ac-E-OH), propionic acid, butyric acid, 2-(N-morpholino) ethanesulfonic acid (MES) buffer, 1-Ethyl-3-[3-dimethylaminopropyl]carbodiimide hydrochloride (EDC HCl), N, N'-Diisopropylcarbodiimide, benzylamine, trifluoroacetic acid (TFA) were purchased from Sigma-Aldrich and used without any further purification unless otherwise indicated. HPLC grade acetonitrile (ACN), and N N-Dimethylformamide were purchased from VWR.

METHODS

Sample preparation. We prepared stock solutions of the precursors by dissolving the acids in 0.2 M MES buffer, then we adjusted the pH to 5.0, 6.0, or 7.0. Benzylamine stocks were prepared freshly in acetonitrile. EDC stock solutions were prepared by dissolving the EDC powder in MQ water. Reaction cycles were started by adding EDC from the freshly prepared stock solution to the precursor.

Peptide synthesis and purification. (S)-2-aminoadipic acid and (S)-2-aminoheptanedioic acid were acetylated using acetic anhydride under ultrasonic conditions as reported before for numerous amino acids, in particular for Glu and Asp.[1] In brief, 100 mg of each amino acid were suspended in 5 mL of acetic anhydride and sonicated for 10 minutes until complete dissolution. Evaporation and further purification of crude solid on a reversed-phase High-Performance Liquid Chromatography (RP-HPLC), detected at 220 nm. The purified acetylated amino acids were lyophilized (Lyophylle: Alpha LDplus, Christ) and characterized by ^{1}H-NMR spectroscopy, HPLC, and Electron Spray Ionisation – Mass Spectrometry (ESI-MS).

Kinetic model. We used a kinetic model to predict the concentration of the anhydride, EDC and N-acylurea over time. We describe the model in supporting Note. The rate constants we used in this work are given in Supporting Table S2 – S6.

Analysis of the reaction kinetics by HPLC. The kinetics of the chemical reaction cycles were monitored over time by analytical HPLC (ThermoFisher Vanquish Duo UHPLC, a Hypersil Gold 100 x 2.1 mm C18 column (3 μm pore size). We used the quenching method[2] to indirectly determine the concentration of the anhydride product by converting it irreversibly into an amide, which we refer to as benzylamine. Also, EDC reacted with benzylamine and was converted irreversibly into a guanidine. After initiating the reaction cycle by adding EDC to the precursor solution, we took a certain amount of reaction solution to the benzylamine solution at each time point. After several hours, the resulting quenched clear solution was measured via HPLC to determine the benzylamide and guanidine concentration. In this work, the ratio of the reaction solution and benzylamine solution (400 mM) was 1:1. 0.5 μL quenched solution was directly injected without further dilution into HPLC and tracked with a UV/Vis detector at 220 and 254 nm. All compounds involved were separated using a method of a linear gradient of H$_2$O: ACN, each with 0.1% TFA.

HPLC Methods.
Method 1. for Propionic acid, Adipic Acid, N-acetyl-L-2-aminoadipic acid and N-acetyl-L-2-aminoheptanedioic acid: H$_2$O/ACN starts from 98/2. ACN keeps at 2 % for the first 5 min, increasing to 25% in 14 min, 1 min increasing to 98 %, followed by 1 min 98 %, 1 min going back to 2%, and finally 3 min 2%.
Method 2. for succinic acid and N-Acetyl-L-aspartic acid (Ac-D-OH): H$_2$O/ACN starts from 99/1. ACN keeps at 1 % for the first 7 min, increasing to 50% in 2 min, followed by 2 min 50 %, 2 min going back to 1%, and finally 4 min 1%.
Method 3. for N-Acetyl-L-glutamic acid (Ac-E-OH): H$_2$O/ACN starts from 98/2. ACN keeps at 2 % for the first 5 min, increasing to 15% in 8 min, 11 min climbing to 17 %, 1 min increasing to 98 %, followed by 1 min 98 %, 1min going back to 2%, and finally 3 min 2%.
Method 4. for N-Acetyl-L-glutamic acid (Ac-E-OH): H$_2$O/ACN starts from 98/2. ACN keeps at 2 % for the first 5 min, increasing to 15% in 8 min, 11 min climbing to 17 %, 1 min increasing to 98 %, followed by 1 min 98 %, 1min going back to 2%, and finally 3 min 2%.
Method 5. for glutaric acid: H$_2$O/ACN starts from 98/2. ACN keeps at 2 % for the first 7 min, increasing to 98% in 2 min, followed by 2 min 98 %, 2 min going back to 2%, and finally 4 min 2%.
Method 6. for Propionic acid when CMC as a fuel: H$_2$O/ACN starts from 98/2. ACN keeps at 2 % for the first 5 min, increasing to 25% in 5 min, 10 min increasing to 98 %, followed by 1 min 98 %, 1 min going back to 2%, and finally 3 min 2%.
Method 7. for Propionic acid when DIC as a fuel (quenched): H$_2$O/ACN starts from 98/2. ACN keeps at 2 % for the first 5 min, increasing to 25% in 14 min, 9 min increasing to 98 %, followed by 2 min 98 %, 2 min going back to 2%, and finally 3 min 2%.

Electron Spray Ionisation – Mass Spectrometry (ESI-MS). We used a Varian 500 MS LC ion trap or an LCQ Fleet Ion Trap Mass Spectrometer (Thermo Scientific) to perform ESI-MS measurements. The samples were diluted in acetonitrile or MQ water before injection into the Mass Spectrometer. All recorded MS data were interpreted using the Thermo Xcalibur Qual Browser 2.2 SP1.48 software or a direct photo by a smartphone.

Dynamic light scattering (DLS). DLS experiments were conducted on Litesizer 500 in the measurement mode of particle size series. The measurements were measured with automatic angle and an equilibration time of 5s. Each measurement consisted of 3 acquisitions with an acquisition time of 10s.

2

Confocal Fluorescence Microscopy. We used a Leica SP5 confocal microscope with a 63x water immersion objective to image the oil droplets. Samples were prepared as described above with a total reaction volume of 30 μL, including 2.5 μM Nile red as a dye. Samples were deposited on an IBIDI 15 wells chambered coverslip with sterilized glass-bottom No. 1.5H non-coated before exciting them with a 552 nm laser and imaging at 580 - 700 nm. All recorded images were analyzed using the ImageJ 1.52p software (Java 1.80_172 (64-bit)).

NMR spectra. NMR spectra were conducted on Bruker AV400US (400 and 500 MHz). Chemical shifts are reported as δ-values in parts per million (ppm) relative to the deuterated solvent peak: DMSO-d_6 (δH: 2.50). For the denotation of the observed signal multiplicities, the following abbreviations were used: m (multiplet), dd (doublet of doublets), d (doublet), and s (singlet).

Turbidity measurements and lifetime determination. Turbidity measurements were carried out at 21 °C on a Microplate Spectrophotometer (Thermo Scientific Multiskan GO, Thermo Scientific SkanIt Software 6.0.1). Measurements were performed in a non-tissue culture treated 96-well plate (Falcon, flat bottom). Every 30 seconds, the absorbance of the 100μL samples was measured at 600 nm. All experiments were performed three times. The lifetime refers to the time it takes for the absorption to drop under 0.01 a.u. (blank subtraction) after EDC addition.

SUPPORTING NOTE

1. Description of the kinetic model

We wrote a kinetic model in Python that described each reaction involved in the chemical reaction network. The concentrations of each reactant were calculated for every 1 minute in the cycle. The model was used to fit the HPLC data that described the evolution of the concentration of precursors, EDC, anhydride, and N-acylurea over time. The model described 5 chemical reactions: direct hydrolysis of EDC (r_0), the activation of acid (r_1), the formation of intermolecular anhydride (r_2), hydrolysis of O-acylurea (r_3), hydrolysis of anhydride (r_4) and the side product formation of N-acylurea by a rearrangement reaction (N to O shift, r_5).

(0) Reaction 0: direct hydrolysis of EDC (k_0). It has a first-order rate constant that can be obtained from experiments. We used analytic HPLC to determine k_0 under different conditions, and the values can be found in Table S5.

(1) Reaction 1: the activation of acid by EDC to form O-acylurea (k_1). This second-order rate constant was determined for each precursor by HPLC by monitoring the EDC consumption.

(2) Reaction 2: the formation of intermolecular anhydride (k_2). This second-order rate constant could not be determined because the O-acylurea was not observed.

(3) Reaction 3: direct hydrolysis of O-acylurea (k_3). This first-order rate constant could not be obtained because the O-acylurea was not observed.

(4) Reaction 4: hydrolysis of anhydride (k_4). As indirectly determined by HPLC using the benzylamine quenching method, the hydrolysis of anhydride takes place with a (pseudo)-first order. The hydrolysis reaction rate was calculated by multiplying the first-order rate constant k_4 with the concentration of anhydride.

(5) Reaction 5: side product formation of N-acylurea (N to O shift, k_5). This first-order rate constant could not be obtained because the O-acylurea was not observed.

3

2. Ordinary differential equations (ODEs).

We used the following set of ODEs to describe the systems by using a steady-state approximation that removed any explicit dependence on the concentration of O-acylurea and used an in house developed python model to fit the experimental data.

The following set of ODEs was used and fitted. Ac stands for acid, F for fuel, W for waste, P for product and N for N-acylurea.

$$\begin{cases} \dfrac{d[Ac]}{dt} = -k_1 \cdot [Ac] \cdot [F] + 2 \cdot k_4 \cdot [P] + \dfrac{k_3}{k_2 \cdot [Ac] + k_3 + k_5} \cdot k_1 \cdot [Ac] \cdot [F] - \dfrac{k_2}{k_2 \cdot [Ac] + k_3 + k_5} \cdot k_1 \cdot [Ac]^2 \cdot [F] \\[3mm] \dfrac{d[F]}{dt} = -k_1 \cdot [Ac] \cdot [F] - k_0 \cdot [F] \\[3mm] \dfrac{d[W]}{dt} = +k_0 \cdot [F] + \dfrac{k_2 \cdot [Ac] + k_3}{k_2 \cdot [Ac] + k_3 + k_5} \cdot k_1 \cdot [Ac] \cdot [F] \\[3mm] \dfrac{d[P]}{dt} = +\dfrac{k_2}{k_2 \cdot [Ac] + k_3 + k_5} \cdot k_1 \cdot [Ac]^2 \cdot [F] - k_4 \cdot [P] \\[3mm] \dfrac{d[N]}{dt} = +\dfrac{k_5}{k_2 \cdot [Ac] + k_3 + k_5} \cdot k_1 \cdot [Ac] \cdot [F] \end{cases}$$

3. Python codes.

To fit the data, we used a homemade code inspired by previous works from Hartley's group.[3][4]

The code can be found on GitHub: https://github.com/BoekhovenLab/Catalyst-poisoning

Briefly, the functions of the code are defined in ODE_symmetric_package.

We solve the ODE system and fit it to the experimental data minimizing an error function. We used *lmfit* package (https://zenodo.org/record/11813). We also did bootstrap in the fitting to generate a distribution of kinetic constants that minimized the error. For the fitting, we used the median of the distribution to be more robust towards outliers compared to the mean. We also calculated the root-squared mean error of the fitting to calculate the 95 % confidence interval. We also calculated R^2 to evaluate the goodness of the fitting.

Then we create a function to run the above package before the fitting of the experimental data.
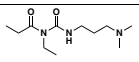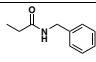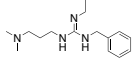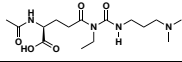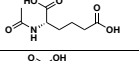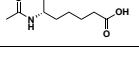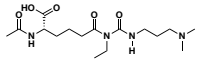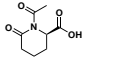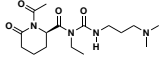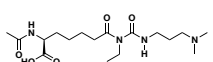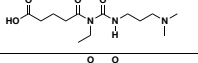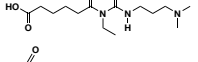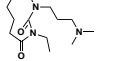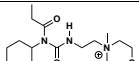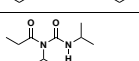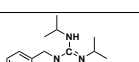
We do another notebook for fitting experimental data. It will first upload the data, then fit and plot it.

Examples of how to fit experimental data are in the GitHub repository.

4

SUPPORTING TABLES

Supporting Table S1. Mass information of all products in this work.

Name	Structure	Exact Mass (gmol^{-1})	Mass found (gmol^{-1})
Proponic acid-N-acylurea (EDC as a fuel)	Two possible isomers (we only show one, same as below)	Mw = 229.18 $C_{11}H_{23}N_3O_2$	229.94 [Mw+H$^+$]
Proponic acid- benzylamide		Mw = 163.1 $C_{10}H_{13}NO$	163.95 [Mw+H$^+$]
EDC-Guanidine		Mw = 262.22 $C_{15}H_{26}N_4$	263.11 [Mw+H$^+$]
Ac-E-N-acylurea		Mw = 344.21 $C_{15}H_{28}N_4O_5$	345.02 [Mw+H$^+$]
N-acetyl-L-2-aminoadipic acid		Mw = 203.08 $C_8H_{13}NO_5$	203.82 [Mw+H$^+$] 647.65 [3Mw+K$^+$]
N-acetyl-L-2-aminoheptanedioic acid		Mw = 217.10 $C_9H_{15}NO_5$	217.86 [Mw+H$^+$] 456.67 [2Mw+Na$^+$]
N-acetyl-L-2-aminoadipic-N-acylurea and other side products		Mw = 358.22 $C_{16}H_{30}N_4O_5$	359.07 [Mw+H$^+$]
		Mw = 185.07 $C_8H_{11}NO_4$	185.76 [Mw+H$^+$] 593.69 [3Mw+K$^+$]
		Mw = 340.21 $C_{16}H_{28}N_4O_4$	341.05 [Mw+H$^+$]
N-acetyl-L-2-aminoheptanedioic -N-acylurea		Mw = 372.24 $C_{17}H_{32}N_4O_4$	373.09 [Mw+H$^+$]
glutaric-N-acylurea		Mw = 287.18 $C_{13}H_{25}N_3O_4$	288.04 [Mw+H$^+$]
adipic-N-acylurea		Mw = 301.20 $C_{14}H_{27}N_3O_4$	302.05 [Mw+H$^+$]
		Mw = 283.19 $C_{14}H_{25}N_3O_3$	283.92 [Mw+H$^+$]
Propionic acid-CMC-N-acylurea		Mw = 326.24 $C_{17}H_{32}N_3O_3$	326.06 [Mw$^+$]
Propionic acid-DIC-N-acylurea		Mw = 200.15 $C_{10}H_{20}N_2O_2$	200.84 [Mw+H$^+$]
DIC- Guanidine		Mw = 233.19 $C_{14}H_{23}N_3O_3$	234.16 [Mw+H$^+$]

5

Supporting Table S2. Rate constants used in the kinetic model for X mM propionic acid with 50 mM EDC without pyridine in MES buffer (200 mM) at pH 6, 21 ºC.

	k_0 [min^{-1}]	k_1 [mM^{-1}min^{-1}]	k_2 [mM^{-1}min^{-1}]	k_3 [min^{-1}]	k_4 [min^{-1}]	k_5 [min^{-1}]	Half-life [min]^a	Yield [%]^b
order	1	2	2	1	1	1		
50	1.80×10^{-4}	4.83×10^{-4}	1.59×10^{-1}	1.45×10^{-2}	7.75×10^{-2}	4.28	9.0	55 and 43
100	1.80×10^{-4}	3.97×10^{-4}	9.00×10^{-2}	8.94×10^{-2}	7.65×10^{-2}	4.82	9.1	60 and 39
200	1.80×10^{-4}	4.19×10^{-4}	6.11×10^{-2}	1.55×10^{-1}	9.36×10^{-2}	5.39	7.4	66 and 32
300	1.80×10^{-4}	5.81×10^{-4}	3.93×10^{-2}	7.81×10^{-1}	1.03×10^{-1}	4.95	6.7	66 and 30

^{a} Half-life of anhydride [min] (calculated by ln(2)/k_4, ^{b} Yield of anhydride and N-acylurea as a fraction of the fuel, respectively. Same as below.

Supporting Table S3. Rate constants used in the kinetic model for 100 mM propionic acid with 50 mM EDC with 10 mM additives in MES buffer (200 mM) at pH 6, 21 ºC.

	k_0 [min^{-1}]	k_1 [mM^{-1}min^{-1}]	k_2 [mM^{-1}min^{-1}]	k_3 [min^{-1}]	k_4 [min^{-1}]	k_5 [min^{-1}]	Half-life [min]^a	Yield [%]^b
order	1	2	2	1	1	1		
No additives	1.80×10^{-4}	3.97×10^{-4}	9.00×10^{-2}	8.94×10^{-2}	7.65×10^{-2}	4.82	9.1	60 and 39
pyridine	1.80×10^{-4}	7.56×10^{-4}	2.94×10^{-1}	1.58	9.13×10^{-1}	9.54×10^{-1}	0.8	93 and 3
DMAP	1.80×10^{-4}	4.16×10^{-4}	8.21×10^{-2}	1.60×10^{-1}	2.52×10^{-1}	4.66	2.8	57 and 38
triazoloe	1.80×10^{-4}	4.97×10^{-4}	9.74×10^{-2}	3.14×10^{-1}	1.52×10^{-1}	4.18	4.6	64 and 32

^{a} ^{b} see Table S2.

Supporting Table S4. Rate constants used in the kinetic model for 100 mM propionic acid with 50 mM EDC with x mM pyridine in MES buffer (200 mM at pH 6, 21 ºC).

	k_0 [min^{-1}]	k_1 [mM^{-1}min^{-1}]	k_2 [mM^{-1}min^{-1}]	k_3 [min^{-1}]	k_4 [min^{-1}]	k_5 [min^{-1}]	Half-life [min]^a	Yield [%]^b
order	1	2	2	1	1	1		
0	1.80×10^{-4}	3.97×10^{-4}	9.00×10^{-2}	8.94×10^{-2}	7.65×10^{-2}	4.82	9.1	60 and 39
5	1.80×10^{-4}	6.52×10^{-4}	1.20×10^{-1}	8.48×10^{-1}	3.79×10^{-1}	1.14	1.8	84 and 9
10	1.80×10^{-4}	7.56×10^{-4}	2.94×10^{-1}	1.58	9.13×10^{-1}	9.54×10^{-1}	0.8	93 and 3
20	1.80×10^{-4}	8.10×10^{-4}	3.92×10^{-1}	1.81	1.25	9.31×10^{-1}	0.6	93 and 2
35	1.80×10^{-4}	7.94×10^{-4}	4.66×10^{-1}	1.92	1.36	9.23×10^{-1}	0.5	95 and 1

^{a} ^{b} see Table S2.

Supporting Table S5. Rate constants used in the kinetic model for 100 mM propionic acid with 50 mM EDC without pyridine in MES buffer (200 mM) at pH x, x ºC.

	k_0 [min^{-1}]	k_1 [mM^{-1}min^{-1}]	k_2 [mM^{-1}min^{-1}]	k_3 [min^{-1}]	k_4 [min^{-1}]	k_5 [min^{-1}]	Half-life [min]^a	Yield [%]^b
order	1	2	2	1	1	1		
pH 6, 5 ºC	5.43×10^{-5}	1.62×10^{-4}	9.36×10^{-2}	7.38×10^{-1}	4.37×10^{-2}	2.60	15.9	69 and 23
pH 6, 21 ºC	1.80×10^{-4}	3.97×10^{-4}	9.00×10^{-2}	8.94×10^{-2}	7.65×10^{-2}	4.82	9.1	60 and 39
pH 6, 35 ºC	1.27×10^{-3}	7.54×10^{-4}	8.51×10^{-2}	1.92×10^{-1}	1.77×10^{-1}	4.93	3.9	57 and 39
pH 5, 21 ºC	1.58×10^{-3}	3.09×10^{-3}	5.72×10^{-2}	3.63	9.26×10^{-2}	1.15	7.5	47 and 12
pH 7, 21 ºC	6.96×10^{-5}	3.48×10^{-5}	6.22×10^{-2}	3.94×10^{-1}	3.61×10^{-2}	5.75	19.2	46 and 48

^{a} ^{b} see Table S2.

6

Supporting Table S6. Rate constants used in the kinetic model for 100 mM propionic acid with 50 mM EDC with x mM pyridine in MES buffer (200 mM) at pH 5, 5 °C

	k_0 [min^{-1}]	k_1 [mM^{-1}min^{-1}]	k_2 [mM^{-1}min^{-1}]	k_3 [min^{-1}]	k_4 [min^{-1}]	k_5 [min^{-1}]	Half-life [min]^a	Yield [%]^b
order	1	2	2	1	1	1		
0	1.32×10^{-4}	9.93×10^{-4}	1.78×10^{-1}	5.01	2.87×10^{-2}	2.20	24.1	64 and 11
5	1.32×10^{-4}	1.37×10^{-4}	1.27	8.97×10^{-1}	1.61×10^{-1}	9.13×10^{-1}	4.3	96.6 and 0.96
10	1.32×10^{-4}	1.45×10^{-3}	1.76	1.08	2.54×10^{-1}	9.08×10^{-1}	2.7	98.5 and 0.6
DIC	1.31×10^{-3}	5.23×10^{-3}	4.40×10^{-2}	3.84	5.13×10^{-2}	0	13.5	42 and 0

$^{a\,b}$ see Table S2.

Supporting Table S7. Retention time of all the compounds in the quenched reaction cycle.

Precursor Retention time / min	precursor	Guanidine	N-acylurea	Benzylamide
Propionic acid (EDC as a fuel)	2.10	14.22	13.43	16.38
Propionic acid (DIC as a fuel)	2.11	22.76	N.D	16.03

Supporting Table S8. Retention time of all the compounds in the reaction cycle without quenching.

Precursor Retention time / min	precursor	N-acylurea
Ac-D-OH	1.41	N.D
Ac-E-OH	1.29	10.64
N-acetyl-L-2-aminoadipic acid	1.97	12.73, 16.36 8.82 (other side product)
N-acetyl-L-2-aminoheptanedioic acid	5.44	14.42, 15.30
Succinic acid	1.87	N.D
Glutaric acid	2.45	4.096
Adipic Acid	5.51	13.94, 15.23
Propionic acid (CMC as fuel)	2.13	12.68, 14.23

Supporting Table S9. Calibration values of the compounds.

Compound	0.5 uL Calibration value / (a.u.) (mM)$^{-1}$)
Propionic acid	0.0294 at 220 nm
Proponic acid-N-acylurea (EDC as a fuel)	3.1892 at 220 nm 0.0415 at 254 nm
Benzylamine	0.2099 at 254 nm
Ac-D-OH	0.304 at 220 nm
Ac-E-OH	0.3488 at 220 nm
N-acetyl-L-2-aminoadipic acid	0.3633 at 220 nm
N-acetyl-L-2-aminoheptanedioic acid	0.3836 at 220 nm
Succinic acid	0.050 at 220 nm
Glutaric acid	0.065 at 220 nm
Adipic Acid	0.0766 at 220 nm

7

SUPPORTING FIGURES
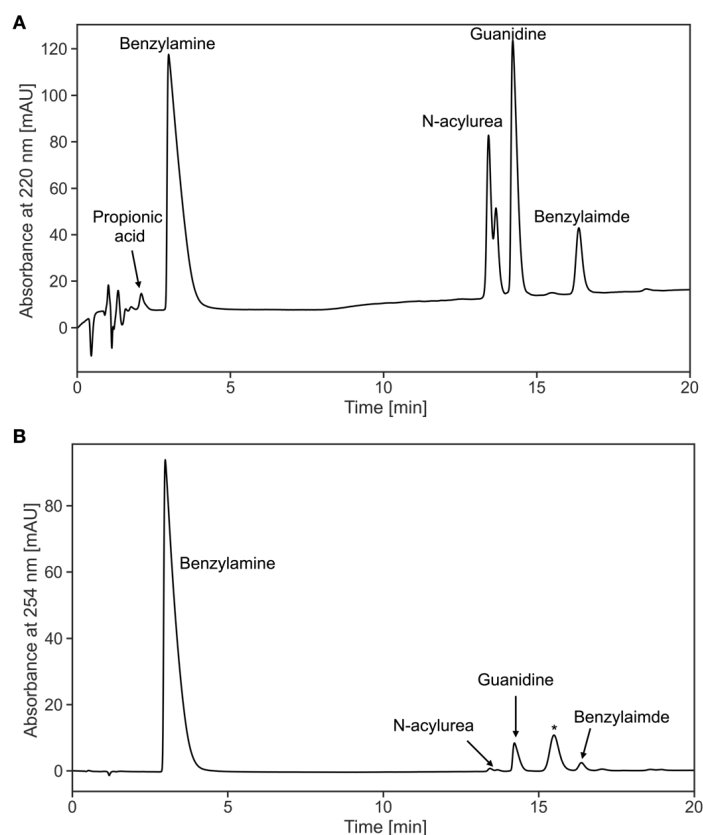
Figure S1. **Examples of HPLC chromatogram of the entire reaction network with benzylamine quenching measured at (A)** 220 nm and **(B)** 254 nm, 20 min after 50 mM EDC added to 100 mM propionic acid in MES buffer (200 mM, pH 6, 21 ℃), injection volume: 0.5 µL. Compounds involved in the reaction network are propionic acid, benzylamine, N-acylurea, guanidine, and benzylamide. * Stands for the impurity from benzylamine solution.

We integrated peaks of guanidine, N-acylurea, and benzylamide to calculate the concentration of fuel, N-acylurea, and intermolecular anhydride to get the kinetics profile of the reaction cycle.

For the rest reaction cycles conducted under different conditions, we summarized their information on HPLC chromatograms in tables S7 and S8 (see above). The corresponding HPLC methods can be found in "**Materials and methods**".

8
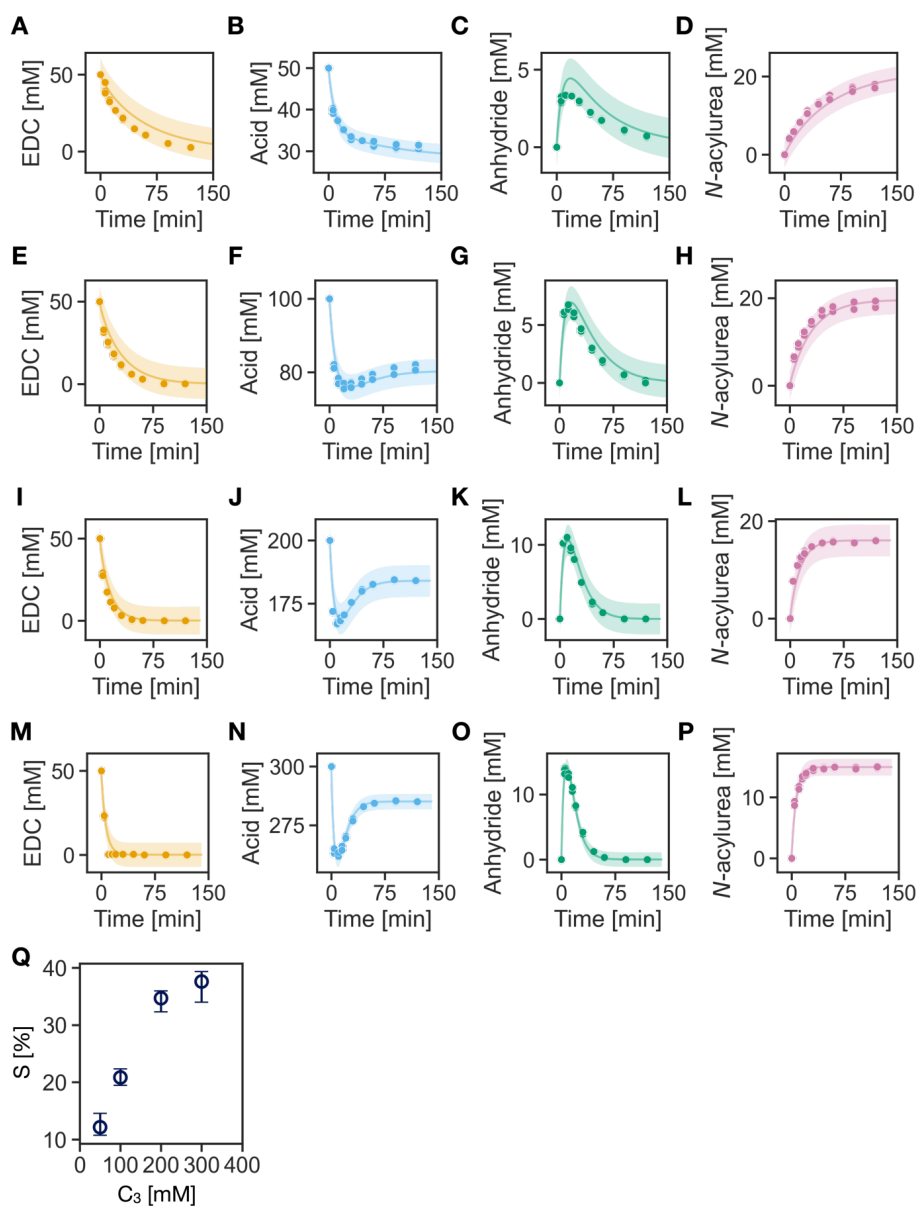
Figure S2. Kinetic profiles of reaction cycles fueled with 50 mM EDC in MES buffer (200 mM, pH 6 at 21ºC) of (A-D) 50 mM propionic acid, **(E-H)** 100 mM propionic acid, **(I-L)** 200 mM propionic acid, **(M-P)** 300 mM propionic acid. Markers represent HPLC data and lines represent data from the kinetic model defined as 95 % confidence interval. The areas stand for the error area of our kinetic fitting. **(R)** Selectivity of the reaction cycle calculated by the kinetic model when different precursor concentration was used. All experiments were conducted in triplicates.

9
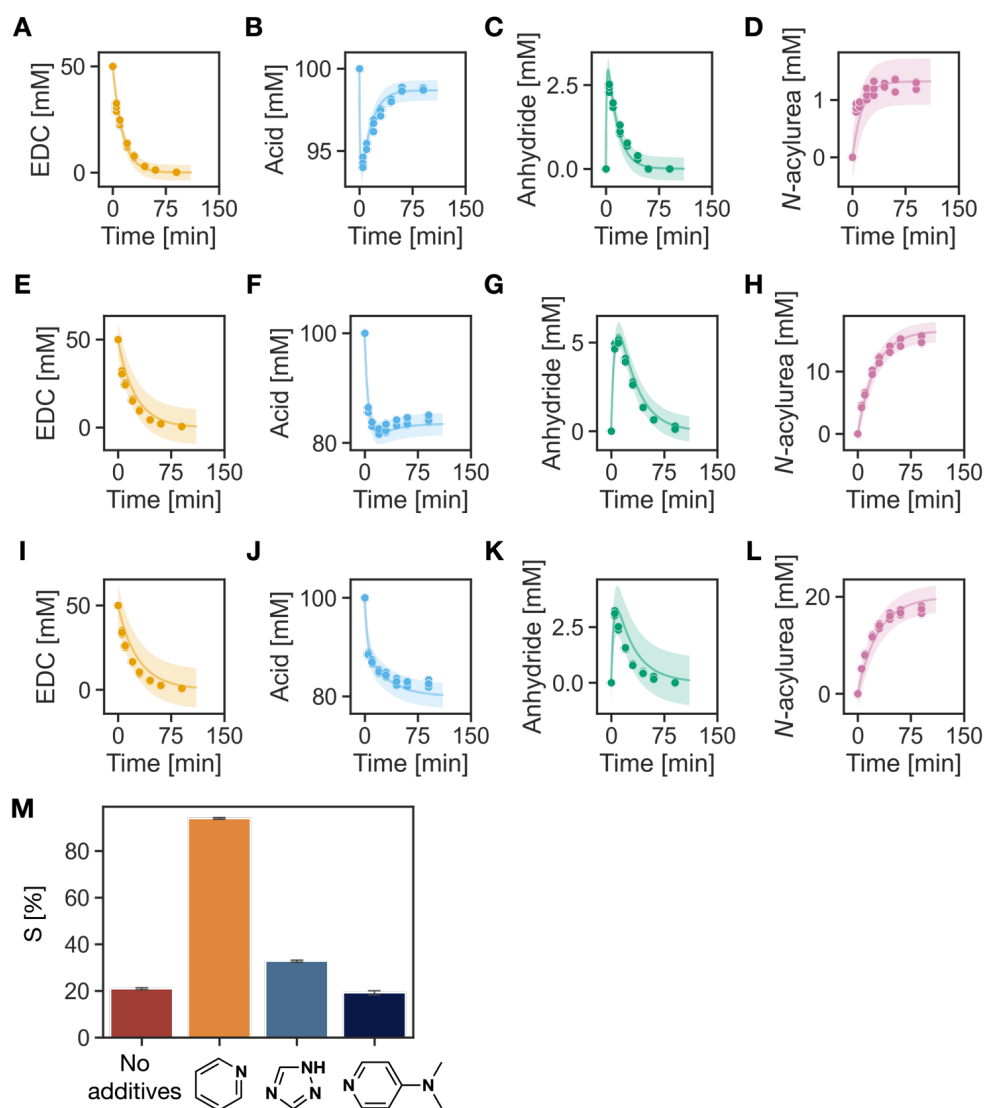
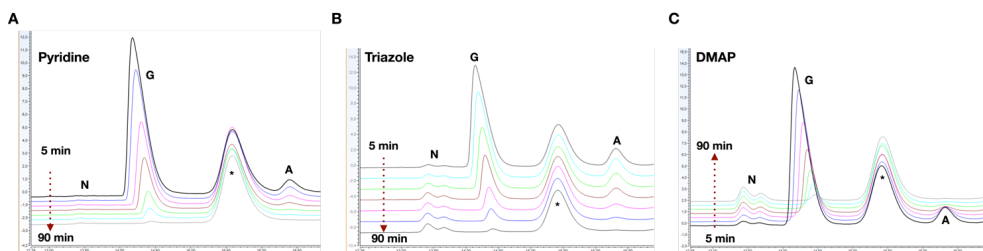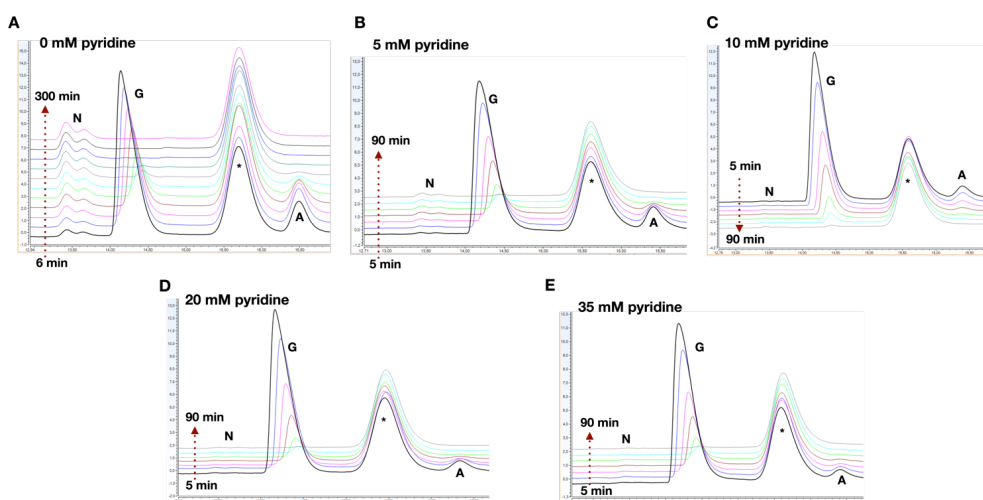**Figure S3. Kinetic profiles of reaction cycles of 100 mM propionic acid fueled with 50 mM EDC in MES buffer (200 mM, pH 6 at 21ºC) with (A-D)** 10 mM pyridine, **(E-H)** 10 mM triazole, **(I-L)** 10 mM DMAP. Markers represent HPLC data and lines represent data from the kinetic model defined as 95 % confidence interval. The areas stand for the error area of our kinetic fitting. **(M)** Selectivity of the reaction cycle calculated by the kinetic model when different additives were used. All experiments were conducted in triplicates.

10
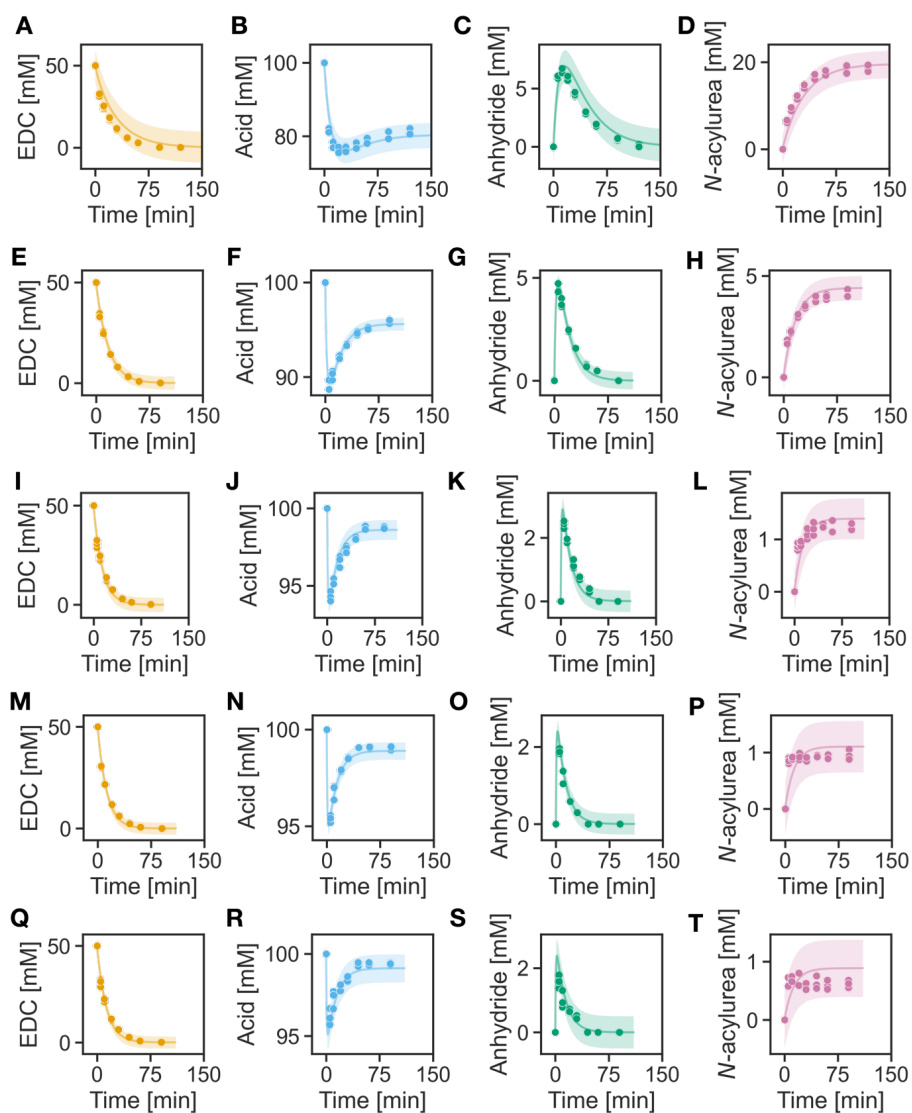
Figure S4. Kinetic profiles of reaction cycles of **100 mM propionic acid fueled with 50 mM EDC in MES buffer (200 mM, pH 6 at 21°C) with (A-D)** 0 mM pyridine, **(E-H)** 5 mM pyridine, **(I-L)** 10 mM pyridine, **(M-P)** 20 mM pyridine, **(Q-T)** 35 mM pyridine. Markers represent HPLC data and lines represent data from the kinetic model. The areas stand for the error area of our kinetic fitting defined as 95 % confidence interval. All experiments were conducted in triplicates.

11
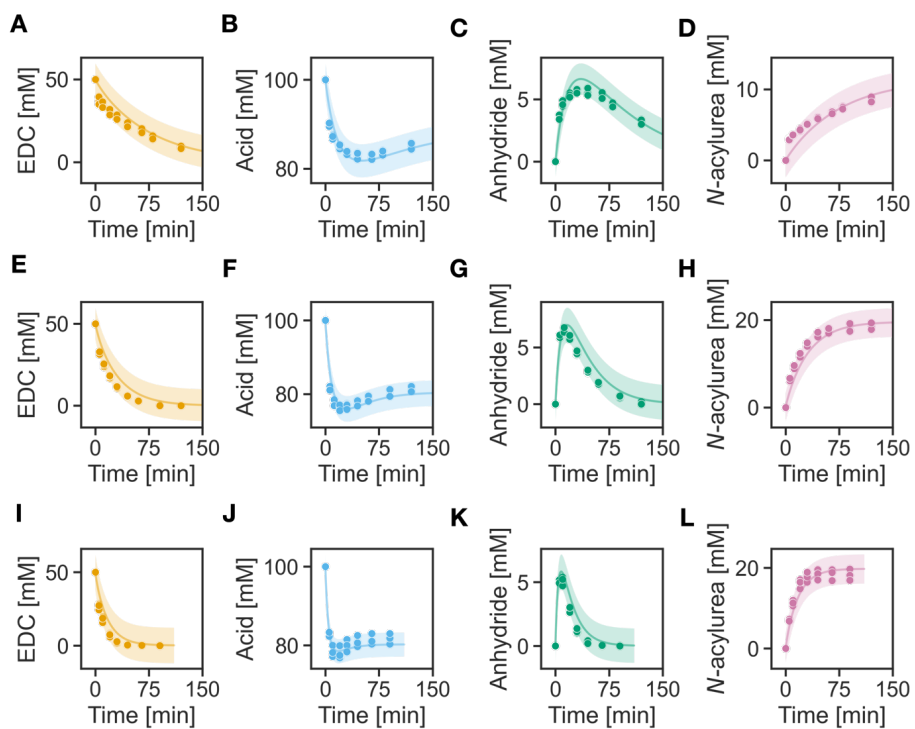
Figure S5. **Kinetic profiles of reaction cycles of 100 mM propionic acid fueled with 50 mM EDC in MES buffer (200 mM, pH 6) at (A-D)** 5 °C, **(E-H)** 21 °C, **(I-L)** 35 °C. Markers represent HPLC data and lines represent data from the kinetic model. The areas stand for the error area of our kinetic fitting defined as 95 % confidence interval. All experiments were conducted in triplicates.
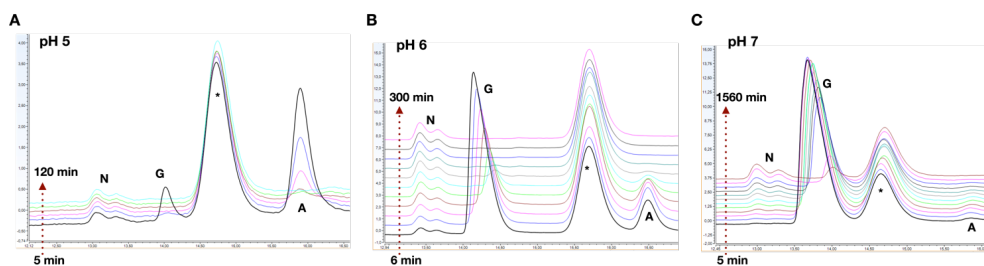
12
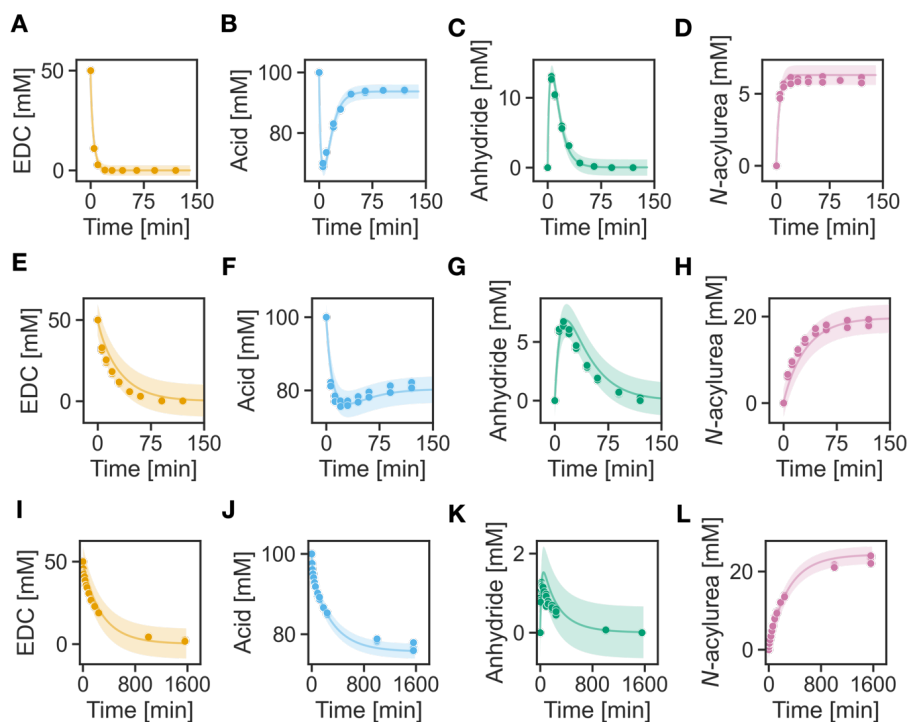
Figure S6. **Kinetic profiles of reaction cycles of 100 mM propionic acid fueled with 50 mM EDC in MES buffer (200 mM, at 21 °C) at pH (A-D)** 5, **(E-H)** 6, **(I-L)** 7. Markers represent HPLC data and lines represent data from the kinetic model. The areas stand for the error area of our kinetic fitting defined as 95 % confidence interval. All experiments were conducted in triplicates.
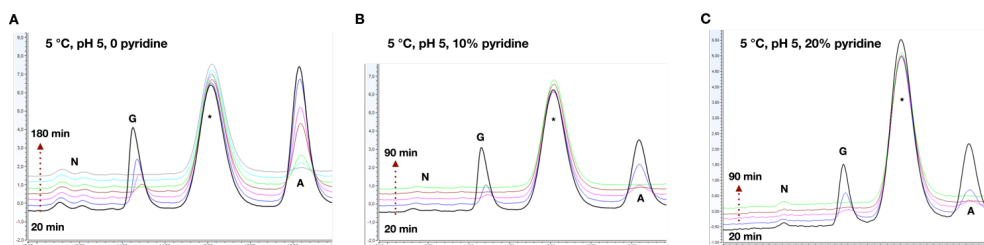
13
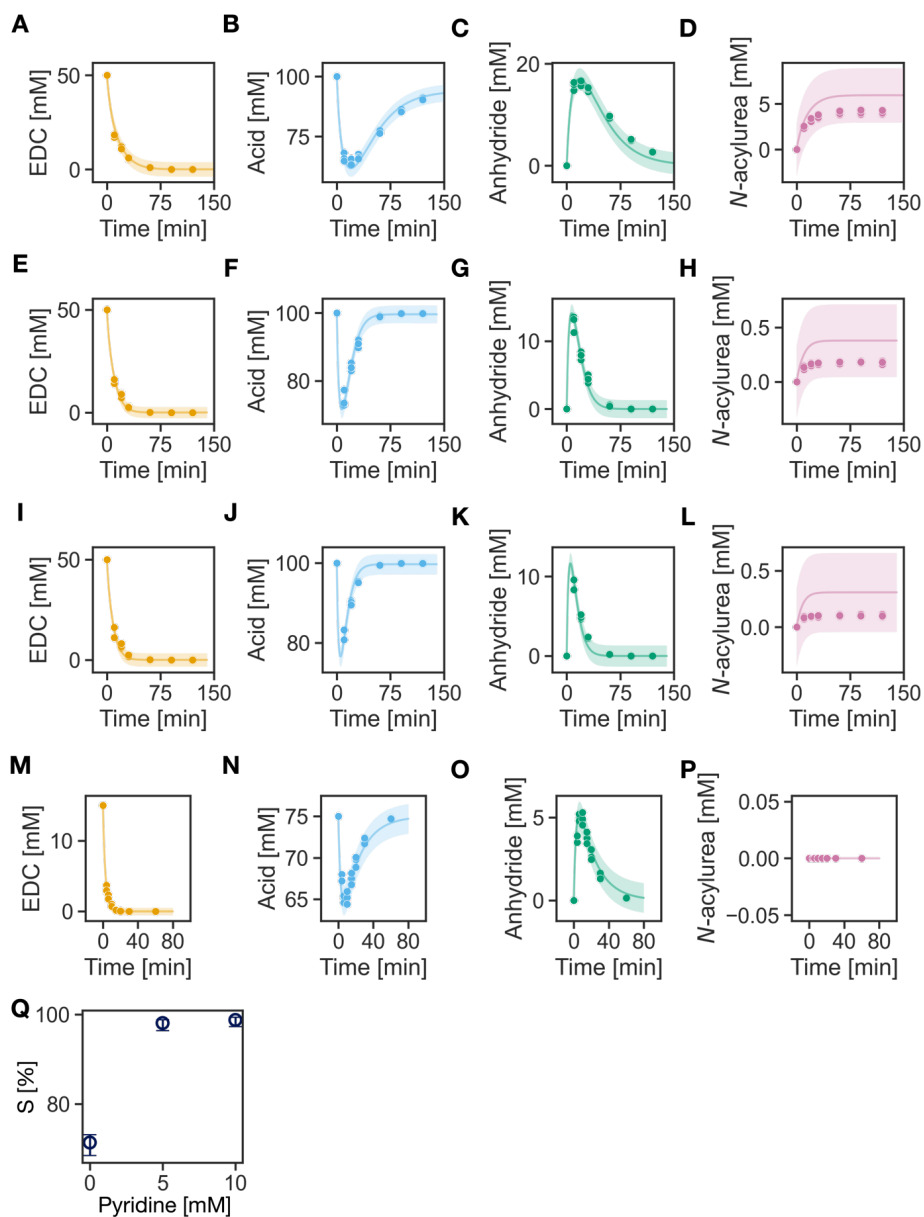
Figure S7. **Kinetic profiles of reaction cycles of 100 mM propionic acid fueled with 50 mM EDC in MES buffer (200 mM, pH 5 at 5 °C) with (A-D)** 0 mM pyridine, **(E-H)** 5 mM pyridine, **(I-L)** 10 mM pyridine. **(Q)** Selectivity of the reaction cycle under the above conditions calculated by the kinetic model. **(M-P) Kinetic profiles of 75 mM propionic acid with 1.5 mM pyridine fueled with 15 mM DIC in MES buffer (200 mM, pH 5 at 5 °C)**. Markers represent HPLC data and lines represent data from the kinetic model. The areas stand for the error area of our kinetic fitting defined as 95 % confidence interval. All experiments were conducted in triplicates.

14
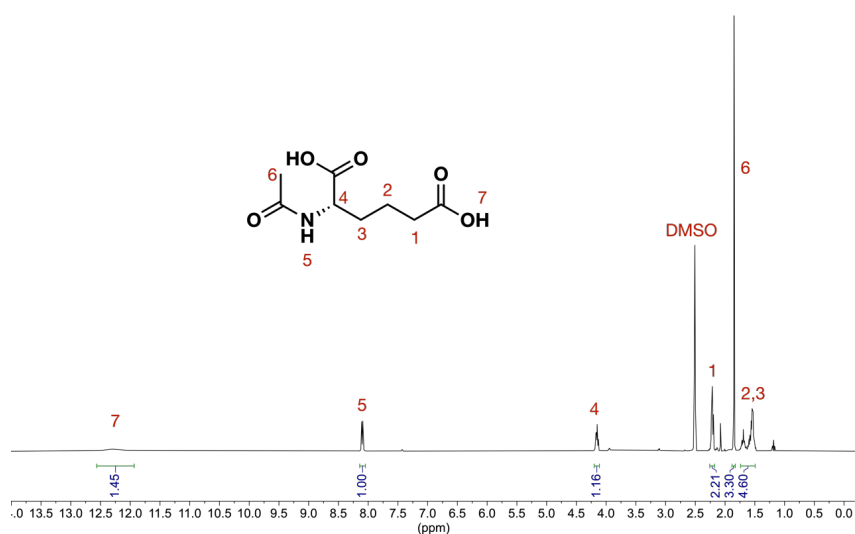
Figure S8. ¹H NMR spectrum (400 MHz, DMSO) of N-acetyl-L-2-aminoadipic acid. δ 12.29 (s, 1H), 8.10 (d, J = 7.8 Hz, 1H), 4.16 (td, J = 8.1, 5.0 Hz, 1H), 2.26 − 2.18 (m, 2H), 1.85 (s, 3H), 1.74 − 1.49 (m, 4H). Peak at δ 2.08 is the solvent ACN.
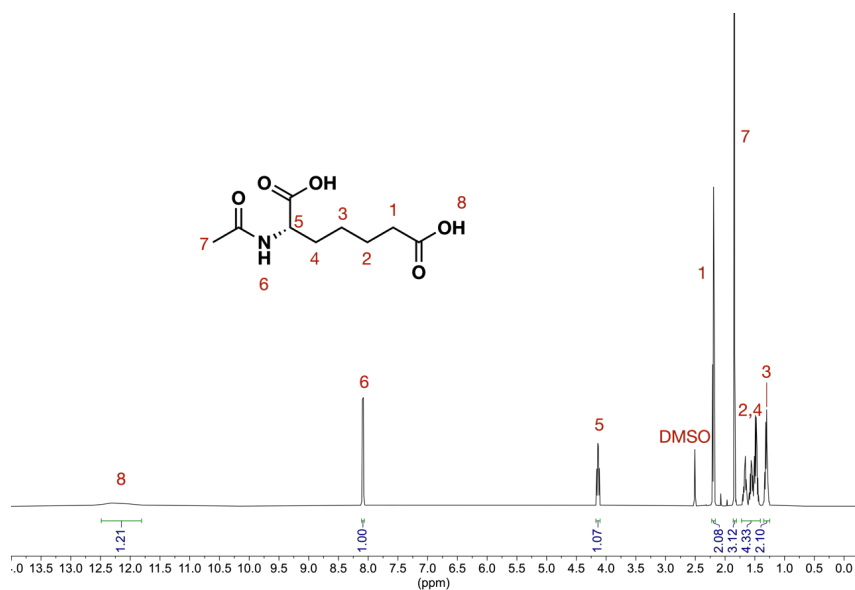
Figure S9. ¹H NMR spectrum (500 MHz, DMSO) of N-acetyl-L-2-aminoheptanedioic acid. δ 12.21 (s, 1H), 8.09 (d, J = 7.8 Hz, 1H), 4.14 (ddd, J = 8.9, 7.7, 4.9 Hz, 1H), 2.19 (t, J = 7.4 Hz, 2H), 1.84 (s, 3H), 1.72 − 1.41 (m, 4H), 1.35 − 1.25 (m, 2H).

15
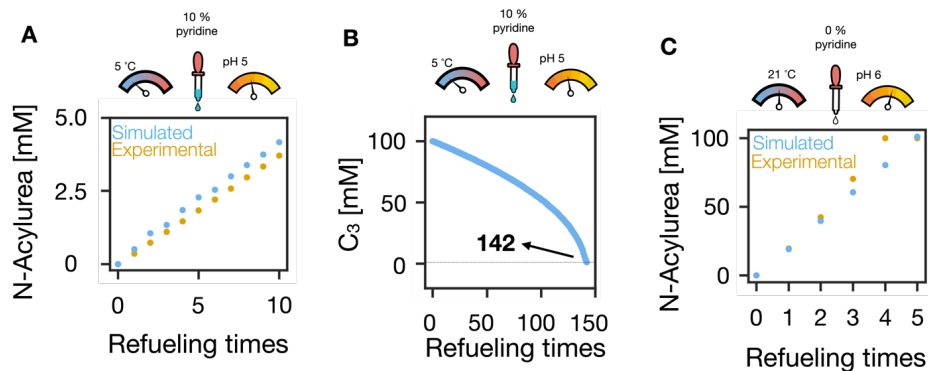
Figure S10: Refueling experiments of 100 mM propionic acid (C_3) fueled with 50 mM EDC in MES buffer under (A) our optimal condition (pH 5, 5°C, 10 % pyridine)**, (B)** the refueling times before the catalyst (C_3) concentration falls below 1 % simulated by our kinetic model and **(C)** the standard condition (pH 6, 21°C, 0 pyridine)**.**
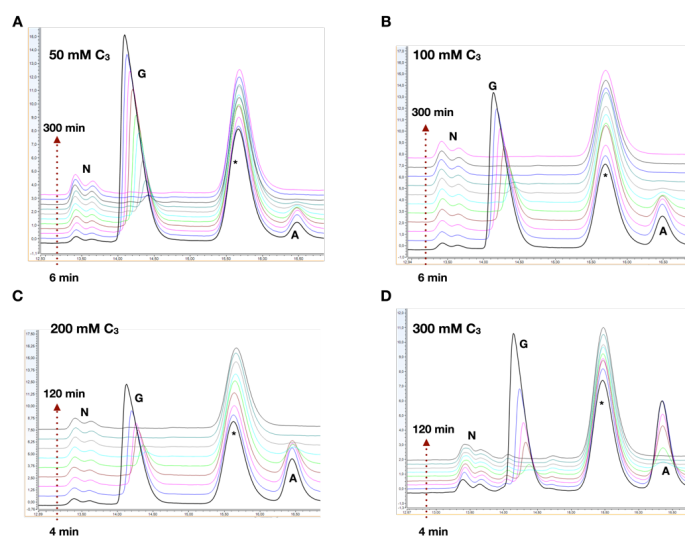
Figure S11: Representative HPLC chromatograms of reaction cycles fueled with 50 mM EDC in MES buffer (200 mM, pH 6 at 21°C) of (A) 50 mM propionic acid (C_3), **(B)** 100 mM C_3, **(C)** 200 mM C_3, **(D)** 300 mM C_3 over time at 254 nm (injection volume: 0.5 µL). Peaks from left to right are N-acylurea (N), guanidine (G), impurity from benzylamine (*) and benzylamide (A), respectively. Time traces from bottom to top are 6, 12, 20, 30, 45, 60, 90, 120, 180, 240, 300 min for 50 and 100 mM C_3. Time traces from bottom to top are 4, 10, 15, 20, 30, 45, 60, 90, 120 min for 200 and 300 mM C_3.

16

Figure S12: Representative HPLC chromatograms of reaction cycles of 100 mM propionic acid fueled with 50 mM EDC in MES buffer (200 mM, pH 6 at 21°C) with (A) 10 mM pyridine, **(B)** 10 mM triazole, **(C)** 10 mM DMAP over time at 254 nm (injection volume: 0.5 μL). Peaks from left to right are N-acylurea (N), guanidine (G), impurity from benzylamine (*) and benzylamide (A), respectively. Time traces from top to bottom are 5, 15, 20, 30, 45, 60, 90 min for pyridine. Time traces from top to bottom are 5, 10, 20, 30, 45, 60, 90 min for triazole. Time traces from bottom to top are 5, 10, 20, 30, 45, 60, 90 min for DMAP.

Figure S13: Representative HPLC chromatograms of reaction cycles of 100 mM propionic acid fueled with 50 mM EDC in MES buffer (200 mM, pH 6 at 21ºC) with (A) 0 mM pyridine, **(B)** 5 mM pyridine, **(C)** 10 mM pyridine, **(D)** 20 mM pyridine, **(E)** 35 mM pyridine over time at 254 nm (injection volume: 0.5 μL). Peaks from left to right are N-acylurea (N), guanidine (G), impurity from benzylamine (*) and benzylamide (A), respectively. Time traces from bottom to top are 6, 12, 20, 30, 45, 60, 90, 120, 180, 240, 300 min for 0 mM pyridine. Time traces from bottom to top are 5, 10, 20, 30, 45, 60, 90 min for 5 mM, 20mM and 35 mM pyridine. Time traces from top to bottom are 5, 15, 20, 30, 45, 60, 90 min for 10 mM pyridine.
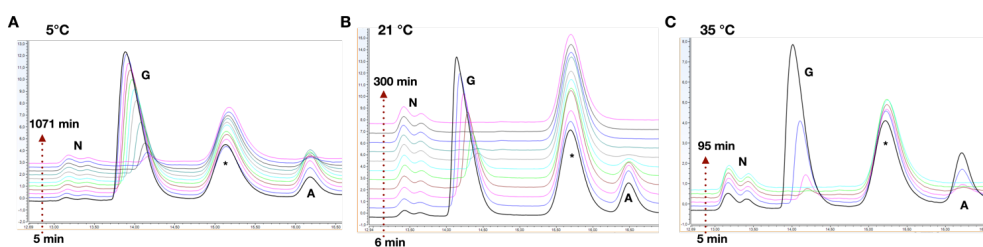
Figure S14: Representative HPLC chromatograms of reaction cycles of 100 mM propionic acid fueled with 50 mM EDC in MES buffer (200 mM, pH 6) at (A) 5 ºC, **(B)** 21 ºC, **(C)** 35 ºC over time at 254 nm (injection volume: 0.5 μL). Peaks from left to right are N-acylurea (N), guanidine (G), impurity from benzylamine (*) and benzylamide (A), respectively. Time traces from bottom to top are 6, 12, 20, 30, 45, 60, 90, 120, 180, 240, 300 min for 21 °C. Time traces from bottom to top are 5, 10, 20, 30, 45, 65, 90, 120,180, 240, 300, 1071 min for 5 °C. Time traces from bottom to top are 5, 10, 20, 30, 45, 65, 95 min for 35 °C.

17

Figure S15: Representative HPLC chromatograms of reaction cycles of 100 mM propionic acid fueled with 50 mM EDC in MES buffer (200 mM, at 21 °C) at pH (A) 5, **(B)** 6, **(C)** 7 over time at 254 nm (injection volume: 0.5 µL). Peaks from left to right are N-acylurea (N), guanidine (G), impurity from benzylamine (*) and benzylamide (A), respectively. Time traces from bottom to top are 6, 12, 20, 30, 45, 60, 90, 120, 180, 240, 300 min for pH 6. Time traces from bottom to top are 5, 10, 20, 30, 45, 65, 90, 120 min for pH 5. Time traces from bottom to top are 5, 10, 20, 30, 45, 60, 90, 120, 180, 240, 1003, 1560 min for pH 7.

Figure S16: Representative HPLC chromatograms of reaction cycles of 100 mM propionic acid fueled with 50 mM EDC in MES buffer (200 mM, pH 5 at 5 °C) with (A) 0 mM pyridine, **(B)** 5 mM (10%) pyridine, **(C)** 10 mM (20%) pyridine over time at 254 nm (injection volume: 0.5 µL). Peaks from left to right are N-acylurea (N), guanidine (G), impurity from benzylamine (*) and benzylamide (A), respectively. Time traces from bottom to top are 20, 30, 45, 60, 90, 120, 180 min for 0 mM pyridine. Time traces from bottom to top are 20, 30, 45, 60, 90 min for 5 and 10 mM pyridine.
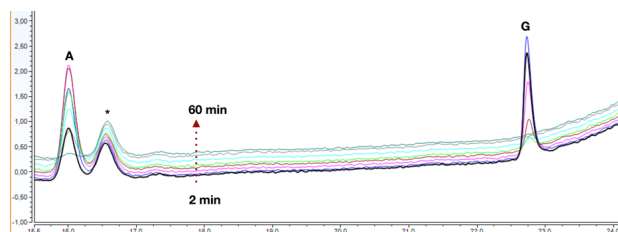
Figure S17: Representative HPLC chromatograms of reaction cycles of 75 mM propionic acid in MES buffer with 1.5 mM pyridine fueled with 15 mM DIC in MES buffer (200 mM, pH 5 at 5°C). Peaks from left to right are benzylamide (A), impurity from benzylamine (*) and guanidine (G), respectively. No N-acylurea was formed. Time traces from bottom to top are 2, 4, 6, 10, 15, 20, 30, 60 min.
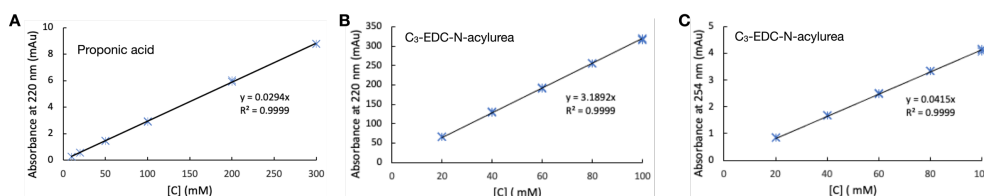
Figure S18: Calibration curves of 0.5 µL injection volume (A) propionic acid (220 nm), **(B)** N-acylurea of propionic acid when EDC is the fuel at 220 nm and **(C)** at 254 nm. Error bar: n = 3.

18
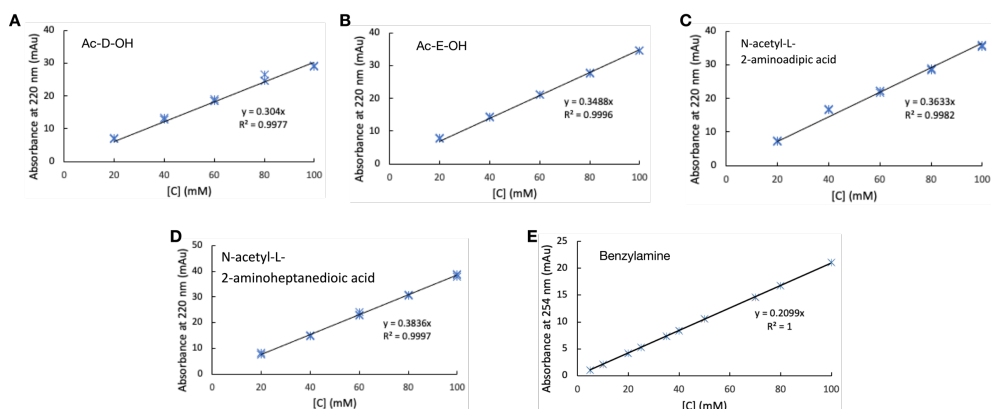
Figure S19: Calibration curves of 0.5 µL injection volume (A) Ac-D-OH (220 nm), **(B)** Ac-E-OH (220 nm), **(C)** N-acetyl-L-2-aminoadipic acid (220 nm), **(D)** N-acetyl-L-2-aminoheptanedioic acid (220 nm), **(E)** benzylamine (254 nm). Error bar: n = 3.
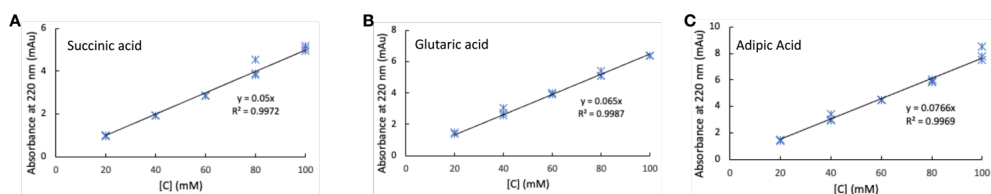
Figure S20: Calibration curves of 0.5 µL injection volume (A) Succinic acid (220 nm), **(B)** Glutaric acid (220 nm), **(C)** Adipic Acid (220 nm). Error bar: n = 3.

REFERENCE

1. A. V. Reddy and B. Ravindranath, Acetylation Under Ultrasonic Conditions: Convenient Preparation of N-Acetylamino Acids, *Synthetic Communications*, 2006, **22**, 257-264.
2. F. Schnitter and J. Boekhoven, A Method to Quench Carbodiimide-Fueled Self-Assembly, *ChemSystemsChem*, 2020, **3**, e2000037.
3. L. S. Kariyawasam and C. S. Hartley, Dissipative Assembly of Aqueous Carboxylic Acid Anhydrides Fueled by Carbodiimides, *J. Am. Chem. Soc.*, 2017, **139**, 11949-11955.
4. L. S. Kariyawasam, J. C. Kron, R. Jiang, A. J. Sommer and C. S. Hartley, Structure-Property Effects in the Generation of Transient Aqueous Benzoic Acid Anhydrides by Carbodiimide Fuels, *J. Org. Chem.*, 2020, **85**, 682-690.

19

7. A Carbodiimide-Fueled Reaction Cycle that Forms Transient 5(*4H*)-Oxazolones

In this chapter, I aimed to develop a carbodiimide-fueled reaction cycle that produced longer-lived activated molecules such that I could catalyze the hydrolysis, and thus tune, their half-life. Unlike other varieties of the carbodiimide-fueled reaction cycle, the proposed cycle forms a transient 5(*4H*)-oxazolone via an intramolecular cyclization, which occurs when precursors bear one carboxylic group and an amide group at the alpha position. This reaction cycle is robust to operate under a wide range of fuel inputs, pH, and temperatures. It is effective in utilizing the fuel to mainly form the transient product oxazolone and versatile to the scope of the precursor, ranging from acetylamino acids to peptides. It can also drive different chemically fueled matter according to the molecular design of precursors, including droplets, fibers, and crystals. Most importantly, the product 5(*4H*)-oxazolone has a longer half-life than the intramolecular anhydride, making it possible to catalyze the hydrolysis of the oxazolone and thus decreasing its half-life without changing the pH or temperature.

Article

A Carbodiimide-Fueled Reaction Cycle That Forms Transient 5(4H)-Oxazolones

Xiaoyao Chen, Michele Stasi, Jennifer Rodon-Fores, Paula F. Großmann, Alexander M. Bergmann, Kun Dai, Marta Tena-Solsona, Bernhard Rieger, and Job Boekhoven*

Read Online

ACCESS | Metrics & More | Article Recommendations | Supporting Information

ABSTRACT: In life, molecular architectures, like the cytoskeletal proteins or the nucleolus, catalyze the conversion of chemical fuels to perform their functions. For example, tubulin catalyzes the hydrolysis of GTP to form a dynamic cytoskeletal network. In contrast, myosin uses the energy obtained by catalyzing the hydrolysis of ATP to exert forces. Artificial examples of such beautiful architectures are scarce partly because synthetic chemically fueled reaction cycles are relatively rare. Here, we introduce a new chemical reaction cycle driven by the hydration of a carbodiimide. Unlike other carbodiimide-fueled reaction cycles, the proposed cycle forms a transient 5(4H)-oxazolone. The reaction cycle is efficient in forming the transient product and is robust to operate under a wide range of fuel inputs, pH, and temperatures. The versatility of the precursors is vast, and we demonstrate several molecular designs that yield chemically fueled droplets, fibers, and crystals. We anticipate that the reaction cycle can offer a range of other assemblies and, due to its versatility, can also be incorporated into molecular motors and machines.
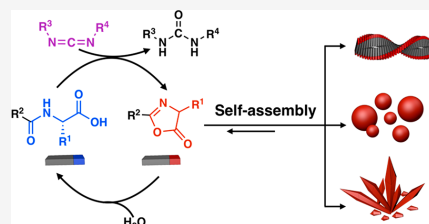
INTRODUCTION

In molecular self-assembly, molecules form supramolecular architectures held together through noncovalent interactions.[1−3] In recent years, such assemblies have led to various materials used in healthcare,[4,5] optoelectronics,[6,7] and catalysis,[8,9] among others.[10] Most of these supramolecular materials exist in or close to equilibrium, contrasting biological assemblies sustained out of equilibrium by the constant transduction of energy harvested from chemical fuels through chemical reaction cycles. For example, the hydrolysis of ATP is catalyzed by actin, and the energy gained from this catalytic reaction cycle is used in the dynamic self-assembly of actin filaments.[11] Similarly, the energy released upon hydrolyzing GTP is used to fuel the dynamic assembly of tubulin into microtubules.[12]

In such chemically fueled self-assembly, a catalytic reaction cycle is responsible for extracting the chemical fuel's energy by converting it into waste (Scheme 1A). A precursor molecule reacts with the chemical fuel, yielding the activated product and a waste molecule, i.e., the activation. In the deactivation, this activated product reverts to the precursor. Thus, the precursor catalytically converts fuel into waste while temporarily becoming activated. If the precursor is well-soluble but the product assembles, the energy harvested from the chemical fuel creates transient building blocks for self-assembly. The dynamic nature of the activation and deactivation process endows chemically fueled assemblies with inherently different material properties compared to

their in-equilibrium counterparts, which include spatiotemporal control over the assemblies and their ability to self-heal.[13,14] Moreover, pattern formation and oscillatory behavior can be expected when feedback mechanisms are incorporated.[15] Besides their unique material properties, synthetic counterparts of these materials serve as a model system for biological assemblies. Alternatively, the chemical fuel can be used to operate a molecular machine or motor.[16,17] The chemical energy of the fuel to waste conversion is in such designs used for directional rotation.

Thus, several chemically fueled reaction cycles have been designed to regulate molecules. The energy transduced by these cycles can come from the oxidation of reducing agents,[18−21] hydrolysis of methylating agents,[22] hydration of carbodiimides,[23−29] and hydrolysis of ATP.[21,30] These cycles lead to a range of assemblies, including fibers,[31−33] droplets,[14,34] vesicles,[35] micelles,[18,36] colloids,[19,23] and particle clusters.[13,37] A well-studied cycle produces energy by hydrating carbodiimides.[23,38] In these cycles, carboxylates react with EDC (1-ethyl-3-(3-(dimethylamino)propyl)carbodiimide) to form an O-acylurea intermediate. A second carboxylate attacks

Scheme 1. Chemical Reaction Cycle That Regulates Molecular Assembly[a]
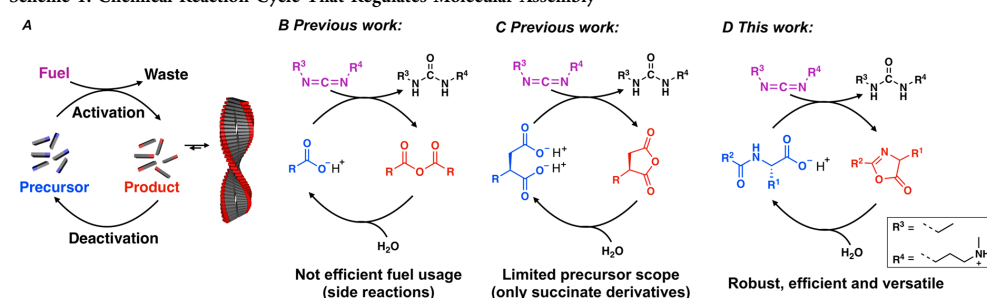
[a](A) Schematic representation of a chemically fueled reaction cycle coupled to self-assembly. Activation and deactivation regulate the self-assembly behavior of a building block. (B) The hydration of a carbodiimide fuel drives a chemically fueled reaction cycle to form an anhydride from two carboxylates or (C) an intramolecular anhydride or (D) an oxazolone from a peptide.

this intermediate to form the anhydride product. Hydrolysis reverts the precursor, which constitutes the deactivation reaction (Scheme 1B and C).

Despite its success in fueling molecular assemblies, a significant downside of this reaction cycle is two unwanted side reactions. First, the *O*-acylurea can rearrange to an unwanted *N*-acylurea. This reaction is irreversible and scales inversely with the concentration of carboxylates. Second, the reactive *O*-acylurea can hydrolyze. This reaction results in the consumption of fuel without the formation of the wanted anhydride product. Both side reactions can be circumvented by precursors that carry a second carboxylate on the gamma position, thus forming an intramolecular anhydride (Scheme 1C).[23] However, these 1,3-dicarboxylate-based precursors drastically limit the scope of the reaction cycle to, for example, C-terminal aspartic acids and succinic acid derivatives.

Therefore, in this work, we developed a new reaction cycle based on the consumption of carbodiimides that yield a transient 5(*4H*)-oxazolone product (Scheme 1D). For brevity, oxazolones refer to 5(*4H*)-oxazolones in the following text. The reaction cycle is less prone to forming the unwanted *N*-acylurea due to a nearby nucleophile. Moreover, almost all carbodiimides activate the precursor into the transient product. Furthermore, the substrate scope of the reaction cycle is diverse, which we demonstrate by coupling it to several precursors, including peptides that assemble.

■ **RESULTS AND DISCUSSION**

We used *N*-acetyl-L-phenylalanine (Ac-F-OH) as a model precursor (Figure 1A) to study the oxazolone-forming reaction cycle by high-performance liquid chromatography (HPLC). We compared the kinetics of the reaction cycle of *N*-acetyl-L-phenylalanine to phenylpropanoic acid because of its similar structure but lacking amide at the α position, which is required for oxazolone formation. Thus, we can compare the intermolecular anhydride-forming cycle (Scheme 1B) to the oxazolone-forming cycle (Scheme 1D). When 100 mM precursor reacted with 45 mM EDC in MES buffer (200 mM, pH 6.0), a transient peak was observed on the 254 nm channel of the analytical HPLC for both reaction cycles. For the cycle with phenylpropanoic acid, the transient peak was attributed to the intermolecular anhydride, which was confirmed by mass spectrometry and FT-IR-spectroscopy (Table S1 and Figures S2B, S3B).
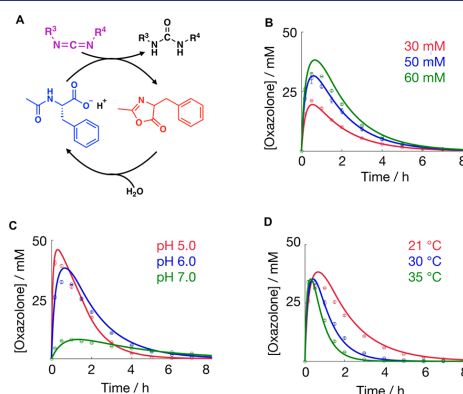

Figure 1. The robustness of the oxazolone reaction cycle with Ac-F-OH as a precursor. (A) Molecular structures of the species in the chemical reaction cycle. HPLC (markers) and kinetic model data (lines) as a function of time when fueled with EDC. All conditions are 100 mM precursor in 200 mM MES buffer. (B) With varying fuel concentrations at pH 6.0 at 21 °C, (C) at different pH values with 60 mM EDC at 21 °C, (D) at different temperatures with 60 mM EDC and pH 6.0. The error bars on the HPLC data represent the standard deviation of the mean value with *n* = 3.

In contrast, a transient peak emerged that corresponded to the oxazolone[39] for the Ac-F-OH as a precursor (Figure S2A). The oxazolone was confirmed by synthesizing it in an organic solvent[40] and characterizing it by HPLC, NMR, FT-IR, and mass spectrometry (Supporting Note 1). To follow the kinetics of the reactions, we used a quenching method,[41] developed by our group, to measure the evolution of the concentration of the product, EDC, and the precursor as a function of time (Figure S1 and Figure S6). We used a kinetic model that predicts the concentrations of all species involved in the chemical reaction cycle every minute by solving a set of ordinary differential equations (Tables S5, S7, Supporting Note 2). The rate constants could be fit to accurately predict the reaction cycle's evolution, and we could calculate the efficiency of the cycle, i.e., how much fuel is used to form the transient product of interest, i.e., the anhydride or oxazolone (Supporting Note 2).

In the oxazolone-forming cycle, $91 \pm 1\%$ fuel was used to form the main product, while the value was $73 \pm 1\%$ in the intermolecular anhydride-forming cycle. Besides the product's formation, the unwanted side product *N*-acylurea was formed in both cycles. Excitingly, only $2 \pm 1\%$ of the fuel is converted to the *N*-acylurea in the oxazolone-forming cycle, which starkly contrasts with the $26 \pm 1\%$ in the intermolecular anhydride-forming cycle (Figure S6A,B). Thus, the oxazolone formation avoids the formation of the unwanted side product *N*-acylurea to a large degree.

Next, we compared the kinetics of the oxazolone-forming reaction cycle to the intramolecular anhydride-forming cycle (Scheme 1C, Figure S6C,D). We used 100 mM Ac-D-OH as a precursor at pH 6.0 fueled with 30 mM EDC, and we measured the concentration of anhydride over time by using the same quenching method. In this reaction cycle, we found no *N*-acylurea and we used the kinetic model to calculate the efficiency of the cycle to be $99 \pm 1\%$. Excitingly, the half-life of the transient intramolecular anhydride is 50 s, which is 85 times shorter than the oxazolone. In other words, we now have two reaction cycles that form transient products efficiently and have vastly different half-lives (Tables S6, S7).

A challenge in developing a reaction cycle is its robustness toward fuel concentration, pH, and temperature, which we tested for the oxazolone-forming cycle next. We measured the effect of the concentration of fuel added while the pH was fixed at 6.0 and the temperature at 21 °C. We fueled 100 mM Ac-F-OH in 200 mM MES with 30, 50, or 60 mM EDC (Figure 1B and Figure S7A). The oxazolone concentration increased at the expense of EDC in the first hour. It then decreased in the following 6 h, highlighting that the deactivation reaction of the cycle is relatively slow. Indeed, using the kinetic model, we established the half-life of the oxazolone to be 71 min under the applied conditions (Table S7). After the reaction cycle with 30, 50, or 60 mM EDC had been completed, there was roughly 1 mM of the *N*-acylurea (Figure S7B).

We tested the robustness of the reaction cycle toward pH (100 mM precursor with 60 mM EDC) by measuring the cycle at pH 5.0, 6.0, and 7.0 at 21 °C (Figure 1C and Figure S7C). At pH 6.0, the activation rate constant was 7.56×10^{-4} mM^{-1} min^{-1}, which increased by 3-fold when we worked at pH 5.0 due to the higher reactivity of EDC (Table S7). The increased activation rate made the overall reaction cycle much faster. In contrast, at pH 7.0, the activation reaction was only 5.95×10^{-5} mM^{-1} min^{-1}. Interestingly, the half-life of the oxazolone product stayed more or less unchanged in this pH range and ranged between 30 min at pH 7.0 and 71 min at pH 6.0. Moreover, under the conditions of pH 5.0 and 6.0, the *N*-acylurea formation is only of $1 \pm 0.5\%$ and $2 \pm 1\%$, respectively, compared to $6 \pm 1\%$ at pH 7.0 (Figure S7D). Finally, the effect of temperature was determined at pH 6.0 (100 mM precursor with 60 mM EDC) by varying it from 21, 30, and 35 °C, respectively. The reaction cycle can reach a comparable efficiency of oxazolone for different temperatures (Figure 1D and Figure S7E,F). However, the half-life of the oxazolone decreased from 71 min at 21 °C to 28 min at 35 °C.

Next, we tested the versatility of the new reaction cycle by testing a range of carboxylate-based derivatives. In these experiments, we were interested in how much of the chemical fuel is used to form the wanted product oxazolone, i.e., the efficiency of the reaction cycle. We also determined the percentage of the added EDC used to form unwanted side product *N*-acylurea. The remainder is the EDC lost due to the

direct hydration of EDC or the hydrolysis of the *O*-acylurea. The concentration of *N*-acylurea could be determined by HPLC directly. Due to the transient nature of the oxazolone, we used the kinetic model to calculate the percentage of the EDC used to form oxazolone (Supporting Note 2). The first precursors we tested were *N*-acetyl-protected amino acids (Ac-). We used 100 mM precursor with 30 mM EDC in MES buffer (200 mM, pH 6.0) at 21 °C. For Ac-F-OH, $2 \pm 1\%$ of the EDC was converted into the unwanted *N*-acylurea (Table 1), while for Ac-G-OH, Ac-A-OH, Ac-H-OH, Ac-M-OH, Ac-

Table 1. *N*-Acetylated Amino Acids as a Precursor in the Oxazolone-Forming Reaction Cycle*

Precursor[b]	Side chain	Main product: Oxazolone (%)	Side product: N-acylurea (%)
Ac-G-OH		99	< 1[d]
Ac-A-OH		99	< 1[d]
Ac-H-OH		99	< 1[d]
Ac-M-OH		99	< 1[d]
Ac-V-OH		86	< 1[d]
Ac-S-OH		85	< 1[d]
Ac-R-OH		53	< 1[d]
Ac-F-OH		91	2
Ac-L-OH		86	9
Ac-I-OH		66	33
Ac-D-OH		0[f]	< 1[d]

*Various precursors compared for their efficiency in forming oxazolone and *N*-acylurea. All yields are expressed as a fraction of the EDC added. We used our kinetic model for the oxazolone efficiency and assumed a calculation error of $\pm 1\%$. For the *N*-acylurea efficiency, we used HPLC data. All conditions are in 200 mM MES at pH 6.0, 21 °C. [a]The formation of *N*-acylurea was negligible, and we assume the values are less than 1%. [b]100 mM precursor with 30 mM EDC. [c]0.6 mM precursor with 0.6 mM EDC. [d]25 mM precursor with 12.5 mM EDC. [e]25 mM precursor with 12.5 mM EDC with 20 mM pyridine. [f]This cycle produces the corresponding intramolecular anhydride.

V-OH, Ac-S-OH, and Ac-R-OH, the formation of *N*-acylurea was too little to integrate on HPLC, and we assume the values are less than 1% (Table 1, Figure S8A–G). More than $90 \pm 1\%$ of the EDC was used to drive the activation reaction for Ac-G-OH, Ac-A-OH, Ac-H-OH, Ac-M-OH, and Ac-F-OH. In other words, the chemical fuel is used highly efficiently to form the main product. However, when Ac-R-OH was used as a precursor, only 53% of the fuel was used to form oxazolone. We hypothesize that the hydrophilic and cationic side chain enhances the hydrolysis of the *O*-acylurea intermediate (Table S8 and Supporting Notes 2). This reaction is reflected in the *K* value, which our kinetic model uses to describe the reactions of the *O*-acylurea; that is, *K* is the ratio between the hydrolysis to urea vs conversion to oxazolone. If *K* is far less than 1, oxazolone formation is more favored than the hydrolysis to

urea. Among all amino acids in Table S8, only Ac-R-OH has a K value of 0.867, close to 1, which means the hydrolysis of the O-acylurea becomes competitive. Moreover, the hydrolysis of its oxazolone was also very fast. Therefore, the formation of oxazolone for Ac-R-OH was decreased.

In contrast, for Ac-I-OH and Ac-L-OH, i.e., amino acids with bulkier side groups, much more N-acylurea was generated ($33 \pm 1\%$ and $9 \pm 1\%$, respectively, Table 1 and Figure S8H,I). We hypothesize the difference is a result of the increased steric hindrance of the bulky groups on the α position. Nevertheless, the remainder of the EDC was used to create oxazolone, pointing to an energy-efficient reaction cycle for these precursors.

When the amino acid was protected with a 9-fluorenylmethoxycarbonyl (Fmoc) or N-($tert$-butoxycarbonyl) (Boc), no oxazolone was found, and the reaction cycle converts more than $50 \pm 1\%$ of the EDC into N-acylurea (Table 2 and Figure

Table 2. Precursors in the Oxazolone-Forming Reaction Cycle[a]

Precursor	Structure	Oxazolone (%)	N-acylurea (%)
Boc-F-OH[c]		-	50
Fmoc-F-OH[c]		-	53
Ac-FG-OH[d]		72	21
Ac-F₂G-OH[d]		71	27
Ac-FG-OH[e]	See above	96	4

[a]See footnote of Table 1.

S9). It is noteworthy that carbamates have lower pK_a's than analogous amides.[42,43] Therefore, the alkoxycarbonyl protecting group decreases its nucleophilicity. Moreover, we suspect that these bulky protecting groups' steric hindrance will affect its reactivity too. When we used di- or tripeptides with a glycine at the C-terminal position, the amount of N-acylurea generated increased with increasing peptide length from Ac-G-OH (<1%) to Ac-FG-OH ($21 \pm 1\%$) and Ac-F₂G-OH (Ac-FFG-OH, $27 \pm 1\%$) (Table 2 and Figures S16A, S18A). This drawback can be overcome by using pyridine, which is known to suppress the formation of N-acylurea,[44] which we screened next. Indeed, adding 20 mM pyridine decreased the N-acylurea formation to $4 \pm 1\%$ of the EDC while keeping the reaction cycle efficient (Figure S16B). Meanwhile, pyridine speeds up the deactivation, resulting in a shorter half-life of the oxazolone (Figure S16C, Table S9).

Based on these data, we describe the requirements for designing suitable precursors in the oxazolone-forming reaction cycle (Scheme 2). It has to possess a C-terminal carboxylic acid and no nearby nucleophiles other than an amide group on the α position for intramolecular heterocyclization. Racemization of the α position by oxazolone

Scheme 2. Detailed Schematic Representation of the Oxazolone Formation and the Reaction Cycle and Proposed Guidelines for the Design of Precursors
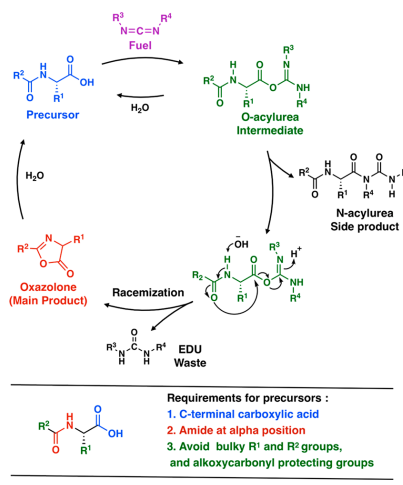
formation is unavoidable.[45,46] Therefore, an achiral amino acid (e.g., glycine) is preferred on the C terminus. Finally, bulky R^1 and R^2 groups and alkoxycarbonyl protecting groups will increase the amount of N-acylurea formed. If bulky protecting groups or larger peptides are required, pyridine can be used to maintain the high efficiency of this reaction cycle.

Next, we studied whether we could induce self-assembly with the new chemical reaction cycle. We designed a small library of peptides to form fibers based on Ac-F$_n$G-OH. We increased the product's propensity to assemble by increasing the number of phenylalanines from $n = 0$ to 3 (Figure 2A). For Ac-G-OH and Ac-F₁G-OH, no evidence of self-assembly was found (Figure 2B,C, Figure S17A,B). In contrast, when we fueled a solution of 30 mM Ac-F₂G-OH and 15 mM pyridine with 80 mM EDC at pH 5.0, 21 °C, the turbidity increased rapidly, forming a hydrogel within 30 min (Figure 2B, Figure S17A). Confocal microscopy confirmed the presence of a fibrillar network (Figure 2C), and cryo-TEM showed the nanometer details of this fiber network (Figure 2D). The hydrogel lasted just over an hour, which was confirmed by oscillatory rheology (Figure 2E). That showed a rapid increase in the sample's storage and loss modulus after applying 80 mM chemical fuel, and the storage modulus was always higher than the loss modulus, indicating that the material was in a gel state for 1.5 h.[27,32,47,48] The loss of the hydrogel coincides with oxazolone concentration vanishing (Figure S18B). Less than 1% as a fraction of fuel was used to form the unwanted side product N-acylurea, suggesting that the transient oxazolone was responsible for the transient self-assembly. When only 50 mM EDC was added, no gel was formed, and no change in the loss and storage moduli was observed (Figure S17C).

Finally, we found that a solution of 4 mM Ac-F₃G-OH formed a hydrogel before the application of fuel at pH 5.0 at 21 °C (Figure 2B), further confirmed by rheology (Figure S17C). Confocal microscopy confirmed the presence of a dense fibrillar network (Figure 2C). Cryo-TEM showed the nano-
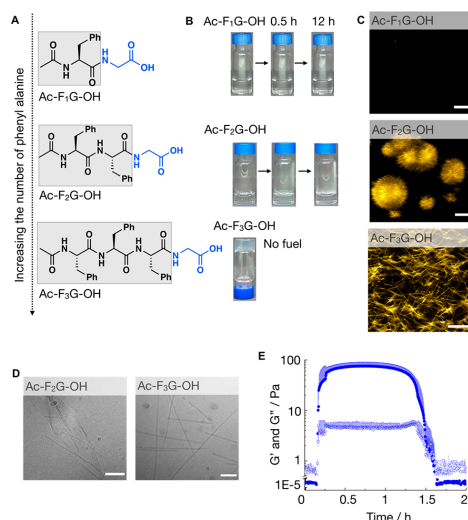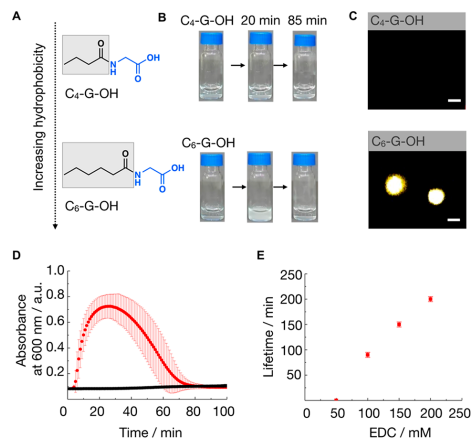
Figure 2. Using the oxazolone-forming reaction cycle to induce transient hydrogels. (A) Molecular design of fiber-forming chemically fueled peptides. All conditions are in 200 mM MES at pH 5.0, 21 °C. (B) Time-lapse photography of solutions of the various precursors in response to EDC. Conditions are 30 mM Ac-FG-OH, Ac-F_2G-OH with 80 mM EDC and 15 mM pyridine, and 4 mM Ac-F_3G-OH without EDC and pyridine. (C) Confocal microscopy images of Ac-FG-OH and Ac-F_2G-OH in response to EDC after 0.5 h and 4 mM Ac-F_3G-OH without EDC. All the scale bars correspond to 10 μm. (D) Cryo-TEM images of the solutions of Ac-F_2G-OH at 65 min after fueling with EDC and 4 mM Ac-F_3G-OH without fuel. All the scale bars correspond to 100 nm. (E) Storage and loss modulus as a function of time, measured by plate−plate rheology of 30 mM Ac-F_2G-OH with 80 mM EDC and 15 mM pyridine. Solid circles represent the storage modulus (G'); empty circles represent the loss modulus (G''). The error bars represent the standard deviation of the average ($n = 3$).

Figure 3. Using the oxazolone-forming reaction cycle to induce transient droplet formation. (A) Molecular design of oil droplet-forming chemically fueled *N*-butyl amino acids. (B) Time-lapse photography of solutions of the various precursors in response to EDC. The condition is 200 mM C_4-G-OH, C_6-G-OH with 100 mM EDC, and 10 mM pyridine in a 200 mM MES buffer at pH 6.0 at 21 °C. (C) Confocal microscopy images of the samples described in B after 0.5 h. All the scale bars correspond to 2 μm. (D) Corresponding absorbance at 600 nm as a measure of turbidity. (E) The lifetime of the droplets in the cycle of 200 mM C_6-G-OH with 10 mM pyridine against initial fuel concentration. Error bars represent the standard deviation of the average ($n = 3$).

meter details of this fiber network (Figure 2D). Taken together, our chemical reaction cycle can convert solutions into hydrogels at the expense of chemical energy.

Next, we explored whether our new reaction cycle could create chemically fueled transient emulsions of oil droplets in water, which have been powerful in delivering hydrophobic drugs with tunable kinetics.[14,49] Thus, we replaced the fiber-forming domain in the previous peptides (Ac-F_n) with an aliphatic domain. Above, we described that N-acetyl-G-OH (Ac-G-OH) does not assemble (Figure S17A,B). Thus, we started with *N*-butyl-G-OH (C_4-G-OH) and *N*-hexyl-G-OH (C_6-G-OH). In this series, the hydrophobicity of the precursor is increased with a simple aliphatic tail aiding the phase separation (Figure 3A). For C_4-G-OH, no evidence of phase separation was found (Figure 3B, C, and D). In contrast, when we fueled 200 mM C_6-G-OH with 100 mM EDC in the presence of 10 mM pyridine in 200 mM MES at pH 6.0, 21 °C, the turbidity increased rapidly and peaked at around 20 min while it completely vanished after 85 min (Figure 3B,D). Confocal microscopy confirmed the presence of oil droplets (Figure 3C). By combining the turbidity data with the kinetics of the kinetic model, we obtained the critical concentration for

droplet formation of 25 mM of the C_6-G-OH oxazolone (Figure S19B). We found that the initial fuel concentration could tune the lifetime of the emulsion. With 50 mM EDC, no turbidity was observed, while the lifetime increased linearly against the fuel added (Figure 3E).

Finally, we explored the new reaction cycle to form amphiphile-based assemblies. We designed and synthesized precursors based on SO_3-C_n-G-OH (Supporting Note 3) inspired by the structure of dodecyl sulfate, a common anionic amphiphile. We assumed that the corresponding oxazolone of SO_3-C_n-G-OH should behave the same as dodecyl sulfate and self-assemble to form micelles. Surprisingly, no micelles formed in the cycle. Instead, we found needle-like crystals in response to EDC. For this class of building blocks, we also investigated a molecular library and increased the hydrophobicity by using a longer carbon chain (Figure 4A). For SO_3-C_{12}-G-OH, no crystals formed in the cycle fueled with EDC (Figure 4B). But we could use this derivative to determine the rate constants for our kinetic model in the absence of assemblies. Crystals emerged in the cycle using 30 mM SO_3-C_{14}-G-OH fueled with 30 mM EDC in 200 mM MES at pH 6.0, 21 °C, that remained for around 16 to 18 h, as evidenced by turbidity data (Figure 4B,D) combined with microscopy (Figure 4C). When crystals were formed, the oxazolone (Figure S20) was present much longer than the nonassembling SO_3-C_{12}-G-OH (Figure S21), which we explain by a self-protection mechanism.[38] Briefly, the crystals protect their oxazolone from hydrolysis because they exclude water. The hydrolysis thus only occurs on the fraction that remains in the solution. Using the kinetic model, we could determine that this concentration was roughly 5 mM of the
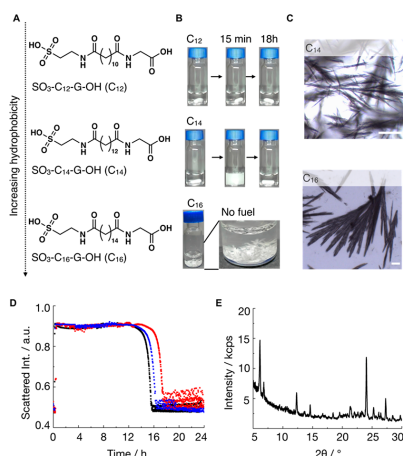
Figure 4. Using the oxazolone-forming reaction cycle to synthesize transient crystals. (A) Molecular library of crystal-forming chemically fueled precursors based on SO_3-C_n-G-OH. All conditions are in 200 mM MES at pH 6.0, 21 °C. (B) Time-lapse photography of solutions of the various precursors in response to EDC. Conditions are 30 mM SO_3-C_{12}-G-OH and SO_3-C_{14}-G-OH with 30 mM EDC and 15 mM SO_3-C_{16}-G-OH without EDC. (C) Microscopy images of 30 mM SO_3-C_{14}-G-OH in response to 30 mM EDC after 0.5 h and 15 mM SO_3-C_{16}-G-OH without EDC. All the scale bars correspond to 100 μm. (D) Turbidity as a function of time of 30 mM SO_3-C_{14}-G-OH in response to 30 mM EDC in 3 independent experiments. (E) Powder X-ray diffraction spectrum of crystals of oxazolone from SO_3-C_{14}-G-OH.

oxazolone of SO_3-C_{14}-G-OH. Sharp peaks in a powder X-ray diffraction spectrum (p-XRD) confirmed that the needle-like precipitates in the cycle are crystalline (Figure 4E). Finally, for 15 mM SO_3-C_{16}-G-OH, needle-like crystals form without fuel, likely because the 16-carbon chain provides enough high hydrophobicity to induce self-assembly (Figure 4B,C and Figure S22).

CONCLUSION

We introduced a new chemical reaction cycle fueled by a carbodiimide to drive 5(*4H*)-oxazolones formation. Unlike other reaction cycles, this one is robust and operates under different temperatures, pH, and fuel input and applies to a wide range of precursors. It uses carbodiimide-based fuel extremely efficiently and does not suffer from significant side reactions. Based on the requirements for the design of precursors, various oxazolones and self-assemblies can be obtained. Future work should explore its potential in forming different self-assemblies and developing new supramolecular materials.

ASSOCIATED CONTENT

Data Availability Statement
The data that support the findings of this study are available from the corresponding author upon reasonable request.

Ⓢ Supporting Information
The Supporting Information is available free of charge at https://pubs.acs.org/doi/10.1021/jacs.3c00273.

Materials and methods description, turbidity data, rheology data, NMR data, FT-IR data, HPLC data, confocal data, mass spectrometry data, and p-XRD data (PDF)

AUTHOR INFORMATION

Corresponding Author
　Job Boekhoven − *Department of Chemistry, School of Natural Sciences, Technical University of Munich, 85748 Garching, Germany;* ⓞ orcid.org/0000-0002-9126-2430; Email: job.boekhoven@tum.de

Authors
　Xiaoyao Chen − *Department of Chemistry, School of Natural Sciences, Technical University of Munich, 85748 Garching, Germany;* ⓞ orcid.org/0000-0002-0545-6395
　Michele Stasi − *Department of Chemistry, School of Natural Sciences, Technical University of Munich, 85748 Garching, Germany*
　Jennifer Rodon-Fores − *Department of Chemistry, School of Natural Sciences, Technical University of Munich, 85748 Garching, Germany;* ⓞ orcid.org/0000-0002-7472-1228
　Paula F. Großmann − *Department of Chemistry, School of Natural Sciences, Technical University of Munich, 85748 Garching, Germany*
　Alexander M. Bergmann − *Department of Chemistry, School of Natural Sciences, Technical University of Munich, 85748 Garching, Germany*
　Kun Dai − *Department of Chemistry, School of Natural Sciences, Technical University of Munich, 85748 Garching, Germany*
　Marta Tena-Solsona − *Department of Chemistry, School of Natural Sciences, Technical University of Munich, 85748 Garching, Germany*
　Bernhard Rieger − *Department of Chemistry, School of Natural Sciences, Technical University of Munich, 85748 Garching, Germany;* ⓞ orcid.org/0000-0002-0023-884X

Complete contact information is available at:
https://pubs.acs.org/10.1021/jacs.3c00273

■ REFERENCES

(1) Whitesides, G. M.; Mathias, J. P.; Seto, C. T. Molecular Self-Assembly and Nanochemistry: A Chemical Strategy for the Synthesis of Nanostructures. *Science* **1991**, *254* (5036), 1312−1319.

(2) Whitesides, G. M.; Grzybowski, B. Self-Assembly at All Scales. *Science* **2002**, *295* (5564), 2418−2421.

(3) Stupp, S. I.; Palmer, L. C. Supramolecular Chemistry and Self-Assembly in Organic Materials Design. *Chem. Mater.* **2014**, *26* (1), 507−518.

(4) Boekhoven, J.; Stupp, S. I. 25th anniversary article: supramolecular materials for regenerative medicine. *Adv. Mater.* **2014**, *26* (11), 1642−59.

(5) Sato, K.; Hendricks, M. P.; Palmer, L. C.; Stupp, S. I. Peptide supramolecular materials for therapeutics. *Chem. Soc. Rev.* **2018**, *47* (20), 7539−7551.

(6) Hirst, A. R.; Escuder, B.; Miravet, J. F.; Smith, D. K. High-tech applications of self-assembling supramolecular nanostructured gel-phase materials: from regenerative medicine to electronic devices. *Angew. Chem., Int. Ed.* **2008**, *47* (42), 8002−18.

(7) Yao, Y.; Zhang, L.; Orgiu, E.; Samori, P. Unconventional Nanofabrication for Supramolecular Electronics. *Adv. Mater.* **2019**, *31* (23), e1900599.

(8) Pluth, M. D.; Bergman, R. G.; Raymond, K. N. Acid catalysis in basic solution: a supramolecular host promotes orthoformate hydrolysis. *Science* **2007**, *316* (5821), 85−8.

(9) Hong, C. M.; Bergman, R. G.; Raymond, K. N.; Toste, F. D. Self-Assembled Tetrahedral Hosts as Supramolecular Catalysts. *Acc. Chem. Res.* **2018**, *51* (10), 2447−2455.

(10) Amabilino, D. B.; Smith, D. K.; Steed, J. W. Supramolecular materials. *Chem. Soc. Rev.* **2017**, *46* (9), 2404−2420.

(11) Dogterom, M.; Koenderink, G. H. Actin-microtubule crosstalk in cell biology. *Nat. Rev. Mol. Cell Biol.* **2019**, *20* (1), 38−54.

(12) Brouhard, G. J.; Rice, L. M. Microtubule dynamics: an interplay of biochemistry and mechanics. *Nat. Rev. Mol. Cell Biol.* **2018**, *19* (7), 451−463.

(13) Grotsch, R. K.; Angi, A.; Mideksa, Y. G.; Wanzke, C.; Tena-Solsona, M.; Feige, M. J.; Rieger, B.; Boekhoven, J. Dissipative Self-Assembly of Photoluminescent Silicon Nanocrystals. *Angew. Chem., Int. Ed.* **2018**, *57* (44), 14608−14612.

(14) Wanzke, C.; Tena-Solsona, M.; Rieß, B.; Tebcharani, L.; Boekhoven, J. Active droplets in a hydrogel release drugs with a constant and tunable rate. *Mater. Horiz.* **2020**, *7* (5), 1397−1403.

(15) Steinkühler, J.; Kamat, N. P. Energy Dissipation at Interfaces Drives Multicompartment Remodeling. *Chem.* **2020**, *6* (5), 1051−1052.

(16) Moller, J. V.; Nissen, P.; Sorensen, T. L.; le Maire, M. Transport mechanism of the sarcoplasmic reticulum Ca2+ -ATPase pump. *Curr. Opin. Struct. Biol.* **2005**, *15* (4), 387−93.

(17) Mo, K.; Zhang, Y.; Dong, Z.; Yang, Y.; Ma, X.; Feringa, B. L.; Zhao, D. Intrinsically unidirectional chemically fuelled rotary molecular motors. *Nature* **2022**, *609*, 293−298.

(18) Morrow, S. M.; Colomer, I.; Fletcher, S. P. A chemically fuelled self-replicator. *Nat. Commun.* **2019**, *10* (1), 1011.

(19) Leira-Iglesias, J.; Tassoni, A.; Adachi, T.; Stich, M.; Hermans, T. M. Oscillations, travelling fronts and patterns in a supramolecular system. *Nat. Nanotechnol.* **2018**, *13* (11), 1021−1027.

(20) Ottelé, J.; Hussain, A. S.; Mayer, C.; Otto, S. Chance emergence of catalytic activity and promiscuity in a self-replicator. *Nat. Catal.* **2020**, *3* (7), 547−553.

(21) Sorrenti, A.; Leira-Iglesias, J.; Sato, A.; Hermans, T. M. Non-equilibrium steady states in supramolecular polymerization. *Nat. Commun.* **2017**, *8*, 15899.

(22) Boekhoven, J.; Brizard, A. M.; Kowlgi, K. N. K.; Koper, G. J. M.; Eelkema, R.; van Esch, J. H. Dissipative self-assembly of a molecular gelator by using a chemical fuel. *Angew. Chem., Int. Ed.* **2010**, *49* (28), 4825−8.

(23) Tena-Solsona, M.; Riess, B.; Grotsch, R. K.; Lohrer, F. C.; Wanzke, C.; Kasdorf, B.; Bausch, A. R.; Muller-Buschbaum, P.; Lieleg, O.; Boekhoven, J. Non-equilibrium dissipative supramolecular materials with a tunable lifetime. *Nat. Commun.* **2017**, *8*, 15895.

(24) Jayalath, I. M.; Gerken, M. M.; Mantel, G.; Hartley, C. S. Substituent Effects on Transient, Carbodiimide-Induced Geometry Changes in Diphenic Acids. *J. Org. Chem.* **2021**, *86* (17), 12024−12033.

(25) Hossain, M. M.; Atkinson, J. L.; Hartley, C. S. Dissipative Assembly of Macrocycles Comprising Multiple Transient Bonds. *Angew. Chem., Int. Ed.* **2020**, *59* (33), 13807−13813.

(26) Kariyawasam, L. S.; Kron, J. C.; Jiang, R.; Sommer, A. J.; Hartley, C. S. Structure-Property Effects in the Generation of Transient Aqueous Benzoic Acid Anhydrides by Carbodiimide Fuels. *J. Org. Chem.* **2020**, *85* (2), 682−690.

(27) Bal, S.; Das, K.; Ahmed, S.; Das, D. Chemically Fueled Dissipative Self-Assembly that Exploits Cooperative Catalysis. *Angew. Chem., Int. Ed.* **2019**, *58* (1), 244−247.

(28) Sun, J.; Vogel, J.; Chen, L.; Schleper, A. L.; Bergner, T.; Kuehne, A. J. C.; von Delius, M. Carbodiimide-Driven Dimerization and Self-Assembly of Artificial, Ribose-Based Amphiphiles. *Chem.—Eur. J.* **2022**, *28* (13), e202104116.

(29) Bal, S.; Ghosh, C.; Ghosh, T.; Vijayaraghavan, R. K.; Das, D. Non-Equilibrium Polymerization of Cross-beta Amyloid Peptides for Temporal Control of Electronic Properties. *Angew. Chem., Int. Ed.* **2020**, *59* (32), 13506−13510.

(30) Maiti, S.; Fortunati, I.; Ferrante, C.; Scrimin, P.; Prins, L. J. Dissipative self-assembly of vesicular nanoreactors. *Nat. Chem.* **2016**, *8* (7), 725−31.

(31) Boekhoven, J.; Hendriksen, W. E.; Koper, G. J. M.; Eelkema, R.; van Esch, J. H. Transient assembly of active materials fueled by a chemical reaction. *Science* **2015**, *349* (6252), 1075−1079.

(32) Dai, K.; Fores, J. R.; Wanzke, C.; Winkeljann, B.; Bergmann, A. M.; Lieleg, O.; Boekhoven, J. Regulating Chemically Fueled Peptide Assemblies by Molecular Design. *J. Am. Chem. Soc.* **2020**, *142* (33), 14142−14149.

(33) Kriebisch, B. A. K.; Jussupow, A.; Bergmann, A. M.; Kohler, F.; Dietz, H.; Kaila, V. R. I.; Boekhoven, J. Reciprocal Coupling in Chemically Fueled Assembly: A Reaction Cycle Regulates Self-Assembly and Vice Versa. *J. Am. Chem. Soc.* **2020**, *142* (49), 20837−20844.

(34) Donau, C.; Spath, F.; Sosson, M.; Kriebisch, B. A. K.; Schnitter, F.; Tena-Solsona, M.; Kang, H. S.; Salibi, E.; Sattler, M.; Mutschler, H.; Boekhoven, J. Active coacervate droplets as a model for membraneless organelles and protocells. *Nat. Commun.* **2020**, *11* (1), 5167.

(35) Wanzke, C.; Jussupow, A.; Kohler, F.; Dietz, H.; Kaila, V. R. I.; Boekhoven, J. Dynamic Vesicles Formed By Dissipative Self-Assembly. *ChemSystemsChem* **2020**, *2* (1), e1900044.

(36) Würbser, M. A.; Schwarz, P.; Heckel, J.; Bergmann, A. M.; Walther, A.; Boekhoven, J. Chemically Fueled Block Copolymer Self-Assembly into Transient Nanoreactors. *ChemSystemsChem* **2021**, *3* (5), e2100015.

(37) Grotsch, R. K.; Wanzke, C.; Speckbacher, M.; Angi, A.; Rieger, B.; Boekhoven, J. Pathway Dependence in the Fuel-Driven Dissipative Self-Assembly of Nanoparticles. *J. Am. Chem. Soc.* **2019**, *141* (25), 9872−9878.

(38) Tena-Solsona, M.; Wanzke, C.; Riess, B.; Bausch, A. R.; Boekhoven, J. Self-selection of dissipative assemblies driven by primitive chemical reaction networks. *Nat. Commun.* **2018**, *9* (1), 2044.

(39) Danger, G.; Michaut, A.; Bucchi, M.; Boiteau, L.; Canal, J.; Plasson, R.; Pascal, R. 5(4H)-oxazolones as intermediates in the carbodiimide- and cyanamide-promoted peptide activations in aqueous solution. *Angew. Chem., Int. Ed.* **2013**, *52* (2), 611−4.

(40) Taylor, L. D.; Platt, T. E. A Convenient Synthesis of 5-Oxazolones. 2-Phenyl-5-Oxazolone. *Org. Prep. Proced. Int.* **1969**, *1* (3), 217−219.

(41) Schnitter, F.; Boekhoven, J. A Method to Quench Carbodiimide-Fueled Self-Assembly. *ChemSystemsChem.* **2021**, *3* (1), e2000037.

(42) Haba, O.; Akashika, Y. Anionic ring-opening polymerization of a five-membered cyclic urethane derived from D-glucosamine. *J. Polym. Sci., Part A: Polym. Chem.* **2019**, *57* (24), 2491−2497.

(43) Helmut, S.; Bruce, M. R. Coordinating properties of the amide bond. Stability and structure of metal ion complexes of peptides and related ligands. *Chem. Rev.* **1982**, *82*, 385−426.

(44) Kariyawasam, L. S.; Hartley, C. S. Dissipative Assembly of Aqueous Carboxylic Acid Anhydrides Fueled by Carbodiimides. *J. Am. Chem. Soc.* **2017**, *139* (34), 11949−11955.

(45) Goodman, M.; Levine, L. Peptide Synthesis uia Active Esters. IV. Racemization and Ring-Opening Reactions of Optically Active Oxazolones. *J. Am. Chem. Soc.* **1964**, *86* (14), 2918−2922.

(46) Miklos, B.; Bodanszky, A. Racemization in peptide synthesis. Mechanism-specific models. *Chem. Commun. (London)* **1967**, *12*, 591−593.

(47) Dodo, O. J.; Petit, L.; Rajawasam, C. W. H.; Hartley, C. S.; Konkolewicz, D. Tailoring Lifetimes and Properties of Carbodiimide-Fueled Covalently Cross-linked Polymer Networks. *Macromolecules* **2021**, *54* (21), 9860−9867.

(48) Afrose, S. P.; Mahato, C.; Sharma, P.; Roy, L.; Das, D. Nonequilibrium Catalytic Supramolecular Assemblies of Melamine- and Imidazole-Based Dynamic Building Blocks. *J. Am. Chem. Soc.* **2022**, *144* (2), 673−678.

(49) Tebcharani, L.; Wanzke, C.; Lutz, T. M.; Rodon-Fores, J.; Lieleg, O.; Boekhoven, J. Emulsions of hydrolyzable oils for the zero-order release of hydrophobic drugs. *J. Controlled Release* **2021**, *339*, 498−505.

📖 **Recommended by ACS**

Supporting Information for:

A Carbodiimide-Fueled Reaction Cycle That Forms Transient 5(4H)-Oxazolones

Xiaoyao Chen,[1] Michele Stasi,[1] Jennifer Rodon-Fores,[1] Paula F. Großmann,[1] Alexander M. Bergmann,[1] Kun Dai,[1] Marta Tena-Solsona,[1] Bernhard Rieger [1] & Job Boekhoven*[1]

[1] Department of Chemistry, School of Natural Sciences, Technical University of Munich, Lichtenbergstrasse 4, 85748 Garching, Germany.

MATERIALS

Materials. N-Acetyl-L-glycine (Ac-G-OH), N-Acetyl-L-alanine (Ac-A-OH), N-Acetyl-L-valine (Ac-V-OH), N-Acetyl-L-isoleucine (Ac-I-OH), N-Acetyl-L-leucine (Ac-L-OH), N-(tert-Butoxycarbonyl)-L-phenylalanine (Boc-F-OH) and HBTU were purchased from Alfa Aesar. Monoethyl dodecanedioate, N-Acetyl-L-histidine monohydrate (Ac-H-OH) and glycine tert-butyl ester hydrochloride were purchased from TCI. 14-(tert-Butoxy)-14-oxotetradecanoic acid, and 16-(tert-Butoxy)-16-oxohexadecanoic acid were purchased from BLDpharm. N-Acetyl-L-phenylalanine (Ac-F-OH (L)), N-Acetyl-D-phenylalanine (Ac-F-OH (D)), 3-phenylpropionic acid or 3-Phenylpropanoic acid, N-Acetyl-L-methionine (Ac-M-OH), N-Acetyl-L-arginine (Ac-R-OH), N-Acetyl-DL-serine (Ac-S-OH), Acetyl-L-Aspartic acid (Ac-D-OH), N-(9-Fluorenylmethoxycarbonyl)-L-phenylalanine (Fmoc-F-OH), benzylamine, 1-ethyl-3-(3-dimethyl aminopropyl)carbodiimide (EDC), 2-(*N*-morpholino) ethanesulfonic acid (MES) buffer, trifluoroacetic acid (TFA), anhydrous acetonitrile (ACN), deuterated dimethyl sulfoxide (DMSO-d_6), Nile Red, triisopropylsilane (TIPS), Fmoc-Gly-Wang resin, ethyl chloroformate, 2-Butanamidoacetic acid, 2-Hexanamidoacetic acid, N, N-Diisopropylethylamine (DIEA), taurine, 1-Hydroxybenzotriazole hydrate (HOBt), 3-[Bis(dimethylamino)methyliumyl]-3H-benzotriazol-1-oxide hexafluorophosphate (HBTU) and triethylamine (TEA) were purchased from Sigma-Aldrich and used without any further purification unless otherwise indicated. HPLC grade acetonitrile (ACN) was purchased from VWR. The peptides used in this study were synthesized using solid-phase peptide synthesis.

METHODS

Sample preparation. We prepared stock solutions of the precursors by dissolving the amino acids or peptides in 0.2 M MES buffer, then we adjusted the pH to pH 5.0, 6.0, or 7.0. Benzylamine stocks were prepared freshly in acetonitrile. EDC stock solutions were prepared by dissolving the EDC powder in MQ water. Reaction cycles were started by adding EDC from the freshly prepared stock solution to the precursor.

Peptide synthesis and purification. Peptides were synthesized on a CEM Liberty microwave-assisted peptide synthesizer. We used the preload Fmoc-Gly-Wang resin, which was freshly swollen in DMF before use. Before the following amino acid-coupling, the N-terminal Fmoc protecting group was removed using a 20% solution of piperidine in DMF. The reaction mixture was heated in the microwave (1×1 minute, 90 °C) and then washed with DMF. We repeated the Fmoc-deprotection twice to get a higher yield. The coupling was achieved by using 4 equivalents (eq.) of Fmoc-protected amino acid in DMF, 4 eq. of DIC, and 4 eq. of ethyl(hydroxyimino)cyanoacetate (Oxyma). To increase the yield, the coupling was repeated twice. After each coupling step, the resin was washed with DMF. The 2x Fmoc-deprotection, washing, 2 × couplings, and washing cycle were repeated until the last amino acid of the respective peptide sequence was coupled. Then, the peptide was cleaved from the resin using a mixture of 95% TFA, 2.5% MQ-water, and 2.5% TIPS. To get crude products, the solvent was removed by co-distillation with diethyl ether under reduced pressure on rotary evaporation. The crude products were in ±50% acetonitrile in water and purified on a reversed-phase High-Performance Liquid Chromatography (RP-HPLC) with gradient elution from 2% to 98% acetonitrile with 0.1% TFA in MQ-water. All compounds were detected at 220 nm and lyophilized (Lyophylle: Alpha LDplus, Christ) and characterized by [1] H-NMR spectroscopy, HPLC, and Electron Spray Ionisation – Mass Spectrometry (ESI-MS).

Kinetic model. We used a kinetic model to predict the oxazolone concentration's evolution over time. We describe the model in supporting Note 1. The rate constants we used in this work are given in Supporting Table S6-S9.

Analysis of the reaction kinetics by HPLC. The kinetics of the chemical reaction cycles were monitored over time by analytical HPLC (ThermoFisher Vanquish Duo UHPLC, a Hypersil Gold 100 x 2.1 mm C18 column (3 μm pore size) and Thermo Fisher Dionex Ultimate 3000, Hypersil Gold 250 × 4.8mm). We used the quenching method[1] to indirectly determine the concentration of the oxazolone product by converting it irreversibly into an amide, which we refer to as benzylamide. Also, EDC reacted with benzylamine and was converted irreversibly into a guanidine. After initiating the reaction network by adding EDC to the precursor solution, we took a certain amount of reaction solution to the benzylamine solution at each time point. After several hours, the resulting quenched clear solution was measured via HPLC to determine the benzylamide and guanidine concentration. For precursors of amino acids, the ratio of the reaction solution and benzylamine solution (400 mM) was 1:1. In comparison, for precursors of peptides, the ratio of the reaction solution and benzylamine solution and H_2O was 1:6:1. Adding water can help the benzylamide dissolve better. In both cases, 1 or 2 μL quenched solution was directly injected without further dilution into HPLC and tracked with a UV/Vis detector at 220 and 254 nm. All compounds involved were separated using a linear gradient of H_2O: ACN, each with 0.1% TFA.

HPLC Methods.

The kinetics of most precursors were monitored on HPLC on a Hypersil Gold 100 x 2.1 mm C18 column (3 μm pore size), while a column of Hypersil Gold 250 × 4.8mm was used to monitor the kinetics of Ac-I-OH, Ac-R-OH.

Ac-F-OH: H_2O/ACN starts from 95/5. ACN increases to 35% in 6 min, 2 min increasing to 45 %, 0.5 min climbing to 98 %, followed by 2 min at 98 % before going back to 5 % and finally 3 min 5 %.

Ac-A-OH: H_2O/ACN starts from 95/5. ACN increases to 35% in 12 min, 0.5 min climbing to 98 %, followed by 2 min 98 %, 1 min going back to 5 % and finally 3 min 5 %.

Ac-G-OH: H_2O/ACN starts from 95/5. ACN increases to 35% in 10 min, 0.5 min climbing to 98 %, followed by 3 min 98 %, 0.5 min going back to 5 % and finally 3 min 5 %.

1

Ac-L-OH: H$_2$O/ACN starts from 98/2. ACN keeps at 2 % for the first 5 min, increasing to 35% in 10 min, 2 min increasing to 45 %, 2 min climbing to 98 %, 4 min 98 %, 1 min going back to 2%, and finally 3 min 2%.

Ac-I-OH: H$_2$O/ACN starts from 95/5. ACN keeps at 5 % for 3 min of equilibration, increasing to 20% in 18.5 min, 3.5 min increasing to 45 %, 6 min climbing to 95 %, 3 min 95 %, 2 min going back to 5%, and finally 4 min 5%.

Ac-R-OH: H$_2$O/ACN starts from 98/2. ACN keeps at 2 % for 3 min of equilibration, increasing to 20% in 22 min, 2 min climbing to 98 %, 1 min 98 %, 2 min going back to 2%, and finally 3 min 2%.

Ac-H-OH: H$_2$O/ACN starts from 99/1. ACN keeps at 1 % for 3 min of equilibration, 1 % for the first 5 min, 13 min increasing to 16.6 %, 3 min climbing to 95 %, 2 min 95 %, 3 min going back to 1%, and finally 3 min 1%.

Ac-S-OH: H$_2$O/ACN starts from 98/2. ACN keeps at 2 % for the first 1 min, increasing to 35% in 9 min, 1 min climbing to 98 %, 2 min 98 %, 1 min going back to 2%, and finally 4 min 2%.

Ac-M-OH: H$_2$O/ACN starts from 98/2. ACN keeps at 2 % for the first 1 min, increasing to 20% in 8 min, 4 min increasing to 50 %, 1 min climbing to 98 %, 1 min 98 %, 2 min going back to 2%, and finally 3 min 2%.

Ac-D-OH: H$_2$O/ACN starts from 98/2. ACN keeps at 2 % for the first 5 min, increasing to 25% in 14 min, 1 min increasing to 98 %, 1 min 98 %, 1 min going back to 2%, and finally 3 min 2%.

Phenylpropanoic acid: H$_2$O/ACN starts from 98/2. ACN increases to 55% in 8 min, 0.2 min climbing to 98 %, followed by 2.8 min 98 %, 0.5 min going back to 5% and finally 2.5 min 5%.

Fmoc/Boc-F-OH: H$_2$O/ACN starts from 95/5. ACN increases to 60% in 6 min, 5 min increasing to 70 %, 3 min increasing to 80 %, 3 min climbing to 98 %, followed by 3min 98 %, 2 min going back to 5% and finally 3 min 5%.

Ac-FG-OH: H$_2$O/ACN starts from 95/5. ACN increases to 35% in 7min, 4 min increasing to 45 %, 2 min climbing to 98 %, then 3min 98 %, 1 min going back to 5 %, and 3 min 5 %.

Ac-FFG-OH: H$_2$O/ACN starts from 95/5. ACN increases to 25% in 10 min, 9 min increasing to 35 %, 4 min climbing to 98 %, followed by 3 min 98 %, 1 min going back to 5 % and finally 3 min 5 %.

C$_4$-G-OH: H$_2$O/ACN starts from 98/2. ACN stays at 2 % for 5 min and increases to 19 % in 11 min, 2 min increasing to 98 %, followed by 2 min 98 %, 2 min going back to 2 % and finally 3 min 2 %.

C$_6$-G-OH: H$_2$O/ACN starts from 98/2. ACN stays at 2 % for 2 min and increases to 50 % in 10 min, 2 min climbing to 98 %, followed by 2 min 98 %, 1 min going back to 2 % and finally 3 min 2 %.

SO$_3$-C$_{12}$-G-OH and SO$_3$-C$_{14}$-G-OH: H$_2$O/ACN start from 95/5. ACN increases to 35% in 19 min, 4 min climbing to 98 %, followed by 3 min 98 %, 1 min going back to 5 % and finally 3 min 5 %.

Calibration curves for the EDC (in H$_2$O) and benzylamine (in ACN) were performed with the method of Ac-F-OH in triplicate. All acids (in MES buffer) were performed with the corresponding method in triplicate. Retention times and calibration values are given in Supporting Table S4.

Confocal Fluorescence Microscopy. We used a Leica SP5 confocal microscope using a 63x oil immersion objective to image the fibers and droplets. Samples were prepared as described above with a total reaction volume of 10 μL, including 25 μM Nile red as a dye. Samples were deposited on an IBIDI 15 wells chambered coverslip with sterilized glass-bottom No. 1.5H non-coated before exciting them with a 552 nm laser and imaging at 580 - 700 nm. Images of 1024 × 1024 were acquired from an area covering 184 × 184 μm. All recorded images were analyzed using the ImageJ 1.52p software (Java 1.80_172 (64-bit)).

Electron Spray Ionisation – Mass Spectrometry (ESI-MS). We used a Varian 500 MS LC ion trap or an LCQ Fleet Ion Trap Mass Spectrometer (Thermo Scientific) to perform ESI-MS measurements. The samples were diluted in acetonitrile or MQ water before injection into the Mass Spectrometer. All recorded MS data were interpreted using the Thermo Xcalibur Qual Browser 2.2 SP1.48 software or a direct photo by a smartphone.

Turbidity measurements and lifetime determination. Turbidity measurements were carried out at 21 °C on a Microplate Spectrophotometer (Thermo Scientific Multiskan GO, Thermo Scientific SkanIt Software 6.0.1). Measurements were performed in a non-tissue culture-treated 96-well plate (Falcon, flat bottom). Every minute, the absorbance of the 100 -120μL samples was measured at 600 nm. All experiments were performed in triplicate. The lifetime refers to the time it takes for the absorption to drop under 0.01 a.u. (blank subtraction) after EDC addition.

Turbidity device. We used a homemade setup to measure the evolutions of the turbidity during the reaction cycle with SO$_3$-C$_{14}$-G-OH as a precursor with continuous stirring.[2] The setup measures the scattering of 660 nm laser light under a 90° angle with a scattering rate at 30-second intervals. An Arduino microcontroller controls the laser and detector. The Arduino script can be available at: https://github.com/fabianschnitter/Script-turbidity-device.git.

Fourier-Transform Infrared Spectroscopy (FTIR). FTIR spectra were obtained on the measurement crystal of the Bruker Vertex 70 FTIR using a Platinum ATR from Bruker. The transmittance of the samples was measured from 4000 cm^{-1} to 600 cm^{-1}. 16 scans were conducted per measurement. The data was processed using OPUS 7.5 software (Copyright Bruker Optik GmbH 2014).

2

NMR spectra. NMR spectra were conducted on Bruker AV400US (400 MHz and 500 MHz). Chemical shifts are reported as δ-values in parts per million (ppm) relative to the deuterated solvent peak: DMSO-d_6 (δH: 2.50). For the denotation of the observed signal multiplicities, the following abbreviations were used: s (singlet), d (doublet), dd (doublet of doublets), and m (multiplet).

Rheology. Rheological measurements were carried out on a research-grade shear rheometer (MCR 302, Antor Paar, SN82923853) using oscillatory rheology with a measuring system of PP25, SN77311. The measurements were performed in torque-controlled mode (by applying small torques of 0.5 μNm and a constant oscillation frequency of 1 Hz). Storage moduli (G') and loss moduli (G'') were recorded over time and one measurement point was recorded every 7.5 seconds. A solvent trap was placed around the sample holder to avoid evaporation. Data were recorded at 21 °C.

3

SUPPORTING NOTES

Supporting Note 1. Description of experiments to prove the formation of the 5(4H)-oxazolone

Except the controlled experiments were conducted using phenylpropanoic acid and N-Acetyl-L-phenylalanine (Ac-F-OH) as precursors, we also did the chiral analysis and synthesized 5(4H)-oxazolone of Ac-F-OH in the organic phase to confirm the formation of the 5(4H)-oxazolone further. For brevity, oxazolones refer to 5(4H)-oxazolones in the following text.

Chiral analysis

Inspired by racemization caused by oxazolones in peptide synthesis[3-4], we conducted chiral column measurements (Figure S2C). We used 100 mM Ac-F-OH (L) with 60 mM EDC in 200 mM MES buffer at pH 6. After 24 hours, when the reaction cycle had finished, we collected the precursor and injected it into a chiral column. The enantiomer (N-Acetyl-D-phenylalanine) was formed, indicating the formation of an oxazolone in the reaction cycle.

Synthesized oxazolone

Scheme S1. Synthesis route of the oxazolone in an organic solvent

Besides, the oxazolone was also synthesized in organic solvent[5] (Scheme S1) and characterized by HPLC, NMR, FT-IR, and mass spectrometry (Table S1) to confirm the results. On the non-chiral HPLC, we monitored the hydrolysis of the oxazolone in 200 mM MES buffer at pH 6 (Figure S2D). We started from freshly synthesized oxazolone, whose retention time is around 6.646 min. With time the peak of the precursor (6.129 min) emerged and increased while the peak of the oxazolone decreased and disappeared. This hydrolysis process is opposite to the process of the oxazolone's formation in the reaction cycle. Since hydrolysis of oxazolone can quickly happen when water is present, the hydrolyzed product (Ac-F-OH) can also be found in the NMR spectra (Figure S4 and Figure S5). After we added extra water, the oxazolone hydrolyzed to Ac-F-OH, and no proton signals of the oxazolone could be found. This is also consistent with the process of oxazolone's hydrolysis on HPLC (Figure S2D). From FT-IR, the peaks around 1820 and 1685 cm^{-1} are attributed to the C=O and C=N of the oxazolone (Figure S3A). The FT-IR spectrum of an oxazolone is different from that of an anhydride. For example, peaks around 1815 and 1747 cm^{-1} are responsible for the O=C-O-C=O of the anhydride of phenylpropanoic acid (Figure S3B). These data further confirm the formation of oxazolone in the reaction cycle.

Supporting Note 2. Description of the kinetic model

1. Oxazolone is the main product.

We wrote a kinetic model in Python that described each reaction involved in the chemical reaction network. The concentrations of each reactant were calculated for every 1 minute in the cycle. The model was used to fit the HPLC data that described the evolution of the concentration of precursors, EDC, oxazolones, and N-acylurea over time. The model described 5 chemical reactions: direct hydrolysis of EDC (r_0), the activation of acid (r_1), the intramolecular heterocyclization to form oxazolone (r_2), hydrolysis of O-acylurea (r_3), hydrolysis of oxazolone (r_4), and the side product formation of N-acylurea by a rearrangement reaction (N to O shift, r_5).

0) Reaction 0: direct hydrolysis of EDC (k_0). It has a first-order rate constant that can be obtained from experiments. We used analytic HPLC to determine k_0 under different conditions, and the values can be found in Table S7.
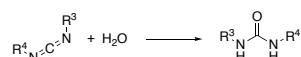
1) Reaction 1: the activation of acid by EDC to form O-acylurea (k_1). This second-order rate constant was determined for each precursor by HPLC by monitoring the EDC consumption.
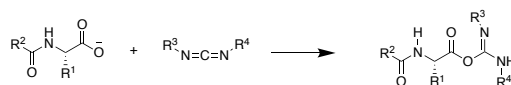
2) Reaction 2: the intramolecular heterocyclization to form oxazolone (k_2). This first-order rate constant could not be determined because the O-acylurea was not observed.
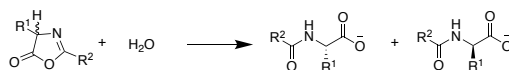

4
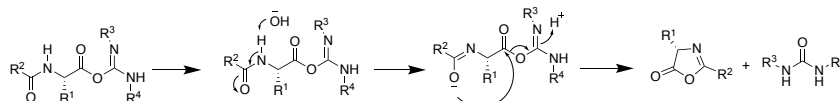
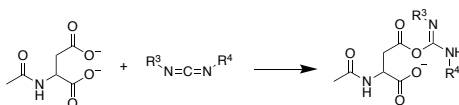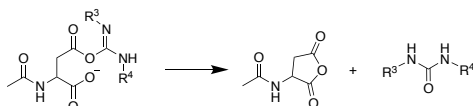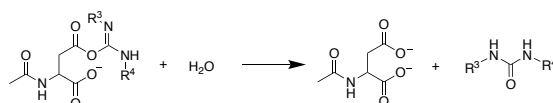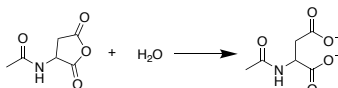3) Reaction 3: direct hydrolysis of O-acylurea (k_3). This first-order rate constant could not be obtained because the O-acylurea was not observed.
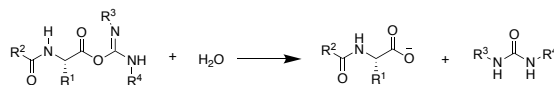
4) Reaction 4: hydrolysis of oxazolone (k_4). As indirectly determined by HPLC using the benzylamine quenching method, the hydrolysis of oxazolone takes place with a (pseudo)-first order. The hydrolysis reaction rate was calculated by multiplying the f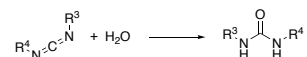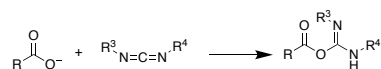irst-order rate constant k_4 with the concentration of oxazolone. Notably, racemization occurs after oxazolone is formed, and an epimer of the precursor was spontaneously formed after hydrolysis of the oxazolone.

5) Reaction 5: side product formation of N-acylurea (N to O shift, k_5). This first-order rate constant could not be obtained because the O-acylurea was not observed.
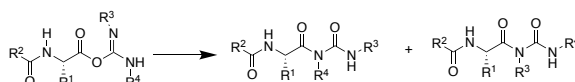
2. Intramolecular anhydride is the main product.

We wrote a kinetic model in Python that described each reaction involved in the chemical reaction network. The concentrations of each reactant were calculated for every 1 minute in the cycle. The model was used to fit the HPLC data that described the evolution of the concentration of precursors, EDC, and anhydride over time. The model described 4 chemical reactions: direct hydrolysis of EDC (r_0), the activation of acid (r_1), the intramolecular cyclization to form intramolecular anhydride (r_2), hydrolysis of O-acylurea (r_3), hydrolysis of anhydride (r_4). No N-acylurea was formed when Ac-D-OH was used as a precursor.
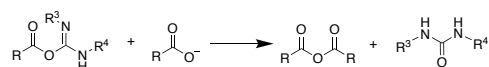
0) Reaction 0: direct hydrolysis of EDC (k_0). It has a first-order rate constant that can be obtained from experiments. We used analytic HPLC to determine k_0 under different conditions, and the values can be found in Table S7.
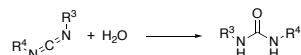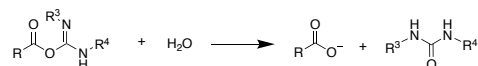

1) Reaction 1: the activation of acid by EDC to form O-acylurea (k_1). This second-order rate constant was determined for each precursor by HPLC by monitoring the EDC consumption.
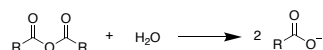

2) Reaction 2: intramolecular cyclization to form anhydride (k_2). This first-order rate constant could not be determined because the O-acylurea was not observed.
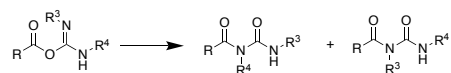

3) Reaction 3: direct hydrolysis of O-acylurea (k_3). This first-order rate constant could not be obtained because the O-acylurea was not observed.

4) Reaction 4: hydrolysis of anhydride (k_4). As indirectly determined by HPLC using the benzylamine quenching method, the hydrolysis of anhydride takes place with a (pseudo)-first order. The hydrolysis reaction rate was calculated by multiplying the first-order rate constant k_4 with the concentration of anhydride.

3. Intermolecular anhydride is the main product.

We wrote a kinetic model in Python that described each reaction involved in the chemical reaction network. The concentrations of each reactant were calculated for every 1 minute in the cycle. The model was used to fit the HPLC data that described the evolution of the concentration of precursors, EDC, anhydride, and N-acylurea over time. The model described 5 chemical reactions: direct hydrolysis of EDC (r_0), the activation of acid (r_1), the formation of intermolecular anhydride (r_2), hydrolysis of O-acylurea (r_3), hydrolysis of anhydride (r_4) and the side product formation of N-acylurea by a rearrangement reaction (N to O shift, r_5).

0) Reaction 0: direct hydrolysis of EDC (k_0). It has a first-order rate constant that can be obtained from experiments. We used analytic HPLC to determine k_0 under different conditions, and the values can be found in Table S7.

1) Reaction 1: the activation of acid by EDC to form O-acylurea (k_1). This second-order rate constant was determined for each precursor by HPLC by monitoring the EDC consumption.

2) Reaction 2: the formation of intermolecular anhydride (k_2). This second-order rate constant could not be determined because the O-acylurea was not observed.

3) Reaction 3: direct hydrolysis of O-acylurea (k_3). This first-order rate constant could not be obtained because the O-acylurea was not observed.

4) Reaction 4: hydrolysis of anhydride (k_4). As indirectly determined by HPLC using the benzylamine quenching method, the hydrolysis of anhydride takes place with a (pseudo)-first order. The hydrolysis reaction rate was calculated by multiplying the first-order rate constant k_4 with the concentration of anhydride.

5) Reaction 5: side product formation of N-acylurea (N to O shift, k_5). This first-order rate constant could not be obtained because the O-acylurea was not observed.

4. Ordinary differential equations (ODEs).

We used the following set of ODEs to describe the systems by using a steady-state approximation that removed any explicit dependence on the concentration of O-acylurea and used the python package kinmodel to fit the experimental data. In this case, all the k-values were free parameters to optimize. The individual values of k_2 and k_3 cannot be accurately extracted, but a condition on their ratio appears i.e. that $k_3/k_2 << 1$, in line with an intramolecular process. Indeed, for amino acids where N-acylurea was negligible on HPLC and assumed to be less than 1%, the system could be successfully fitted even with a simpler model that depends only on k_1 (reaction of the acid with EDC) and k_4 (hydrolysis of oxazolone), suggesting that all the EDC which reacts with the amino acid is funneled into the oxazolone. On the other end, when N-acylurea becomes a significant product of the reaction, as for Isoleucine, the conditions that $k_3/k_2 << 1$ is maintained but k_5/k_2 spans from 0.01 to 10, highlighting a relevance for the reaction pathway that leads to the formation of N-acylurea. We believe that at this level, it is not useful to overinterpret the individual k-values obtained for the cyclization and N-acylurea formation, and it does not invalidate the experimental results.

A. For Oxazolone-forming or intramolecular anhydride-forming reaction cycle:

1. The corresponding set of ODEs is the following:

(F = EDC, W = EDU, Ac = Acid Precursor, P = Oxazolone or Intramolecular Anhydride, N = N-acylurea)

6

$$\begin{cases} \frac{d[Ac]}{dt} = -k_1 \cdot [Ac] \cdot [F] + k_4 \cdot [P] + \frac{k_3}{(k_2 + k_3 + k_5)} \cdot k_1 \cdot [Ac] \cdot [F] \\[2mm] \frac{d[F]}{dt} = -k_1 \cdot [Ac] \cdot [F] - k_0 \cdot [F] \\[2mm] \frac{d[W]}{dt} = +k_0 \cdot [F] + \frac{k_2 + k_3}{k_2 + k_3 + k_5} \cdot k_1 \cdot [Ac] \cdot [F] \\[2mm] \frac{d[P]}{dt} = +\frac{k_2}{k_2 + k_3 + k_5} \cdot k_1 \cdot [Ac] \cdot [F] - k_4 \cdot [P] \\[2mm] \frac{dN}{dt} = \frac{k_5}{k_2 + k_3 + k_5} \cdot k_1 \cdot [Ac] \cdot [F] \end{cases}$$

When N-acylurea was negligible on HPLC and assumed to be less than 1%, k_5 was set to 0 and the system reduced to the following set of ODEs ($K = k_3/k_2$)

$$\begin{cases} \frac{d[Ac]}{dt} = -k_1 \cdot [Ac] \cdot [F] + k_4 \cdot [P] + \frac{K}{(K+1)} \cdot k_1 \cdot [Ac] \cdot [F] \\[2mm] \frac{d[F]}{dt} = -k_1 \cdot [Ac] \cdot [F] - k_0 \cdot [F] \\[2mm] \frac{d[W]}{dt} = +k_0 \cdot [F] + k_1 \cdot [Ac] \cdot [F] \\[2mm] \frac{d[P]}{dt} = +\frac{k_1 \cdot [Ac] \cdot [F]}{K+1} - k_4 \cdot [P] \end{cases}$$

2. The calculation of products' yield:

a. When k_5 is not set as 0:

We first compute the concentration of all the compounds of the cycle:

$[F](t+1) = [F](t) - r_0(t) - r_1(t)$
$[Ac](t+1) = [Ac](t) - r_1(t) + r_3(t) + r_4(t)$
$[W](t+1) = [W](t) + r_0(t) + r_2(t) + r_3(t)$
$[P](t+1) = [P](t) + r_2(t) - r_4(t)$
$[N](t+1) = [N](t) + r_5(t)$

Where

$r_0(t) = k_0 \cdot [F]$
$r_1(t) = k_1 \cdot [Ac] \cdot [F]$
$r_2(t) = \dfrac{k_2}{(k_2 + k_3 + k_5)} \cdot k_1 \cdot [Ac] \cdot [F]$
$r_3(t) = \dfrac{k_3}{(k_2 + k_3 + k_5)} \cdot k_1 \cdot [Ac] \cdot [F]$
$r_4(t) = k_4 \cdot [P]$
$r_5(t) = \dfrac{k_5}{(k_2 + k_3 + k_5)} \cdot k_1 \cdot [Ac] \cdot [F]$

b. When k_5 is set as 0, $K = k_3/k_2$:

We first compute the concentration of all the compounds of the cycle:

$[F](t+1) = [F](t) - r_0(t) - r_1(t)$
$[Ac](t+1) = [Ac](t) - r_1(t) + r_3(t) + r_4(t)$
$[W](t+1) = [W](t) + r_0(t) + r_2(t) + r_3(t)$
$[P](t+1) = [P](t) + r_2(t) - r_4(t)$

Where

$r_0(t) = k_0 \cdot [F]$
$r_1(t) = k_1 \cdot [Ac] \cdot [F]$
$r_2(t) = \dfrac{k_1}{(K+1)} \cdot [Ac] \cdot [F]$
$r_3(t) = \dfrac{K \cdot k_1}{(K+1)} \cdot [Ac] \cdot [F]$

7

$$r_4(t) = k_4 \cdot [P]$$

c. Then the concentration of the product without hydrolysis:

$$P_{sum} = \sum_{t=0}^{T} r_2(t)$$

Where T is the reaction time. Then the yield of the product is:

$$P_{yield} = 100 \cdot \frac{P_{sum}}{[F]_0}$$

B. For the intermolecular anhydride-forming reaction cycle:

1. The following set of ODEs was used and fitted:

$$\begin{cases} \frac{d[Ac]}{dt} = -k_1 \cdot [Ac] \cdot [F] + 2 \cdot k_4 \cdot [P] + \frac{k_3}{k_2 \cdot [Ac] + k_3 + k_5} \cdot k_1 \cdot [Ac] \cdot [F] - \frac{k_2}{k_2 \cdot [Ac] + k_3 + k_5} \cdot k_1 \cdot [Ac]^2 \cdot [F] \\ \frac{d[F]}{dt} = -k_1 \cdot [Ac] \cdot [F] - k_0 \cdot [F] \\ \frac{d[W]}{dt} = +k_0 \cdot [F] + \frac{k_2 \cdot [Ac] + k_3}{k_2 \cdot [Ac] + k_3 + k_5} \cdot k_1 \cdot [Ac] \cdot [F] \\ \frac{d[P]}{dt} = +\frac{k_2}{k_2 \cdot [Ac] + k_3 + k_5} \cdot k_1 \cdot [Ac]^2 \cdot [F] - k_4 \cdot [P] \\ \frac{d[N]}{dt} = +\frac{k_5}{k_2 \cdot [Ac] + k_3 + k_5} \cdot k_1 \cdot [Ac] \cdot [F] \end{cases}$$

2. The calculation of products' yield:

We first compute the concentration of all the compounds of the cycle:

$$[F](t + 1) = [F](t) - r_0(t) - r_1(t)$$
$$[Ac](t + 1) = [Ac](t) - r_1(t) - r_2(t) + r_3(t) + 2 \cdot r_4(t)$$
$$[W](t + 1) = [W](t) + r_0(t) + r_2(t) + r_3(t)$$
$$[P](t + 1) = [P](t) + r_2(t) - r_4(t)$$
$$[N](t + 1) = [N](t) + r_5(t)$$

Where

$$r_0(t) = k_0 \cdot [F]$$
$$r_1(t) = k_1 \cdot [Ac] \cdot [F]$$
$$r_2(t) = \frac{k_2}{(k_2 \cdot [Ac] + k_3 + k_5)} \cdot k_1 \cdot [Ac]^2 \cdot [F]$$
$$r_3(t) = \frac{k_3}{(k_2 \cdot [Ac] + k_3 + k_5)} \cdot k_1 \cdot [Ac] \cdot [F]$$
$$r_4(t) = k_4 \cdot [P]$$
$$r_5(t) = \frac{k_5}{(k_2 \cdot [Ac] + k_3 + k_5)} \cdot k_1 \cdot [Ac] \cdot [F]$$

Then the concentration of products without hydrolysis:

$$P_{sum} = \sum_{t=0}^{T} r_2(t)$$

Where T is the reaction time. Then the yield of products is:

$$P_{yield} = 100 \cdot \frac{P_{sum}}{[F]_0}$$

8

5. Python codes.

To fit the data, we used the package kinmodel available here https://github.com/scotthartley/kinmodel. The model file used is provided below (OxazoloneModel.py)

A. Oxazolone-forming reaction cycle without N-acylurea formation:

Note: "An" represents the product (oxazolone).

```python
import textwrap
from kinmodel import KineticModel

def equations(concs, t, *ks):
    Ac, E, U, An = concs
    k1, K, k2, k0 = ks

    return [- k1*E*Ac + k2*An + (k1*K*Ac*E)/(K+1),
            - k1*E*Ac -k0*E,
            + k1*E*Ac +k0*E,
            + (k1*Ac*E)/(K+1) - k2*An]

model = KineticModel(
    name="OxazoloneModel",
    description=textwrap.dedent("""\
        Diacid kinetics w/o catalysis:

            Ac + E ---> I        (k1)
                 I ---> An + U   (kiAn)
                 I ---> Ac + U   (kiAc)
               An ---> Ac        (k2)

        Steady-state approximation with K = kiAc/kiAn.
        Orders: k1, K, k2, k0; Ac, E, U, An.\
        """),
    kin_sys=equations,
    ks_guesses=[1e-2, 0.01, 1.2],
    ks_constant=[1.8e-4],
    conc0_guesses=[100, 20],
    conc0_constant=[0, 0],
    k_var_names=["k1", "K","k2"],
    k_const_names=["k0"],
    conc0_var_names=["[Acid]0","[EDC]0"],
    conc0_const_names=["[U]0", "[Ox]0"],
    legend_names=["Acid", "EDC", "Urea", "Ox"],
    top_plot=[1, 2],
    bottom_plot=[0, 3],
    sort_order=[1, 3, 2, 0],
    int_eqn=[
            lambda cs, ks: ks[2]*cs[3], ],
    int_eqn_desc=[
            "k2*An", ],
    lifetime_conc=[3],
    rectime_conc=[0],
    )
```

9

B. Oxazolone-forming reaction cycle with N-acylurea formation:

Note: "An" represents the product (oxazolone).

```python
import textwrap
from kinmodel import KineticModel

def equations(concs, t, *ks):
    Ac, E, U, An, N = concs
    k1, kiAn, kiAc, k2, kn= ks

    return [- k1*E*Ac + k2*An + (kiAc*k1*Ac*E)/(kiAn+kiAc+kn),
            - k1*E*Ac,
            + (kiAc*k1*Ac*E)/(kiAn+kiAc+kn) +(kiAn*k1*Ac*E)/(kiAn+kiAc+kn),
            + (kiAn*k1*Ac*E)/(kiAn+kiAc+kn) - k2*An,
            + (kn*k1*Ac*E)/(kiAn+kiAc+kn)]

model = KineticModel(
    name="OxazoloneModel_Nacyl",
    description=textwrap.dedent("""\
        Diacid kinetics w/o catalysis and N-acylurea:

            Ac + E ---> I        (k1)
                I ---> An + U  (kiAn)
                I ---> Ac + U  (kiAc)
            I ---> N  (kn)
                An ---> Ac        (k2)


        Orders: k1, kiAn, kiAc, k2, kn; Ac, E, U, An, N.\
        """),
    kin_sys=equations,
    ks_guesses=[4e-4, 1, 1, 1e-2,1e-5],
    ks_constant=[],
    conc0_guesses=[100, 30],
    conc0_constant=[0, 0, 0],
    k_var_names=["k1", "kiAn","kiAc","k2","kn"],
    k_const_names=[],
    conc0_var_names=["[Acid]0", "[EDC]0"],
    conc0_const_names=["[U]0", "[An]0","[NAcyl]0"],
    legend_names=["Acid", "EDC", "Urea", "Anhydride","N-acylurea"],
    top_plot=[1, 2, 4],
    bottom_plot=[0, 3],
    sort_order=[1, 3, 4, 2, 0],
    int_eqn=[
            lambda cs, ks: ks[3]*cs[3], ],
    int_eqn_desc=[
            "k2*An", ],
    lifetime_conc=[3],
    rectime_conc=[0],
    )
```

10

Supporting Note 3. The synthesis of SO₃-Cₙ-G-OH
Scheme S2. Synthesis route of SO₃-C₁₄-G-OH and SO₃-C₁₆-G-OH in DMF
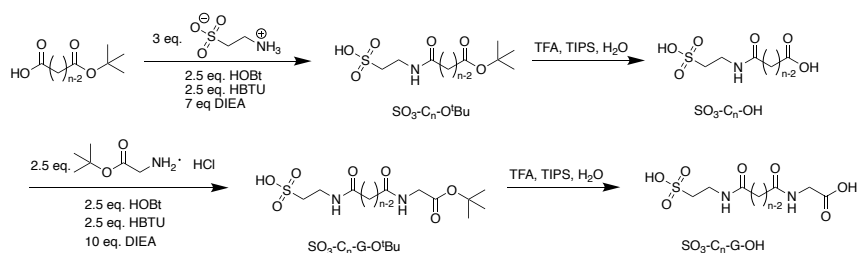
SO₃-C₁₄-G-OH: To a solution of 14-(tert-Butoxy)-14-oxotetradecanoic acid (500 mg, 1.59 mmol) in DMF (8 mL) was added HOBt (537.12 mg, 3.97 mmol), DIEA (1.44 g, 11.13 mmol) and HBTU (1.51 g, 3.97 mmol) under N_2 at room temperature with stirring for 5 mins. Then, taurine (596.93 mg, 4.77 mmol) was added, stirring the mixture overnight. DMF was removed under vacuum, and 30 mL MQ-water was added to dissolve the mixture. A small amount of HCl was added to adjust pH to neutral. Afterward, the solution was filtered with a PTFE filter and injected into a reversed-phase High-Performance Liquid Chromatography (RP-HPLC) with gradient elution from 2% to 98% acetonitrile with 0.1% TFA in MQ-water to get the product SO₃-C₁₄-O'Bu. After being lyophilized, a white powder of SO₃-C₁₄-O'Bu (548 mg, 1.3 mmol) was obtained. TFA (4.75 mL), TIPS (0.125 mL), and MQ-water (0.125 mL) were added to SO₃-C₁₄-O'Bu. After 1 hour of stirring, TFA was removed by co-distillation with diethyl ether under reduced pressure on rotary evaporation to get SO₃-C₁₄-OH (475 mg, 1.3 mmol). Then, SO₃-C₁₄-OH was dissolved in 8 mL DMF. HOBt (439.16 mg, 3.25 mmol), DIEA (1.68 g, 13 mmol) and HBTU (1.23 g, 3.25 mmol) were added under N_2 at room temperature with stirring for 5 mins. Glycine tert-butyl ester hydrochloride (544.81 mg, 3.25 mmol) was added, stirring the mixture overnight. DMF was removed under vacuum, and 30 mL MQ-water was added to dissolve the mixture. A small amount of HCl was added to adjust the pH to neutral and purification was conducted on RP-HPLC, followed by lyophilizing to get SO₃-C₁₄-G-O'Bu. Finally, TFA (4.75 mL), TIPS (0.125 mL), and MQ-water (0.125 mL) were added to SO₃-C₁₄-G-O'Bu for 1-hour stirring. After the removal of TFA, purification on RP-HPLC and lyophilizing were conducted to get pure SO₃-C₁₄-G-OH which was characterized by ¹H-NMR spectroscopy, HPLC, and Electron Spray Ionisation – Mass Spectrometry (ESI-MS).

SO₃-C₁₆-G-OH was synthesized in the same way as SO₃-C₁₄-G-OH and 16-(tert-Butoxy)-16-oxohexadecanoic acid was used in the first coupling step.
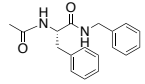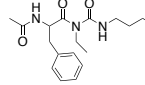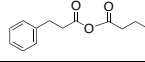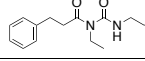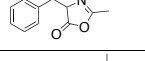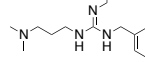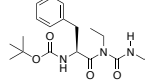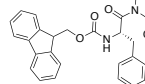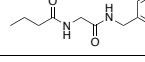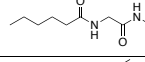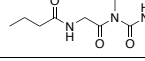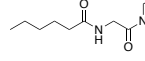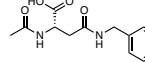
Scheme S3. Synthesis route of SO₃-C₁₂-G-OH in DMF
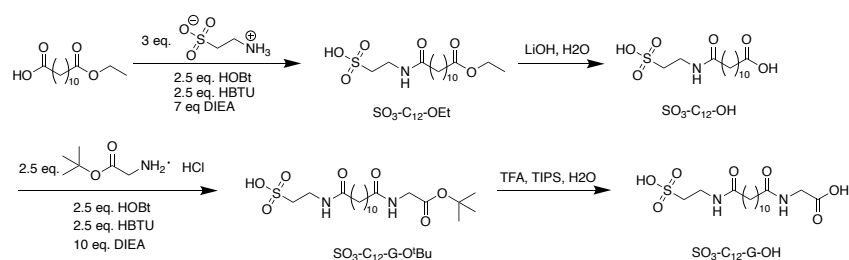
SO₃-C₁₂-G-OH: To a solution of monoethyl dodecanedioate (500 mg, 1.94 mmol) in DMF (8 mL) was added HOBt (653.77 mg, 4.84 mmol), DIEA (1.75g, 13.55 mmol) and HBTU (1.83 g, 4.84 mmol) under N_2 at room temperature with stirring for 5 mins. Then, taurine (726.56 mg, 5.81 mmol) was added, stirring the mixture overnight. DMF was removed under vacuum, and 30 mL MQ-water was added to dissolve the mixture. A small amount of HCl was added to adjust the pH to neutral. Afterward, the solution was filtered with a PTFE filter and injected into a reversed-phase High-Performance Liquid Chromatography (RP-HPLC) with gradient elution from 2% to 98% acetonitrile with 0.1% TFA in MQ-water to get the product SO₃-C₁₂-OEt. After being lyophilized, a white powder of SO₃-C₁₂-OEt was obtained. 1 M LiOH aqueous solution (10 mL) was added to SO₃-C₁₂-OEt. LC-MS was used to monitor the deprotection. After the deprotection was finished, HCl was added to adjust the pH to neutral, followed by purification on RP-HPLC and lyophilizing to get SO₃-C₁₂-OH (506 mg, 1.5 mmol). Then, SO₃-C₁₄-OH was dissolved in 8 mL DMF. HOBt (506.72 mg, 3.75 mmol), DIEA (1.94 g, 15 mmol), and HBTU (1.42 g, 3.75 mmol) were added under N_2 at room temperature with stirring for 5 mins. Glycine tert-butyl ester hydrochloride (628.62 mg, 3.75 mmol) was added, stirring the mixture overnight. DMF was removed under vacuum, and 30 mL MQ-water was added to dissolve the mixture. A small amount of HCl was added to adjust the pH to neutral and purification was conducted on RP-HPLC, followed by lyophilizing to get SO₃-C₁₂-G-O'Bu. Finally, TFA (4.75 mL), TIPS (0.125 mL), and MQ-water (0.125 mL) were added to SO₃-C₁₂-G-O'Bu for 1-hour stirring. After the removal of TFA, purification on RP-HPLC and lyophilizing were conducted to get pure SO₃-C₁₂-G-OH which was characterized by ¹H-NMR spectroscopy, HPLC, and Electron Spray Ionisation – Mass Spectrometry (ESI-MS).

11

SUPPORTING TABLES

Supporting Table S1. Mass information of all the products of Ac-F-OH, Phenylpropanoic acid, Boc-F-OH, Fmoc-F-OH, Ac-D-OH, C$_4$-G-OH, C$_6$-G-OH and 1-Benzyl-3-(3-(dimethyl amino) propyl)-2-ethyl guanidine (Guanidine).

Name	Structure	Exact Mass (gmol^{-1})	Mass found (gmol^{-1})
Ac-F-benzylamide		Mw = 296.15 C$_{18}$H$_{20}$N$_2$O$_2$	296.96 [Mw+H$^+$] 319.26 [Mw+Na$^+$]
Ac-F-N-acylurea	Two possible isomers (we only show one, same as below)	Mw = 362.23 C$_{19}$H$_{30}$N$_4$O$_3$	363.12 [Mw+H$^+$]
Phenylpropanoic acid-anhydride		Mw = 282.13 C$_{18}$H$_{18}$O$_3$	304.9 [Mw+Na$^+$]
Phenylpropanoic acid-N-acylurea		Mw = 305.21 C$_{17}$H$_{27}$N$_3$O$_2$	306.13 [Mw+H$^+$]
Ac-F-oxazolone		Mw = 189.08 C$_{11}$H$_{21}$NO$_2$	189.89 [Mw+H$^+$]
Guanidine		Mw = 262.22 C$_{15}$H$_{26}$N$_4$	263.04 [Mw+H$^+$]
Boc-F-N-acylurea		Mw = 420.27 C$_{22}$H$_{36}$N$_4$O$_4$	421.06 [Mw+H$^+$]
Fmoc-F-N-acylurea		Mw = 542.29 C$_{32}$H$_{38}$N$_4$O$_4$	543.12 [Mw+H$^+$]
C$_4$-G-benzylamide		Mw = 234.14 C$_{13}$H$_{18}$N$_2$O$_2$	235.48 [Mw+H$^+$]
C$_6$-G-benzylamide		Mw = 262.17 C$_{15}$H$_{22}$N$_2$O$_2$	263.57 [Mw+H$^+$] 285.44 [Mw+Na$^+$]
C$_4$-G-N-acylurea		Mw = 300.22 C$_{14}$H$_{28}$N$_4$O$_3$	301.08 [Mw+H$^+$]
C$_6$-G-N-acylurea		Mw = 328.25 C$_{16}$H$_{32}$N$_4$O$_3$	329.11 [Mw+H$^+$]
Ac-D-benzylamide		Mw = 264.11 C$_{13}$H$_{16}$N$_2$O$_4$	264.83 [Mw+H$^+$]
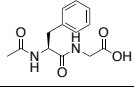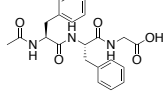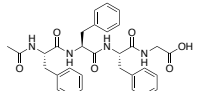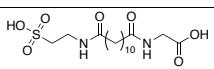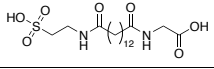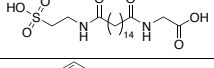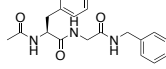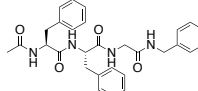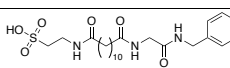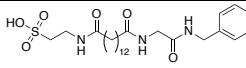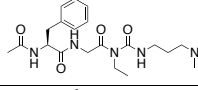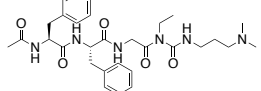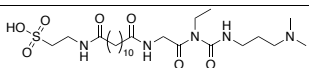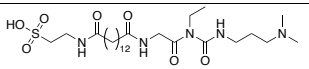
12

Supporting Table S2. Mass information of all the products of amino acids.

Name	Structure	Exact Mass (gmol^{-1})	Mass found (gmol^{-1})
Ac-L-benzylamide		Mw = 262.17 $C_{15}H_{22}N_2O_2$	262.82 [Mw+H$^+$] 285.08 [Mw+Na$^+$]
Ac-I-benzylamide		Mw = 262.17 $C_{15}H_{22}N_2O_2$	262.81 [Mw+H$^+$] 285.08 [Mw+Na$^+$]
Ac-G-benzylamide		Mw = 206.11 $C_{11}H_{14}N_2O_2$	206.85 [Mw+H$^+$] 228.99 [Mw+Na$^+$]
Ac-A-benzylamide		Mw = 220.12 $C_{12}H_{16}N_2O_2$	220.82 [Mw+H$^+$] 242.98 [Mw+Na$^+$]
Ac-V-benzylamide		Mw = 248.15 $C_{14}H_{20}N_2O_2$	248.79 [Mw+H$^+$] 271.06 [Mw+Na$^+$]
Ac-R-benzylamide		Mw = 305.19 $C_{15}H_{23}N_5O_2$	306.11 [Mw+H$^+$]
Ac-H-benzylamide		Mw = 286.14 $C_{15}H_{18}N_4O_2$	286.94 [Mw+H$^+$]
Ac-S-benzylamide		Mw = 236.12 $C_{12}H_{16}N_2O_3$	236.86 [Mw+H$^+$]
Ac-M-benzylamide		Mw = 280.12 $C_{14}H_{20}N_2O_2S$	280.89 [Mw+H$^+$]
Ac-G-N-acylurea		Mw = 272.18 $C_{12}H_{24}N_4O_3$	272.98 [Mw+H$^+$]
Ac-A-N-acylurea		Mw = 286.2 $C_{13}H_{26}N_4O_3$	286.98 [Mw+H$^+$]
Ac-V-N-acylurea		Mw = 314.23 $C_{15}H_{30}N_4O_3$	315.04 [Mw+H$^+$]
Ac-L-N-acylurea		Mw = 328.25 $C_{16}H_{32}N_4O_3$	329.17 [Mw+H$^+$]
Ac-I-N-acylurea		Mw = 328.25 $C_{16}H_{32}N_4O_3$	329.28 [Mw+H$^+$]
Ac-R-N-acylurea		Mw = 371.26 $C_{16}H_{33}N_7O_3$	372.09 [Mw+H$^+$]
Ac-H-N-acylurea		Mw = 352.2 $C_{16}H_{28}N_6O_3$	352.80 [Mw+H$^+$]
Ac-S-N-acylurea		Mw = 302.2 $C_{13}H_{26}N_4O_4$	303.03 [Mw+H$^+$]
Ac-M-N-acylurea		Mw = 346.2 $C_{15}H_{30}N_4O_3S$	347.04 [Mw+H$^+$]

13

Supporting Table S3. Mass information of the synthesized peptides and all their products in the reaction cycle quenched by benzylamine.

| Name	Structure	Exact Mass (gmol^{-1})	Mass found (gmol^{-1})
Ac-FG-OH		Mw = 264.11 $C_{13}H_{16}N_2O_4$	264.78 $[Mw+H^+]$ 287.08 $[Mw+Na^+]$
Ac-F$_2$G-OH		Mw = 411.48 $C_{22}H_{25}N_3O_5$	412.09 $[Mw+H^+]$ 434.38 $[Mw+Na^+]$
Ac-F$_3$G-OH		Mw = 558.25 $C_{31}H_{34}N_4O_6$	559.13 $[Mw+H^+]$ 1117.10 $[2Mw+H^+]$
SO$_3$-C$_{12}$-G-OH		Mw = 394.18 $C_{16}H_{30}N_2O_7S$	395.80 $[Mw+H^+]$
SO$_3$-C$_{14}$-G-OH		Mw = 422.21 $C_{18}H_{34}N_2O_7S$	423.56 $[Mw+H^+]$
SO$_3$-C$_{16}$-G-OH		Mw = 450.24 $C_{20}H_{38}N_2O_7S$	451.17 $[Mw+H^+]$
Ac-FG-benzylamide		Mw = 353.17 $C_{20}H_{23}N_3O_3$	353.79 $[Mw+H^+]$ 376.18 $[Mw+Na^+]$
Ac- F$_2$G – benzylamide		Mw = 500.24 $C_{29}H_{32}N_4O_4$	500.94 $[Mw+H^+]$ 523.37 $[Mw+Na^+]$
SO$_3$-C$_{12}$-G-benzylamide		Mw = 483.24 $C_{23}H_{37}N_3O_6S$	484.81 $[Mw+H^+]$
SO$_3$-C$_{14}$-G-benzylamide		Mw = 511.27 $C_{25}H_{41}N_3O_6S$	512.97 $[Mw+H^+]$
Ac-FG-N-acylurea		Mw = 419.25 $C_{21}H_{33}N_5O_4$	419.85 $[Mw+H^+]$ 441.79 $[Mw+Na^+]$
Ac- F$_2$G-N-acylurea		Mw = 566.32 $C_{30}H_{42}N_6O_5$	567.19 $[Mw+H^+]$ 589.14 $[Mw+Na^+]$
SO$_3$-C$_{12}$-G-N-acylurea		Mw = 549.32 $C_{24}H_{47}N_5O_7S$	550.22 $[Mw+H^+]$ 572.06 $[Mw+Na^+]$
SO$_3$-C$_{14}$-G-N-acylurea		Mw = 577.35 $C_{26}H_{51}N_5O_7S$	578.53 $[Mw+H^+]$ 600.30 $[Mw+Na^+]$

14
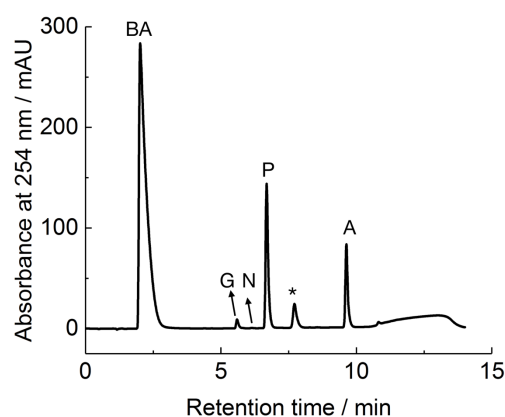
Figure S1. An example of HPLC chromatogram of the entire reaction network with benzylamine quenching measured at 254 nm, 30 min after 45 mM EDC added to 100 mM Ac-F-OH in MES buffer (200 mM, pH 6), injection volume: 1 μL. Representation: BA for benzylamine, G for guanidine, N for N-acylurea, P for precursor, A for benzylamide and * for the impurity from benzylamine solution.

We integrated peaks of guanidine, N-acylurea, precursor and benzylamide to calculate the concentration of EDC, N-acylurea, precursor and oxazolone to get the kinetics profile of each precursor. For the rest precursors, we summarized their information of HPLC chromatograms into a table (see below). The corresponding HPLC methods can be found in "**Materials and methods**".

Supporting Table S4. Retention time of all the compounds in the reaction cycle.

Precursor Retention time / min	precursor (P) (1 uL Calibration value / (a.u.) (mM)$^{-1}$)	Guanidine (G)	N-acylurea (N)	Benzylamide (A)
Ac-F-OH	6.68 (0.39 at 254 nm)	5.51	6.12	9.61
Ac-G-OH	1.133 (0.36 at 220 nm)	6.50	-	6.10
Ac-A-OH	1.442 (0.61 at 220 nm)	6.86	-	7.32
Ac-V-OH	8.99 (0.82 at 220 nm)	12.96	-	16.76
Ac-I-OH	17.042 (0.3035 at 220 nm)	16.534	17.375	26.78
Ac-L-OH	12.56 (0.73 at 220 nm)	12.25	12.07	16.92
Ac-R-OH	6.067 (0.2563 at 220 nm)	19.974	-	20.588
Ac-H-OH	8.4318 (0.2563 at 220 nm)	16.434	-	15.550
Ac-S-OH	1.151 (0.449 at 220 nm)	7.238	-	7.772
Ac-M-OH	6.388 (2.4004 at 220 nm)	9.284	-	13.309
Ac-D-OH	1.180 (0.6271 at 220 nm)	14.051	-	12.851, 13.601
Boc-F-OH	7.95 (0.36 at 254 nm)	-	7.41	-
Fmoc-F-OH	9.54 (1.13 at 254 nm)	-	8.721	-
Ac-FG-OH	6.22 (0.27 at 254 nm)	5.89	7.22	9.62
Ac-F$_2$G-OH	14.18 (0.73 at 254 nm)	7.42	15.78	21.03
C$_4$-G-OH	2.45 (0.42 at 220 nm)	14.56	12.84, 14.38	18.19
C$_6$-G-OH	8.93 (0.41 at 220 nm)	8.18	10.00, 10.48	12.39
SO$_3$-C$_{12}$-G-OH	11.78 (0.77 at 220 nm)	7.32	13.80, 14.67	16.81
SO$_3$-C$_{14}$-G-OH	16.33 (0.76 at 220 nm)	7.33	17.61, 18.38	20.46

15

Supporting Table S5. Rate constants used in the kinetic model for phenylpropionic acid which forms an intermolecular anhydride in MES buffer (200 mM, pH 6) with EDC at 21 °C.

	k_0 [min^{-1}]	k_1 [mM^{-1}min^{-1}]	k_2 [mM^{-1}min^{-1}]	k_3 [min^{-1}]	k_4 [min^{-1}]	k_5 [min^{-1}]	Half-life of anhydride / min (calculated by $\ln(2)/k_4$
order	1	2	2	1	1	1	
Phenylpropanoic acid	1.8×10^{-4}	9.09×10^{-4}	1.29×10^{1}	8.34×10^{-10}	3.84×10^{-3}	2.77×10^{2}	180

Supporting Table S6. Rate constants used in the kinetic model for Ac-D-OH which forms an intramolecular anhydride in MES buffer (200 mM, pH 6) with EDC at 21 °C. No N-acylurea was formed.

	k_0 [min^{-1}]	k_1 [mM^{-1}min^{-1}]	$K = k_3 / k_2$	k_4 [min^{-1}]	Half-life of anhydride / min (calculated by $\ln(2)/k_4$
order	1	2	-	1	
Ac-D-OH	1.8×10^{-4}	4.79×10^{-3}	9.03×10^{-17}	8.38×10^{-1}	0.827

Supporting Table S7. Rate constants used in the kinetic model of Ac-F-OH which forms an oxazolone in MES buffer (200 mM) with EDC at different temperatures and pH.

Ac-F-OH	k_0 [min^{-1}]	k_1 [mM^{-1}min^{-1}]	k_2 [min^{-1}]	k_3 [min^{-1}]	k_4 [min^{-1}]	k_5 [min^{-1}]	Half-life of oxazolone / min (calculated by $\ln(2)/k_4$
order	1	2	1	1	1	1	
pH 6, 21°C	1.8×10^{-4}	7.56×10^{-4}	1.54×10^{1}	1.27×10^{0}	9.77×10^{-3}	2.5×10^{-1}	71
pH 6, 30°C	6.9×10^{-4}	9.35×10^{-4}	4.33×10^{1}	1.59×10^{0}	1.69×10^{-2}	9×10^{-1}	41
pH 6, 35°C	1.27×10^{-3}	1.29×10^{-3}	2.23×10^{1}	6.88×10^{-1}	2.46×10^{-2}	4.37×10^{-1}	28
pH 5, 21°C	1.58×10^{-3}	2.19×10^{-3}	3.19×10^{1}	3.18×10^{-18}	1.13×10^{-2}	2.52×10^{-1}	61
pH 7, 21°C	6.96×10^{-5}	5.95×10^{-5}	8.56×10^{1}	1.03×10^{-9}	2.29×10^{-2}	6.45×10^{0}	30

Supporting Table S8. Rate constants used in the kinetic model for amino acids which form oxazolones in MES buffer (200 mM, pH 6) with EDC at 21 °C. The formation of N-acylurea is negligible.

	k_0 [min^{-1}]	k_1 [mM^{-1}min^{-1}]	$K = k_3 / k_2$	k_4 [min^{-1}]	Half-life of oxazolone / min (calculated by $\ln(2)/k_4$
order	1	2	-	1	
Ac-G-OH	1.8×10^{-4}	3.55×10^{-4}	1.75×10^{-17}	1.55×10^{-2}	45
Ac-H-OH	1.8×10^{-4}	3.92×10^{-4}	1.17×10^{-10}	7.02×10^{-2}	10
Ac-R-OH	1.8×10^{-4}	3.18×10^{-4}	8.67×10^{-1}	3.49×10^{-2}	20
Ac-A-OH	1.8×10^{-4}	6.14×10^{-4}	8.3×10^{-3}	2.14×10^{-2}	32
Ac-S-OH	1.8×10^{-4}	2.14×10^{-3}	1.78×10^{-1}	1.92×10^{-2}	36
Ac-M-OH	1.8×10^{-4}	5.29×10^{-4}	8.76×10^{-19}	1.23×10^{-2}	56
Ac-V-OH	1.8×10^{-4}	7.87×10^{-4}	1.62×10^{-1}	3.67×10^{-3}	189

16

Supporting Table S9. Rate constants used in the kinetic model of precursors which form oxazolones in MES buffer (200 mM, pH 6) with EDC at 21 ºC. *

|	k_0 [min^{-1}]	k_1 [mM^{-1}min^{-1}]	k_2 [min^{-1}]	k_3 [min^{-1}]	k_4 [min^{-1}]	k_5 [min^{-1}]	Half-life of oxazolone / min (calculated by ln(2)/k_4
order	1	2	1	1	1	1	
Ac-L-OH	1.8×10^{-4}	1.12×10^{-3}	1.67×10^{1}	9.68×10^{-1}	9.45×10^{-3}	1.65×10^{0}	73
Ac-I-OH	1.8×10^{-4}	1.29×10^{-3}	3.87×10^{1}	5.57×10^{-15}	1.87×10^{-3}	1.99×10^{1}	371
Ac-FG-OH	1.8×10^{-4}	7.43×10^{-4}	9.53×10^{1}	7.58×10^{0}	3.77×10^{-2}	2.8×10^{1}	18
Ac-FG-OH With pyridine	1.8×10^{-4}	1.05×10^{-3}	3.62×10^{1}	7.8×10^{-32}	7.55×10^{-2}	1.21×10^{0}	9
Ac-F$_2$G-OH	1.8×10^{-4}	7.43×10^{-4}	2.7×10^{0}	4.52×10^{-20}	2.33×10^{-2}	1.02×10^{0}	30
Ac-F$_2$G-OH With pyridine at pH 5	1.58×10^{-3}	5.57×10^{-3}	1.66×10^{1}	2.77×10^{1}	3.35×10^{-2}	3.40×10^{-1}	21
C$_4$-G-OH	1.8×10^{-4}	2.41×10^{-4}	1.26×10^{1}	1.56×10^{0}	1.86×10^{-2}	1.54×10^{0}	37
C$_6$-G-OH	1.8×10^{-4}	2.35×10^{-4}	1.25×10^{1}	9.09×10^{-1}	1.91×10^{-2}	2.09×10^{0}	36
SO$_3$-C$_{12}$-G-OH	1.8×10^{-4}	5.40×10^{-4}	1.05×10^{3}	1.57×10^{-12}	1.24×10^{-2}	1.42×10^{-10}	56
SO$_3$-C$_{14}$-G-OH	1.8×10^{-4}	6.24×10^{-4}	3.06×10^{3}	7.14×10^{-16}	8×10^{-3}	3.23×10^{-23}	87

17

SUPPORTING FIGURES
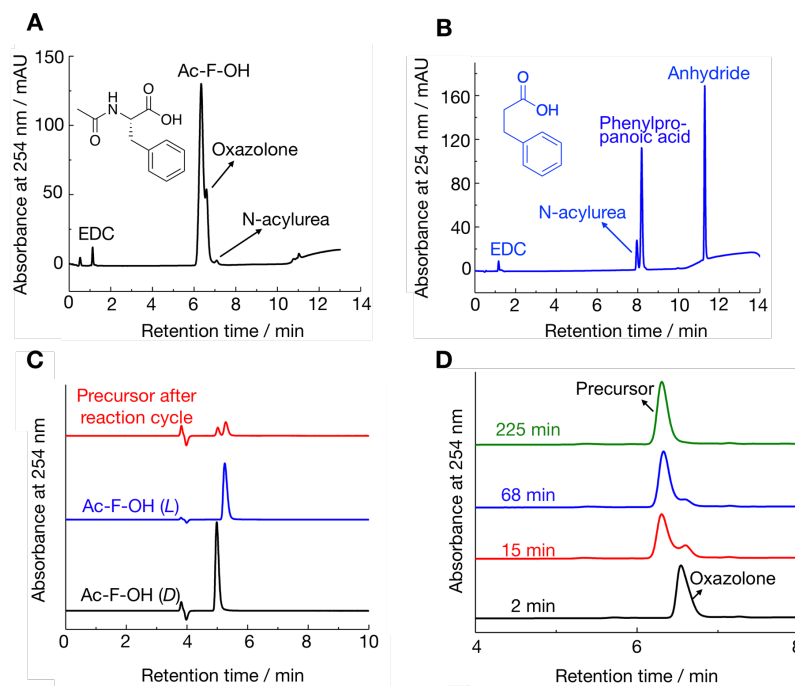
Figure S2. The formation of the oxazolone. Examples of HPLC chromatograms of the entire reaction network measured at 254 nm, 30 min after 45 mM EDC was added to 100 mM precursor in MES buffer (200 mM, pH 6), injection volume: 1 µL. **A)** Ac-F-OH and **B)** phenylpropanoic acid as precursors without benzylamine quenching; **C)** Chiral analysis of the precursor (Ac-F-OH) after a reaction cycle of 100 mM Ac-F-OH with 60 mM EDC at pH 6; **D)** Hydrolysis of synthesized oxazolone.
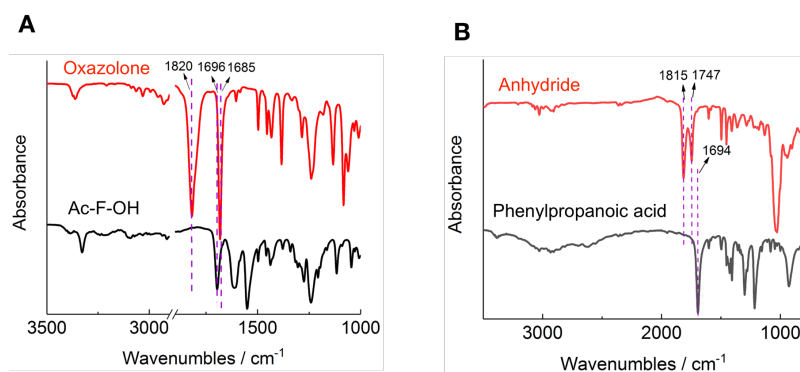

Figure S3. FT-IR spectra. A) Ac-F-OH and its corresponding oxazolone. 1820 and 1685 cm^{-1} are attributed to the C=O and C=N of the oxazolone, respectively. 1696 cm^{-1} is attributed to the C=O of the acid. B) Phenylpropanoic acid and its corresponding symmetric anhydride. 1815 and 1747 cm^{-1} are attributed to the O=C-O-C=O of the anhydride. 1694 cm^{-1} is attributed to the C=O of the acid.
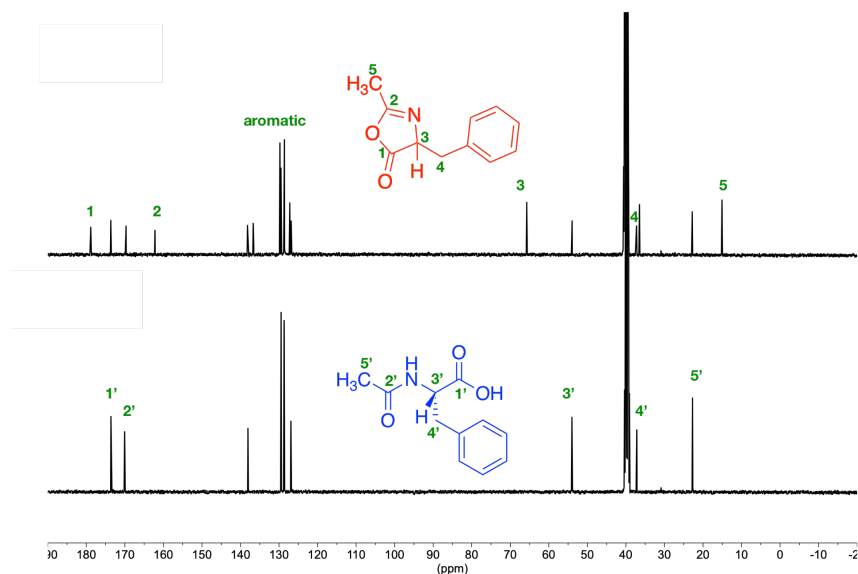
18
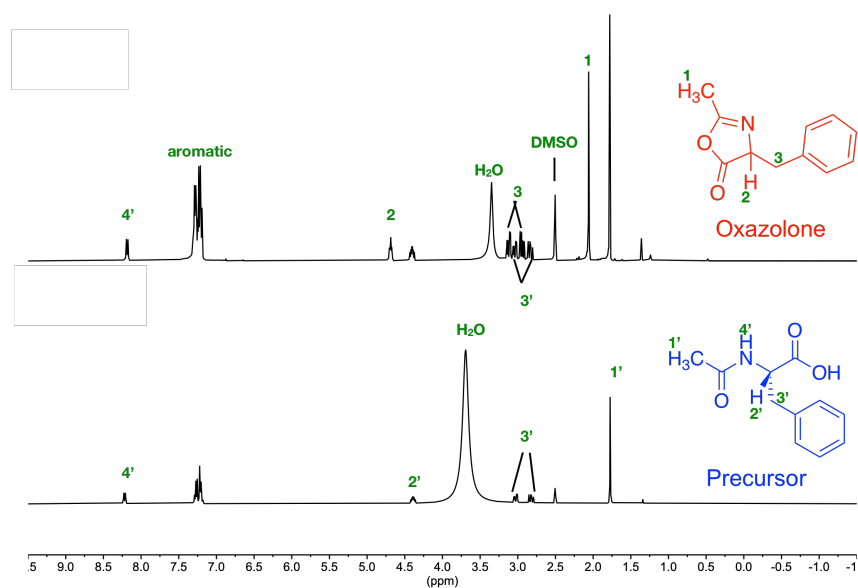
Figure S4. ¹H NMR spectra (400 MHz, DMSO-d₆) of the synthesized oxazolone of Ac-F-OH (top) and its product (Ac-F-OH) after hydrolysis (bottom).

Oxazolone: δ 7.34 – 7.17 (m, 5H), 4.69 (tt, *J* = 5.1, 2.3 Hz, 1H), 3.12 (dd, *J* = 14.0, 5.1 Hz, 1H), 2.94 (dd, *J* = 14.1, 7.6 Hz, 1H), 2.06 (d, *J* = 2.1 Hz, 3H). **Ac-F-OH:** δ 8.18 (d, *J* = 8.1 Hz, 1H), 7.34 – 7.17 (m, 5H), 4.40 (ddd, *J* = 9.5, 8.0, 4.9 Hz, 1H), 3.04 (dd, *J* = 13.8, 4.9 Hz, 1H), 2.83 (dd, *J* = 13.8, 9.6 Hz, 1H), 1.78 (s, 3H).

Figure S5. ¹³C NMR spectra (400 MHz, DMSO-d₆) of the synthesized oxazolone of Ac-F-OH (top) and its product (Ac-F-OH) after hydrolysis (bottom).

Oxazolone: δ 178.84, 162.19, 136.69, 129.77, 128.60, 127.20, 65.72, 37.23, 15.07. **Ac-F-OH:** δ 173.61, 170.06, 138.06, 129.47, 128.68, 126.92, 54.00, 37.18, 22.71.

19

92
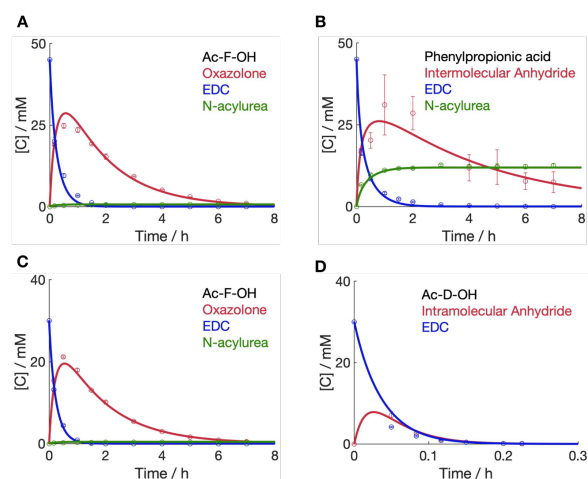
Figure S6. Kinetic profiles in MES buffer (200 mM, pH 6) at 21°C. **A)** 100 mM Ac-F-OH fueled with 45 mM EDC, 91 ± 1 % and 2 ± 1 % of the fuel are converted to form oxazolone and N-acylurea, respectively. **B)** 100 mM Phenylpropanoic acid fueled with 45 mM EDC, 73 ± 1 % and 26 ± 1 % of the fuel are converted to form intermolecular anhydride and N-acylurea, respectively. **C)** 100 mM Ac-F-OH fueled with 30 mM EDC, 91 ± 1 % and 2 ± 1 % of the fuel are converted to form oxazolone and N-acylurea, respectively. **D)** 100 mM Ac-D-OH fueled with 30 mM EDC, 99 ± 1 % of the fuel is converted to form intramolecular anhydride, and no N-acylurea is formed. HPLC (markers), and the kinetic model (lines). Error bars represent the standard deviation of the average (n = 3).
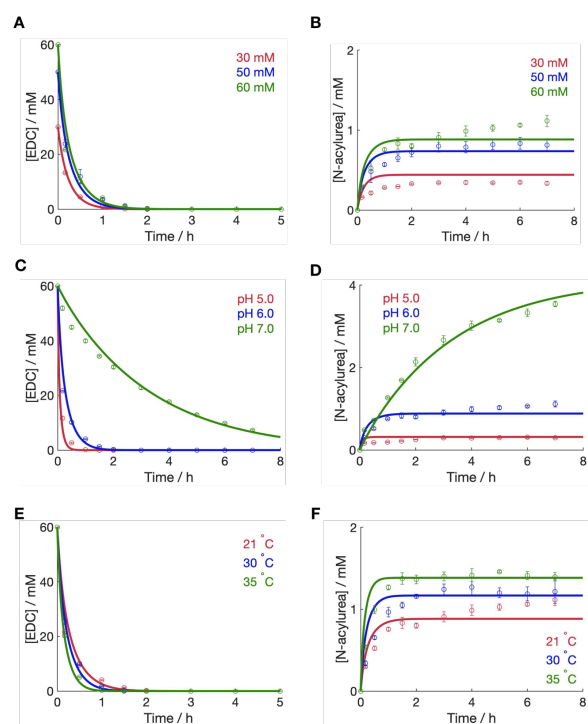
Figure S7. Robustness of the oxazolone formation cycle. The EDC consumption profiles and the N-acylurea concentration profiles of fueling 100 mM Ac-F-OH in 200 mM MES buffer with **A-B**) different fuel concentrations at pH 6 at 21°C, **C-D**) 60 mM EDC at different pH at 21 °C, and **E-F**) 60 mM EDC at different temperatures at pH 6. HPLC (markers) and the kinetic model (lines). Error bars represent the standard deviation of the mean value (n = 3).
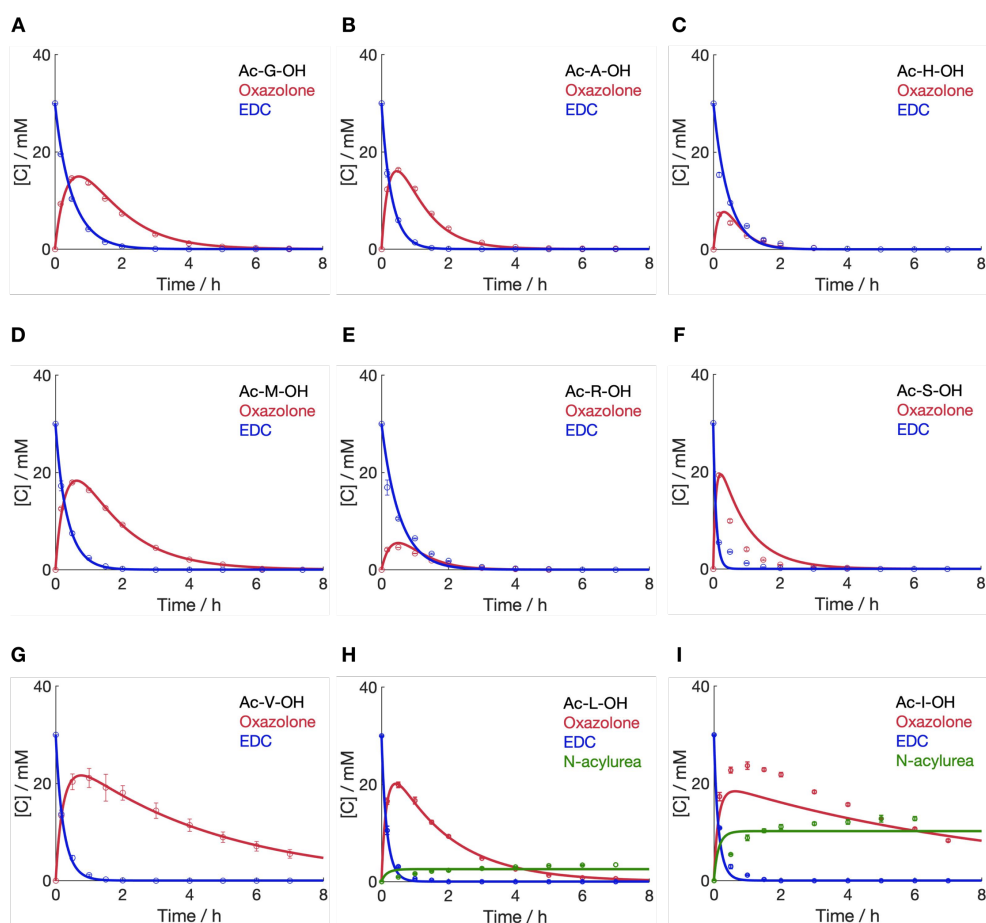
20

Figure S8. Kinetic profiles of 100 mM precursor based on N-acetyl-protected amino acids in MES buffer (200 mM, pH 6) fueled with 30 mM EDC at 21°C. For Ac-G-OH, Ac-A-OH, Ac-V-OH, Ac-R-OH, Ac-H-OH, Ac-S-OH, and Ac-M-OH, the formation of N-acylurea was too little to integrate on HPLC, and we assume the values are less than 1 %. HPLC (markers) and the kinetic model (lines). Error bars represent the standard deviation of the average (n = 3).
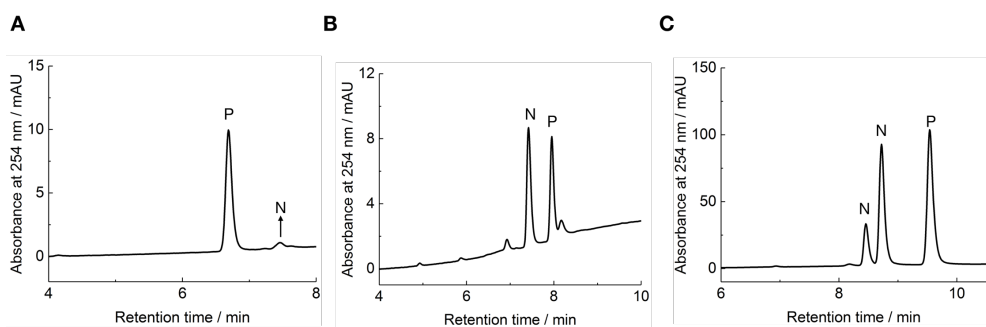

Figure S9. Examples of HPLC chromatograms of the entire reaction network 64 h after 0.6 mM EDC was added to 0.6 mM precursors in MES buffer (200 mM, pH 6) at 21°C. **A**) Ac-F-OH; **B**) Boc-F-OH; **C**) Fmoc-F-OH.

21

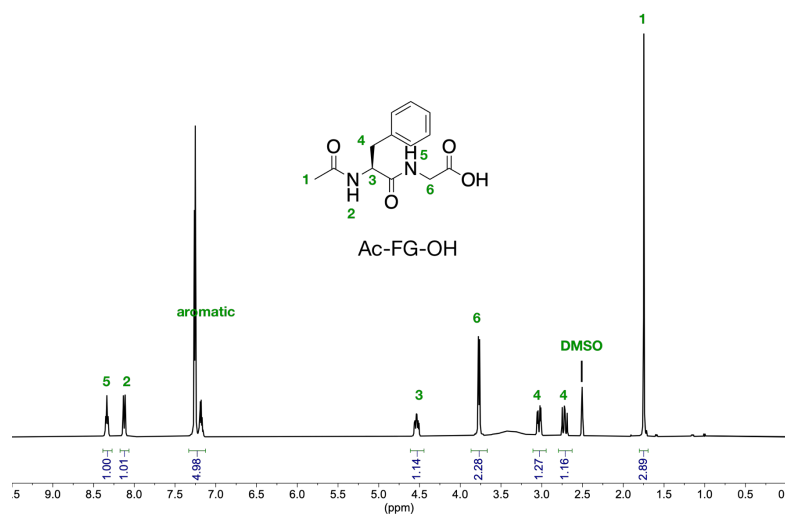**Figure S10. ¹H NMR spectrum (500 MHz, DMSO-d₆) of the synthesized peptide Ac-FG-OH.** δ 8.34 (t, J = 5.9 Hz, 1H), 8.12 (d, J = 8.6 Hz, 1H), 7.33 – 7.12 (m, 5H), 4.54 (ddd, J = 10.2, 8.6, 4.2 Hz, 1H), 3.77 (d, J = 5.8 Hz, 2H), 3.03 (dd, J = 13.8, 4.2 Hz, 1H), 2.72 (dd, J = 13.8, 10.3 Hz, 1H), 1.75 (s, 3H).
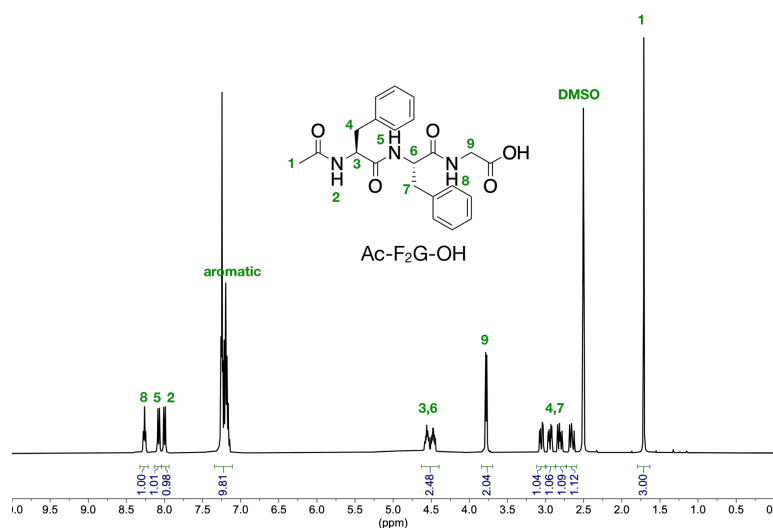

Figure S11. ¹H NMR spectrum (500 MHz, DMSO-d₆) of the synthesized peptide Ac-F₂G-OH. δ 8.26 (t, J = 5.8 Hz, 1H), 8.08 (d, J = 8.3 Hz, 1H), 8.00 (d, J = 8.4 Hz, 1H), 7.34 – 7.11 (m, 10H), 3.78 (d, J = 5.8 Hz, 2H), 3.06 (dd, J = 13.9, 4.5 Hz, 1H), 2.94 (dd, J = 13.9, 4.3 Hz, 1H), 2.81 (dd, J = 13.9, 9.3 Hz, 1H), 2.65 (dd, J = 13.9, 10.0 Hz, 1H), 1.71 (s, 3H).
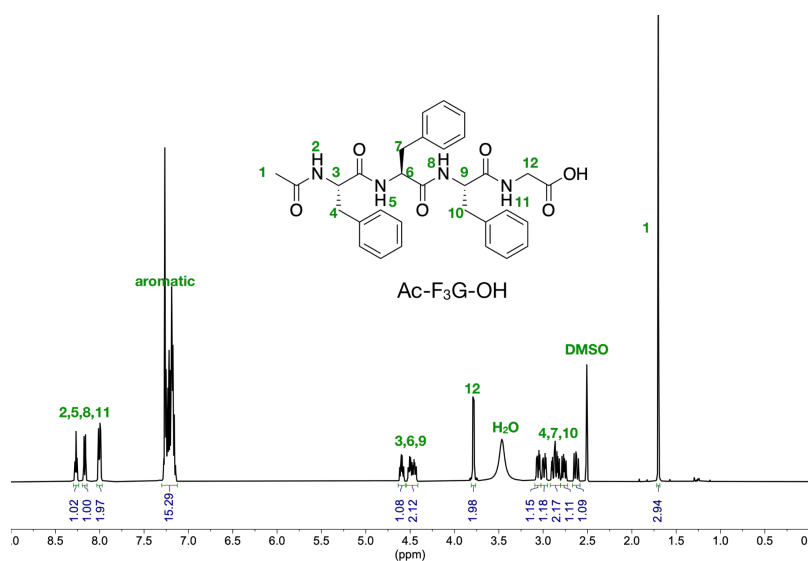
22

Figure S12. ¹H NMR spectrum (500 MHz, DMSO-d₆) of the synthesized peptide Ac-F₃G-OH. δ 8.27 (t, J = 5.9 Hz, 1H), 8.17 (d, J = 8.3 Hz, 1H), 8.00 (dd, J = 8.4, 4.1 Hz, 2H), 7.30 – 7.12 (m, 15H), 4.59 (td, J = 8.8, 4.8 Hz, 1H), 4.54 – 4.41 (m, 2H), 3.79 (dd, J = 5.7, 1.3 Hz, 2H), 3.06 (dd, J = 14.0, 4.7 Hz, 1H), 2.99 (dd, J = 14.0, 4.6 Hz, 1H), 2.92 – 2.80 (m, 2H), 2.76 (dd, J = 14.0, 9.1 Hz, 1H), 2.63 (dd, J = 13.9, 10.3 Hz, 1H), 1.70 (s, 3H).
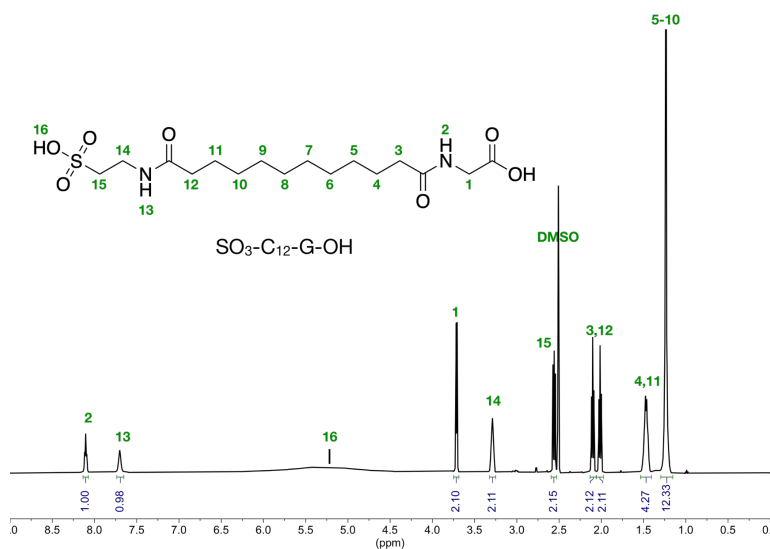

Figure S13. ¹H NMR spectrum (500 MHz, DMSO-d₆) of the synthesized SO₃-C₁₂-G-OH. δ 8.10 (t, J = 6.0 Hz, 1H), 7.70 (s, 1H), 3.71 (d, J = 5.7 Hz, 2H), 3.32 – 3.25 (m, 2H), 2.59 – 2.53 (m, 2H), 2.10 (t, J = 7.4 Hz, 2H), 2.01 (t, J = 7.5 Hz, 2H), 1.47 (dt, J = 14.6, 7.3 Hz, 4H), 1.24 (d, J = 3.5 Hz, 12H).

23
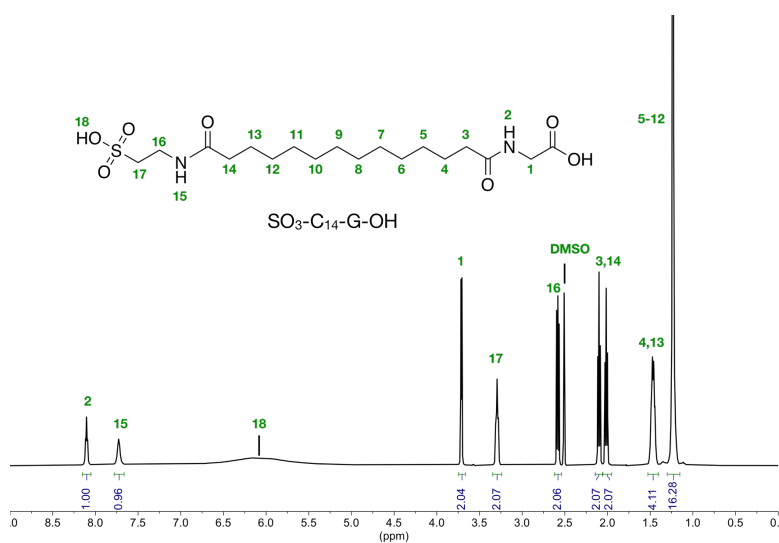
Figure S14. ¹H NMR spectrum (500 MHz, DMSO-d₆) of the synthesized SO₃-C₁₄-G-OH. δ 8.10 (t, J = 5.9 Hz, 1H), 7.73 (s, 1H), 3.71 (d, J = 5.5 Hz, 2H), 3.28 (s, 2H), 2.62 – 2.54 (m, 2H), 2.10 (t, J = 7.4 Hz, 2H), 2.02 (t, J = 7.5 Hz, 2H), 1.53 – 1.40 (m, 4H), 1.23 (s, 16H).
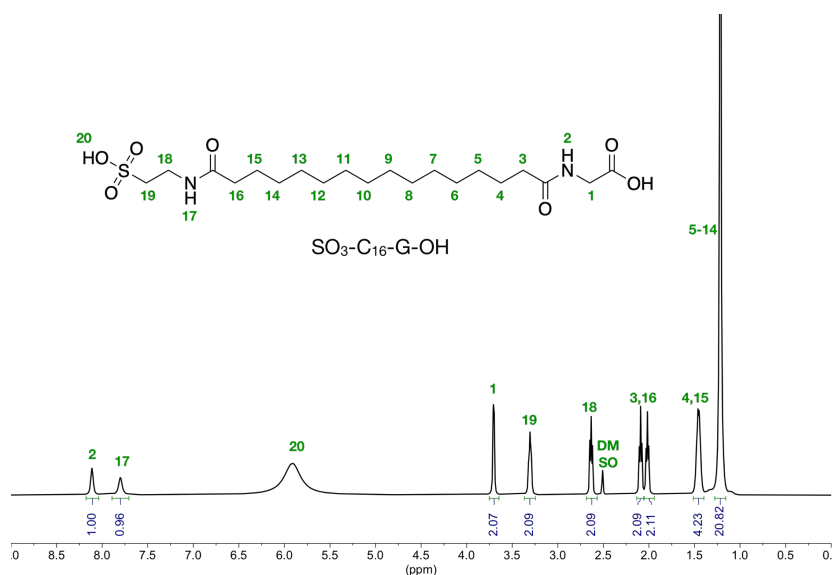
Figure S15. ¹H NMR spectrum (500 MHz, DMSO-d₆) of the synthesized SO₃-C₁₆-G-OH. δ 8.11 (t, J = 5.9 Hz, 1H), 7.80 (s, 1H), 3.70 (d, J = 4.4 Hz, 2H), 3.30 (d, J = 14.5 Hz, 2H), 2.63 (t, J = 7.4 Hz, 2H), 2.09 (t, J = 7.4 Hz, 2H), 2.02 (t, J = 7.5 Hz, 2H), 1.46 (h, J = 7.0 Hz, 4H), 1.22 (s, 20H).
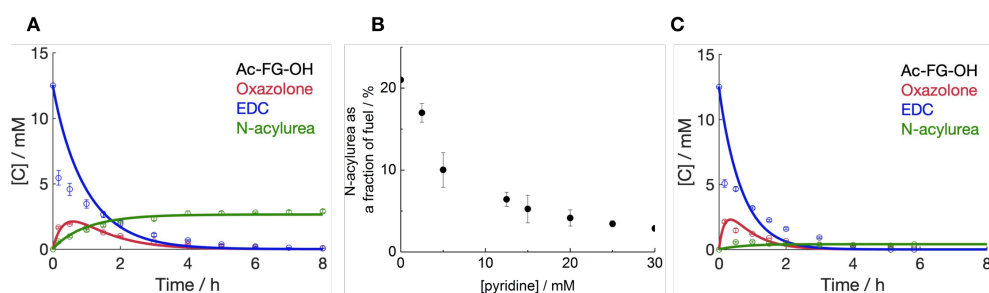
24

Figure S16. Kinetic profiles of Ac-FG-OH in response to EDC. A) 25 mM Ac-FG-OH in MES buffer (200 mM, pH 6) fueled with 12.5 mM EDC without pyridine at 21 °C. 72 ± 1 % and 21 ± 1 % of the fuel are converted to form oxazolone and N-acylurea, respectively. **B**) The influence of pyridine on the formation of N-acylurea with 25 mM Ac-FG-OH fueled with 12.5 mM EDC in MES buffer (200 mM, pH 6) at 21 °C; **C**) 25 mM Ac-FG-OH in MES buffer (200 mM, pH 6) with 20 mM pyridine fueled with 12.5 mM EDC at 21 °C. 96 ± 1 % and 4 ± 1 % of the fuel are converted to form oxazolone and N-acylurea, respectively. HPLC (markers) and the kinetic model (lines). Error bars represent the standard deviation of the mean value (n = 3).
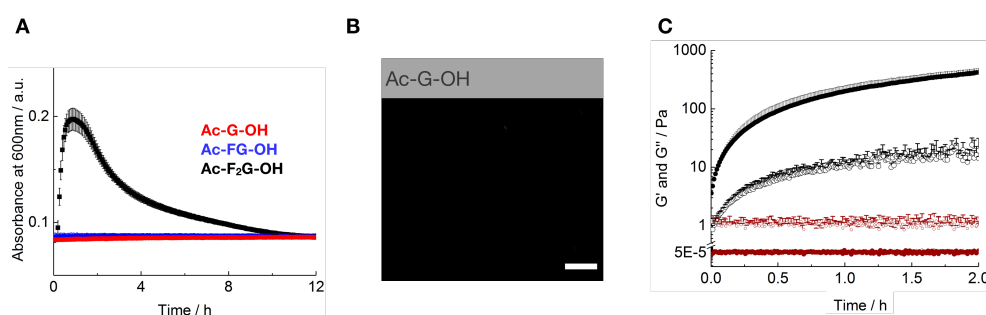
Figure S17. Self-assembly behavior of Ac-F$_n$G-OH. A) Absorbance at 600 nm as a measure of turbidity of 30 mM precursor in MES buffer (200 mM, pH 5) fueled with 80 mM EDC in the presence of 15 mM pyridine at 21 °C; Ac-G-OH and Ac-FG-OH show no turbidity while Ac-F$_2$G-OH shows transient turbidity. **B**) Confocal micrograph of a solution of 30 mM Ac-G-OH, 60 min after the addition of 80 mM EDC in the presence of 2.5 μM Nile Red and 15 mM pyridine at pH 5 at 21 °C. The scale bar responds to 10 μm; **C**) Storage and loss modulus as a function of time, measured by plate–plate rheology of 30 mM Ac-F$_2$G-OH with 50 mM EDC and 15 mM pyridine (dark red) and 4 mM Ac-F$_3$G-OH without fuel and pyridine (black) at pH 5 at 21 °C. No gel was formed under this condition for Ac-F$_2$G-OH and a stable gel was formed for Ac-F$_3$G-OH. Solid circles represent the storage modulus (G′); empty circles represent the loss modulus (G″). The error bars represent the standard deviation of the mean value (n = 3).
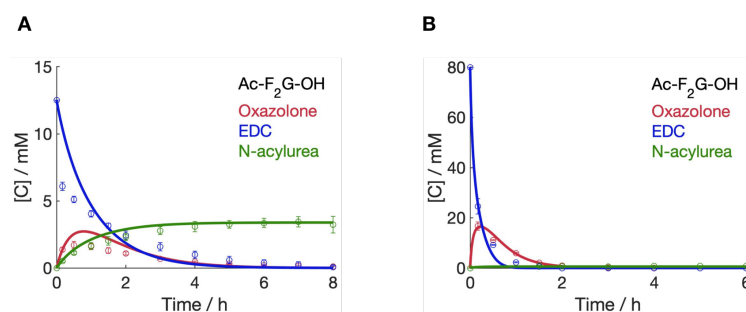
Figure S18. Kinetic profiles of Ac-F$_2$G-OH in response to EDC. A) 25 mM Ac-F$_2$G-OH in MES buffer (200 mM, pH 6) fueled with 12.5 mM EDC at 21 °C; 71 ± 1 % and 27 ± 1 % of the fuel are converted to form oxazolone and N-acylurea, respectively. **B**) 30 mM Ac-F$_2$G-OH in MES buffer (200 mM, pH 5) fueled with 80 mM EDC in the presence of 15 mM pyridine at 21 °C. 37 ± 1 % and less than 1 % of the fuel are converted to form oxazolone and N-acylurea, respectively. HPLC (markers) and the kinetic model (lines). Error bars represent the standard deviation of the mean value (n = 3).

25

Figure S19. Kinetic profiles of 200 mM precursor in response to 100 mM EDC with 10 mM pyridine in MES buffer (200 mM, pH 6) at 21 ºC. A) C_4-G-OH, 80 ± 1 % and 10 ± 1 % of the fuel are converted to form oxazolone and N-acylurea, respectively. **B)** C_6-G-OH, 80 ± 1 % and 13 ± 1 % of the fuel are converted to form oxazolone and N-acylurea, respectively. HPLC (markers) and the kinetic model (lines). Error bars represent the standard deviation of the mean value (n = 3).
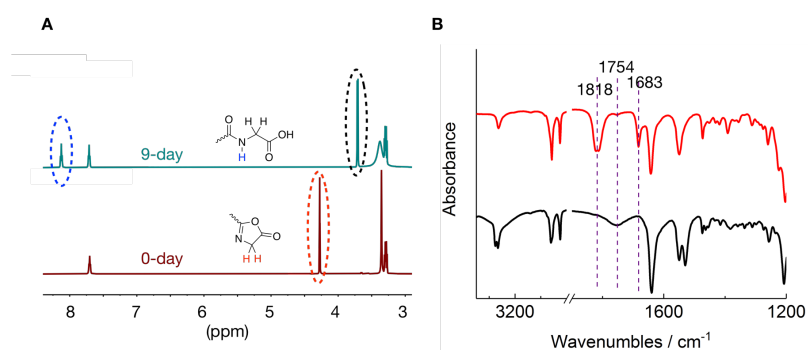
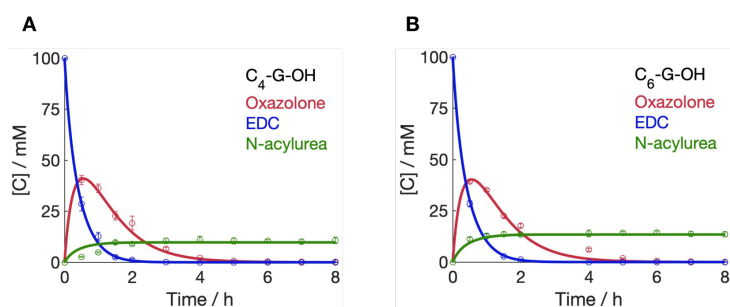**Figure S20. Characterization of the crystals separated from the cycle when 30 mM SO$_3$-C$_{14}$-G-OH was fueled with 30 mM EDC at pH 6 at 21 ºC. A)** ^{1}H NMR spectra (500 MHz, DMSO-d$_6$) of the crystals (oxazolone, bottom) and the acid (top) after oxazolone hydrolysis. Oxazolone was hydrolyzed back to acid after 9 days in the NMR tube. **B)** FT-IR of the oxazolone and the precursor of SO$_3$-C$_{14}$-G-OH. 1818 and 1683 cm^{-1} are attributed to the C=O and C=N of the oxazolone, respectively. 1754 cm^{-1} is attributed to the C=O of the acid.
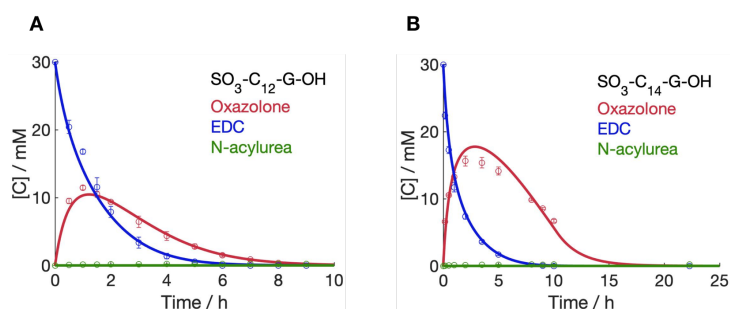
Figure S21. Kinetic profiles of 30 mM precursor in response to 30 mM EDC in MES buffer (200 mM, pH 6) at 21 ºC. A) SO$_3$-C$_{12}$-G-OH, 98 ± 1 % and 1 ± 0.5 % of the fuel are converted to form oxazolone and N-acylurea, respectively. **B)** SO$_3$-C$_{14}$-G-OH, 98 ± 1 % and 1 ± 0.5 % of the fuel are converted to form oxazolone and N-acylurea, respectively. HPLC (markers) and the kinetic model (lines). Error bars represent the standard deviation of the mean value (n = 3).

26
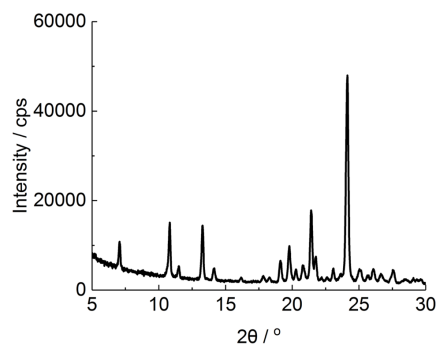
Figure S22. Powder X-Ray diffraction (p-XRD) spectrum of crystal of SO₃-C₁₆-G-OH. Sharp peaks confirmed that the needle-like precipitates of SO₃-C₁₆-G-OH are crystalline.

REFERENCES.

1.   Schnitter, F.;Boekhoven, J. A Method to Quench Carbodiimide-Fueled Self-Assembly. *ChemSystemsChem* **2020,** *3* (1), e2000037.
2.   Schnitter, F.; Riess, B.; Jandl, C.;Boekhoven, J. Memory, switches, and an OR-port through bistability in chemically fueled crystals. *Nat. Commun.* **2022,** *13* (1), 2816.
3.   Miklos, B.;Bodanszky., A. Racemization in peptide synthesis. Mechanism-specific models *Chem. Commun. (London)* **1967,** *12,* 591-593.
4.   Goodman Murray, L. L. Peptide Synthesis uia Active Esters. IV. Racemization and Ring-Opening Reactions of Optically Active Oxazolones. *J. Am. Chem. Soc.* **1964,** *86* (14), 2918-2922.
5.   Taylor, L. D.;Platt, T. E. A Convenient Synthesis of 5-Oxazolones. 2-Phenyl-5-Oxazolone. *Org. Prep. Proced. Int.* **1969,** *1* (3), 217-219.

8. Regulating Droplet Properties by Decreasing Activated Molecules' Half-Life

Abstract

In chemically fueled self-assembly, the activated molecules assemble before deactivating. Hence, the half-lives of the activated molecules are critical to the properties of the assembly. Theoretic models have also predicted how the half-life of the activated molecules would affect the properties of the chemically fueled assembly. However, experimental models that reveal the relationship between the half-life and the properties are missing. In this Chapter, we succeed in achieving tunable properties of coacervate droplets by decreasing the half-life of the activated molecules in a carbodiimide-fueled reaction cycle that forms oxazolones. By increasing the pyridine concentration, the hydrolysis of oxazolone is accelerated, and thus, the half-life of the oxazolone is decreased from 15 minutes to 5 minutes. In a steady state, with a decreasing half-life, droplets took a longer time to emerge and reach a stationary state. More importantly, the droplets' stable size also varies with the half-life of the droplet material. This work can serve as an inspiring experimental model to illustrate the relationship between the reaction cycle's kinetics and the properties of chemically fueled matter. This chapter has not been published in a peer-reviewed journal.

Introduction

Theoretic models developed by Jülicher group have predicted the relationship between the half-life of activated molecules and the size of the active droplets driven by a chemical reaction cycle. In this model, two chemical reactions that take place simultaneously regulate active droplets, i.e., an activation reaction that converts soluble precursor A into a self-assembling product B at the expense of a chemical fuel and a deactivation reaction that reverts product B to precursor A. Since the droplets are regulated by the chemical reaction cycle, they exhibit different properties from droplets in equilibrium, i.e., they can resist Ostwald ripening and evolve to a stable droplet size. Interestingly, the stable size of multiple droplets in a steady state can be regulated by the deactivation rate constant (k_b) and is proportional to $k_b^{-1/3}$, indicating that a faster deactivation or a shorter half-life of activated molecules leads to droplets with smaller size.[102] Moreover, theoretical predictions showed that the length of the spherical shell obtained in the intramolecular anhydride-forming reaction cycle driven by a carbodiimide decreases initially with increasing deactivation rate constant but then becomes stable over a broad range of rate constants.[83] However, the hydrolysis of intramolecular anhydrides cannot

be catalyzed because they hydrolyze rapidly by reaction with water, i.e., the half-life of intramolecular anhydrides cannot be decreased by catalyst. That means it is not feasible to achieve tunable properties of coacervate droplets in a steady state by decreasing the half-life of the intramolecular anhydrides when peptides with a sequence of Ac-F(RG)$_n$D-OH are used. In Chapter 6, I discussed that pyridine could suppress the side product *N*-acylurea to make the carbodiimide-fueled reaction cycle more efficient. It can also be used to decrease the half-life of the intermolecular anhydrides. Notably, in Chapter 7, I showed oxazolones that are formed via an intramolecular cyclization in a carbodiimide-fueled reaction cycle have long half-lives of up to 6 hours. Their long half-lives can be decreased by pyridine due to their accelerated hydrolysis. Thus, oxazolones can be a desired candidate for carbodiimide-fueled coacervate droplets with a tunable size in a steady state. In this Chapter, I first demonstrate that adding pyridine can decrease the half-life of oxazolones. Then, I confirm that chemically fueled coacervate droplets can be obtained in the oxazolone-forming cycle. Last, I show that the droplet's stable size can be decreased by decreasing the half-life of the oxazolone in a steady state.

Results and discussion

Decreasing the half-life of oxazolones by pyridine

As discussed in Chapter 3, Boekhoven Group used the carbodiimide-fueled intramolecular anhydride-forming reaction cycle to prepare chemically fueled coacervate droplets.[80] Inspired by the sequence of Ac-F(RG)$_n$D-OH, we replaced the aspartic acid (D) with glycines (G) to form oxazolone with the sequence of Ac-F(RG)$_n$G-OH, (RG)$_n$, n = 1, 2, 3 (Figure 8.1A). As described in Chapter 6, pyridine can suppress *N*-acylurea and catalyze intermolecular anhydride hydrolysis, thereby tuning intermolecular anhydrides' half-life. Then, we tested if pyridine as an additive can also tune the half-life of oxazolones (Figure 8.1B). Unless stated differently, we used 12 mM (RG)$_2$ in 200 mM MES buffer at pH 5.3 at 21 °C in all experiments. We added 20 mM EDC into the reaction solution with 3 and 10 mM pyridine, respectively, to start the cycle. To follow the kinetics of the reaction cycle, we used a benzylamine quenching method developed by our group to measure the concentration of the product by converting the oxazolone to a stable amide detected on high-performance liquid chromatography (HPLC).[74] We also used a kinetic model to fit the experimental data of species involved in the reaction cycle every minute by solving a set of ordinary differential equations. The rate constants were determined by the model, and we could calculate the half-life of oxazolones. In all cases, side product N-acylurea was under 5% as a fraction of fuel. As observed in Chapter 6, increasing

pyridine from 3 mM to 10 mM resulted in a lower maximum concentration of oxazolone (from 1.2 mM to 0.6 mM) and a decrease in the half-life of oxazolone (from 15 to 5 minutes) (Figure 8.1 C, Figure S8.5, Table S8.2).
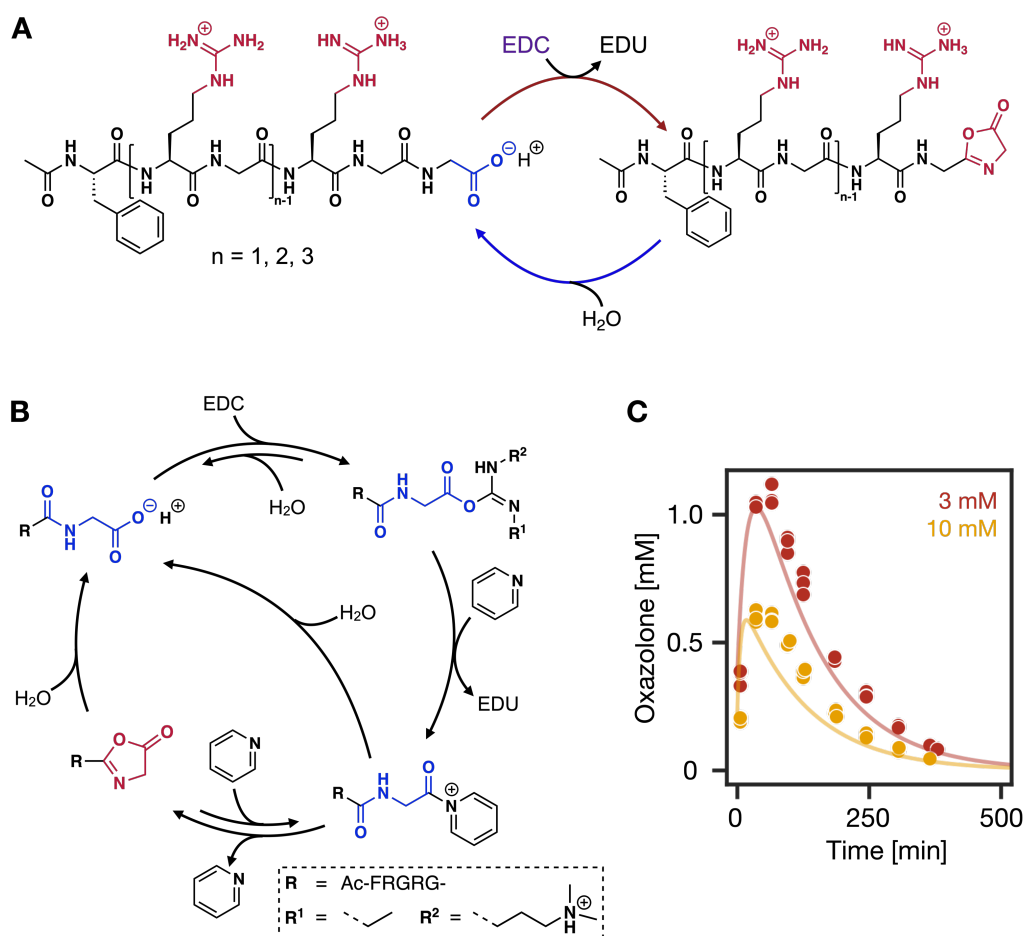

Figure 8.1. Pyridine can tune the half-life of oxazolone. **(A)** Simplified representation of the oxazolone-forming reaction cycle. Upon activation by EDC, the precursor converts to its oxazolone. Followed by deactivation, the oxazolone reverts to its precursor state. **(B)** Simplified representation of the reaction cycle with pyridine. Pyridine not only traps *O*-acylurea to suppress N-acylurea formation but catalyzes the hydrolysis of oxazolone. **(C)** The kinetics profiles of oxazolone in the reaction cycles of 12 mM Ac-F(RG)$_2$G-OH, (RG)$_2$, fueled with 20 mM EDC in MES buffer (200 mM, pH 5.3 at 21 °C) with 3 and 10 mM pyridine. HPLC data (markers) and the kinetic model (lines), n = 3.

Coacervate Droplets Obtained in the Oxazolone-Forming Cycle

Next, we added PSS in the reaction cycle to get coacervate-based droplets (Figure 8.2 A). Upon activation, the peptide has an increased affinity for PSS and forms coacervate-based droplets. Simultaneously, hydrolysis of the oxazolone reverts the activation, undoing its affinity for PSS. Consequently, droplet material flows into the droplets by activation and droplet material leaves the droplet through deactivation. First, we focused on how the peptide design affects droplets' emergence. We varied the number of RG-repeats in our peptide design to tune the electrostatic interactions between our peptides and PSS. (RG)$_1$ peptide consisted of one RG-repeat, while

(RG)$_3$ peptide comprised three RG-repeats. Given that C-terminal glycine has a −1 charge, the overall charge of the precursor state of the peptides is 0, +1, +2, respectively (Figure 8.2 B).
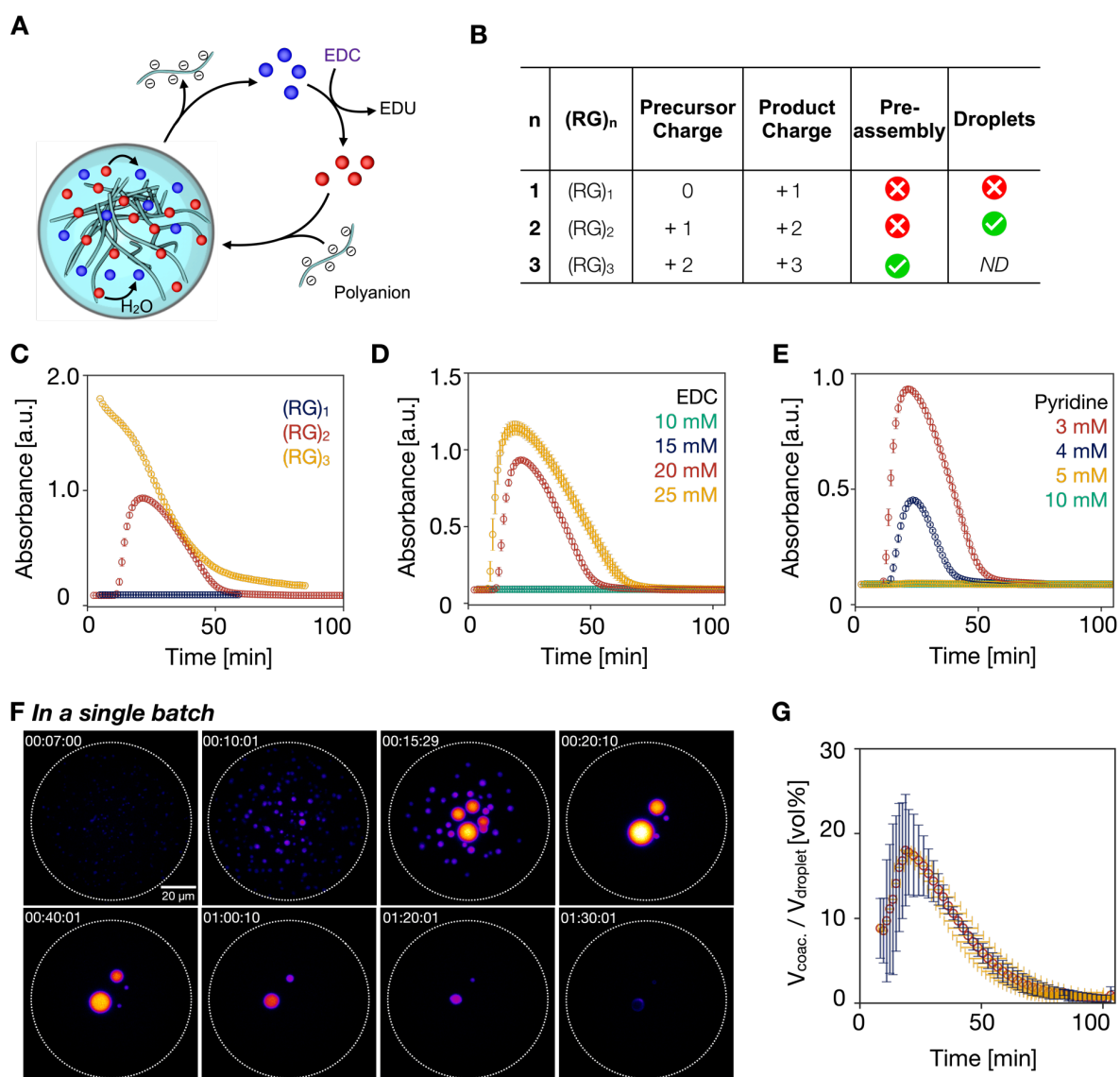

Figure 8.2. Chemically fueled coacervate based droplets can be produced by oxazolone with PSS. **(A)** Schematic representation of an active coacervate-based droplet. **(B)** Summary of the changes in charges of different peptides and their response to PSS with and without fuel. **(C)** Absorbance at 600 nm by UV/vis spectroscopy as a measure of turbidity of the reaction cycles of (RG)$_1$ and (RG)$_2$ in response to 20 mM EDC with 12.5 mM PSS. (RG)$_3$ preassembles with PSS without EDC. All conditions are in MES buffer (200 mM, pH 5.3 at 21 °C) unless otherwise indicated. Absorbance at 600 nm of the reaction cycles of 12 mM (RG)$_2$ **(D)** with 3 mM pyridine fueled with 10, 15, 20, and 25 mM EDC, **(E)** fueled with 20 mM EDC with 3, 4, 5, 10 mM pyridine. **(F)** Representative images over one cycle of droplet evolution (emerging, growing, and decaying) in a microreactor in a single batch of 12 mM (RG)$_2$ with 20 mM EDC, 3 mM pyridine, and 12.5 mM PSS. **(G)** Analysis of the total volume of droplets over the entire reaction cycle under the condition of **F**. The total volume is given as volume percent, defined as the total volume of droplets divided by the total volume of the microfluidic droplet, n = 3.

We used UV/vis spectroscopy to measure the absorbance at 600 nm as an indication for turbidity, which also indicates coacervate-based droplet formation. We used 12 mM peptide

with 3 mM pyridine. Only $(RG)_3$ peptide formed coacervate droplets before adding fuel due to its strong electrostatic interactions with PSS (Figure 8.2 C). The addition of 20 mM EDC to $(RG)_1$ did not show any turbidity, indicating no droplets were formed. In contrast, $(RG)_2$ showed a transient turbidity which emerged around 10 minutes and vanished around 1 hour. Therefore, we focused our investigation on $(RG)_2$ as it can form dynamic droplets in response to fuel.

We tested the effect of peptide-to-EDC ratios on droplet formation. Lower amounts of EDC (10 and 15 mM EDC) did not result in droplet formation, whereas higher amounts of EDC (20 and 25 mM) led to droplets and their lifetimes prolonged with increasing amounts of fuel (Figure 8.2 D). Furthermore, we tested the effect of pyridine-to-EDC ratios on droplet formation by adding 20 mM EDC into 12 mM $(RG)_2$ with 3, 4, 5, and 10 mM pyridine, respectively. As discussed before, increasing pyridine decreases the maximum concentration of oxazolone, resulting in no droplets when the amount of pyridine is higher than 5 mM. Even though 4 mM pyridine led to droplet formation, the turbidity is much lower compared to 3 mM pyridine and the lifetime of droplets is also shorter (Figure 8.2 E). Combined with our kinetic model, the critical coacervation concentration (CCC) can be calculated to be around 0.7 mM. Then, we used confocal microscopy to follow each coacervate-based droplet's emergence, evolution, and decay in a single batch in aqueous microreactors. We made these aqueous microreactors by preparing a stable emulsion of water droplets in a fluorinated oil phase.[83] The water droplets (microreactors) contained all reagents including the peptide, buffer, polyanion, and fuel. The condition was 12 mM $(RG)_2$ fueled with 20 mM EDC in MES with 12.5 mM PSS and 3 mM pyridine. Due to the time of mixing before imaging, we were not able to detect the nucleation time but droplets with weak fluorescence were detected around 7 minutes. Afterward, the droplets grew predominantly through fusion until two big droplets remained around 20 minutes (Figure 8.2 F). Then, these two remaining droplets start to shrink until the droplet size falls below the detection limit of the tracking software. Interestingly, at the end of the cycle around 90 minutes, the droplets also started to form vacuoles, after which the droplets vanished. This decay phenomenon is consistent with observation of droplets formed by intramolecular anhydride-forming cycle, suggesting that the deactivation also occurs inside of the droplets. Moreover, we measured the total droplet volume throughout the reaction cycle. The total droplet volume increased significantly in the first 20 minutes due to the fusion-induced growth. After 20 minutes, it gradually collapsed due to droplet decay (Figure 8.2 G).

Regulating coacervate droplet properties in a steady state

Thanks to the low solubility of DIC in water, DIC can partition into the aqueous solution and saturate the solution to reach a steady state. This approach does not require continuous stirring, which breaks the droplets, but cannot be applied to EDC due to EDC's high solubility in water. Therefore, we performed experiments in a steady state by applying pure DIC onto a 0.5% w/v agarose gel that contained the aqueous solution of 12 mM $(RG)_2$, 12.5 mM PSS, and pyridine. This agarose gel is used to decrease droplet fusion. For 3 mM pyridine, 18 minutes after DIC was applied on top of the gel, droplets emerged and grew, but no fusion was observed throughout the observation time. To better quantify the size of droplets, we calculated their volume from their radius. Droplets reached a volume of 1.47 μm^3 (Figure 8.3 A, B, C, red) within 60 minutes after DIC was applied and kept at this volume with time. That is, droplets reached a stable size. Similarly, the number of droplets remained constant once droplets reached their stable size (Figure S8.6 A, B red), indicating that those droplets reached a stationary state. Those results confirmed that the chemically fueled droplets can withstand Ostwald ripening. Moreover, to quantify the deviation of the droplets' size, we calculated the polydispersity index (PDI) ($p = \sigma/\mu$, where σ is the mean radius and μ is the standard deviation of the mean) after droplets reached their stable size. PDI was only 0.13, indicating a narrow size distribution (Figure 8.D, red). All observation provides an experimental droplet model where the chemical reaction cycle can exert control over the droplets' size and the mechanism can be explained by the theoretic model discussed in Chapter 3 about suppressing Ostwald ripening with a system where the activation occurs predominantly outside the droplets, and the deactivation occurs predominantly inside the droplets (*vide supra*).

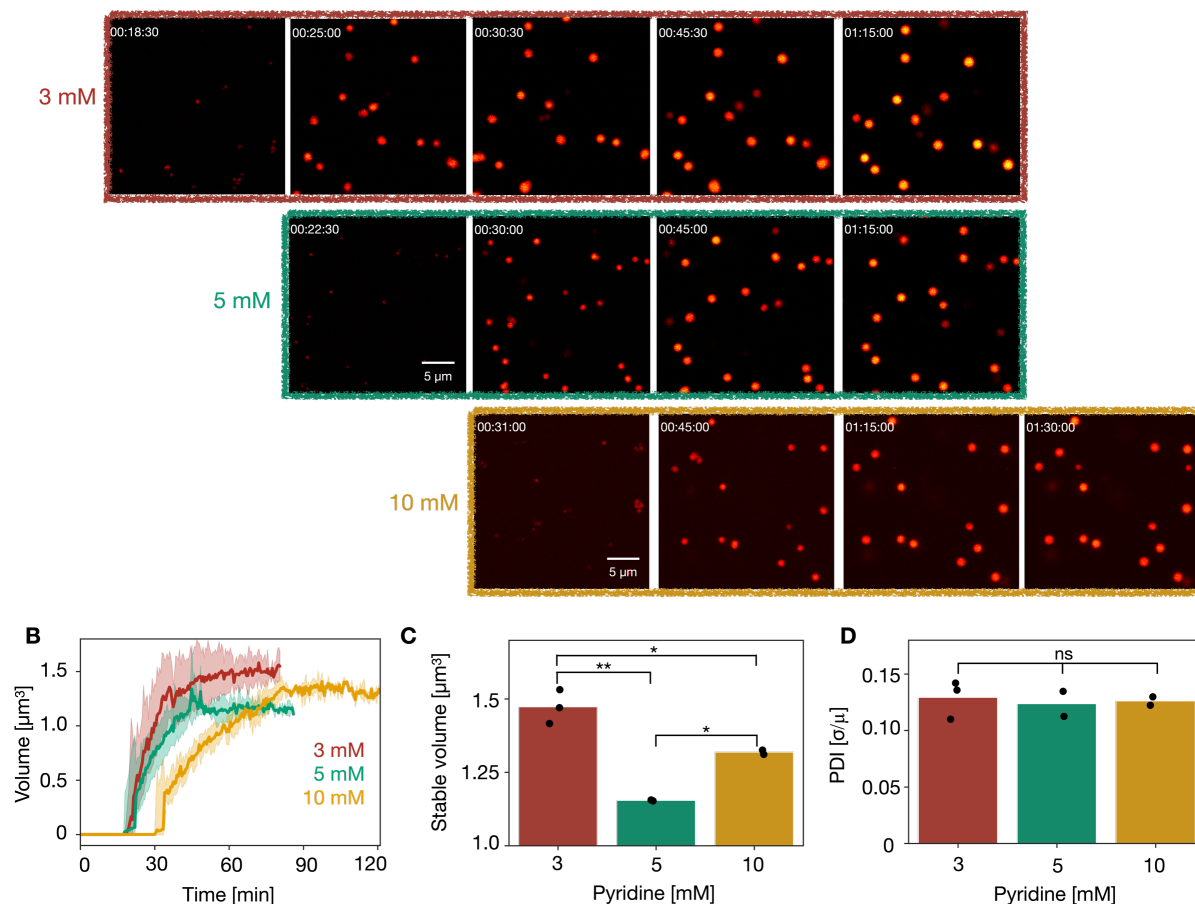**A** *In a steady state with 3, 5 and 10 mM pyridine*

Figure 8.3. Tunable properties of coacervate droplets in a steady state with DIC as a fuel. **(A)** Representative images over one cycle of droplet evolution (emerging, growing, and stabilizing) in a steady state. Conditions are 12 mM $(RG)_2$ with 12.5 mM PSS with 3, 5 and 10 mM pyridine. Experiments were repeated at least twice. **(B)** Analysis of the mean volume of droplets over the entire reaction cycle. **(C)** The stable volume of droplets is obtained in a steady state. The stable volumes obtained under the 3 conditions show significant differences with $P < 0.001$ for 3 vs. 5 mM pyridine, $P < 0.05$ for 3 vs. 5, and 5 vs. 10 mM pyridine. **(D)** The polydispersity index (PDI) of droplets in a steady state. Droplets obtained under the 3 conditions are uniform, with a similar PDI of around 0.12.

Then, we conducted the same experiment with 5 and 10 mM pyridine. Increasing pyridine leads to a decreasing half-life of oxazolone (Figure S8.5, Table S8.2) and, thereby, a decreasing concentration, delaying when droplets emerge. Compared to 3 mM pyridine, droplets emerged slightly later with 5 mM pyridine, while with 10 mM pyridine, droplets took a much longer time to emerge (Figure 8.3 A). By using the rate constants of the reaction cycle with EDC, our kinetic model predicts that the stationary concentration of oxazolone with 10 mM pyridine is half of that with 3 mM pyridine ((Figure S8.7). Despite differences in rate constants between the reaction cycle with EDC and DIC, the trend of decreasing oxazolone concentration with increasing pyridine should persist. Assuming the critical coacervation concentration (CCC) is not altered by pyridine, droplets would take longer to form with a lower oxazolone concentration. Still, droplets obtained with 5 and 10 mM pyridine also grew without fusion and

reached a stationary state with a stable size and a similar narrow size distribution (Figure 8.3 A, B, C). They also had a narrow size distribution. Droplets obtained with 5 mM pyridine reached a stationary state rapidly in a similar fashion as droplets obtained with 3 mM pyridine, while droplets with 10mmM pyridine slowly reached a stationary state in a significantly delayed way.

Moreover, as predicted by the theoretical model, shorter half-life of active molecules, i.e., faster deactivation, leads to droplets with smaller size;[102] droplets obtained with 5 mM pyridine were much smaller with a volume of 1.15 μm^3 compared to droplets obtained with 3 mM pyridine. However, increasing pyridine to 10 mM led to droplets with a stable volume of 1.31 μm^3, which was not a further drop in droplets' size but a rise. We do not know exactly what caused this rise, but we cannot exclude the potential influence of pyridine and accumulated urea (DIU in this case) on droplets. As pyridine (pKa = 5.23) is half protonated at pH 5.3, would it interactive with polyanion (PSS in this case) to promote droplet formation or growth when its amount increases? How small would the droplets be with other pyridine concentration like 7.5 mM or 15 mM? Besides, since the deactivation of the reaction cycle is accelerated with increasing pyridine, the turnover of precursor is accelerated. Therefore, the consumption of fuel is also speed up in a steady state, resulting in more DIU accumulated in the system. DIU has poor solubility in water. Once it is formed, it should ideally diffuse into the DIC oil phase and get out of the agarose gel. However, it might crystalize in the agarose gel before entering DIC oil phase. Would this DIU waste in the agarose gel affect the droplets size? Therefore, further work should test the influence of pyridine and DIU.

Conclusion

In this Chapter, we confirmed that the oxazolone-forming reaction cycle enables tunable half-life of activated molecules by pyridine. Specifically, pyridine can catalyze the hydrolysis of oxazolone, thus decreasing its half-life. By designing the peptide precursor carefully, we were able to obtain complex coacervate droplets via the coacervation of a polyanion and the activated cationic peptide. We regulated the properties of droplets by increasing the pyridine amount, thus by decreasing the half-life of the oxazolones. The decreased half-life of oxazolone led to a delay in the emerging time of droplets and a shortened droplet lifetime in a single batch. Similarly, in a steady state, the emerging time of droplets was also delayed, and droplets took longer to reach a stable size. Besides, to some extent, the stable size of droplets was decreased significantly with pyridine, but further increasing pyridine concentration did not lead to a

further drop in droplets' size but a rise. This rise could result from the higher amount of pyridine and the accumulated urea waste. Further work should test the influence of pyridine and urea on the droplet's properties. Overall, this work serves as an inspiring experimental model illustrating how the kinetics of a chemical reaction cycle can exert control over the behavior of chemically fueled matter.

SUPPORTING INFORMATION

MATERIALS

Diisopropylethylamine (DIPEA), N, N'-Diisopropylcarbodiimide (DIC), Dichloromethane (DCM), N, N-Dimethylformamide (DMF), Ethyl (hydroxyimino)cyanoacetate (oxyma) (Novabiochem®), Triisopropylsilane (TIPS), O-(1H-6-Chlorobenzotriazole-1-yl)-1,1,3,3-tetramethyluronium hexafluorophosphate (HCTU), Fmoc-Gly-Wang resin (100-200 mesh, loading: 0.68 mmolg-1), Piperazine, Acetic anhydride, Fmoc-F-OH, Fmoc-G-OH, Fmoc-Arg(Pbf)-OH, Trifluoroacetic acid (TFA), acetonitrile (ACN) (High-performance liquid chromatography (HPLC) grade), Poly(styrene sulfonate) sodium salt analytical standards (17 kg/mol, Supelco®), Sulforhodamine B, Pyridine, Benzylamine, 1-Ethyl-3-(3-dimethylaminopropyl)carbodiimide hydrochloride (EDC • HCl), 4-Morpholineethanesulfonic acid (MES) buffer, LMP agarose, Deuterated dimethyl sulfoxide (DMSO-d_6) were purchased from Sigma-Aldrich unless indicated otherwise. All peptides were synthesized using solid-phase peptide synthesis (SPPS) on Wang resin (see METHODS - Peptide synthesis and purification). All chemicals were used without any further purification.

METHODS

Sample preparation: We prepared stock solutions of the precursors by dissolving the peptides in 0.5 M MES buffer, then we adjusted the pH to pH 5.3. Benzylamine stocks were prepared freshly in acetonitrile. Stocks of EDC, PSS, pyridine and sulforhodamine B were prepared by dissolving or mixing them in MQ water the fluorescent dyes were also prepared in MQ water without pH adjustment. EDC stocks were prepared freshly every time before use. Stocks of PSS, pyridine and peptides were filtered with a syringe filter (PTFE, 0.2 μm pore size). Reaction cycles were started by adding EDC, pyridine, PSS, MES buffer, MQ water to the precursor.

Peptide synthesis procedure: Ac-F(RG)$_n$-OH were synthesized from N- to C-terminus on a 0.25 mmol scale following a given synthesis protocol. Preloaded Fmoc-Gly-Wang resin was swelled for 30 minutes in 10 mL of DMF at room temperature and then transferred to a reaction vessel. This vessel was connected to an N$_2$-flow for agitation and a waste container-water pump for draining via a three-way cock. The peptide synthesis was carried out at 68°C by placing the reaction vessel in a silicon oil bath. The resin was first swelled for 5 minutes at 68°C in 10 mL DMF under N$_2$. DMF was then drained. A 10 mL mixture of 5% (volume percentage) piperazine in DMF was added with N$_2$ agitation for one minute and then was drained.

Subsequently, 10 mL of 5% piperazine in DMF was added and agitated for 6 minutes and then was drained. These two steps were used to deprotect the Fmoc group. Then, the resin was washed with 10 mL DMF 4 times, followed by adding 3 eq amino acid, 6 eq DIPEA and 2.8 eq HCTU in 4 mL DMF to allow coupling. After 6-minute agitation, the reaction solution was drained and the resin was washed with 10 mL DMF 4 times. The Fmoc-deprotection, washing, amino acid coupling, and washing cycle was repeated for every amino acid until the last amino acid (Fmoc-F-OH) was coupled. Once Fmoc-F-OH was coupled, acetylation with 142 μL acetic acid and 290 μL DIEA was carried out in the same procedure, but all the steps from the last 2 times of washing were performed at room temperature. Last, peptides were cleaved from the resin using a 10 mL mixture of 95% TFA, 2.5% TIPS, and 2.5% MQ-water, and the solution was removed under reduced pressure on rotary evaporation. The crude products were then purified on a reversed-phase High-Performance Liquid Chromatography (RP-HPLC) with gradient elution from 2% to 98% acetonitrile with 0.1% TFA in MQ-water. All compounds were detected at 220 nm and lyophilized (Lyophylle: Alpha LDplus, Christ) and characterized by ^{1}H-NMR spectroscopy, HPLC, and Electron Spray Ionisation – Mass Spectrometry (ESI-MS).

Kinetic model: The same kinetic model for oxazolone in Chapter 7 was used to predict the oxazolone concentration's evolution over time. The rate constants we used in this work are given in Supporting Table S8.2.

Analysis of the reaction kinetics by HPLC: We followed the kinetics of the reaction cycles over time on analytical HPLC (Thermo Fisher Dionex Ultimate 3000, Hypersil Gold 250 × 4.8mm). We used a quenching method68 to indirectly determine the concentration of the oxazolone and EDC by converting them irreversibly into an amide (benzylamide) and a guanidine, respectively. After initiating the reaction, we took 10 μL reaction solution to 10μL benzylamine solution (400 mM) in ACN at certain time points. After several hours, 2 μL resulting clear quenched solution was injected into HPLC with a UV/Vis detector at 220 and 254 nm. All compounds involved were separated with a linear gradient of ACN (2% to 98%) and water with 0.1% TFA.

HPLC Methods: H_2O/ACN starts from 98/2 with 1 minute pre-equilibrium. ACN increases to 30% in 21 min, 2 min increasing to 98 %, followed by 2 min at 98 % before going back to 2 % and finally 3 min 2 %.

Calibration for (RG)$_2$G and N-acylurea was performed with this method. Calibration for EDC and benzylamine was also performed with this method but with ACN quickly going back to 2% after they came off.

Electron Spray Ionisation – Mass Spectrometry (ESI-MS): ESI-MS measurements were performed on a Varian 500 MS LC ion trap or a LCQ Fleet Ion Trap Mass Spectrometer (Thermo Scientific). Samples were diluted in acetonitrile or MQ water before injection. All recorded MS data were interpreted on the Thermo Xcalibur Qual Browser 2.2 SP1.48 software. Confocal Fluorescence Microscopy. We imaged the coacervate droplets in microfluidic reactors (microreactors) and in a bulk gel on a Leica SP5 confocal microscope with a 63x oil immersion objective. Samples were excited at 552 nm and imaged at 565 - 700 nm. All recorded images were analyzed with ImageJ 1.52p software (Java 1.80_172 (64-bit)).

Microfluidic reactors: 50 µL reaction solutions with 0.1 µM Sulforhodamine B were prepared as described above. 5 µL reaction solution was mixed with perfluorinated oil (Novec 7500, 50 µL) containing the fluorosurfactant. Then 5 µL water/oil mixture was applied to a chamber on glass slide and the chamber was then sealed to prevent evaporation.

Bulk gel: A solution excluding fuel was mixed with 0.1% (w/v) LMP agarose (200 mM MES buffer, pH5.3). The volume ratio of the reaction solution and the agarose solution was 1:1. Then the mixture was applied to an IBIDI chamber that was coated with PVA. Once the mixture solution turned to a gel, pure DIC was applied to the top of the gel to initiate the reaction cycle. Turbidity measurements. Turbidity measurements were carried out on a Microplate Spectrophotometer (Thermo Scientific Multiskan GO, Thermo Scientific SkanIt Software 6.0.1) at 600 nm by every minute in triplicate. Measurements were performed in a non-tissue culture-treated 96-well plate (Falcon, flat bottom). Every minute, the absorbance of the samples was measured at 600 nm. The lifetime droplets refer to the time when the absorption drops under 0.01 a.u. (blank subtraction) after EDC addition.

NMR spectra: NMR spectra were carried out on Bruker AV400US (500 MHz). Chemical shifts are reported as δ-values in ppm (parts per million) relative to DMSO-d_6 (δH: 2.50). For the denotation of the observed signal multiplicities, the following abbreviations were used m (multiplet), dd (doublet of doublets), d (doublet) and s (singlet).

SUPPORTING TABLES

Supporting Table S8.1 Mass information of all the synthesized peptides and products in the reaction cycle.

Name	Structure	Exact Mass (gmol^{-1})	Mass found (gmol^{-1})
Ac-F(RG)$_1$G-OH (RG)$_1$		Mw = 477.23 $C_{21}H_{31}N_7O_6$	478.36 [Mw+H]$^+$
Ac- F(RG)$_2$G -OH (RG)$_2$		Mw = 690.36 $C_{29}H_{46}N_{12}O_8$	691.39 [Mw+H]$^+$ 346.42 [Mw]$^{2+}$
Ac- F(RG)$_3$G -OH (RG)$_3$		Mw = 903.48 $C_{37}H_{61}N_{17}O_{10}$	904.6 [Mw+H]$^+$ 453.11 [Mw]$^{2+}$
Guanidine		Mw = 262.22 $C_{15}H_{26}N_4$	263.07 [Mw+H]$^+$
(RG)$_2$-N-acylurea	Two possible isomers (we only show one, same as below)	Mw = 845.50 $C_{37}H_{63}N_{15}O_8$	846.38 [Mw+H]$^+$ 423.92 [Mw]$^{2+}$
(RG)$_2$-benzylamide		Mw = 779.42 $C_{36}H_{53}N_{13}O_7$	780.32 [Mw+H$^+$] 390.98 [Mw]$^{2+}$

Supporting Table S8.2 Rate constants used in the kinetic model of Ac-F(RG)$_2$G-OH in MES buffer (200 mM) with EDC with pyridine at 21 °C, pH 5.3.

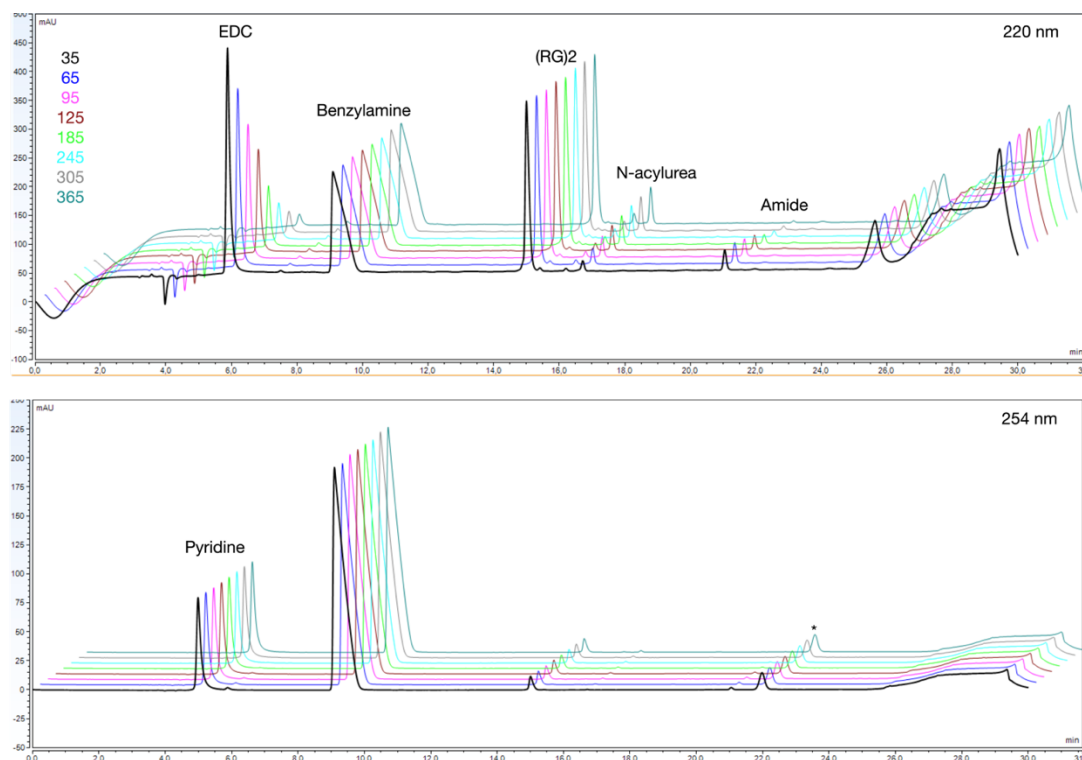| Pyridine [mM]	k$_0$ [min^{-1}]	k$_1$ [mM^{-1}min^{-1}]	k$_2$ [min^{-1}]	k$_3$ [min^{-1}]	k$_4$ [min^{-1}]	k$_5$ [min^{-1}]	Half-life of oxazolone / min (calculated by ln(2)/k$_4$
order	1	2	1	1	1	1	
3	1.58 x 10^{-3}	5.76 x 10^{-4}	2.07 x 10^{-1}	2.51 x 10^{-1}	4.63 x 10^{-2}	3.01 x 10^{-2}	15
10	1.58 x 10^{-3}	5.44 x 10^{-4}	1.24 x 10^1	4.80 x 10^{-1}	1.50 x 10^{-1}	3.06 x 10^{-2}	5

Figure S8.1. Examples of representative HPLC chromatograms of reaction cycles of 12 Ac-F(RG)₂G-OH fueled with 20 mM EDC in MES buffer with 3 mM pyridine, pH 5.3, 21 °C. injection volume: 2 µL. * stands for the impurity from benzylamine solution.
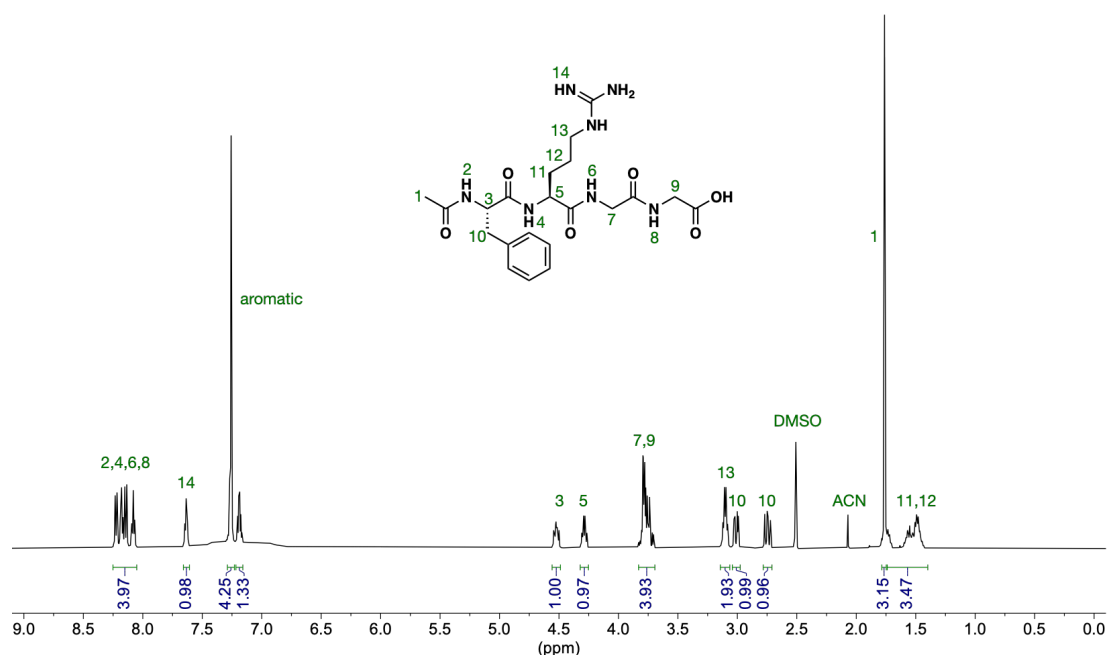

Figure S8.2 ^{1}H NMR spectrum (500 MHz, DMSO) of Ac-F(RG)₁G-OH. δ 8.25 – 8.05 (m, 4H), 7.64 (t, *J* = 5.8 Hz, 1H), 7.26 (d, *J* = 4.3 Hz, 4H), 7.18 (dt, *J* = 8.7, 4.1 Hz, 1H), 4.52 (ddd, *J* = 10.1, 8.0, 4.4 Hz, 1H), 4.29 (td, *J* = 8.0, 5.5 Hz, 1H), 3.83 – 3.69 (m, 4H), 3.14 – 3.06 (m, 2H), 3.01 (dd, *J* = 14.0, 4.4 Hz, 1H), 2.75 (dd, *J* = 13.9, 10.1 Hz, 1H), 1.76 (s, 3H), 1.74 – 1.40 (m, 4H).
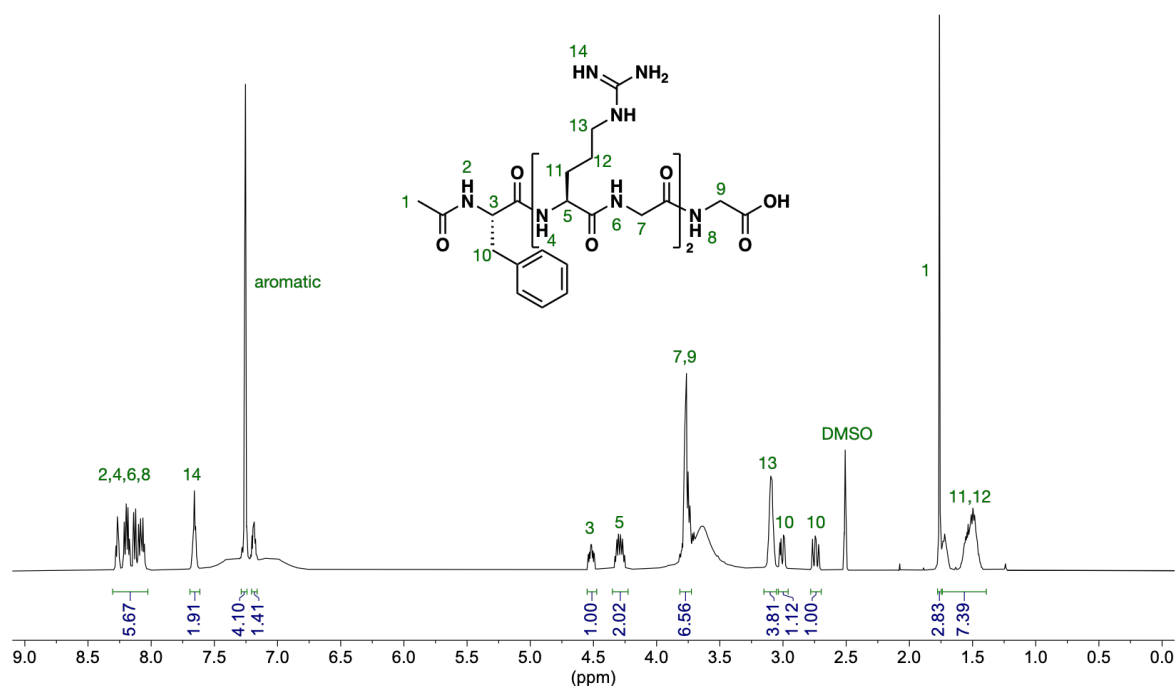
Figure S8.3 ¹H NMR spectrum (500 MHz, DMSO) of Ac-F(RG)₂G-OH. δ 8.30 – 8.03 (m, 6H), 7.66 (t, *J* = 5.8 Hz, 2H), 7.26 (d, *J* = 5.2 Hz, 4H), 7.18 (tt, *J* = 4.7, 3.3 Hz, 1H), 4.52 (ddd, *J* = 10.2, 8.1, 4.3 Hz, 1H), 4.29 (dtd, *J* = 16.3, 7.9, 5.5 Hz, 2H), 3.82 – 3.72 (m, 6H), 3.10 (tt, *J* = 8.2, 4.6 Hz, 4H), 3.01 (dd, *J* = 13.9, 4.3 Hz, 1H), 2.74 (dd, *J* = 13.9, 10.1 Hz, 1H), 1.76 (s, 3H), 1.74 – 1.39 (m, 8H).
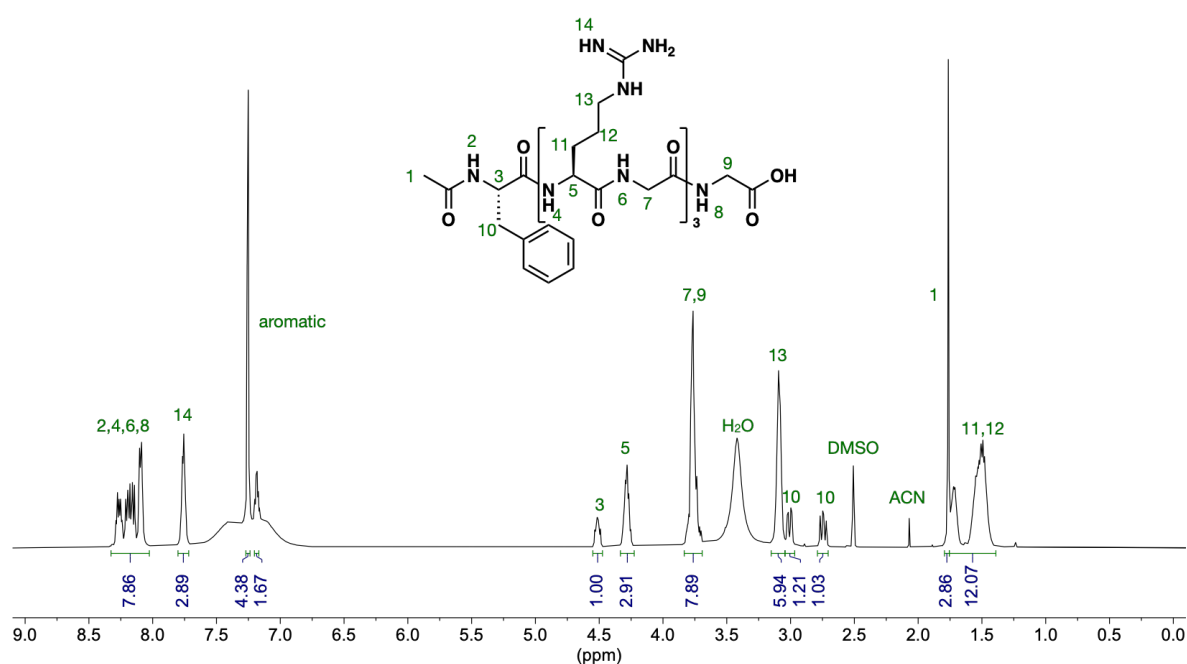

Figure S8.4 ¹H NMR spectrum (500 MHz, DMSO) of Ac-F(RG)₃G-OH. δ 8.33 – 8.03 (m, 8H), 7.76 (t, *J* = 5.6 Hz, 3H), 7.26 (d, *J* = 4.4 Hz, 4H), 7.19 (q, *J* = 4.4 Hz, 1H), 4.51 (ddd, *J* = 10.0, 8.1, 4.4 Hz, 1H), 4.33 – 4.23 (m, 3H), 3.83 – 3.69 (m, 8H), 3.09 (q, *J* = 6.2 Hz, 6H), 3.01 (dd, *J* = 14.0, 4.3 Hz, 1H), 2.74 (dd, *J* = 13.9, 10.1 Hz, 1H), 1.76 (s, 3H), 1.76 – 1.39 (m, 12H).
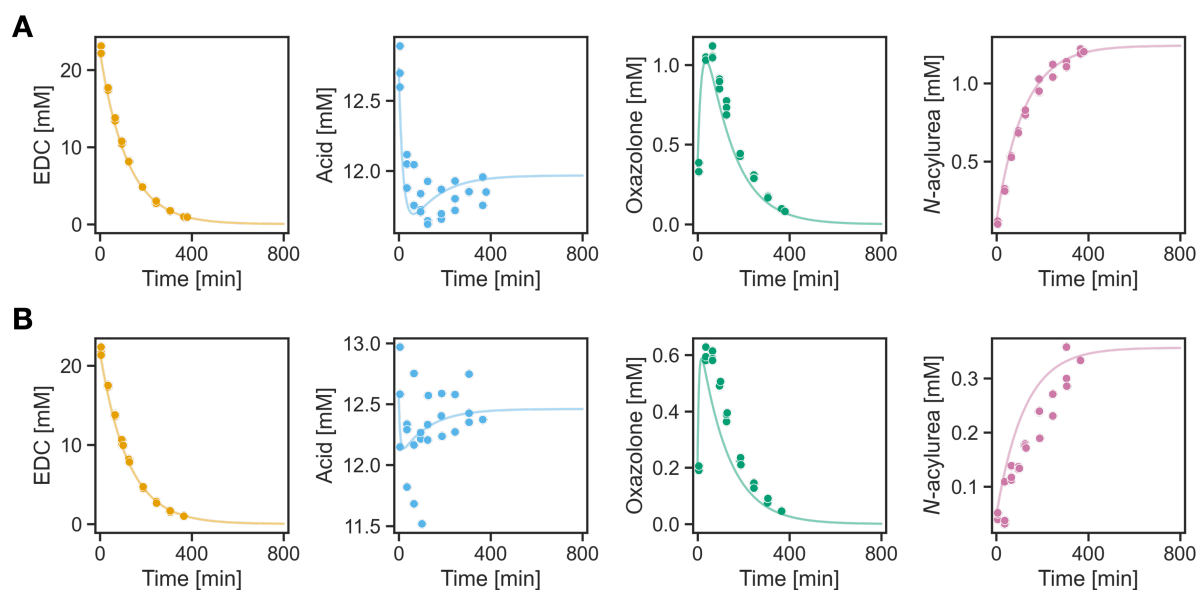
Figure S8.5 Kinetic profiles of reaction cycles of 12 mM Ac-F(RG)$_2$G-OH fueled with 20 mM EDC in MES buffer, pH 5.3, 21 °C with (A) 3 mM pyridine, (B) 10 mM pyridine. Markers represent HPLC data, and lines represent data from the kinetic model. All experiments were conducted in triplicates.
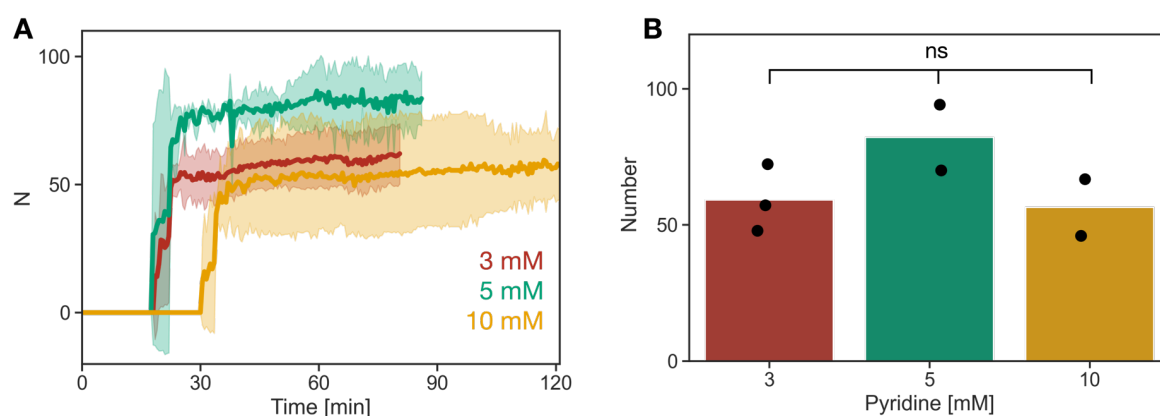

Figure S8.6 Analysis of the numbers of droplets over the entire reaction cycle of 12 mM Ac-F(RG)$_2$G-OH fueled with DIC in a steady state with 3, 5, and 10 mM pyridine.
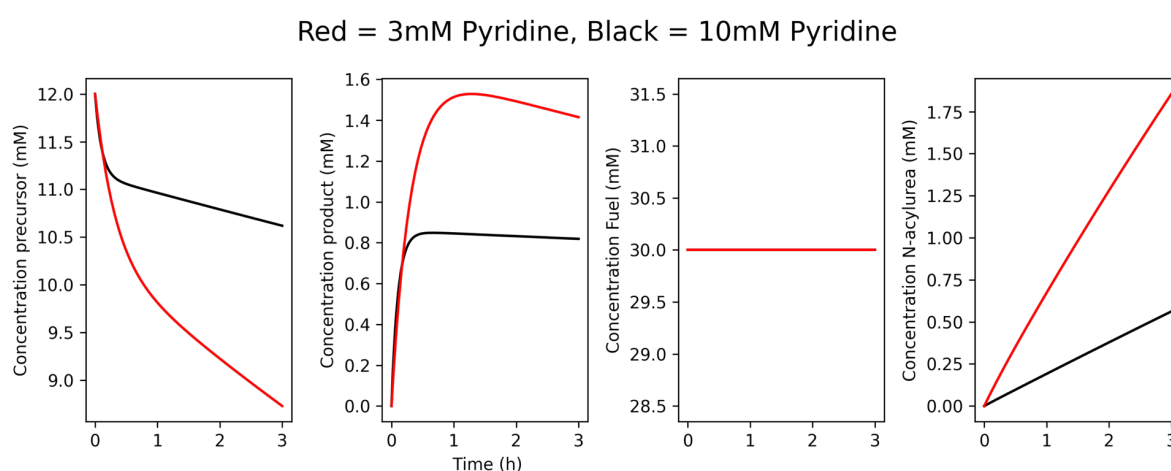

Figure S8.7 Simulated evolution of compounds in the reaction cycle of 12 mM Ac-F(RG)$_2$G-OH fueled with DIC in a steady state with 3 and 10 mM pyridine by using the rate constants obtained with EDC.

9. Conclusion and Outlook

This thesis managed to obtain synthetic dissipative matter driven by a chemically fueled reaction cycle and test the response of such matter to the kinetics of the reaction cycle.

In Chapter 1, I demonstrated the feature of dissipative matter: sustained by a continuous supply of energy, kinetically controlled, and thermodynamically labile. I also explicated how life is a prime example of dissipative matter driven by energy. Since the most compelling illustrations of the functional richness of dissipative systems are still found in biology, in Chapter 2, I used biological chemically fueled matter from microtubules, molecular machinery to membraneless organelles, to demonstrate how chemical fuels are transduced to endow cells with diverse functions, such as the emergence of ordered structures, maintenance of concentration gradients, force exertion, and the regulation of regents in a compartment. Sparked by the unique properties of biological dissipative matter, the quest for synthetic analogues has attracted significant interest and had a distinct impact on the field of systems chemistry. Therefore, in Chapter 3, I demonstrated the recently reported synthetic chemically fueled reaction cycle based on the hydrolysis of methylating agents, oxidation of reducing agents, hydrolysis of ATP, hydration of carbodiimides, and others. I also exemplified the dissipative matter obtained in these reaction cycles, such as fibers, oil droplets, and coacervates. Moreover, I showed how theoretic models had been used to predict and understand the kinetically regulated properties of chemically fueled droplets.

The practical work of this thesis aimed to achieve tunable properties of chemically fueled coacervates by decreasing the active molecules' half-life. In Chapter 6, I optimized the working conditions to achieve a highly effective carbodiimide-fueled reaction cycle. The optimal condition is a combination of low temperature, low pH, and 10% pyridine as a fuel fraction. In chapter 7, I introduced a robust, efficient, and versatile carbodiimide-fueled reaction cycle that forms transient 5(*4H*)-oxazolones. The long half-life of the oxazolone product allows the deactivation (hydrolysis) of the oxazolone to be accelerated by catalysts without changing the pH or temperature. Finally, in Chapter 8, I showed that chemically fueled coacervates could be formed in the oxazolone-forming cycle as well as their tunable properties by decreasing the oxazolone's half-life. With the decreasing half-life of the oxazolones, droplets took longer to emerge and reach a stable size in a steady state. Most importantly, droplets' stable size was decreased, but with a further higher amount of pyridine, droplets' stable size did not show significant decrease.

In conclusion, this thesis obtained synthetic chemically fueled coacervates driven by a carbodiimide-fueled reaction cycle and tested how the properties of the coacervates respond to the kinetics of the deactivation reaction. This thesis could propose a new strategy in the field of system chemistry to create synthetic dissipative matter and serve as an inspiring experimental model to demonstrate the relationship between reaction cycle kinetics and the properties of chemically fueled matter.

However, further experiments need to be conducted to test the influence of pyridine and Urea on droplets' properties in the oxazolone-forming reaction cycle. Beside, although theoretical calculations can predict the exciting properties of chemically fueled matter by simply modifying the kinetics of deactivation, experimental verification of such matter is still a long way off. The current lack of chemically fueled reaction cycles presents a major bottleneck for further developing chemically fueled matter. Therefore, future research on chemically fueled matter should prioritize identifying new reaction cycles that do not suffer from side reactions and allow for fine-tuned deactivation without affecting activation. Side reactions can reduce the fuel's efficiency and significantly affect the properties of the chemically fueled matter, especially in a steady state. For instance, the effects of N-acylurea on the properties of coacervates, such as their stable size, cannot be ignored, even though we have not yet examined its effects. Overcoming this bottleneck would open new opportunities to achieve chemically fueled matter with more exciting kinetically controlled properties and improve our understanding of dissipative matter.

10. Further Publications

Apart from the two publications reprinted in Chapters 6 and 7 and the review discussed in Chapter 3, I contributed to one more publication in the group of Prof. Job Boekhoven.

The following section is a full list of my achievements throughout my Ph.D.

[1] Chen, X., Stasi, M., Rodon-Fores, J., Großmann, P. F., Bergmann, A.M., Dai, K., Tena-Solsona, M., Rieger, B. and Boekhoven, J.* "A Carbodiimide-Fueled Reaction Cycle That Forms Transient 5(4H)-Oxazolones." *J. Am. Chem. Soc.*, **2023**, 145, 12, 6880-6887.

[2] Chen, X.,[+] Würbser, M.[+] and Boekhoven, J.* "Chemically fueled supramolecular materials." *Acc. Mater. Res.* **2023**, 4, 5, 416-426.

[3] Chen, X.,[+] Kriebisch, B.[+] and Boekhoven, J.* "Design rules for reciprocal coupling in chemically fueled assembly." *Chem. Sci.* **2023**, 14, 10176-10183.

[4] Chen, X., Soria-Carrera, H., Zozulia, O. and Boekhoven, J.* "Suppressing catalyst poisoning in the carbodiimide-fueled reaction cycle." *Chem. Sci.*, **2023**,14, 12653-12660.

11. Acknowledgements

During my final year of master's studies, I made the decision to step out of my comfort zone and pursue a Ph.D. abroad. In January 2019, I reached out to Prof. Job Boekhoven inquiring about any available Ph.D. positions. Although he did not have any positions available at the time, he responded quickly and offered to assist me with the application process for the CSC scholarship. Fortunately, I was granted the scholarship and commenced my Ph.D. in October 2019. Therefore, I want to thank CSC for funding me to pursue my Ph.D. abroad and all the funding involved in my projects of this thesis.

Then, Job, I want to thank you for giving me the wonderful opportunity to pursue my Ph.D. under your guidance. Throughout my Ph.D. journey, I have learned a lot from you. Your enthusiasm toward scientific research, critical thinking, and innovative ideas have greatly influenced me and deepened my understanding of being a scientist. Moreover, I was trained under your guidance to design and execute projects in a well-planned and organized manner. Your supervision taught me how to remain focused on the overarching goals without losing track, prioritize multiple projects, and convert experimental data into a clear and concise scientific paper. I appreciate your open-minded and inclusive attitude towards different cultures. Thank you for your warm-hearted help with my application for future positions and your valuable life advice.

Thanks to Job, we could gather in a wonderful and international group. It was a special and beautiful period in my life: I worked with people from different cultures, not as competitors but as teammates and colleagues who gave me a lot of help. Without them, I could not have completed my Ph.D. in such an enjoyable way. Therefore, I want to thank all my colleagues.

First, I want to thank Jennifer for supervising me at the beginning of my Ph.D. Thank you for your patience and the time you spent analyzing data with me, your time for performing experiments on confocal microscopy and rheology meter, your willingness to listen to my presentations even on weekends, and your encouragement when I got upset.

Michele, thank you for helping me with the oxazolone project. Without your suggestions, I would have spent more time on figuring out what was formed in the oxazolone-forming reaction cycle. Without your help with the kinetic model, I would not have finished this project so smoothly. You are so knowledgeable that I always turn to you when dealing with experimental problems. Also, thank you for your suggestions of being a patient listener (80% of the time) to my complaints and problems in my life and telling me to be more polite and less

direct when I speak English. Even though you imitated how I spoke and walked and sometimes made fun of me, you made my Ph.D. more interesting.

Hector, thank you for your help fitting all the data in the kinetic model for the N-acylurea project and the oxazolone-droplet project. Your critical thinking, patience, and persistence made the model sounder. Thank you for reviewing my presentations, giving helpful feedback on them, correcting my paper, and teaching me how to code in Python. Also, thank you for always listening to my complaints and problems in my life and giving helpful advice. You are a very humorous and pleasant person to talk with, so thank you for making the last part of my Ph.D. even more interesting.

Brigitte, thank you for helping with the project of tuning reciprocal coupling via molecular design. We collaborated very well, and I really enjoyed working with you. Thank you for explaining many technical protocols, such as the ThT / Nile red assay, NMR kinetics, titration, ibid chamber coating, sample preparations for confocal experiments, video analysis of confocal kinetics in Fiji, etc. Also, thank you very much for helping me with the paperwork, like "Dienstreiseantrag," and making calls to my doctors.

Michi, thank you for writing a review with me and giving us a safety introduction every year. I enjoyed the cheerful lunch on Tuesday when you brought us "Kapfel". Despite not having a sweet tooth, it was still a great time with you.

Alex, thank you for preparing all the samples for cryo-TEM and taking the images for my projects. Sometimes, you repeat several times, which is quite time-consuming and complicated. Thank you for showing me how to synthesize gold nanoparticles and answering all my (stupid) questions regarding coacervates very patiently every time. Also, you like Asian food and can be resistant to spicy food. You are always an active participant in our hotpot, which also motivates me to organize it.

Laura, thank you for showing me how to synthesize gold nanoparticles and peptides manually and how to use the plate reader, Andrew robot, and DLS. You are skilled at initiating conversations and creating a lively atmosphere in our group, especially during every lunch. You have excellent organizational skills and often plan post-work activities. Also, you helped me a lot with my life: making phone calls for me or going together with me whenever German is the communicating language, helping me with moving, giving suggestions for my tricky problems, and comforting me when I feel sad. Thank you, Laura, for all these things. Without you, my Ph.D. life abroad would be boring and difficult.

Kun, thank you for helping me with technical guidance on most instruments in our lab, measuring a lot of MS samples for me, and introducing me to our group when I joined. Also,

12. References

1.   Tiezzi, E. B. P.; Pulselli, R. M.; Marchettini, N.;Tiezzi, E., *Dissipative structures in nature and human systems. Design & Nature IV: Comparing design in nature with science and engineering*. WitPress: Boston, 2008.

2.   Bergé, P.;Dubois, M. Rayleigh-bénard convection. *Contemp. Phys.* **2006,** *25* (6), 535-582.

3.   Ackerson, B. J.; Beier, R. A.;Martin, D. L. Ground level air convection produces frost damage patterns in turfgrass. *Int. J. Biometeorol.* **2015,** *59* (11), 1655-65.

4.   Zhabotinsky, A. Belousov-Zhabotinsky reaction. *Scholarpedia* **2007,** *2* (9).

5.   Hudson, J. L.;Mankin, J. C. Chaos in the Belousov–Zhabotinskii reaction. *J. Chem. Phys.* **1981,** *74* (11), 6171-6177.

6.   Kondepudi, D. K.; De Bari, B.;Dixon, J. A. Dissipative Structures, Organisms and Evolution. *Entropy* **2020,** *22* (11), 1305.

7.   Goldbeter, A. Dissipative structures in biological systems: bistability, oscillations, spatial patterns and waves. *Phil. Trans. R. Soc. A* **2018,** *376* (2124), 20170376.

8.   van Rossum, S. A. P.; Tena-Solsona, M.; van Esch, J. H.; Eelkema, R.;Boekhoven, J. Dissipative out-of-equilibrium assembly of man-made supramolecular materials. *Chem. Soc. Rev.* **2017,** *46* (18), 5519-5535.

9.   Mattia, E.;Otto, S. Supramolecular systems chemistry. *Nat. Nanotechnol.* **2015,** *10* (2), 111-9.

10.   Whitesides, G. M.;Grzybowski, B. Self-assembly at all scales. *Science* **2002,** *295* (5564), 2418-21.

11.   Luisi, P. L. About various definitions of life. *Orig. Life. Evol. Biosph.* **1998,** *28* (4-6), 613-22.

12.   Szostak, J. W.; Bartel, D. P.;Luisi, P. L. Synthesizing life. *Nature* **2001,** *409* (6818), 387-90.

13.   Yewdall, N. A.; Mason, A. F.;van Hest, J. C. M. The hallmarks of living systems: towards creating artificial cells. *Interface Focus* **2018,** *8* (5), 20180023.

14.   Mazzarello, P. A unifying concept: the history of cell theory. *Nat. Cell. Biol.* **1999,** *1* (1), E13-5.

15.   Lammer, H.; Bredehöft, J. H.; Coustenis, A.; Khodachenko, M. L.; Kaltenegger, L.; Grasset, O.; Prieur, D.; Raulin, F.; Ehrenfreund, P.; Yamauchi, M.; Wahlund, J. E.; Grießmeier, J. M.; Stangl, G.; Cockell, C. S.; Kulikov, Y. N.; Grenfell, J. L.;Rauer, H. What makes a planet habitable? *Astron. Astrophys. Rev.* **2009,** *17* (2), 181-249.

16.   Benner, S. A. Defining life. *Astrobiology* **2010,** *10* (10), 1021-30.

17.   Schrodinger, E., *What is Life?: With Mind and Matter and Autobiographical Sketches*. Cambridge University Press: 2012.

18.   van Ravensteijn, B. G. P.; Voets, I. K.; Kegel, W. K.;Eelkema, R. Out-of-Equilibrium Colloidal Assembly Driven by Chemical Reaction Networks. *Langmuir* **2020,** *36* (36), 10639-10656.

19.   Needleman, D.;Dogic, Z. Active matter at the interface between materials science and cell biology. *Nat. Rev. Mater.* **2017,** *2* (9), 17048.

20.   Das, M.; Schmidt, C. F.;Murrell, M. Introduction to Active Matter. *Soft Matter* **2020,** *16* (31), 7185-7190.

21.   Walsh, C. T.; Tu, B. P.;Tang, Y. Eight Kinetically Stable but Thermodynamically Activated Molecules that Power Cell Metabolism. *Chem. Rev.* **2018,** *118* (4), 1460-1494.

22.   Conde, C.;Caceres, A. Microtubule assembly, organization and dynamics in axons and dendrites. *Nat. Rev. Neurosci.* **2009,** *10* (5), 319-32.

23.   Cooper, G. M., *The Cell: A Molecular Approach. 2nd edition*. Sinauer Associates: 2000.

24.   Horio, T.;Murata, T. The role of dynamic instability in microtubule organization. *Front. Plant. Sci.* **2014,** *5*, 511.

25.   Brouhard, G. J.;Rice, L. M. Microtubule dynamics: an interplay of biochemistry and mechanics. *Nat. Rev. Mol. Cell. Biol.* **2018,** *19* (7), 451-463.

26.   Lodish, H.; Berk, A.; Matsudaira, P.; Kaiser, C. A.; Krieger, M.; Scott, M. P.; Zipursky, L.;Darnell, J., *Molecular Cell Biology: 5th Edition*. W. H. Freeman: 2003.

27.   Sweeney, H. L.;Holzbaur, E. L. F. Motor Proteins. *Cold. Spring. Harb. Perspect. Biol.* **2018,** *10* (5), a021931

28.   Sugi, H.; Minoda, H.; Inayoshi, Y.; Yumoto, F.; Miyakawa, T.; Miyauchi, Y.; Tanokura, M.; Akimoto, T.; Kobayashi, T.; Chaen, S.;Sugiura, S. Direct demonstration of the cross-bridge recovery stroke in muscle thick filaments in aqueous solution by using the hydration chamber. *Proc. Natl. Acad. Sci.* **2008,** *105* (45), 17396-401.

29.   Gomes, E.;Shorter, J. The molecular language of membraneless organelles. *J. Biol. Chem.* **2019,** *294* (18), 7115-7127.

30.   Zhang, Y.; Kang, J. Y.; Liu, M.;Huang, Y. Diverse roles of biomolecular condensation in eukaryotic translational regulation. *RNA. Biol.* **2023,** *20* (1), 893-907.

31.   Boeynaems, S.; Alberti, S.; Fawzi, N. L.; Mittag, T.; Polymenidou, M.; Rousseau, F.; Schymkowitz, J.; Shorter, J.; Wolozin, B.; Van Den Bosch, L.; Tompa, P.;Fuxreiter, M. Protein Phase Separation: A New Phase in Cell Biology. *Trends. Cell. Biol.* **2018,** *28* (6), 420-435.

32.   Sehgal, P. B.; Westley, J.; Lerea, K. M.; DiSenso-Browne, S.;Etlinger, J. D. Biomolecular condensates in cell biology and virology: Phase-separated membraneless organelles (MLOs). *Anal. Biochem.* **2020,** *597*, 113691.

33.   Banani, S. F.; Lee, H. O.; Hyman, A. A.;Rosen, M. K. Biomolecular condensates: organizers of cellular biochemistry. *Nat. Rev. Mol. Cell Biol.* **2017,** *18* (5), 285-298.

34.   Alberti, S.;Hyman, A. A. Biomolecular condensates at the nexus of cellular stress, protein aggregation disease and ageing. *Nat. Rev. Mol. Cell. Biol.* **2021,** *22* (3), 196-213.

35.   Alberti, S.;Dormann, D. Liquid-Liquid Phase Separation in Disease. *Annu. Rev. Genet.* **2019,** *53*, 171-194.

36.   Nedelsky, N. B.;Taylor, J. P. Bridging biophysics and neurology: aberrant phase transitions in neurodegenerative disease. *Nat. Rev. Neurol.* **2019,** *15* (5), 272-286.

37.   Tsang, B.; Arsenault, J.; Vernon, R. M.; Lin, H.; Sonenberg, N.; Wang, L. Y.; Bah, A.;Forman-Kay, J. D. Phosphoregulated FMRP phase separation models activity-dependent translation through bidirectional control of mRNA granule formation. *Proc. Natl. Acad. Sci.* **2019,** *116* (10), 4218-4227.

38.   Snead, W. T.;Gladfelter, A. S. The Control Centers of Biomolecular Phase Separation: How Membrane Surfaces, PTMs, and Active Processes Regulate Condensation. *Mol. Cell.* **2019,** *76* (2), 295-305.

39.   Lee, J. M.; Hammaren, H. M.; Savitski, M. M.;Baek, S. H. Control of protein stability by post-translational modifications. *Nat. Commun.* **2023,** *14* (1), 201.

40.   Santoro, M. R.; Bray, S. M.;Warren, S. T. Molecular mechanisms of fragile X syndrome: a twenty-year perspective. *Annu. Rev. Pathol.* **2012,** *7*, 219-45.

41.   D'Incal, C.; Broos, J.; Torfs, T.; Kooy, R. F.;Vanden Berghe, W. Towards Kinase Inhibitor Therapies for Fragile X Syndrome: Tweaking Twists in the Autism Spectrum Kinase Signaling Network. *Cells* **2022,** *11* (8), 1325.

42.   Bartley, C. M.; O'Keefe, R. A.; Blice-Baum, A.; Mihailescu, M. R.; Gong, X.; Miyares, L.; Karaca, E.;Bordey, A. Mammalian FMRP S499 Is Phosphorylated by CK2 and Promotes Secondary Phosphorylation of FMRP. *eNeuro* **2016,** *3* (6), e0092.

43.   Wang, J. T.; Smith, J.; Chen, B. C.; Schmidt, H.; Rasoloson, D.; Paix, A.; Lambrus, B. G.; Calidas, D.; Betzig, E.;Seydoux, G. Regulation of RNA granule dynamics by phosphorylation of serine-rich, intrinsically disordered proteins in C. elegans. *Elife* **2014,** *3*, e04591.

44.   Popkin, G. The physics of life. *Nature* **2016,** *529* (7584), 16-8.

45.   Westheimer, F. H. Why nature chose phosphates. *Science* **1987,** *235* (4793), 1173-8.

46.   Kiani, F. A.;Fischer, S. Comparing the catalytic strategy of ATP hydrolysis in biomolecular motors. *Phys. Chem. Chem. Phys.* **2016,** *18* (30), 20219-33.

47.   Heuser, T.; Steppert, A. K.; Lopez, C. M.; Zhu, B.;Walther, A. Generic concept to program the time domain of self-assemblies with a self-regulation mechanism. *Nano. Lett.* **2015,** *15* (4), 2213-9.

48.   Chen, X.; Wurbser, M. A.;Boekhoven, J. Chemically Fueled Supramolecular Materials. *Acc. Mater. Res.* **2023,** *4* (5), 416-426.

49.   Sorrenti, A.; Leira-Iglesias, J.; Sato, A.;Hermans, T. M. Non-equilibrium steady states in supramolecular polymerization. *Nat. Commun.* **2017,** *8*, 15899.

50.   Boekhoven, J.; Brizard, A. M.; Kowlgi, K. N.; Koper, G. J.; Eelkema, R.;van Esch, J. H. Dissipative self-assembly of a molecular gelator by using a chemical fuel. *Angew. Chem. Int. Ed.* **2010,** *49* (28), 4825-8.

51.   Boekhoven, J.; Hendriksen, W. E.; Koper, G. J.; Eelkema, R.;van Esch, J. H. Transient assembly of active materials fueled by a chemical reaction. *Science* **2015,** *349* (6252), 1075-9.

52.   van Ravensteijn, B. G. P.; Hendriksen, W. E.; Eelkema, R.; van Esch, J. H.;Kegel, W. K. Fuel-Mediated Transient Clustering of Colloidal Building Blocks. *J. Am. Chem. Soc.* **2017,** *139* (29), 9763-9766.

53.   Leira-Iglesias, J.; Tassoni, A.; Adachi, T.; Stich, M.;Hermans, T. M. Oscillations, travelling fronts and patterns in a supramolecular system. *Nat. Nanotechnol.* **2018,** *13* (11), 1021-1027.

54.   Sharko, A.; Spitzbarth, B.; Hermans, T. M.;Eelkema, R. Redox-Controlled Shunts in a Synthetic Chemical Reaction Cycle. *J. Am. Chem. Soc.* **2023,** *145* (17), 9672-9678.

55.   Yang, S.; Schaeffer, G.; Mattia, E.; Markovitch, O.; Liu, K.; Hussain, A. S.; Ottele, J.; Sood, A.;Otto, S. Chemical Fueling Enables Molecular Complexification of Self-Replicators*. *Angew. Chem. Int. Ed.* **2021,** *60* (20), 11344-11349.

56.   Singh, N.; Lainer, B.; Formon, G. J. M.; De Piccoli, S.;Hermans, T. M. Re-programming Hydrogel Properties Using a Fuel-Driven Reaction Cycle. *J. Am. Chem. Soc.* **2020,** *142* (9), 4083-4087.

57.   Singh, N.; Lopez-Acosta, A.; Formon, G. J. M.;Hermans, T. M. Chemically Fueled Self-Sorted Hydrogels. *J. Am. Chem. Soc.* **2022,** *144* (1), 410-415.

58.   Dambenieks, A. K.; Vu, P. H. Q.;Fyles, T. M. Dissipative assembly of a membrane transport system. *Chem. Sci.* **2014,** *5* (9), 3396-3403.

59.   Morrow, S. M.; Colomer, I.;Fletcher, S. P. A chemically fuelled self-replicator. *Nat. Commun.* **2019,** *10* (1), 1011.

60.   Klemm, B.; Lewis, R. W.; Piergentili, I.;Eelkema, R. Temporally programmed polymer - solvent interactions using a chemical reaction network. *Nat. Commun.* **2022,** *13* (1), 6242.

61.   Fusi, G.; Del Giudice, D.; Skarsetz, O.; Di Stefano, S.;Walther, A. Autonomous Soft Robots Empowered by Chemical Reaction Networks. *Adv. Mater.* **2023,** *35* (7), e2209870.

62.   Heuser, T.; Weyandt, E.;Walther, A. Biocatalytic Feedback-Driven Temporal Programming of Self-Regulating Peptide Hydrogels. *Angew. Chem. Int. Ed.* **2015,** *54* (45), 13258-62.

63.   Tena-Solsona, M.; Riess, B.; Grotsch, R. K.; Lohrer, F. C.; Wanzke, C.; Kasdorf, B.; Bausch, A. R.; Muller-Buschbaum, P.; Lieleg, O.;Boekhoven, J. Non-equilibrium dissipative supramolecular materials with a tunable lifetime. *Nat. Commun.* **2017,** *8*, 15895.

64.   Kariyawasam, L. S.;Hartley, C. S. Dissipative Assembly of Aqueous Carboxylic Acid Anhydrides Fueled by Carbodiimides. *J. Am. Chem. Soc.* **2017,** *139* (34), 11949-11955.

65.   Gilles, M. A.; Hudson, A. Q.;Borders, C. L., Jr. Stability of water-soluble carbodiimides in aqueous solution. *Anal. Biochem.* **1990,** *184* (2), 244-8.

66.   Tena-Solsona, M.; Wanzke, C.; Riess, B.; Bausch, A. R.;Boekhoven, J. Self-selection of dissipative assemblies driven by primitive chemical reaction networks. *Nat. Commun.* **2018,** *9* (1), 2044.

67.   Schnitter, F.; Bergmann, A. M.; Winkeljann, B.; Rodon Fores, J.; Lieleg, O.;Boekhoven, J. Synthesis and characterization of chemically fueled supramolecular materials driven by carbodiimide-based fuels. *Nat. Protoc.* **2021,** *16* (8), 3901-3932.

68.   Grotsch, R. K.; Angi, A.; Mideksa, Y. G.; Wanzke, C.; Tena-Solsona, M.; Feige, M. J.; Rieger, B.;Boekhoven, J. Dissipative Self-Assembly of Photoluminescent Silicon Nanocrystals. *Angew. Chem. Int. Ed.* **2018,** *57* (44), 14608-14612.

69.   Grotsch, R. K.; Wanzke, C.; Speckbacher, M.; Angi, A.; Rieger, B.;Boekhoven, J. Pathway Dependence in the Fuel-Driven Dissipative Self-Assembly of Nanoparticles. *J. Am. Chem. Soc.* **2019,** *141* (25), 9872-9878.

70.   Dai, K.; Fores, J. R.; Wanzke, C.; Winkeljann, B.; Bergmann, A. M.; Lieleg, O.;Boekhoven, J. Regulating Chemically Fueled Peptide Assemblies by Molecular Design. *J. Am. Chem. Soc.* **2020,** *142* (33), 14142-14149.

71.   Kriebisch, B. A. K.; Jussupow, A.; Bergmann, A. M.; Kohler, F.; Dietz, H.; Kaila, V. R. I.;Boekhoven, J. Reciprocal Coupling in Chemically Fueled Assembly: A Reaction Cycle Regulates Self-Assembly and Vice Versa. *J. Am. Chem. Soc.* **2020,** *142* (49), 20837-20844.

72.   Lomant, A. J.;Fairbanks, G. Chemical probes of extended biological structures: synthesis and properties of the cleavable protein cross-linking reagent [35S]dithiobis(succinimidyl propionate). *J. Mol. Biol.* **1976,** *104* (1), 243-61.

73.   Moore, J. S.;Stupp, S. I. Room temperature polyesterification. *Macromolecules* **2002,** *23* (1), 65-70.

74.   Schnitter, F.;Boekhoven, J. A Method to Quench Carbodiimide-Fueled Self-Assembly. *ChemSystemsChem* **2020,** *3* (1), e2000001.

75.   Panja, S.;Adams, D. J. Chemical crosslinking in 'reactive' multicomponent gels. *Chem. Commun.* **2022,** *58* (37), 5622-5625.

76.   Panja, S.; Dietrich, B.;Adams, D. J. Chemically Fuelled Self-Regulating Gel-to-Gel Transition. *ChemSystemsChem* **2019,** *2* (1), e1900038.

77.   Bal, S.; Das, K.; Ahmed, S.;Das, D. Chemically Fueled Dissipative Self-Assembly that Exploits Cooperative Catalysis. *Angew. Chem. Int. Ed.* **2019,** *58* (1), 244-247.

78.   Mondal, S.;Haldar, D. A transient non-covalent hydrogel by a supramolecular gelator with dynamic covalent bonds. *New J. Chem.* **2021,** *45* (10), 4773-4779.

79.   Chen, X.; Kriebisch, B. A. K.; Bergmann, A. M.;Boekhoven, J. Design rules for reciprocal coupling in chemically fueled assembly. *Chem. Sci.* **2023,** *14* (37), 10176-10183.

80.   Donau, C.; Spath, F.; Sosson, M.; Kriebisch, B. A. K.; Schnitter, F.; Tena-Solsona, M.; Kang, H. S.; Salibi, E.; Sattler, M.; Mutschler, H.;Boekhoven, J. Active coacervate droplets as a model for membraneless organelles and protocells. *Nat. Commun.* **2020,** *11* (1), 5167.

81.   Spath, F.; Donau, C.; Bergmann, A. M.; Kranzlein, M.; Synatschke, C. V.; Rieger, B.;Boekhoven, J. Molecular Design of Chemically Fueled Peptide-Polyelectrolyte Coacervate-Based Assemblies. *J. Am. Chem. Soc.* **2021,** *143* (12), 4782-4789.

82.   Donau, C.; Spath, F.; Stasi, M.; Bergmann, A. M.;Boekhoven, J. Phase Transitions in Chemically Fueled, Multiphase Complex Coacervate Droplets. *Angew. Chem. Int. Ed.* **2022,** *61* (46), e202211905.

83.   Bergmann, A. M.; Bauermann, J.; Bartolucci, G.; Donau, C.; Stasi, M.; Holtmannspotter, A. L.; Julicher, F.; Weber, C. A.;Boekhoven, J. Liquid spherical shells are a non-equilibrium steady state of active droplets. *Nat. Commun.* **2023,** *14* (1), 6552.

84.   Spath, F.; Maier, A. S.; Stasi, M.; Bergmann, A. M.; Halama, K.; Wenisch, M.; Rieger, B.;Boekhoven, J. The Role of Chemically Innocent Polyanions in Active, Chemically Fueled Complex Coacervate Droplets. *Angew. Chem. Int. Ed.* **2023,** *62* (41), e202309318.

85.   Niebuur, B. J.; Hegels, H.; Tena-Solsona, M.; Schwarz, P. S.; Boekhoven, J.;Papadakis, C. M. Droplet Formation by Chemically Fueled Self-Assembly: The Role of Precursor Hydrophobicity. *J. Phys. Chem. B.* **2021,** *125* (49), 13542-13551.

86.   Schwarz, P. S.; Laha, S.; Janssen, J.; Huss, T.; Boekhoven, J.;Weber, C. A. Parasitic behavior in competing chemically fueled reaction cycles. *Chem. Sci.* **2021,** *12* (21), 7554-7560.

87.   Schwarz, P. S.; Tebcharani, L.; Heger, J. E.; Muller-Buschbaum, P.;Boekhoven, J. Chemically fueled materials with a self-immolative mechanism: transient materials with a fast on/off response. *Chem. Sci.* **2021,** *12* (29), 9969-9976.

88.   Wanzke, C.; Tena-Solsona, M.; Rieß, B.; Tebcharani, L.;Boekhoven, J. Active droplets in a hydrogel release drugs with a constant and tunable rate. *Mater. Horiz.* **2020,** *7* (5), 1397-1403.

89.   Riess, B.; Wanzke, C.; Tena-Solsona, M.; Grotsch, R. K.; Maity, C.;Boekhoven, J. Dissipative assemblies that inhibit their deactivation. *Soft Matter* **2018,** *14* (23), 4852-4859.

90.   Wanzke, C.; Jussupow, A.; Kohler, F.; Dietz, H.; Kaila, V. R. I.;Boekhoven, J. Dynamic Vesicles Formed By Dissipative Self-Assembly. *ChemSystemsChem* **2019,** *2* (1), e1900044.

91.   Englert, A.; Vogel, J. F.; Bergner, T.; Loske, J.;von Delius, M. A Ribonucleotide <--> Phosphoramidate Reaction Network Optimized by Computer-Aided Design. *J. Am. Chem. Soc.* **2022,** *144* (33), 15266-15274.

92.   Würbser, M. A.; Schwarz, P. S.; Heckel, J.; Bergmann, A. M.; Walther, A.;Boekhoven, J. Chemically Fueled Block Copolymer Self-Assembly into Transient Nanoreactors**. *ChemSystemsChem* **2021,** *3* (5), e2100015.

93.   Borsley, S.; Kreidt, E.; Leigh, D. A.;Roberts, B. M. W. Autonomous fuelled directional rotation about a covalent single bond. *Nature* **2022,** *604* (7904), 80-85.

94.   Borsley, S.; Leigh, D. A.; Roberts, B. M. W.;Vitorica-Yrezabal, I. J. Tuning the Force, Speed, and Efficiency of an Autonomous Chemically Fueled Information Ratchet. *J. Am. Chem. Soc.* **2022,** *144* (37), 17241-17248.

95.   Stasi, M.; Monferrer, A.; Babl, L.; Wunnava, S.; Dirscherl, C. F.; Braun, D.; Schwille, P.; Dietz, H.;Boekhoven, J. Regulating DNA-Hybridization Using a Chemically Fueled Reaction Cycle. *J. Am. Chem. Soc.* **2022,** *144* (48), 21939-21947.

96.   Rodon-Fores, J.; Wurbser, M. A.; Kretschmer, M.; Riess, B.; Bergmann, A. M.; Lieleg, O.;Boekhoven, J. A chemically fueled supramolecular glue for self-healing gels. *Chem. Sci.* **2022,** *13* (38), 11411-11421.

97.   Dodo, O. J.; Petit, L.; Rajawasam, C. W. H.; Hartley, C. S.;Konkolewicz, D. Tailoring Lifetimes and Properties of Carbodiimide-Fueled Covalently Cross-linked Polymer Networks. *Macromolecules* **2021,** *54* (21), 9860-9867.

98.   Cheng, M.; Qian, C.; Ding, Y.; Chen, Y.; Xiao, T.; Lu, X.; Jiang, J.;Wang, L. Writable and Self-Erasable Hydrogel Based on Dissipative Assembly Process from Multiple Carboxyl Tetraphenylethylene Derivative. *ACS. Mater. Lett.* **2020,** *2* (4), 425-429.

99.   Kriebisch, B. A. K.; Kriebisch, C. M. E.; Bergmann, A. M.; Wanzke, C.; Tena-Solsona, M.;Boekhoven, J. Tuning the Kinetic Trapping in Chemically Fueled Self-Assembly**. *ChemSystemsChem* **2022,** *5* (1), e202200035.

100.   Shin, Y.;Brangwynne, C. P. Liquid phase condensation in cell physiology and disease. *Science* **2017,** *357* (6357), 1253.

101.   Lyon, A. S.; Peeples, W. B.;Rosen, M. K. A framework for understanding the functions of biomolecular condensates across scales. *Nat. Rev. Mol. Cell. Biol.* **2021,** *22* (3), 215-235.

102.   Zwicker, D.; Hyman, A. A.;Julicher, F. Suppression of Ostwald ripening in active emulsions. *Phys. Rev. E Stat. Nonlinear Soft Matter Phys.* **2015,** *92* (1), 012317.

103.   Zwicker, D.; Seyboldt, R.; Weber, C. A.; Hyman, A. A.;Jülicher, F. Growth and division of active droplets provides a model for protocells. *Nat. Phys.* **2016,** *13* (4), 408-413.

104.   Weber, C. A.; Zwicker, D.; Julicher, F.;Lee, C. F. Physics of active emulsions. *Rep. Prog. Phys.* **2019,** *82* (6), 064601.

105.   Fryd, M. M.;Mason, T. G. Advanced nanoemulsions. *Annu. Rev. Phys. Chem.* **2012,** *63*, 493-518.

106.   Taylor, P. Ostwald ripening in emulsions. *Adv. Colloid Interface Sci.* **1998,** *75* (2), 107-163.

107.   Ostwald, W. Studien über die Bildung und Umwandlung fester Körper. *Z. Phys. Chem.* **1897,** *22U* (1), 289-330.

108.   Navascues, G. Liquid surfaces: theory of surface tension. *Rep. Prog. Phys.* **1979,** *42* (7), 1131-1186.

109.   Donau, C.;Boekhoven, J. The chemistry of chemically fueled droplets. *Trends Chem.* **2023,** *5* (1), 45-60.

110.   Zwicker, D.; Decker, M.; Jaensch, S.; Hyman, A. A.;Julicher, F. Centrosomes are autocatalytic droplets of pericentriolar material organized by centrioles. *Proc. Natl. Acad. Sci.* **2014,** *111* (26), E2636-45.

111.   Tena-Solsona, M.; Janssen, J.; Wanzke, C.; Schnitter, F.; Park, H.; Rieß, B.; Gibbs, J. M.; Weber, C. A.;Boekhoven, J. Accelerated Ripening in Chemically Fueled Emulsions**. *ChemSystemsChem* **2020,** *3* (2), e2000034

112.   Abbas, M.; Lipinski, W. P.; Wang, J.;Spruijt, E. Peptide-based coacervates as biomimetic protocells. *Chem. Soc. Rev.* **2021,** *50* (6), 3690-3705.

113.   Yewdall, N. A.; André, A. A. M.; Lu, T.;Spruijt, E. Coacervates as models of membraneless organelles. *Curr. Opin. Colloid Interface Sci.* **2021,** *52*, 101416.

114.   Sing, C. E.;Perry, S. L. Recent progress in the science of complex coacervation. *Soft Matter* **2020,** *16* (12), 2885-2914.

115.   Blocher, W. C.;Perry, S. L. Complex coacervate-based materials for biomedicine. *Wiley Interdiscip. Rev. Nanomed. Nanobiotechnol.* **2017,** *9* (4), e1442.

116.   Küffner, A. M.; Prodan, M.; Zuccarini, R.; Capasso Palmiero, U.; Faltova, L.;Arosio, P. Acceleration of an Enzymatic Reaction in Liquid Phase Separated Compartments Based on Intrinsically Disordered Protein Domains. *ChemSystemsChem* **2020,** *2* (4), e2000001.

117.   Faltova, L.; Kuffner, A. M.; Hondele, M.; Weis, K.;Arosio, P. Multifunctional Protein Materials and Microreactors using Low Complexity Domains as Molecular Adhesives. *ACS Nano* **2018,** *12* (10), 9991-9999.

118.   Abbas, M.; Lipinski, W. P.; Nakashima, K. K.; Huck, W. T. S.;Spruijt, E. A short peptide synthon for liquid-liquid phase separation. *Nat. Chem.* **2021,** *13* (11), 1046-1054.

119.   Sun, Y.; Lau, S. Y.; Lim, Z. W.; Chang, S. C.; Ghadessy, F.; Partridge, A.;Miserez, A. Phase-separating peptides for direct cytosolic delivery and redox-activated release of macromolecular therapeutics. *Nat. Chem.* **2022,** *14* (3), 274-283.

120.   van der Gucht, J.; Spruijt, E.; Lemmers, M.;Cohen Stuart, M. A. Polyelectrolyte complexes: bulk phases and colloidal systems. *J. Colloid Interface Sci.* **2011,** *361* (2), 407-22.

121.   Spruijt, E.; Westphal, A. H.; Borst, J. W.; Cohen Stuart, M. A.;van der Gucht, J. Binodal Compositions of Polyelectrolyte Complexes. *Macromolecules* **2010,** *43* (15), 6476-6484.

122.   Chollakup, R.; Smitthipong, W.; Eisenbach, C. D.;Tirrell, M. Phase Behavior and Coacervation of Aqueous Poly(acrylic acid)−Poly(allylamine) Solutions. *Macromolecules* **2010,** *43* (5), 2518-2528.

123.   Turgeon, S. L.; Schmitt, C.;Sanchez, C. Protein–polysaccharide complexes and coacervates. *Curr. Opin. Colloid Interface Sci.* **2007,** *12* (4-5), 166-178.

124.   Elbaum-Garfinkle, S.; Kim, Y.; Szczepaniak, K.; Chen, C. C.; Eckmann, C. R.; Myong, S.;Brangwynne, C. P. The disordered P granule protein LAF-1 drives phase separation into droplets with tunable viscosity and dynamics. *Proc. Natl. Acad. Sci. U.S.A.* **2015,** *112* (23), 7189-94.

125.   de Kruif, C. G.; Weinbreck, F.;de Vries, R. Complex coacervation of proteins and anionic polysaccharides. *Curr. Opin. Colloid Interface Sci.* **2004,** *9* (5), 340-349.

126.   Schmitt, C.;Turgeon, S. L. Protein/polysaccharide complexes and coacervates in food systems. *Adv. Colloid Interface Sci.* **2011,** *167* (1-2), 63-70.

127.   Priftis, D.;Tirrell, M. Phase behaviour and complex coacervation of aqueous polypeptide solutions. *Soft Matter* **2012,** *8* (36), 9396-9405.

128.   Black, K. A.; Priftis, D.; Perry, S. L.; Yip, J.; Byun, W. Y.;Tirrell, M. Protein Encapsulation via Polypeptide Complex Coacervation. *ACS Macro Lett.* **2014,** *3* (10), 1088-1091.

129.   Cao, S.; Ivanov, T.; Heuer, J.; Ferguson, C. T. J.; Landfester, K.;Caire da Silva, L. Dipeptide coacervates as artificial membraneless organelles for bioorthogonal catalysis. *Nat. Commun.* **2024,** *15* (1), 39.

130.   Aumiller, W. M., Jr.; Pir Cakmak, F.; Davis, B. W.;Keating, C. D. RNA-Based Coacervates as a Model for Membraneless Organelles: Formation, Properties, and Interfacial Liposome Assembly. *Langmuir* **2016,** *32* (39), 10042-10053.

131.   Aumiller, W. M., Jr.;Keating, C. D. Phosphorylation-mediated RNA/peptide complex coacervation as a model for intracellular liquid organelles. *Nat. Chem.* **2016,** *8* (2), 129-37.

132.   Jain, A.;Vale, R. D. RNA phase transitions in repeat expansion disorders. *Nature* **2017,** *546* (7657), 243-247.

133.   Spoelstra, W. K.; van der Sluis, E. O.; Dogterom, M.;Reese, L. Nonspherical Coacervate Shapes in an Enzyme-Driven Active System. *Langmuir* **2020,** *36* (8), 1956-1964.

134.   Rekhi, S.; Garcia, C. G.; Barai, M.; Rizuan, A.; Schuster, B. S.; Kiick, K. L.;Mittal, J. Expanding the molecular language of protein liquid-liquid phase separation. *Nat. Chem.* **2024.**

135.   Kudlay, A.; Ermoshkin, A. V.;Olvera de la Cruz, M. Complexation of Oppositely Charged Polyelectrolytes: Effect of Ion Pair Formation. *Macromolecules* **2004,** *37* (24), 9231-9241.

136. Tsuchida, E. Formation of Polyelectrolyte Complexes and Their Structures. *J. Macromol. Sci. A* **1994,** *31* (1), 1-15.

137. Fisher, R. S.;Elbaum-Garfinkle, S. Tunable multiphase dynamics of arginine and lysine liquid condensates. *Nat. Commun.* **2020,** *11* (1), 4628.

138. Gallivan, J. P.;Dougherty, D. A. Cation-pi interactions in structural biology. *Proc. Natl. Acad. Sci. U.S.A.* **1999,** *96* (17), 9459-64.

139. Perry, S.; Li, Y.; Priftis, D.; Leon, L.;Tirrell, M. The Effect of Salt on the Complex Coacervation of Vinyl Polyelectrolytes. *Polymers* **2014,** *6* (6), 1756-1772.

140. Bohidar, H.; Dubin, P. L.; Majhi, P. R.; Tribet, C.;Jaeger, W. Effects of protein-polyelectrolyte affinity and polyelectrolyte molecular weight on dynamic properties of bovine serum albumin-poly(diallyldimethylammonium chloride) coacervates. *Biomacromolecules* **2005,** *6* (3), 1573-85.

141. Nakashima, K. K.; Baaij, J. F.;Spruijt, E. Reversible generation of coacervate droplets in an enzymatic network. *Soft Matter* **2018,** *14* (3), 361-367.

142. Martin, N.; Tian, L.; Spencer, D.; Coutable-Pennarun, A.; Anderson, J. L. R.;Mann, S. Photoswitchable Phase Separation and Oligonucleotide Trafficking in DNA Coacervate Microdroplets. *Angew. Chem. Int. Ed.* **2019,** *58* (41), 14594-14598.

143. Wee, W. A.; Sugiyama, H.;Park, S. Photoswitchable single-stranded DNA-peptide coacervate formation as a dynamic system for reaction control. *iScience* **2021,** *24* (12), 103455.

144. Deng, J.;Walther, A. Programmable and Chemically Fueled DNA Coacervates by Transient Liquid-Liquid Phase Separation. *Chem* **2020,** *6* (12), 3329-3343.